AC/DC : Automatic Crater Detection and Characterization

AC/DC : Détection et Caractérisation Automatique de Cratères

Thèse de doctorat de l'université Paris-Saclay

École doctorale n° 579, Sciences Mécaniques et Energétiques, Matériaux et Géosciences (SMEMaG)
Spécialité de doctorat: Géosciences
Graduate School : Géosciences, Climat, Environnement, Planètes.
Référent : Faculté des sciences d'Orsay

Thèse préparée dans l'unité de recherche **GEOPS (Université Paris-Saclay, CNRS)**, sous la direction de **Frédéric SCHMIDT**, Professeur et le co-encadrement de **François ANDRIEU**, Ingénieur de Recherche

Thèse soutenue à Paris-Saclay, le 06 Octobre 2025, par

Léonard MARTINEZ

Composition du jury

Membres du jury avec voix délibérative

Sylvain BOULEY Professeur, GEOPS, Université Paris-Saclay	Président
Marc HUERTAS-COMPANY Maître de Conférence HDR, Instituto de Astrofísica de Canarias	Rapporteur & Examinateur
Stéphane LE MOUELIC Ingénieur de Recherche HDR, LPG, Université de Nantes	Rapporteur & Examinateur
Myriam LEMELIN Professeure, CARTEL, Université de Sherbrooke	Examinatrice
Cathy QUANTIN-NATAF Professeure, LGL-TPE, Université Claude-Bernard Lyon1	Examinatrice

THESE DE DOCTORAT

NNT : 2025UPASJ015

“Pour explorer le champ des possibles,
le bricolage est la méthode la plus efficace.”

— Hubert Reeves

université
PARIS-SACLAY

ÉCOLE DOCTORALE
Sciences mécaniques et
énergétiques, matériaux
et géosciences (SMEMAG)

Titre: AC/DC : Détection et Caractérisation Automatique de Cratères

Mots clés: Planétologie ; Cratère d'impact ; Intelligence Artificielle ; Géomorphologie ; Géochronologie ; Télédétection.

Résumé: L'étude des cratères d'impact à la surface des corps telluriques constitue un outil central pour dater les terrains et reconstruire l'histoire géologique des planètes. Cette méthode repose toutefois sur une connaissance fine de la morphologie des cratères, car certaines morphologies, comme les cratères secondaires ou fortement dégradés, doivent être exclus des comptages sous peine de biaiser les résultats. Pendant cette thèse, nous avons développé de nouvelles méthodes de traitement en combinant à la fois des techniques d'apprentissage à base de réseaux de neurone artificiels et des méthodes de traitement d'images et d'analyse géomorphologique avancée. Grâce à cela nous sommes capables de détecter automatiquement les cratères présents dans les images à haute résolution, de corriger leur géométrie, puis de les classifier selon leur morphologie. Nous nous appuyons sur les mosaïques globales de Mars acquises par la caméra CTX et sur une base de données de cratères classifiés, que nous avons améliorées par une méthode de détection de cercles fondée sur la transformée de Hough. Cette étape améliore la précision géométrique des annotations, en recentrant automatiquement les cratères et en ajustant leur rayon au plus proche de la structure visible sur l'image. Nous avons ensuite conçu une méthode de détection multi-échelle permettant d'identifier tous les cratères, quelles que soient leur taille, géométrie, éclairement ou position en latitude / longitude. Chaque image est analysée à différentes résolutions, et les résultats sont fusionnés pour éviter les redondances. Nous avons entraîné un modèle de classification profond (YOLOv11) capable d'attribuer à chaque cratère l'une des quatre classes géomorphologiques : ordinaire, secondaire, fantôme ou à rempart fluidisé. La dernière partie porte sur la détermination de l'ordre de superposition des cratères, lorsqu'ils se recouvrent. L'ensemble constitue une suite d'outils robuste pour automatiser la cartographie géomorphologique planétaire, améliorer la fiabilité des datations et, à terme, faciliter l'analyse d'autres corps. Tous ces outils ont été évalués et validés sur des données totalement indépendantes de l'entrainement pour une utilisation scientifique avec des incertitudes maitrisées. En perspective, cette suite d'outils permettra de mieux appréhender les larges volumes de données de l'imagerie astronomique, car les objets d'intérêts sont souvent présents à plusieurs échelles. En particulier, nous proposons d'étudier la détection et la caractérisation de cratères à la surface des planètes et autres corps du système solaire.

Title: AC/DC: Automatic Crater Detection and Characterization

Keywords: Planetary Sciences ; Impact craters, Artificial Intelligence ; Geomorphology ; Geochronology ; Remote-sensing.

Abstract: The study of impact craters on the surface of terrestrial bodies is a central tool for dating geological units and reconstructing planetary histories. However, this method relies on a detailed understanding of crater morphology, as certain types — such as secondary or heavily degraded craters — must be excluded from crater counting to avoid significant biases. The objective of this thesis is to develop new methods that combine deep learning techniques based on artificial neural network architectures with advanced image processing and geomorphological analysis, in order to automatically detect craters in high-resolution imagery, refine their geometry, and classify them by morphology. We rely on global mosaics acquired by the CTX camera on Mars and on an existing classified crater database, which we refined using a circle detection method based on the Hough transform. This step improves the geometric accuracy of annotations by automatically recentering craters and adjusting their radii to best match the visible structures on the image. We then designed a multi-scale detection method capable of identifying all craters, regardless of their size, geometry, illumination conditions or position in latitude / longitude. Each image is analyzed at different resolutions, and results are merged to avoid redundancy. We trained a deep classification model (YOLOv11) capable of assigning each crater to one of four morphological classes: regular, secondary, ghost, or layered-rimmed. The last part consist in the determination of the superposition order, when the crater are overlapping each other. The resulting pipelines are a robust suite of tools for automating planetary geomorphological mapping, improving the reliability of surface dating, and ultimately supporting the analysis of other planetary bodies. All the tools have been evaluated and validated with data totally independent from the training dataset in order to have a scientific use with known uncertainties. In perspective, this suite of tools will help to better apprehend the large datasets of astronomical imaging, as objects of interest often appear at multiple spatial scales. In particular, we propose the detection and characterization of craters on planets and other planetary bodies of the Solar System.

Avant-Propos

Ce travail de thèse a été rédigé en anglais à l'aide de l'éditeur de texte Visual Studio Code ainsi que du système de composition de documents LaTeX, un choix motivé par la volonté d'assurer une présentation professionnelle tout au long du manuscrit et compte-tenu de la contribution au financement par l'Agence Spatiale Européenne (ESA). L'utilisation de l'anglais s'inscrit dans une démarche d'accessibilité et de science ouverte. En effet, la recherche en sciences planétaires étant une discipline impliquant bien souvent des collaborations internationales, il me tenait à coeur de rendre ce travail lisible et compréhensible par le plus grand nombre, qu'il s'agisse de chercheurs et de chercheuses, d'étudiants et d'étudiantes ou autre, en France comme à l'étranger. Les lecteurs et lectrices non-anglophones pourront lire une synthèse de ce travail en français dans la section Synthèse.

Afin de garantir la qualité linguistique du texte, un modèle de langage basé sur l'intelligence artificielle a été utilisé pour corriger les fautes d'orthographe et améliorer la clarté des formulations. Cette assistance numérique a permis de renforcer la rigueur et la lisibilité du manuscrit. Dans un souci de conservation de la précision scientifique du propos, ces modèles de langages n'ont jamais servi à générer du texte tel quel sans intervention humaine. Des modèles de langages ont également été utilisés pour générer du code Python et plus particulièrement pour la création de figures ou résoudre les problèmes liés à LaTeX.

Le contenu de cette thèse s'appuie sur trois années de recherche et de collaborations au sein de la communauté scientifique. Les travaux présentés ont conduit à la publication de trois articles dans des revues internationales à comité de lecture présentés dans ce manuscrit, dans les chapitres 3 et 4. Le chapitre 5 est en préparation et fera l'objet d'une publication qui sera soumise prochainement.

- **L.Martinez**, F. Andrieu, F. Schmidt, H. Talbot and M. S. Bentley, "Robust automatic crater detection at all latitudes on Mars with Deep-learning", 2025. In: Planetary and Space Science 260. doi: 10.1016/j.pss.2025.106053.

- **L.Martinez**, F. Andrieu, F. Schmidt and M. S. Bentley, "Automatic Crater Classification Using a Deep-learning-based Pipeline", 2025. In: Journal of Geophysical Research: Machine learning & Computation. Under Review (manuscript ID: 2025JH000737).

- Z. Zhang, F. Schmidt, Y. Su, ... , **L.Martinez**, & al. "A gigantic flow on Mars revealed by the Zhurong rover", 2025. In: PNAS. Under Review (manuscript ID: XXXXXXX).

- **L.Martinez**, F. Schmidt, F. Andrieu, "Deep Learning Approach for Crater Superposition Analysis: Towards Improved Planetary Surface Dating", 202X. In prep.

Ce travail m'a aussi donné l'opportunité de pouvoir présenter mes recherches dans un certain nombre de séminaires et de conférences dont trois oraux lors de conférences internationales majeures du domaine. Pour consulter la liste complète des conférences auxquelles j'ai participé, je vous invite à en consulter la liste sur ma page personnelle.

Je vous souhaite une bonne lecture de ce manuscrit et j'espère qu'il saura vous intéresser et vous apporter des connaissances voire de nouvelles idées quant à l'utilisation de l'intelligence artificielle dans le domaine des sciences planétaires.

Foreword

This doctoral work was written in English using the Visual Studio Code text editor and the LATEXdocument preparation system, a choice motivated by the desire to ensure a professional presentation throughout the manuscript and given the funding contribution of European Space Agency. The use of English is part of an approach aimed at accessibility and open science. Indeed, research in planetary sciences often involves international collaborations, and it was important to me to make this work readable and understandable to as many people as possible, whether researchers, students, or others. Non-English-speaking readers can find a summary of this work in French in section Synthesis.

To ensure the linguistic quality of the text, an artificial intelligence-based language model was used to correct spelling mistakes and improve the clarity of the formulations. This assistance helped me to enhance the rigor and readability of the manuscript. In order to preserve the scientific accuracy of the content, these language models were never used to generate text as-is without human intervention. Large language models were also used during this project to generate Python code, particularly for creating figures or debugging problems with LATEX.

The content of this thesis is based on three years of research and collaborations within the scientific community. The work presented has led to the publication of three articles in international peer-reviewed journals, which are included in this manuscript in chapters 3 and 4. Chapter 5 is in preparation and will be submitted for publication soon.

- **L. Martinez**, F. Andrieu, F. Schmidt, H. Talbot and M. S. Bentley, “Robust automatic crater detection at all latitudes on Mars with Deep-learning”, 2025. In: Planetary and Space Science 260. doi: 10.1016/j.pss.2025.106053.

- **L. Martinez**, F. Andrieu, F. Schmidt and M. S. Bentley, “Automatic Crater Classification Using a Deep-learning-based Pipeline”, 2025. In: Journal of Geophysical Research: Machine learning & Computation. Under Review (manuscript ID: 2025JH000737).

- Z. Zhang, F. Schmidt, Y. Su, ... , **L.Martinez**, & al. “A gigantic flow on Mars revealed by the Zhurong rover”, 2025. In: PNAS. Under Review (manuscript ID: XXXXXXX).

- **L.Martinez**, F. Schmidt, F. Andrieu, “Deep Learning Approach for Crater Superposition Analysis: Towards Improved Planetary Surface Dating”, 202X. In prep.

This work also gave me the opportunity to present my research at a number of seminars and conferences, including three oral presentations at major international conferences in the world. To see the complete list of conferences I have attended, please visit my personal page.

I wish you an enjoyable reading of this manuscript and hope that it will interest you and provide you with knowledge, or even new ideas, regarding the use of artificial intelligence in the field of planetary sciences.

Financement

Le travail présenté dans ce manuscrit a été financé en partie par l'Agence Spatiale Européenne (référence de financement *4000139120/22/ES/CM*). Nous remercions le soutien de l'**Institut National des Sciences de l'Univers** (INSU), du **Centre National de la Recherche Scientifique** (CNRS) et du **Centre National d'Études Spatiales** (CNES) à travers le **Programme National de Planétologie** (PNP).

Funding

The work presented in this manuscript was partly funded by European Space Agency (funding reference *4000139120/22/ES/CM*). We acknowledge support from the **Institut National des Sciences de l'Univers** (INSU), the **Centre National de la Recherche Scientifique** (CNRS) and **Centre National d'Etudes Spatiales** (CNES) through the **Programme National de Planétologie** (PNP).

Remerciements

Ça y est, ce moment tant attendu est enfin arrivé : l'écriture de la section *remerciements*. L'écriture de cette section d'une importance capitale, est ce qui selon moi permet à la thèse de prendre vie. De mettre des noms sur toutes les personnes qui m'ont tant aidé.e.s ou accompagné.e.s durant ces trois années. Car cette thèse, ça n'est pas qu'un manuscrit de 225 pages (références comprises). Les trois années qui ont précédé l'écriture de ces lignes furent pour moi une expérience enrichissante comme nulle autre. Cela a avant tout été le fruit d'une aventure collective portée par de superbes directeurs de thèse, des collègues d'une grande valeur et des proches qui ont su me soutenir dans les moments moins faciles.

Ainsi, mes premiers remerciements, je les dois à mes directeurs de thèse *Frédéric* et *François*. Je ne sais que vous dire d'autre que MERCI pour ces années durant lesquelles vous avez été ce que je définirais de ma modeste expérience comme d'excellents encadrants. Je vous remercie pour la confiance que vous avez su m'accorder. Pour votre accompagnement dans les moments nécessaires mais aussi pour la liberté que vous m'avez accordée dans les autres moments. Vous avez su trouver cet équilibre qui m'a permis de gagner en autonomie sans jamais m'avoir donné l'impression d'être "fliqué". Je vous remercie pour votre soutien, votre patience, votre aide. Je vous remercie pour la pertinence de vos questions et la rigueur professionnelle avec laquelle vous m'avez encadré. Je tiens aussi à vous remercier pour votre préparetion à l'oral qui je suis sur, sans vous n'aurait jamais atteind cette qualité. Egalement vous remercie aussi de m'avoir donné l'opportunité de pouvoir présenter mon travail dans un nombre considérable de conférences: du PNP à Lyon jusque l'EPSC-DPS d'Helsinki tous ensemble j'ai fais un chemin qui n'aurait été possible sans vous.

Mes seconds remerciements, j'aimerais les porter à mon comité de suivi de thèse qui a pu voir ce travail évoluer durant ces deux années. *Cathy Quantin-Nataf*, depuis notre rencontre en 2021 tu as toujours su m'apporter des commentaires avisés et toujours bienveillants sur mon travail. Quel plaisir d'avoir pu travailler avec toi et je te suis reconnaissant de l'aide que tu m'as apportée et que tu m'apportes toujours. *Alexandre Boucaud* : si ce sujet en est là, c'est en grande partie grâce à toi et je t'en remercie. Merci aussi pour tes conseils avisés et ta sympathie permanente.

Je tiens aussi à remercier les membres de mon jury de thèse qui ont accepté de me lire pour ensuite évaluer mon travail. Tout d'abord un grand merci à mes rapporteurs *Stéphane Le Mouelic* et *Marc Huertas-Compagny* pour vos suggestion pertinantes qui m'ont beaucoup aidée à améliorer le contenu de cette thèse. Ensuite je voudrais remercier mes examinatrices et examinateurs *Cathy Quantin-Nataf*, *Myriam Lemelin* et *Sylvain Bouley* pour votre expérience et pour les questions que vous m'avez posés.

Je souhaite aussi remercier *Hugues Talbot* pour la lumière que tu as su nous apporter, notamment dans la première partie de cette thèse. Merci pour tes commentaires car je suis sûr que sans toi, ce premier papier n'aurait pas été d'une si bonne qualité.

J'aimerais aussi remercier le *bâtiment 509*. Pas le bâtiment en lui même évidemment, même s'il fut un superbe lieu pour réaliser une thèse dans de bonnes conditions et avec un grand bureau qui fut parfois le siège de quelques invasions. Je tiens à remercier Julien dit *Bobby* et *Laure* véritables ténors de la maison *509* pour toutes les discussions enrichissantes que nous avons pu avoir.

En parlant de Ténors (avec un grand T), je voudrais remercier chaleureusement *Valérie* pour tout ce que tu as fait pour ce laboratoire et, parce que je suis convaincu que l'on ne te remerciera jamais assez j'aimerais insister sur tes qualités de générosité, et de bienveillance, au moins à l'égard des doctorants, dont tu fais part. Sans toi je suis convaincu que nous n'aurons ni terrain de pétanque, ni table de Ping-pong, ni Baby-foot. Tu as fais de ce laboratoire un lieu de travail, d'étude et de vie bien meilleur que ce qu'il n'a jamais été et tu as de quoi être fière de toi pour tout cela.

Comme disait *Frédéric*, une thèse c'est un marathon, le plus dur c'est pas de démarrer mais c'est de tenir la distance. Et pour tenir la distance, rien de mieux qu'une bonne équipe de soutien. Je tiens donc à remercier chaleureusement tous mes collègues de *GEOPS* : Tout d'abord cette promotion 2022 de doctorants et de doctorantes : Merci à *Agathe* pour tout, pour ces photos à peine dossier, pour ces petits verres au PMU hyper cringe du Guichet puis pour tous les autres moments et les grandes discussion qu'on a pu avoir dans votre superbe bureau. Merci *Hugo* pour tout, les soirées à Massy, les discussions et les merveilleux débats qu'on a pu avoir sur à peu près tout et n'importe quoi. Sans toi, la géologie serait probablement, dans le fond comme dans la forme, un immense mystère à mes yeux. Et puis *Sarah*, je suis très reconnaissant d'avoir pu partager ces trois années avec toi, on a encore pas mal d'aventures à vivre ensemble et c'est pour moi tellement rassurant de savoir qu'on va partir ensemble à Sherbrooke. Merci à *Mathilde* pour, entre autre la co-organisation de cette soutenance de thèse et pour tout le reste. Tu as vraiment un chouette appart au Guichet. Merci à *Charlie* pour tout ces bons moments, merci pour la visite de ta superbe carrière. Ça fait vraiment quelque chose de descendre officiellement ;) Dans la même lignée je voudrais remercier tous les autres sous-terreux *Bobo*, *Titi*, *Zeze*, *Favé*, *Machette* et les autres sans oublier évidemment notre maitre à toute et à tous : *Merlin*. Merci à vous les champion.ne.s pour ces soirées passées sous terre à refaire le monde. Merci à *Karim* pour ta bienveillance permanente, à *Adrien* pour les chouette soirées passés ensemble. Merci *Jean* pour ces moments en conf où on a franchement bien rigolé, j'espère qu'on se reverra à l'EPSC2026. Puis aux premières et deuxièmes années : *Théo*, *Hélène*, *Léna*, *Guillaume*, *Hugo*, *Baptiste* et *Anne* pour tout ces moments passés ensemble. Puis Merci aussi à tout les anciens du labo. *Guillaume*, tu as vraiment été un grand frère pour moi au début de ma thèse, tu m'a beaucoup inspiré et je t'en remercie. Merci à *Cyril* mon autre frère de thèse sans qui les choses aurait été bien différentes. Nos discussions à propos de la politique et de l'art me manquent déjà et il me tarde de trouver un nouveau sujet de débat entre nous :) Merci à *Pauline*, tu as su me redonner un coup de boost et de motivation dans les moments difficiles notamment en milieu de thèse, je te suis extrêmement reconnaissant. Merci *Max* et *Wil* pour ces soirées mémorables à Massy et aux salon des Vignerons indépendants. Merci aussi à *Perrine*, *Titouan*, *Kévin* et tous les autres que j'oublie sûrement. Durant cette thèse il m'a aussi été donné l'opportunité de pouvoir encadrer des stages de la 3ème à la licence et je voudrais remercier chaleureusement tous les stagiaires que j'ai pu avoir la chance d'encadrer : Tout d'abord *Maxime*, tu as fais un super travail de datation des sites d'atterissages lunaires dont je me suis servi par la suite pour illustrer le chapitre 6 et je t'en remercie. Ensuite *Lola*, *Lou*, *Hortense* et *Daphné* puis par la suite *Gabriel* pour vos super stages de découverte de la recherche qui furent la fondation du chapitre 5 de ce manuscrit. Pour finir je voudrais remercier *Corentin* pour ton stage de Master qui m'a aussi apporté une belle collaboration avec l'équipe PRISMARCTYC. Merci à vous toutes et tous pour votre travail, votre sérieux et votre bonne humeur.

Pour réussir une thèse il est bon aussi d'être bien entouré en dehors du travail. Durant ces plus de quatres années passées en île-de-France j'ai pu compter sur le soutien indéfectible de mes plus proches amis que j'aimerais aussi remercier. *Béranger*, je te remercie d'avoir été le témoin de cet évènement qui fût si important pour moi. Quel courage tu as eu d'avoir fait 30km pour voir un pote passer tout l'après midi à parler d'IA et de géologie martienne. Ça me touche énormément. Merci à *Sarah*, *Chloé*, *Lucie*, *Léa* et *Maël* pour toutes les aventures —des week-ends au Val-André aux soirées d'Halloween— d'avoir été toujours présents :) Merci à mes potes de longue date *Antoine*, *Thomas*, *Coco* et *Dam* d'avoir toujours été là malgré la distance qui maintenant nous sépare. Vos mots dans le livre d'or m'ont vraiment beaucoup touché. Merci à *Amadéa*, *Keegan*, *Brian* et *Maya* pour votre soutien, votre amitié et toutes ces longues discussion qu'on a pu avoir ensemble. Vous avez su être présent.e.s dans les moments importants et je vous en suis extrêmement reconnaissant.

J'aimerais prendre un moment pour remercier mes anciens professeur.e.s. Même si je n'étais certainement pas le meilleur des éléments du collège au master, certains et certaines d'entre vous m'ont beaucoup marqués. Tout d'abord *André Brou*, vous avez su me donner l'envie d'apprendre des choses complexe mais surtout la discipline nécessaire pour bien les présenter. Je crois me rappeler que vos séance de présentation "jalon" de projet était craintes de toutes et tous mais elles m'ont appris et donnés énormément pour la suite. *Dominique Prigent*, même si la prépa n'a pas été pour moi le commencement d'une carrière d'ingénieur, vous avez su me transmettre l'amour de la physique avec humanité et passion. Je vous suis extrêmement reconnaissant et je n'oublierais jamais vos cours qui, aussi rigoureux soient-ils, étaient toujours plus passionnant les uns que les autres. Plus tard, sur les bancs de la fac j'ai eu l'immense honneur de suivre les cours de *Marianne Bedel* et *Pierre-Emmanuel Durand* qui m'ont tous deux donné l'envie de faire de l'astrophysique de la planétologie. Ensuite, en master j'ai eu la chance de suivre les cours de *Emeric Spiga*, *Alice Le Gall*, *Emmanuel Marcq* ou encore *François Forget* et bien sûr *Frédéric Schmidt* qui m'ont toutes et tous donné l'envie et la passion de continuer dans cette voie. Merci à vous tou.te.s pour votre passion, votre patience et votre bienveillance.

Comme il est apparament coutume de garder le meilleur pour la fin, je voudrais remercier mille fois ma chère et tendre *Alicia*. Tu as su être présente dans les moments les plus durs de cette thèse, tu as su m'encourager, me soutenir, parfois me challenger et me remotiver quand j'en avais le plus besoin. Tu as su comprendre mes absences, mes moments de doutes et mes périodes de stress intense. Tu as su m'apporter cette sérénité dont j'avais besoin pour avancer. Tu as vraiment réussi à sublimer ce moment notamment en organisant une incroyable soirée de thèse. Je te suis infiniment reconnaissant pour tout ce que tu as fait pour moi et pour tout ce que tu fais chaque jour. Merci pour ton amour, ta patience, ta bienveillance et ton soutien inconditionnel. Je t'aime.

Je voudrais, pour finir, remercier ma famille en commençant par mes parents et mon frère et ma soeur. Merci pour tout l'amour et le soutien que vous m'avez apporté depuis toujours. C'est vous qui avez su me transmettre cette curiosité permanente, cette envie de découvrir et d'explorer ce qu'il y a au delà. Après tout c'est vous qui m'avez donnés ce livre sur le système solaire que je promenais tous les jours à l'école étant petit avant même de savoir lire. Depuis le temps à filé, les planètes ont tourné, Pluton n'en est plus une et moi, à ma petite échelle j'ai, un petit peu grâce à vous, fini ce manuscrit de thèse. Je voudrais remercier mes grands parents qui m'ont toujours soutenu et encouragé dans mes études. Puis ma famille élargie, celle que je continue de voir régulièrement : *Gaël*, *Florence*, *Yannick*, *Corinne*, *Erwan*, *Loïck*, *Maewenn*, *Annaëlle*, *Nolwenn*, *Tristan*, *Kana*, *Manon* et *Tetsuya*. Merci pour votre soutien depuis si longtemps et votre présence lors de ma soutenance ça m'a fait très plaisir. Et puis, ma famille plus éloignée : *Les Martinez*, *Les Radenac*, *Les Vallée*, *Les Martin*, *Les Dormois* et tout les autres. Je n'oublie pas non plus *Tata et Tonton Le Bihan*, les copains et professeurs du *Judo* et *la famille Ung* pour tout ce que vous avez fait pour moi. Merci à vous toutes et tous pour votre soutien et les superbes discussions qu'on a pu avoir.

Contents

Foreword **7**

Funding **8**

Remerciements **9**

Synthèse **17**
- 0.1 Contexte général . . . 18
- 0.2 La détection automatique d'objets dans des images : concepts et définitions . . . 21
  - 0.2.1 Intelligence Artificielle, Deep Learning et Réseaux de Neurones Convolutionnels 21
  - 0.2.2 Méthodologie typique d'utilisation d'un algorithme d'intelligence artificielle . . 26
  - 0.2.3 Précision, rappel et autres : métriques pour évaluer une détection et une classification . . . 29
- 0.3 Détection automatique de cratères . . . 33
- 0.4 Classification automatique de cratères . . . 37
- 0.5 Détermination automatique des ordres de superposition des cratères . . . 42
- 0.6 Conclusion générale . . . 44

1 General Introduction **45**
- 1.1 From Dust and Gaz to Planets . . . 46
- 1.2 Remote sensing, datation and crater counting . . . 51
  - 1.2.1 Mosaic and datasets . . . 52
  - 1.2.2 Absolute Lunar datation using radiometric dating . . . 53
  - 1.2.3 Relative datation on the Moon using crater counting . . . 54
  - 1.2.4 Transfer function curves for Mars and other planetary bodies . . . 59
- 1.3 Example of studies on Impact Craters . . . 62
  - 1.3.1 Erosion and Degradation of Craters . . . 62
  - 1.3.2 Origin of Martian Meteorites . . . 66
- 1.4 Crater detection method: A review of the bibliography . . . 69
  - 1.4.1 Manual crater Database . . . 69
  - 1.4.2 Machine learning for crater detection or recognition . . . 70
  - 1.4.3 Typical methodology to set a machine learning algorithm . . . 77
  - 1.4.4 Precision, Recall and others : Metric to evaluate a detection and classification . 82
  - 1.4.5 Deep-learning-based Crater Detection Methods . . . 87
- 1.5 Problematic . . . 90

2 Crater database improvement using automatic circle detection 93
2.1 Introduction . . . 94
2.2 Data . . . 95
2.2.1 Re-projection and database cutting . . . 95
2.3 Method: Automatic crater circle improvement . . . 96
2.3.1 Edge detection . . . 96
2.3.2 Hough transform . . . 98
2.3.3 Best circle selection . . . 100
2.4 Results and evalution . . . 104
2.4.1 Examples . . . 104
2.4.2 Evaluation . . . 108
2.4.3 Final dataset . . . 109
2.5 Conclusion . . . 112

3 Robust automatic crater detection at all latitudes on Mars with Deep-learning 115
3.1 Abstract . . . 116
3.2 Introduction . . . 117
3.3 Data and Methods . . . 118
3.3.1 Input Images . . . 118
3.3.2 Improved ground truth crater database . . . 119
3.3.3 Preprocessing . . . 119
3.4 Crater Detection Algorithm . . . 121
3.4.1 Faster-RCNN . . . 121
3.4.2 Training . . . 122
3.4.3 Evaluation metrics . . . 123
3.5 Results . . . 125
3.5.1 Global crater detection . . . 125
3.5.2 Size dependence . . . 126
3.5.3 Latitude/illumination dependence . . . 126
3.5.4 Crater-like feature . . . 127
3.5.5 Miss-classification . . . 128
3.5.6 Test on other planets . . . 132
3.6 Discussion . . . 132
3.7 Conclusion . . . 136

4 Automatic Crater Classification Using a Deep-learning-based Pipeline 139
4.1 Abstract . . . 140
4.2 Introduction . . . 141
4.3 Data . . . 142
4.3.1 The most complete classified crater database on Mars . . . 142
4.3.2 CTX V01: A New Global Mosaic . . . 143
4.4 Pre-processing . . . 145
4.4.1 Crater bounding-box improvement using Hough Circle detection . . . 145

4.4.2 Data Preparation . . . 146
4.4.3 System Setup . . . 148
4.5 Method . . . 149
4.5.1 Classifier . . . 149
4.5.2 Metrics . . . 149
4.5.3 Training . . . 151
4.5.4 Validation . . . 151
4.6 Results and Discussion . . . 152
4.6.1 Global Performances . . . 152
4.6.2 Application : Dating and analysis of an Early Amazonian Terrain . . . 153
4.6.3 Discussion . . . 154
4.7 Conclusion . . . 156

5 Detection of crater superposition order using a classification approach 163
5.1 Introduction . . . 164
5.2 Crater superposition order definition . . . 165
5.2.1 Crater superposition order definition . . . 165
5.3 Building a reference dataset : collaborative labellisation approach . . . 166
5.4 Deep-learning processing . . . 170
5.4.1 Training . . . 170
5.4.2 Evaluation . . . 170
5.4.3 Global scale crater superposition order . . . 173
5.5 Results discussion . . . 174
5.5.1 Example . . . 174
5.5.2 Cumulative crater frequency distribution analysis . . . 174
5.5.3 Crater density maps analysis . . . 174
5.6 Conclusion and perspectives . . . 180

6 Automatic Age Estimation using ACDC 181
6.1 Dataset . . . 182
6.2 Age estimation algorithm . . . 183
6.2.1 Images reprojection and multiscale cutting . . . 183
6.2.2 Crater detection . . . 185
6.2.3 Merging duplicated detection . . . 185
6.2.4 Improvement of our detection . . . 187
6.2.5 Restriction to a geological unit . . . 188
6.2.6 Classification . . . 189
6.2.7 Age determination . . . 190
6.3 Results — datations . . . 191
6.3.1 Mars . . . 191
6.3.2 Moon (Kaguya-based analyses) . . . 195
6.4 Discussion and conclusion . . . 196

7 Conclusion et perspectives 199
7.1 General conclusion 199
7.2 Advances in Automatic Crater Detection 200
7.3 Automatic Crater Characterization 200
7.4 Automatic Determination of Crater Superposition Order 201
7.5 ACDC: A New Tool for Planetary GIS Applications 202

8 Global Perspectives 203

References 206

Synthèse

Le travail accompli au cours de cette thèse est présenté dans ce manuscrit rédigé en anglais. Conformément aux règlements de l'Université Paris Saclay et de l'école doctorale SMEMaG, une synthèse de ce travail, rédigée en français, est également proposée ci-dessous pour les lecteurs francophones intéressés. En vous souhaitant une bonne lecture.

Contents

0.1 Contexte général 18
0.2 La détection automatique d'objets dans des images : concepts et définitions 21
  0.2.1 Intelligence Artificielle, Deep Learning et Réseaux de Neurones Convolutionnels 21
  0.2.2 Méthodologie typique d'utilisation d'un algorithme d'intelligence artificielle . . 26
  0.2.3 Précision, rappel et autres : métriques pour évaluer une détection et une classification 29
0.3 Détection automatique de cratères 33
0.4 Classification automatique de cratères 37
0.5 Détermination automatique des ordres de superposition des cratères 42
0.6 Conclusion générale 44

0.1 - Contexte général

Sur le spectre des disciplines scientifiques, la géologie planétaire, qu'ici nous qualifierons plus généralement comme la science qui s'intéresse à l'étude des **planètes solides**, fait partie des sciences dites "naturelles". Comme toutes les sciences naturelles, elle repose sur l'observation et l'expérimentation pour comprendre les phénomènes naturels. Cependant, contrairement à d'autres disciplines comme la physique ou la chimie, la géologie ne peut pas toujours s'appuyer sur des expériences contrôlées en laboratoire. En effet, les processus géologiques se déroulent souvent sur des échelles de temps et d'espace qui dépassent largement celles accessibles à l'expérimentation humaine directe. Par conséquent, l'un des enjeux majeurs dans l'étude des planètes solides est de reconstituer l'histoire géologique à partir des observations actuelles. Sur les corps planétaires dont nous disposons d'échantillons de roches associés à un contexte géologique, il est relativement facile de mesurer un âge et donc de pouvoir dater les surfaces planétaires à l'aide de méthodes radiométriques (Boltwood, 1907; McDougall et al., 1999). C'est ce qui a été fait pour la Terre lorsque l'on a voulu déterminer l'âge des plus vieilles roches terrestres par exemple (Wilde et al., 2001). Mais on peut aussi effectuer cette analyse sur les roches lunaires grâce aux plus de 385 kg d'échantillons prélevés durant les missions Apollo, Luna et Chang'e (Turner et al., 1973b; Fernandes et al., 2013; Zellner, 2017; Cui et al., 2024), ou encore dater les roches qui constituèrent les premières briques d'un Système solaire en formation par l'analyse d'un certain nombre de météorites (Bouvier et al., 2010; Malarewicz et al., 2025).

Cependant, pour la majorité des corps planétaires, y compris Mars, nous ne disposons pas d'échantillons de roches dont nous connaissons le contexte géologique. Il est donc impossible de dater directement ces surfaces planétaires à l'aide de méthodes radiométriques classiques. C'est dans ce contexte qu'historiquement, de nouveaux modèles de datation ont vu le jour (Hartmann, 1970; Neukum, 1983). Ces nouvelles méthodes de datation des surfaces planétaires reposent largement sur l'analyse statistique des cratères d'impact. En effet, sur la plupart des corps telluriques, l'érosion et le volcanisme récent sont absents ou limités, la densité de cratères constitue un excellent indicateur de l'ancienneté des terrains. Cette méthode, connue sous le nom de datation relative par comptage de cratères, s'appuie sur le principe que plus une surface est ancienne, plus elle a accumulé de cratères (Shoemaker et al., 1970).

Le comptage consiste à inventorier tous les cratères présents sur une zone de même âge comme par exemple une coulée volcanique, une plaine, etc.. Nous appellerons cette surface d'intérêt *unité géologique*. Il suffira ensuite de comparer la distribution en taille de ces cratères avec des courbes de production calibrées (Hartmann, 2005; Neukum et al., 2001). Ces courbes relient la densité de cratères à l'âge absolu du terrain, sur la base d'étalonnages obtenus à partir des échantillons lunaires rapportés par les missions Apollo et Luna, pour lesquels des datations radiométriques sont disponibles. Les travaux pionniers de Hartmann (1965b) and Hartmann (1966) et de Neukum (1983) ont permis de formaliser ces relations pour généraliser l'âge de la lune à tous les terrains (y compris ceux où il n'a été fait aucun prélèvement). Il furent plus tard étendus pour être utilisés sur Mars (Ivanov, 2001; Neukum et al., 2001). Aujourd'hui, ces méthodes largement utilisées pour estimer les âges des surfaces sur Mars, Mercure ou les satellites glacés. Une introduction est présente au chapitre 1.

Toutefois, la méthode comporte plusieurs sources d'incertitude. Premièrement, l'identification correcte des cratères est une tâche certes simple mais vu que la distribution des cratères par rapport à leur taille évolue en loi de puissance (Fielder, 1961), cette tache peut s'avérer longue (notamment lorqu'il faut compter les petits cratères), répétitive et sujette à des biais humains pouvant introduire assez rapidement de nombreuses erreurs (See et al., 1995; Benedix et al., 2020). Historiquement, les inventaires de cratères étaient réalisés manuellement par des experts, en interprétant visuellement les images. Mais l'augmentation massive de la quantité d'images à haute résolution, notamment avec la caméra CTX à bord de la mission Mars Reconnaissance Orbiter (Malin et al., 2007; Dickson et al., 2024) qui image la surface de Mars à une résolution de $\sim$ 5m/pixel, rend désormais le comptage manuel irréaliste à l'échelle globale.

Face à cette problématique, des méthodes automatiques ont été développées. Les premières approches s'appuyaient sur des techniques de traitement d'images classiques, telles que la détection de contours, ou l'analyse morphologique (Kim et al., 2005; Salamunićcar et al., 2012; Galloway et al., 2014). Si elles ont permis des avancées notables, ces méthodes se heurtent à la grande variabilité morphologique des cratères, aux variations d'éclairage et aux artefacts d'imagerie.

Les progrès récents en intelligence artificielle, et en particulier l'essor du deep learning, ont profondément renouvelé le domaine. Les réseaux de neurones convolutionnels (CNN) permettent de détecter et de classer les cratères de manière robuste dans des contextes très variés (Lecun et al., 1998). Couplés à des bases de données annotées de grande taille, ces modèles peuvent apprendre détecter des cratères de manière précises ainsi qu'à reconnaître les cratères primaires des cratères secondaires et à estimer leur état de conservation(Martinez et al., 2025; La Grassa et al., 2025; Benedix et al., 2020; Wang et al., 2025). Cette capacité ouvre la voie à des inventaires homogènes et rapides à l'échelle planétaire, réduisant significativement les biais liés à l'observation humaine. Le chapitre 2 décrit notre méthode de pré-traitement pour améliorer la base de données manuelle. Le chapitre 3 présente notre approche.

Une autre limitation inhérante à la datation par comptage de cratère est la confusion entre *cratères primaires*, issus de la collision avec un impacteur arrivant à des vitesses de l'ordre de 10 $km \cdot s^{-1}$ par rapport aux *cratères secondaires* issus de l'éjecta d'un impact primaire retombant à des vitesses beaucoup plus faibles. Également, un certain nombre de cratères peuvent être érodés ou enfouis par des processus géologiques d'âge antérieur à celui de l'unité géologique d'étude est primordial. L'idée générale est que nous ne voulons pas intégrer ces impacts secondaires ou érodés dans le comptage de cratère nécessaire à la datation. Ceci met en évidence un second défi pouvant introduire une source d'erreur majeure dans la datation par comptage de cratères : la classification de cratères sur des critères géomorphologiques (voir chapitre 4).

Un troisième aspect qui va nous intéresser dans le chapitre 5 de cette thèse est la superposition des cratères entre eux. En effet, lorsqu'un cratère se forme, il peut partiellement ou totalement recouvrir des cratères présent dans la zone ultérieurement. Ainsi, en étudiant les relations de superposition entre cratères, il est possible de reconstituer une chronologie relative des impacts. Connaître le degré de superposition des cratères peut fournir des informations précieuses sur l'histoire d'une surface, en particulier dans les régions très cratérisées où les impacts se sont succédés au fil du temps. Cependant, cette information est très difficile à extraire manuellement, en raison du grand nombre de cratères et de la complexité des relations de superposition. Là encore, les techniques d'intelligence artificielle, offrent des outils qui démontrent une efficacité redoutable pour automatiser cette tâche. En entraînant des modèles sur des exemples annotés de cratères superposés, il fut possible d'apprendre à reconnaître les indices visuels qui indiquent quel cratère est le plus récent dans une situation de superposition.

Ainsi, nous avons pu construire une base de données à l'échelle globale de Mars ouvrant de nouvelles perspectives pour l'étude de l'histoire des impacts sur la planète rouge.

Le dernier chapitre 6 présente la chaine de données proposée durant cette thèse. Les chapitres de conclusion 7 et de perspectives 8 closent ce manuscrit. L'ensemble de ces chapitres sont résumés ici en Français.

0.2 - La détection automatique d'objets dans des images : concepts et définitions

L'application des techniques d'apprentissage automatique à la détection de cratères a progressé de manière constante au cours des deux dernières décennies, évoluant de systèmes fondés sur des règles simples vers des modèles plus sophistiqués, incluant des approches basées sur les données. Cette évolution a été largement motivée par la disponibilité croissante d'images planétaires à haute résolution et par l'impraticabilité de l'annotation manuelle des cratères à l'échelle globale. Dans un premier temps, nous introduirons ce que sont l'apprentissage automatique, le *deep learning* et les réseaux de neurones convolutionnels. Dans un second temps, nous présenterons la méthodologie typique d'utilisation d'un algorithme d'intelligence artificielle pour la détection de cratères et plus généralement d'objets dans des images. Cette section résume le chapitre 1.

0.2.1 - Intelligence Artificielle, Deep Learning et Réseaux de Neurones Convolutionnels

Afin de situer la détection des cratères dans le cadre plus large de l'intelligence artificielle, il est nécessaire d'introduire quelques concepts fondamentaux. Les modèles de détection d'objets reposent sur des algorithmes d'apprentissage automatique. L'apprentissage automatique est un domaine de l'intelligence artificielle fondé sur les mathématiques appliquées et les statistiques. Il consiste à programmer un algorithme de manière à ce qu'il apprenne à réaliser une tâche à partir d'exemples, plutôt que de s'appuyer sur des règles explicitement définies (Bishop, 1995; Mitchell, 1997). Plusieurs paradigmes d'apprentissage existent pour entraîner un ordinateur :

- **Apprentissage supervisé :** Cette approche consiste à entraîner un modèle à partir d'un jeu de données annoté — c'est-à-dire un ensemble d'exemples dont les sorties attendues sont connues. Le modèle apprend à partir de ces exemples, puis est testé sur de nouvelles données pour évaluer ses capacités de généralisation.

- **Apprentissage par renforcement :** À l'image des techniques de dressage animal, ce paradigme repose sur le principe de la récompense. Le modèle reçoit un retour sous la forme d'un score et apprend à maximiser cette récompense en interagissant avec son environnement.

- **Apprentissage non supervisé :** Dans ce cas, le modèle est exposé à un ensemble de données non annotées. Il apprend à identifier des motifs ou des similarités au sein du jeu de données, qui peuvent ensuite être utilisés pour des tâches telles que le regroupement (*clustering*) ou la réduction de dimensionnalité.

Les algorithmes de reconnaissance d'objets utilisés dans ce travail reposent sur l'apprentissage supervisé. Autrement dit, lors de la phase d'entraînement, le modèle apprend à partir d'exemples annotés, ce qui lui permet d'effectuer des prédictions fiables lorsqu'il est appliqué à de nouvelles données. Dans les sections suivantes, nous examinerons les types d'algorithmes employés pour la détection d'objets dans les images. Néanmoins, bien que les principes fondamentaux restent identiques à ceux de l'apprentissage automatique classique — un système reçoit des données et un algorithme d'optimisation est utilisé pour minimiser les erreurs — les modèles utilisés en détection d'objets reposent sur des architectures différentes, spécifiquement adaptées aux images.

Définition — *deep learning* et réseau de neurones En 1943, le neurologue Warren McCulloch et le mathématicien Walter Pitts ont modélisé pour la première fois le fonctionnement des neurones biologiques en considérant qu'un neurone pouvait être représenté par une fonction logique de transfert. Pour en comprendre le fonctionnement, il est utile d'examiner celui des neurones biologiques. Ceux-ci sont les cellules fondamentales du cerveau. Comme illustré en Fig. 1, un neurone est constitué d'un corps cellulaire, d'un ou plusieurs dendrites qui reçoivent l'information entrante, et d'un axone qui transmet l'information. Pour envoyer un signal, le neurone libère des neurotransmetteurs, substances chimiques qui se lient aux dendrites des neurones suivants. Le signal reçu peut être de deux types : excitateur (+) ou inhibiteur (–). Les neurones artificiels ont été conçus de façon analogue. Comme montré en Fig. 2, ils sont représentés par des fonctions de transfert prenant en entrée des signaux x et produisant une sortie y. Ce type de neurone artificiel est appelé *perceptron*.

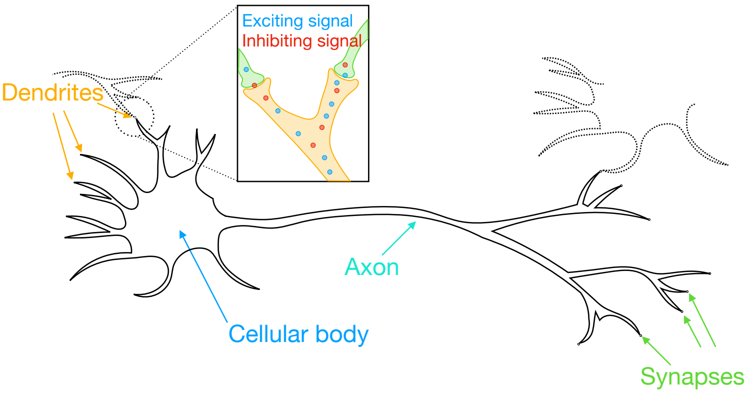

Figure 1: Représentation schématique d'un neurone biologique. Il est constitué d'un corps cellulaire, de dendrites recevant les signaux entrants, et d'un axone transmettant le signal sortant.

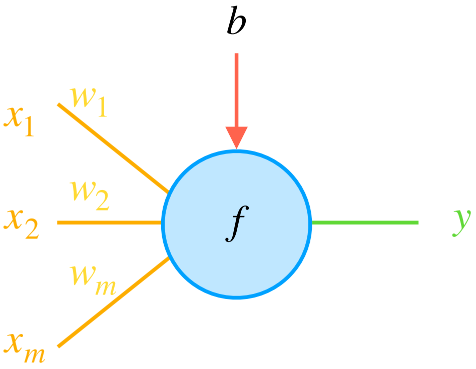

Figure 2: Représentation schématique d'un neurone artificiel (perceptron). x_m représente l'information en entrée et le coefficient w_m le poids synaptique. Le terme b est un biais ajustable permettant de décaler le seuil d'activation.

Cette fonction suit deux étapes principales. La première est l'agrégation, consistant à sommer le produit des entrées x par des coefficients w, comme montré dans l'Éqn. 1. Le poids w représente l'activité synaptique et peut être compris entre -1 et 1. Le biais b joue le rôle d'un paramètre supplémentaire permettant de décaler le seuil d'activation indépendamment des entrées pondérées.

$$\text{Agrégation: } f = \left(\sum_{i=1}^{m} w_i \cdot x_i\right) + b \tag{1}$$

La seconde étape est la phase de transfert, qui décide si le neurone est activé ou non. Dans ce travail, nous utilisons la fonction ReLU (*Rectified Linear Unit*, Éqn. 2), bien que d'autres existent (sigmoïde, tangente hyperbolique).

$$\text{Transfert: } y(x) = \max(0, x) \tag{2}$$

McCulloch et al. (1943) ont montré que ce modèle permettait de reproduire des opérations logiques simples comme les portes AND et OR. En connectant plusieurs neurones, il devient possible de résoudre des problèmes bien plus complexes. La Fig. 3 illustre un réseau de neurones multicouches composé d'une couche d'entrée et d'une couche de sortie.

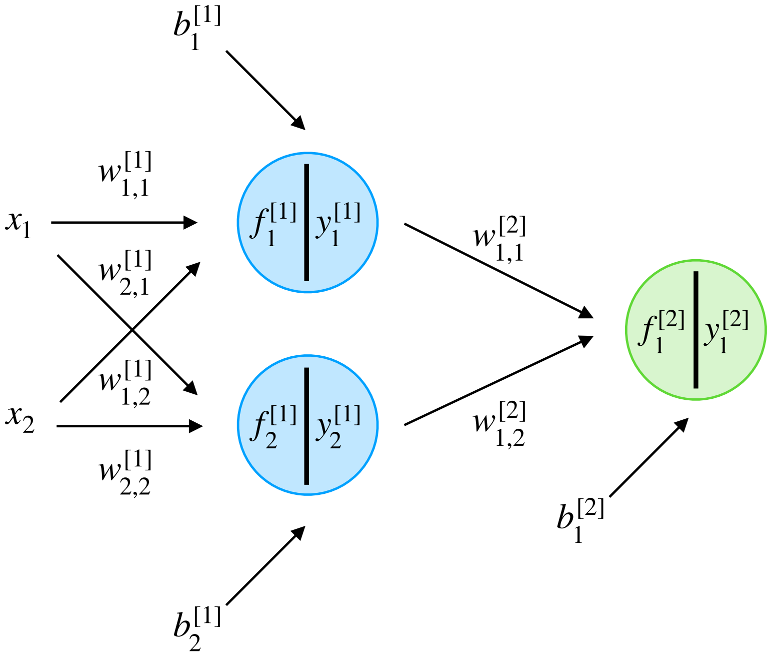

Figure 3: Représentation schématique du fonctionnement d'un réseau de neurones artificiels multicouche (*multilayer perceptron*).

Bien que fondateur, ce modèle ne comportait pas d'algorithme d'apprentissage ; il fallait déterminer manuellement les poids w_i et biais b_i. Ce n'est qu'avec les travaux de Frank Rosenblatt en 1957 que l'apprentissage par perceptron multicouche fut introduit (Rosenblatt, 1961), donnant naissance aux réseaux de neurones modernes (Fig. 4).

Réseaux de neurones convolutionnels et détection d'objets Les réseaux de neurones convolutionnels (CNN) constituent une classe particulière de réseaux largement utilisée pour la détection d'objets dans les images. Comme illustré en Fig. 5, un CNN est composé de trois types de couches principales :

- **Couches convolutionnelles :** elles traitent localement des portions de l'image via une opération de convolution.
- **Couches de *pooling* :** elles réduisent la dimension des représentations extraites.
- **Couches entièrement connectées (FC) :** elles réalisent la classification finale.

Les couches convolutionnelles appliquent des filtres parcourant l'image en réalisant des convolutions (Fig. 6).

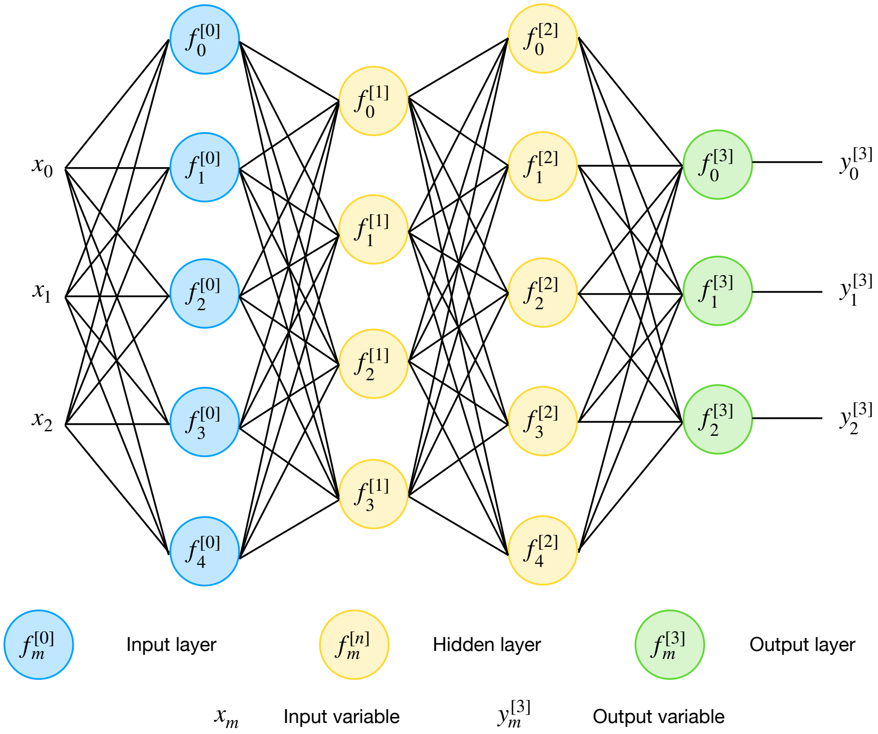

Figure 4: Exemple d'un réseau de neurones artificiel à cinq couches. **Note :** La notation utilisée pour identifier les neurones est la suivante : les fonctions d'agrégation sont notées $f_m^{[n]}$ et les fonctions de transfert $y_m^{[n]}$, où n désigne l'indice de couche et m celui du neurone.

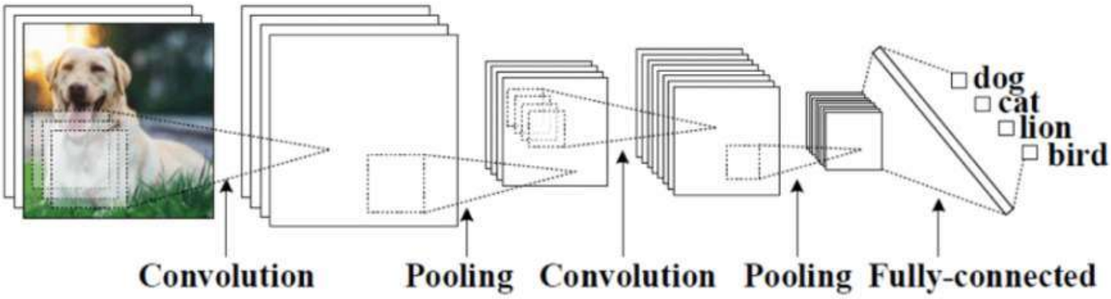

Figure 5: Représentation schématique du fonctionnement d'un réseau de neurones convolutionnel. Source : Medium.com.

Les couches de *pooling* visent à réduire la quantité d'informations en effectuant un sous-échantillonnage. Les deux plus répandues sont le *max pooling* (sélection du maximum de la zone filtrée) et le *average pooling* (moyenne des valeurs de la zone filtrée), comme montré Fig. 7.

Enfin, la *fully connected* (FC) est utilisée pour optimiser la classification finale (Fig. 8).

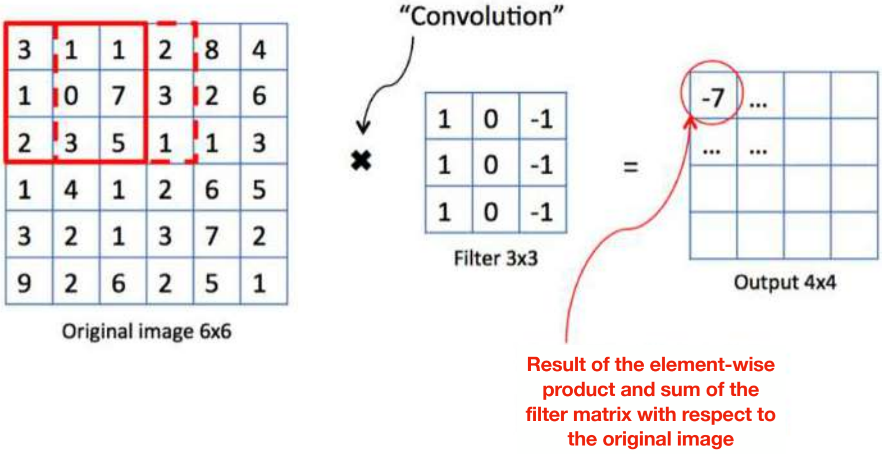

Figure 6: Illustration de l'opération de convolution. Source : Medium.com.

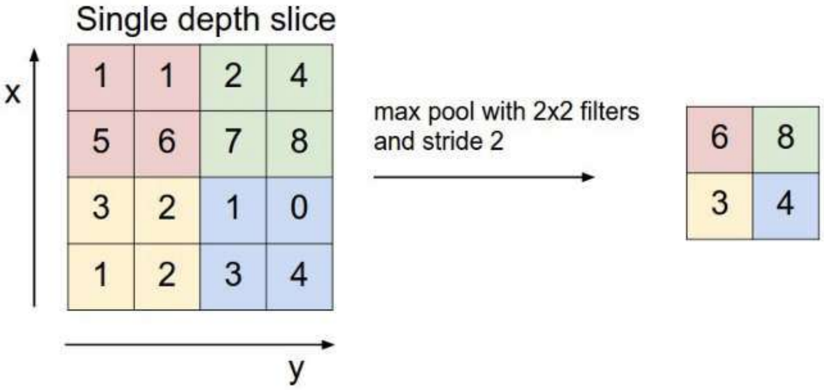

Figure 7: Illustration de l'opération de *pooling*. Source : Medium.com.

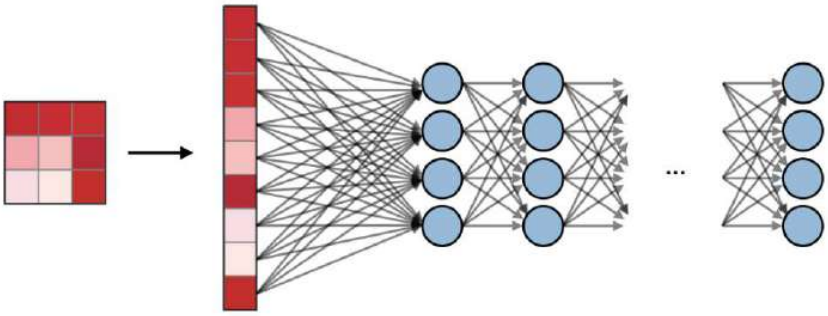

Figure 8: Représentation de la couche *fully connected*. Source : stanford.edu.

0.2.2 - Méthodologie typique d'utilisation d'un algorithme d'intelligence artificielle

Dans cette section, nous détaillons la méthode générale suivi lors du développement d'un modèle de *deep learning* pour la détection de cratères, depuis la préparation du jeu de données de référence jusqu'à l'évaluation du modèle final entraîné. Le processus commence généralement par la création d'un jeu de données annoté. L'étape suivante consiste à définir l'architecture du modèle, qui, dans la majorité des tâches de détection de cratères, est un réseau de neurones convolutionnel (CNN), bien que d'autres architectures puissent être utilisées selon les besoins spécifiques. Les paramètres du modèle (poids et biais) sont initialisés et associés à une fonction coût, qui quantifie l'écart entre les sorties prédites et la vérité terrain. Une stratégie d'entraînement est ensuite appliquée pour minimiser ce coût, en recourant le plus souvent à la descente de gradient stochastique ou à l'une de ses variantes, avec une mise à jour des poids par lots afin d'optimiser l'efficacité du calcul.

Création d'un jeu de données pour l'IA Afin d'entraîner un modèle de détection d'objets — qu'il s'agisse de cratères ou de toute autre cible — la première étape essentielle est de constituer un jeu de données dédié. La qualité et la représentativité de ce jeu de données ont un impact direct sur la capacité du modèle à apprendre des caractéristiques pertinentes et à généraliser à de nouvelles données. Dans cette section, nous ne détaillons pas les étapes de prétraitement spécifiques développées dans cette thèse, mais nous proposons une vue d'ensemble de la procédure standard de création d'un jeu de données pour des tâches de détection par intelligence artificielle. Un jeu de données est généralement divisé en trois sous-ensembles distincts. Le *jeu d'entraînement* constitue la majorité des données et est utilisé pour ajuster itérativement les paramètres du modèle au cours de l'apprentissage. Le *jeu de validation* sert à suivre le comportement du modèle à chaque itération d'entraînement (*epoch*), afin de vérifier que l'apprentissage progresse correctement. Enfin, le *jeu de test* n'est utilisé qu'une fois l'entraînement terminé, pour fournir une évaluation des performances du modèle sur un échantillon statistiquement représentatif. Il est crucial que le jeu de test reste totalement caché pendant l'entraînement et la validation, de manière à ce que les performances rapportées reflètent réellement la capacité du modèle à traiter de nouvelles données. Dans notre cas, nous avons alloué 85% des données disponibles à l'entraînement, 5% à la validation et les 10% restants au test. Pour garantir une pertinence scientifique, le jeu de test a été composé de sites martiens bien étudiés, incluant tous les sites d'atterrissage passés et planifiés (Fig.9a). Nous avons également sélectionné des régions présentant des densités de cratères contrastées, comme la région densément cratérisée de Noachis Terra et la plaine relativement lisse d'Isidis Planitia, afin de couvrir une large gamme de contextes géologiques. Les ensembles d'entraînement et de validation ont ensuite été complétés en assignant aléatoirement les images restantes selon la répartition 85%/10%/5%. La distribution spatiale complète du jeu de données est présentée en Fig. 9b.

Définition du modèle Une fois le jeu de données préparé, l'étape suivante consiste à définir l'architecture du modèle utilisé pour la détection des cratères. La plupart des études récentes reposent sur des réseaux de neurones convolutionnels (CNN), particulièrement adaptés à l'analyse d'images grâce à leur capacité à apprendre des motifs localisés, tels que les rebords de cratères, les ombres ou les nappes d'éjecta. Comme détaillé en section 0.2.1, un CNN est composé d'une série de couches — convolution-

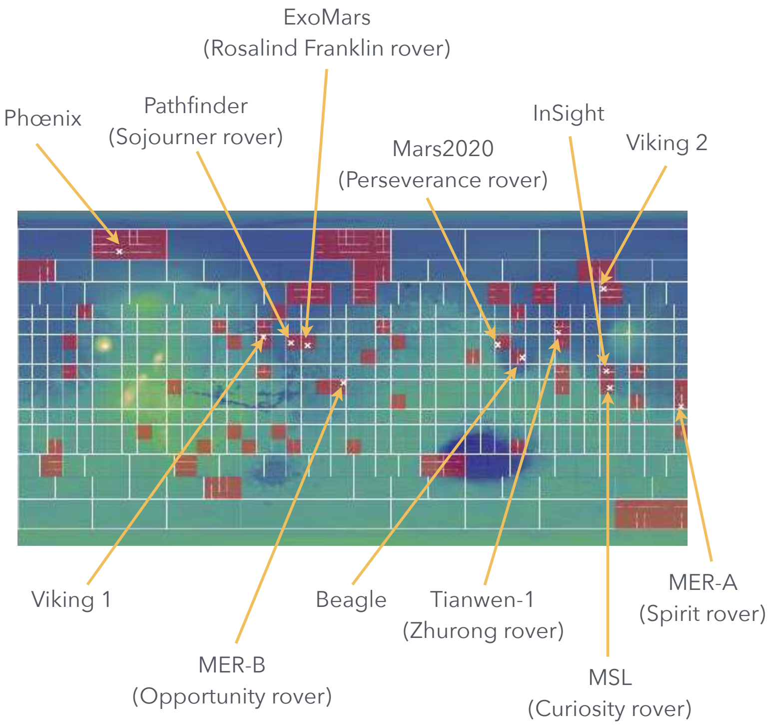

(a) Répartition spatiale des sites inclus dans le jeu de test. La sélection couvre les sites d'atterrissage martiens passés et futurs, ainsi que des régions présentant des densités de cratères contrastées, telles que Noachis Terra (forte densité) et Isidis Planitia (faible densité).

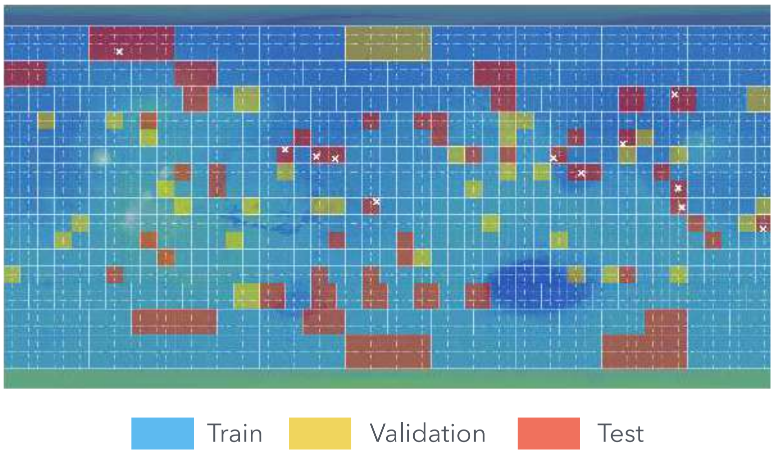

(b) Répartition spatiale du jeu de données complet utilisé pour l'entraînement, la validation et le test du modèle de détection de cratères. Les couleurs indiquent la répartition entre les sous-ensembles d'entraînement (85%), de validation (5%) et de test (10%).

Figure 9: Répartition spatiale des sites utilisés dans cette étude. (a) Localisation du jeu de test, incluant les sites d'atterrissage martiens passés et futurs. (b) Répartition du jeu de données complet utilisé pour l'entraînement, la validation et le test du modèle.

nelles, de *pooling* et *fully connected* — qui extraient et combinent progressivement des caractéristiques à partir des pixels bruts pour produire une sortie de détection. Quelle que soit l'architecture choisie, le modèle est caractérisé par un ensemble de paramètres entraînables appelés *poids* ($w_i^{[n]}$ dans la Fig.3). Ces poids déterminent l'intensité et le signe des connexions entre neurones dans les couches successives. Durant l'apprentissage, leurs valeurs sont ajustées de manière itérative pour minimiser l'erreur entre les prédictions et la vérité terrain. Des paramètres de *biais* ($b_i^{[n]}$ dans la Fig.3) sont également appris, permettant de décaler les seuils d'activation et d'adapter le modèle aux données. Bien que les CNN soient le choix le plus fréquent pour la détection de cratères, d'autres architectures — telles que les modèles à transformeurs ou les approches hybrides — peuvent être utilisées selon la résolution des images, la taille du jeu de données ou les ressources de calcul disponibles.

Fonction coût et minimisation La fonction coût (parfois aussi appelée fonction objectif) est une expression mathématique qui mesure l'écart entre les prédictions du modèle et les annotations de référence. En d'autre termes : elle mesure la "distance" entre les boites englobantes (*bounding boxes* de prédiction et de vérité terrain) ainsi que l'erreur sur l'étiquetage détéctée. La fonction coût guide le processus d'apprentissage car un coût plus faible indique que les sorties du modèle se rapprochent des résultats attendus. En détection de cratères, comme dans la plupart des tâches de détection d'objets, la fonction coût combine généralement deux objectifs complémentaires : un objectif de **classification**, qui garantit que le modèle identifie correctement si une région contient un cratère ou non et un objectif de **localisation**, qui s'assure que les boîtes englobantes prédites correspondent fidèlement aux positions et tailles des cratères. La classification repose en général sur une fonction coût appelée *binary cross-entropy*, définie par l'équation 1.8 du chapitre 1. La localisation de l'objet elle est généralement quantifiée via une fonction coût de régression. Souvent en détection d'objet, on utilisera la fonction *Smooth L1* définie dans le chapitre 1 par l'équation 1.9 qui combine la robustesse de la norme L1 face aux grandes erreurs et la stabilité de la norme L2 pour les petites erreurs. Dans le cadre de notre projet (voir chapitre 3), nous avons utilisé un algorithme de détection appelé Faster R-CNN (Ren et al., 2017) dont la fonction coût totale $\mathcal{L}$ est la somme des coût issues de plusieurs étages de réseaux de neurones, chacun incluant un coût de classification et un coût de régression (Éqn. 1.10).

Stratégie d'entraînement Une fois le jeu de données, le modèle et l'optimiseur définis, une stratégie d'entraînement est mise en place pour coordonner l'ensemble du processus et déterminer comment les paramètres du modèle sont mis à jour de manière itérative afin de minimiser la fonction coût et d'atteindre des performances optimales. Dans nos expériences, nous utilisons l'algorithme adaptatif ADAM (Kingma et al., 2014), qui ajuste dynamiquement le *taux d'apprentissage* pour chaque paramètre en fonction des premiers et seconds moments des gradients. Ce taux d'apprentissage est un hyperparamètre clé : trop élevé, il conduit à des oscillations et une instabilité ; trop faible, il ralentit la convergence et risque de piéger le modèle dans un minimum local. L'adaptativité d'ADAM lui confère une plus grande robustesse que la descente de gradient stochastique classique avec momentum. Le processus d'entraînement est organisé en *epochs*, chacune correspondant à un passage complet sur le jeu d'entraînement. Les données sont subdivisées en *batches*, ce qui permet des mises à jour fréquentes et stables des paramètres tout en optimisant l'usage de la mémoire. Le choix de la taille de lot est un hyperparamètre déterminant, influençant directement la stabilité et la vitesse de convergence. Des techniques d'initialisation des poids et de régularisation (telles que le *weight decay* ou le *dropout*) sont également employées afin d'améliorer la convergence et de limiter le surapprentissage. Tout au long de l'entraînement, les performances sont évaluées sur le jeu de validation, permettant d'orienter l'ajustement des hyperparamètres. Une fois le modèle entraîné, la dernière étape consiste à évaluer rigoureusement ses performances à l'aide de métriques appropriées.

0.2.3 - Précision, rappel et autres : métriques pour évaluer une détection et une classification

Dans cette section, nous présentons les métriques utilisées pour évaluer les performances d'un algorithme de détection d'objets. Nous commencerons par définir les métriques, puis nous expliquerons leur calcul à travers des exemples, avant de discuter de leur interprétation dans le contexte de la détection de cratères.

Précision et rappel Pour évaluer les performances d'un algorithme de détection d'objets, deux métriques fondamentales sont utilisées : la **précision** et le **rappel** (aussi appelé sensibilité) (Buckland et al., 1994). Ces métriques, définies respectivement dans les équations 3 et 4, reposent sur la matrice de confusion (Fig. 10), qui regroupe toutes les combinaisons possibles de résultats.

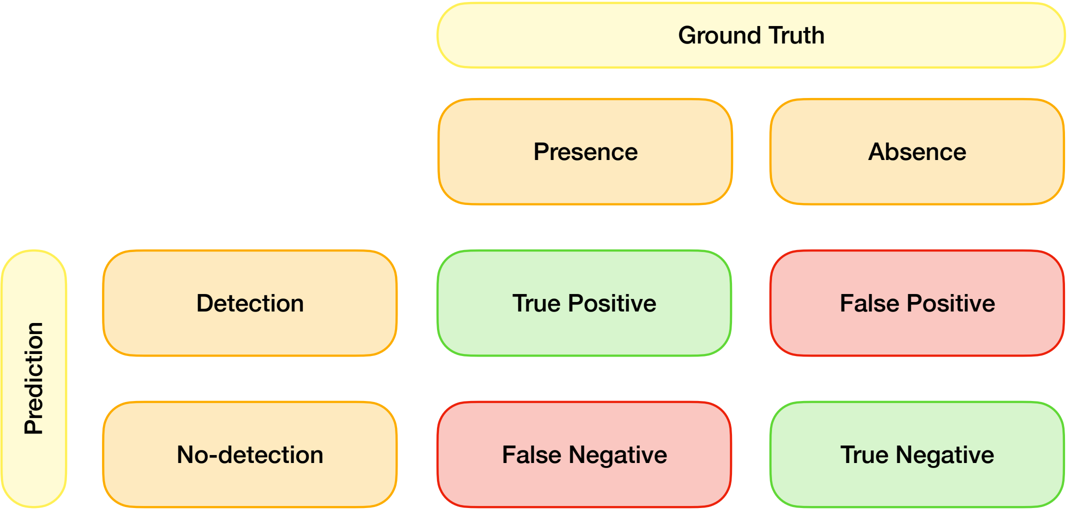

		Ground Truth	
		Presence	Absence
Prediction	Detection	True Positive	False Positive
	No-detection	False Negative	True Negative

Figure 10: Matrice de confusion pour un problème binaire : *cratère détecté* ou *pas de cratère détecté.*

Pour illustrer le fonctionnement de cette matrice, considérons un exemple binaire : tester notre algorithme sur une image de Mars. La vérité terrain est fournie sous forme de fichier d'annotations contenant le nombre de cratères et leurs positions. Pour chaque détection, quatre cas sont possibles :

- **Vrai négatif** (TN) : l'image ne contient pas de cratère et l'algorithme ne détecte rien.
- **Vrai positif** (TP) : l'image contient un cratère et l'algorithme le détecte correctement.
- **Faux négatif** (FN) : l'image contient un cratère mais l'algorithme ne le détecte pas.

- **Faux positif** (FP) : l'image ne contient pas de cratère mais l'algorithme en détecte un.

Afin d'évaluer la localisation des cratères détectés, on utilise la métrique de l'*Intersection over Union* (IoU), qui mesure le recouvrement entre les boîtes prédites et la vérité terrain (Figs. 11 et 12).

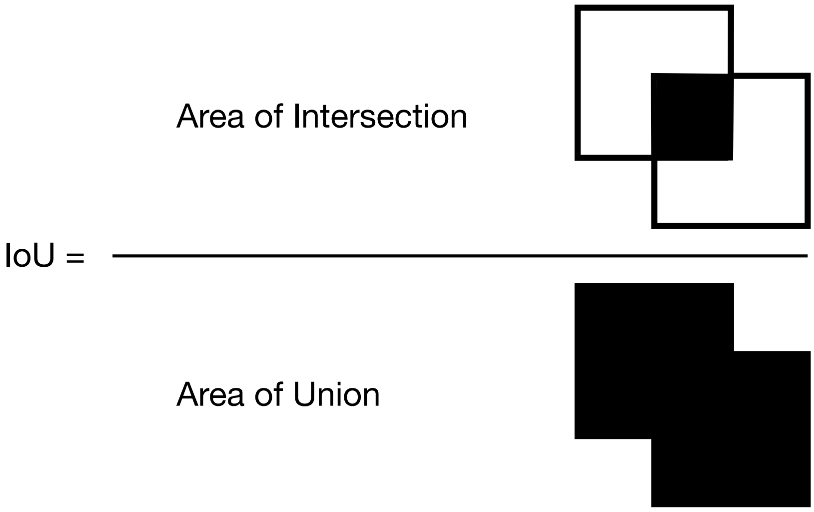

Figure 11: Calcul de l'Intersection over Union (IoU).

Si la boîte prédite ne chevauche pas la vérité terrain, l'IoU est nul ; si elle coïncide parfaitement, l'IoU vaut 1. Une prédiction est considérée comme valide si son IoU dépasse un certain seuil (IoU_{thr}).

Ainsi, la précision et le rappel sont définis par :

$$\mathrm{P}IoUthr = \frac{TP}{TP + FP} \tag{3}$$

$$\mathrm{R}IoUthr = \frac{TP}{TP + FN} \tag{4}$$

où TP sont les vrais positifs, FP les faux positifs et FN les faux négatifs. En pratique, un détecteur parfait aurait P = 1 et R = 1. En réalité, ce compromis est difficile à atteindre à cause des variations d'illumination, de résolution, d'érosion des cratères ou encore de l'imperfection des annotations humaines.

Courbe précision–rappel Comme il est peu intuitif d'évaluer un modèle avec deux métriques séparées, il est courant d'utiliser la **courbe précision–rappel** (PR curve) (Saito et al., 2015). Celle-ci illustre le compromis entre précision et rappel en fonction du seuil appliqué au score de confiance des détections (Fig. 13).

Un détecteur idéal produirait une courbe carrée avec précision et rappel égaux à 1. Dans la pratique, la courbe est toujours décroissante : en abaissant le seuil, on augmente le rappel mais au prix d'une diminution de la précision.

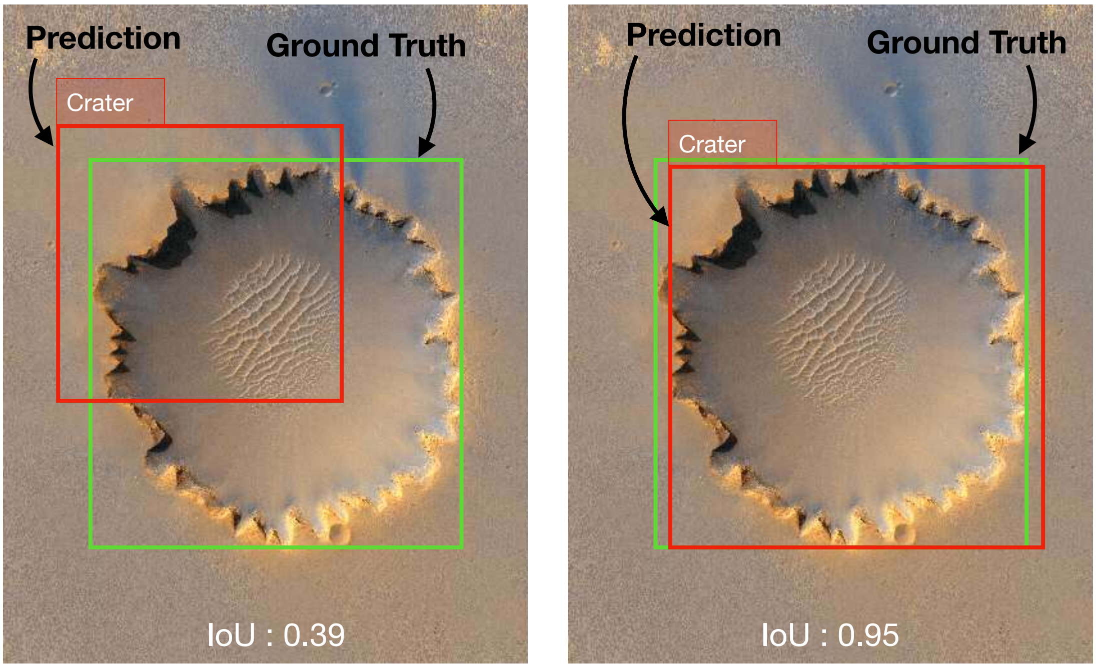

Figure 12: Exemple de deux détections. À gauche, l'IoU est de 0.39 (faux positif avec $IoU_{thr} = 0.5$). À droite, l'IoU est de 0.95 (vrai positif).

Précision moyenne — mAP — *mean Average Precision* La performance globale d'un détecteur peut être résumée par l'aire sous la courbe PR, appelée *mean Average Precision* (mAP). Plus cette valeur est élevée, meilleur est le compromis entre précision et rappel.

F1-score Une autre métrique largement utilisée est le F1-score, qui combine précision et rappel sous la forme de leur moyenne harmonique :

$$F_1 = 2 \cdot \frac{\text{Précision} \cdot \text{Rappel}}{\text{Précision} + \text{Rappel}} \tag{5}$$

Un F1-score de 1 correspond à un détecteur parfait, tandis qu'une valeur proche de 0 indique une mauvaise performance.

Exactitude (Accuracy) Dans le domaine des classifieurs, une métrique couramment utilisée est l'*accuracy*, qui mesure la proportion de prédictions correctes parmi l'ensemble des instances :

$$\text{Accuracy} = \frac{TP + TN}{TP + TN + FP + FN} \tag{6}$$

Limites et incohérences dans l'usage de la précision et du rappel Bien que la précision et le rappel soient largement utilisés, leur application aux études de détection de cratères demeure hétérogène. Il n'existe pas de protocole d'évaluation universellement accepté : les seuils d'IoU varient, les définitions de vrai positif diffèrent, et certains travaux omettent même le rappel. De plus,

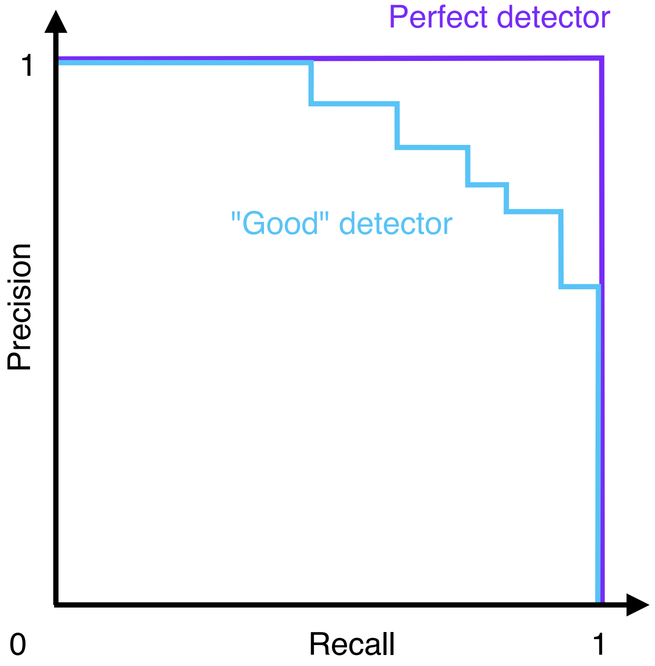

Figure 13: Deux exemples théoriques de courbes précision–rappel : un détecteur parfait (violet) et un détecteur réaliste (bleu).

les différences de jeux de données, de résolutions d'images ou de prétraitements introduisent des biais supplémentaires, rendant les comparaisons directes difficiles. Cette absence de standardisation souligne la nécessité d'un cadre commun d'évaluation dans la communauté des sciences planétaires, afin d'améliorer la reproductibilité et de faciliter les comparaisons entre méthodes. Un tel cadre permettrait non seulement d'évaluer de manière équitable les nouveaux algorithmes, mais aussi d'accélérer les progrès méthodologiques dans le domaine.

0.3 - Détection automatique de cratères

Maintenant que les concepts fondamentaux de l'apprentissage automatique et des réseaux de neurones ont été introduits, nous allons pouvoir nous intéresser à leur application spécifique à la détection de cratères d'impact sur les surfaces planétaires telle que décrit plus en détail dans le chapitre 3 de ce manuscrit.

Les surfaces planétaires subissent une évolution constante, gouvernée par des phénomènes géologiques tels que les impacts (Leighton et al., 1965) ou les éruptions volcaniques (Carr, 1973). L'analyse de la distribution et de la densité des cratères à l'aide de la méthode dite du *comptage de cratères* permet d'estimer l'âge d'une surface planétaire (Hartmann et al., 2001; Neukum et al., 2001). Cet âge constitue un indicateur précieux de l'histoire géologique et de l'évolution des surfaces planétaires (Benedix et al., 2020). Comprendre la distribution des cratères d'impact est donc essentiel pour appréhender les processus géologiques (Hartmann, 2005), incluant la déformation tectonique, le volcanisme, l'érosion, le transport, ainsi que le cratérisme lui-même (Hartmann et al., 2001). Historiquement, la détection des cratères reposait sur une analyse manuelle. Pour Mars et la Lune en particulier, plusieurs bases de données manuelles existent (Head et al., 2001; Robbins, 2019; Robbins et al., 2012). Même corrigées (Lagain et al., 2021a), ces bases restent soumises aux limites humaines. En effet, des études ont montré que l'attention diminue rapidement après 30 minutes de tâches répétitives, comme le comptage de cratères, entraînant des erreurs (See et al., 1995). De plus, le comptage manuel souffre de subjectivité et d'un manque de capacité d'adaptation à grande échelle. Ces limites peuvent être surmontées par l'emploi d'approches basées sur l'apprentissage automatique (*Machine Learning*, ML). Pour cette raison, la détection des cratères à l'aide de méthodes de vision par ordinateur a été largement explorée au cours de la dernière décennie. Une première preuve de concept fut proposée par Vinogradova et al. (2002), obtenant de bons résultats mais limités par la résolution des images. Certaines études se sont appuyées sur des critères géométriques pour la détection (Salamuniccar et al., 2010; Galloway et al., 2014). Ces méthodes, peu coûteuses en ressources, permettent de détecter efficacement des cratères relativement récents, mais elles peinent à identifier les cratères érodés (Salamuniccar et al., 2010) et ne différencient pas les cratères des autres structures circulaires (caldeiras, cônes de scories) présentes à la surface de Mars (Head et al., 2001). D'autres approches ont utilisé les modèles numériques de terrain (MNT) (Di et al., 2014; Zhou et al., 2018; Chen et al., 2018; Lee, 2019; Wang et al., 2019). Bien que pertinentes, elles nécessitent un prétraitement complexe pour produire le MNT, basé sur des acquisitions stéréoscopiques ou des mesures lidar/radar. Dans ce travail, nous nous concentrons sur la détection de cratères à partir d'images uniques. Salamunićcar et al. (2011) a recensé 77 travaux, répartis entre approches fondées sur les images et approches fondées sur les MNT. Depuis, l'avènement des algorithmes de *deep learning* tels que R-CNN (Girshick et al., 2014), YOLO (Redmon et al., 2016) ou encore les réseaux pyramidaux (Yang et al., 2022) a permis des avancées majeures (Benedix et al., 2020; La Grassa et al., 2023). Ces nouvelles techniques surpassent largement les performances de la génération précédente, mais leur robustesse reste perfectible, notamment aux hautes latitudes (>45°) et à l'échelle planétaire. Cependant, elles offrent l'avantage d'une grande polyvalence, comme l'illustrent des applications réussies à l'identification de linéaments sur Europe (Haslebacher et al., 2023), à la détection d'éboulements sur Mars (Bickel et al., 2020) ou encore à l'étude des blocs de glace sur les calottes polaires martiennes (Su et al., 2023). Des approches basées sur la segmentation, telles que l'architecture U-Net (Ronneberger et al., 2015) ou Mask-RCNN (He et al., 2017), ont également été explorées (Silburt et al., 2019; Downes et al., 2020; Latorre et al., 2023; Ali-Dib et al., 2020). Plus récemment, Giannakis et al. (2024) ont démontré qu'il est possible d'utiliser le modèle SAM (*Segment Anything Model*) de Meta (Kirillov et al., 2023) pour détecter des cratères. Ces travaux soulignent l'adaptabilité et l'efficacité des méthodes d'apprentissage profond dans des environnements planétaires variés. Ce projet de recherche vise à développer un algorithme de vision par ordinateur robuste, spécifiquement conçu pour détecter automatiquement les cratères dans les images de surfaces planétaires. Notre algorithme a été conçu pour s'adapter aux différentes latitudes et aux faux positifs liés à d'autres structures circulaires, garantissant ainsi des performances homogènes sur divers corps planétaires. Comme montré par Benedix et al. (2020), les performances des détecteurs diminuent fortement aux hautes latitudes, en raison à la fois des biais de reprojection (les projections équatoriales déforment fortement les pôles) et des conditions d'illumination (plus faibles élévations solaires aux pôles). Ces difficultés sont accentuées dans le cas des satellites héliosynchrones, pour lesquels chaque latitude est observée à la même heure locale. De plus, notre algorithme est capable de distinguer les cratères d'autres structures circulaires telles que les caldeiras (Masson, 1984; Williams et al., 2007), les cônes de scories (Brož et al., 2014) ou les tunnels de lave (Warner et al., 2003), grâce à une base d'apprentissage globale. Enfin, l'échelle des cratères est également un paramètre clé : alors que Benedix et al. (2020) se limitaient à la gamme 1,5–10 km, nous proposons ici un outil capable de détecter les cratères de diamètre supérieur à 1 km. Nos résultats confirment que la détection devient plus difficile au-delà de 45° de latitude, mais nous avons amélioré les performances en introduisant une reprojection stéréographique locale et en enrichissant l'entraînement avec des exemples polaires soumis à des conditions extrêmes d'illumination. Ces modifications ont accru les performances de notre détecteur, en particulier dans les zones traditionnellement difficiles. Comme prévu, les ombres portées deviennent plus importantes aux hautes latitudes, réduisant la performance mais dans une mesure limitée, et le détecteur conserve de bons résultats.

Une autre contribution notable de notre recherche est la capacité de l'algorithme à différencier cratères et autres structures circulaires. Si certains succès sont observés, la distinction entre cratères et caldeiras reste un défi à perfectionner. En pratique, cette limitation est peu problématique car les caldeiras sont rares dans le système solaire. Nos résultats soulignent ainsi le potentiel mais aussi les limites d'un modèle *Faster-RCNN* pour la détection automatique des cratères à l'échelle planétaire. L'algorithme présente de bonnes performances sur l'ensemble des latitudes et des échelles de cratères, ainsi que dans la différenciation avec d'autres structures circulaires. Toutefois, comme l'illustre la Fig. 14, la détection peut échouer pour des cratères incomplets dans l'image, très érodés ou de taille inférieure au seuil de 10 pixels.

Le développement et l'évaluation de cet algorithme de vision par ordinateur marquent une avancée significative dans la détection automatique des cratères à l'échelle planétaire. Grâce à un modèle de pointe, nous avons pu évaluer ses performances en fonction de la latitude, de l'échelle des cratères et de sa capacité à différencier les structures circulaires. Ces résultats ouvrent de nouvelles perspectives de recherche et d'amélioration. Notre algorithme étant open-source, des comparaisons plus exhaustives avec d'autres méthodes pourront être menées. À l'avenir, ce travail prépare le terrain pour des algorithmes de nouvelle génération, capables de fonctionner à travers instruments, corps planétaires et conditions d'observation variées. En conclusion, si notre détecteur basé sur *Faster-RCNN* représente

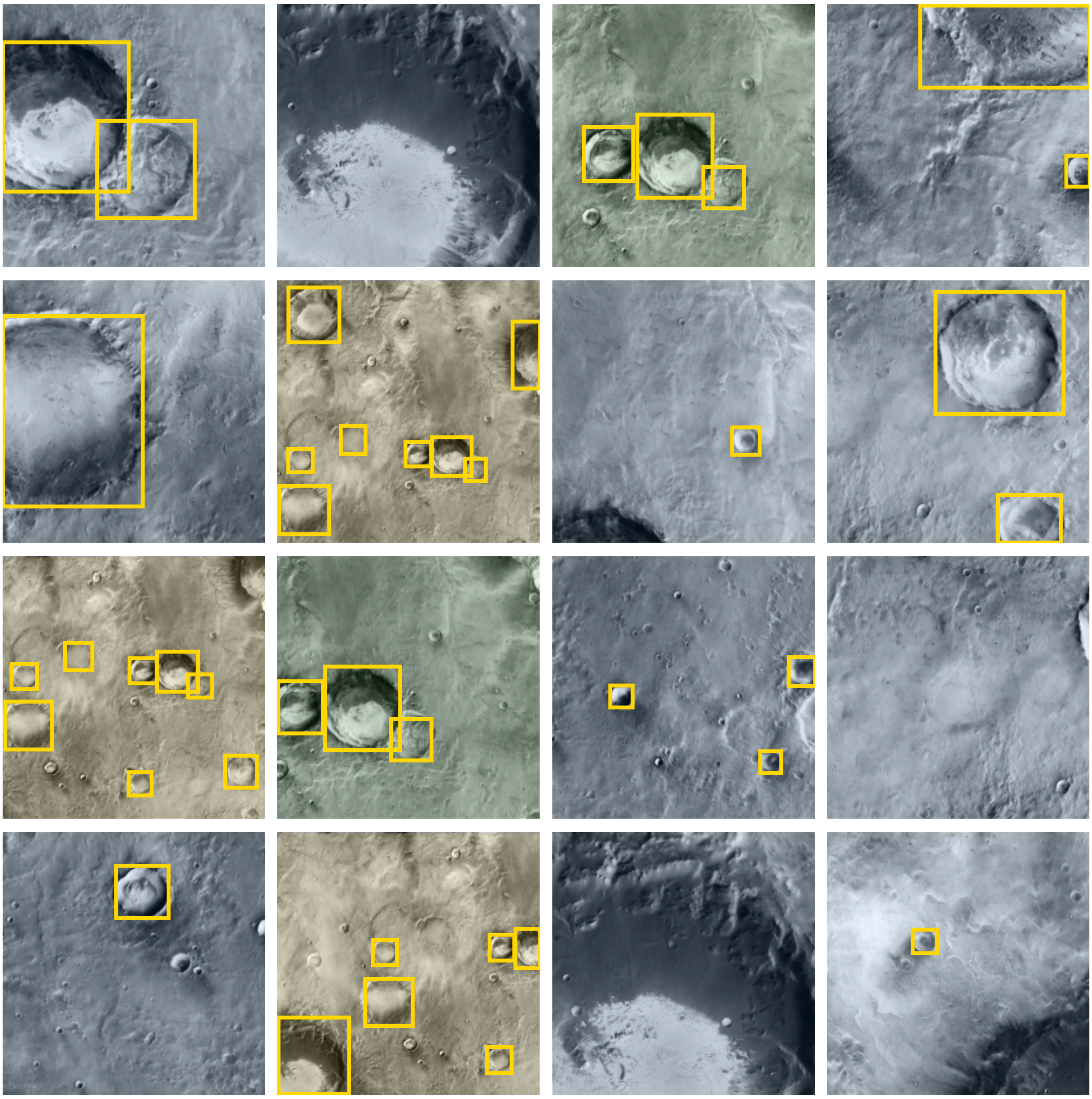

Figure 14: Exemples d'inférences de détection sur des images CTX de la région Arabia Terra (04°W, 08°S). Les patchs font 224 × 224 pixels. Bleu : résolution 100 m/px ; vert : 200 m/px ; jaune : 400 m/px.

une avancée importante, il met également en lumière la complexité et les défis persistants du domaine. Des recherches continues et une collaboration élargie seront essentielles pour dépasser ces limites et améliorer encore les capacités des systèmes de détection automatique de cratères.

0.4 - Classification automatique de cratères

Le second volet de cette thèse, détaillé dans le chapitre 4, porte sur la classification automatique des cratères d'impact martiens en fonction de leur morphologie, en utilisant des techniques de *deep learning*.

Les cratères d'impact figurent parmi les structures géomorphologiques les plus marquantes observées à la surface des corps planétaires solides (Leighton et al., 1965). Leur morphologie, leur distribution spatiale et leur état de dégradation fournissent des informations essentielles sur l'histoire géologique, les processus de surface, ainsi que sur l'âge relatif et absolu des terrains planétaires (Neukum et al., 2001; Hartmann et al., 2001). De plus, le comptage de cratères constitue la seule méthode de datation disponible pour les surfaces planétaires dont aucun échantillon n'a encore été rapporté. À ce jour, seules quelques zones de la Lune et deux astéroïdes ont pu être datés de manière absolue grâce aux méthodes radiochronologiques. Mars, en revanche, a été largement datée par la méthode des densités de cratères (Neukum et al., 1976c; Benedix et al., 2020). Au cours des dernières décennies, divers algorithmes automatiques de détection de cratères ont été proposés, en particulier pour Mars. Ces approches se répartissent généralement en trois catégories : (1) les méthodes de corrélation de gabarits (*template matching*) (Salamuniccar et al., 2010), (2) les algorithmes fondés sur les modèles numériques de terrain (MNT) utilisant des dérivées topographiques (Zuo et al., 2016; Chen et al., 2018; Lee et al., 2021; Tao et al., 2021a), et (3) les méthodes modernes d'apprentissage automatique et de *deep learning* (Benedix et al., 2020; La Grassa et al., 2023; Martinez et al., 2025). Les techniques d'apprentissage automatique ont également été utilisées pour détecter d'autres structures géomorphologiques telles que les nappes de glace (Su et al., 2023), les cônes cratériformes (Mills et al., 2024) ou les éboulements rocheux (Bickel et al., 2020). Récemment, l'application des réseaux de neurones convolutionnels (CNN) et des modèles de détection d'objets a considérablement amélioré la précision de la détection de cratères, en particulier grâce à l'utilisation d'images à haute résolution telles que les données CTX (5 m/pixel). En dépit de ces avancées dans la détection des cratères, la classification des cratères selon leur état morphologique ou leur origine reste un domaine relativement peu exploré. Une exception notable est le travail de Lagain et al., 2021a, qui a classé manuellement plus de 376 000 cratères martiens de diamètre supérieur à 1 km en quatre catégories : *réguliers*, *stratifiés*, *fantômes* et *secondaires*. Cependant, cette classification repose entièrement sur une inspection manuelle, intrinsèquement chronophage, sujette aux biais humains et difficilement extensible à grande échelle. Par ailleurs, des études comme celle de See et al. (1995) ont montré que les tâches répétitives, telles que l'annotation manuelle, entraînent une dégradation rapide des performances après de courtes périodes de concentration. Dans cette étude, nous présentons la première chaîne de classification automatique des cratères basée sur le *deep learning*, capable de distinguer les morphologies de cratères à partir d'images CTX haute résolution. Notre approche repose sur l'architecture YOLOv11 — un cadre de détection d'objets de pointe — entraînée pour assigner chaque cratère à l'une des quatre classes définies par Lagain et al., 2021a : *régulier*, *fantôme*, *stratifié* et *secondaire*. En intégrant une étape de prétraitement fondée sur la détection de cercles de Hough (Duda et al., 1972) pour affiner les boîtes englobantes des cratères, notre méthode améliore l'alignement entre les caractéristiques visuelles et les annotations, réduisant ainsi les erreurs de classification (voir chapitre 2). À notre connaissance, il s'agit de la première tentative de classification de cratères martiens par approche *deep learning*, allant au-delà de la simple détection pour permettre une interprétation géomorphologique automatisée à l'échelle planétaire. Ici, nous développons une méthode visant uniquement à classer les cratères, en choisissant de ne pas combiner classification et détection afin de simplifier le problème. Nous évaluons les performances de notre modèle à l'aide d'un jeu de test distribué sur plusieurs quadrilatères de Mars à l'échelle globale, offrant ainsi des indications sur les variations régionales de précision de la classification. Enfin, nous discutons de la manière dont une telle classification pourrait être étendue à d'autres corps planétaires et, à terme, contribuer à affiner la datation des surfaces en excluant les structures trompeuses, telles que les cratères secondaires ou dégradés.

Comme le montre la Fig. 4.8, certaines régions présentent des scores de précision nettement plus faibles que d'autres. Par exemple, dans la zone comprise entre 108° et 120°E de longitude et 40° à 52°N de latitude, la précision chute à environ 0,598. Dans cette région, où l'on compte 233 cratères *Réguliers*, 40 *Secondaires*, 18 *Stratifiés* et 18 *Fantômes*, de nombreux cratères ont été classés comme *Fantômes* alors qu'ils apparaissent en réalité comme *Réguliers*. En effet, en Fig.15, sur la première ligne, trois cratères sur quatre classés comme fantômes ne présentent pas clairement les caractéristiques typiques de ce type. Leur classification comme cratères fantômes relève ici de l'interprétation humaine. De plus, la base de données de classification initiale établie par Lagain et al. (2021a) a été réalisée manuellement par plus de 60 opérateurs différents. À la lumière de cela, nous interprétons ces quadrilatères à score particulièrement faible comme étant liés à des « valeurs aberrantes » dans la classification humaine.

On observe également en Fig 4.8 du chapitre 4 que certaines régions présentent des précisions de classification nettement plus élevées, comme le quadrilatère défini par les longitudes -100° à -92°E et les latitudes 0° à 8°S, où la précision atteint 0,924 (voir Fig.16). Dans ce quadrilatère, Lagain et ses collaborateurs ont identifié 185 cratères *Réguliers*, 10 *Stratifiés*, 4 *Fantômes* et aucun *Secondaire*. Les performances exceptionnelles observées ici s'expliquent en grande partie par la prédominance des cratères *Réguliers*, qui représentent 93% des cratères de cette région. De plus, parmi les prédictions effectuées pour cette classe, 93% ont été correctement identifiées comme des cratères *Réguliers*.

Pour conclure, nous avons présenté dans cette étude une approche innovante de classification automatique des cratères sur Mars par *deep learning*, reposant sur l'architecture YOLOv11. Notre méthodologie utilise des images à haute résolution issues de la caméra CTX de la sonde Mars Reconnaissance Orbiter et une base de données de cratères affinée. La classification visait quatre catégories géomorphologiques de cratères définies par Lagain et al. (2021a) : *Réguliers*, *Fantômes*, *Stratifiés* et *Secondaires*. Une étape de prétraitement notable, fondée sur la détection de cercles de Hough, a permis d'améliorer l'alignement entre les vérités terrain et les caractéristiques visuelles observées, renforçant ainsi la qualité et la fiabilité du modèle de classification. Le modèle proposé, basé sur YOLOv11, a atteint une précision globale robuste de 80%, démontrant sa capacité à classer de manière fiable différents types de cratères à l'échelle planétaire. Nous avons toutefois observé des variations géographiques de performance, particulièrement marquées entre 40° et 52°N de latitude et 108° à 120°E de longitude, soulignant des zones nécessitant des ajustements et analyses supplémentaires. Notre méthodologie établit un précédent pour des analyses planétaires totalement automatisées, dépassant largement les limites et biais des techniques d'annotation manuelle traditionnellement utilisées en géomorphologie planétaire. Cette classification automatisée permet non seulement d'accélérer le processus, mais aussi de produire des résultats cohérents, reproductibles et applicables systématiquement à de larges jeux de données. Pour aller plus loin, plusieurs perspectives de développement se dessinent.

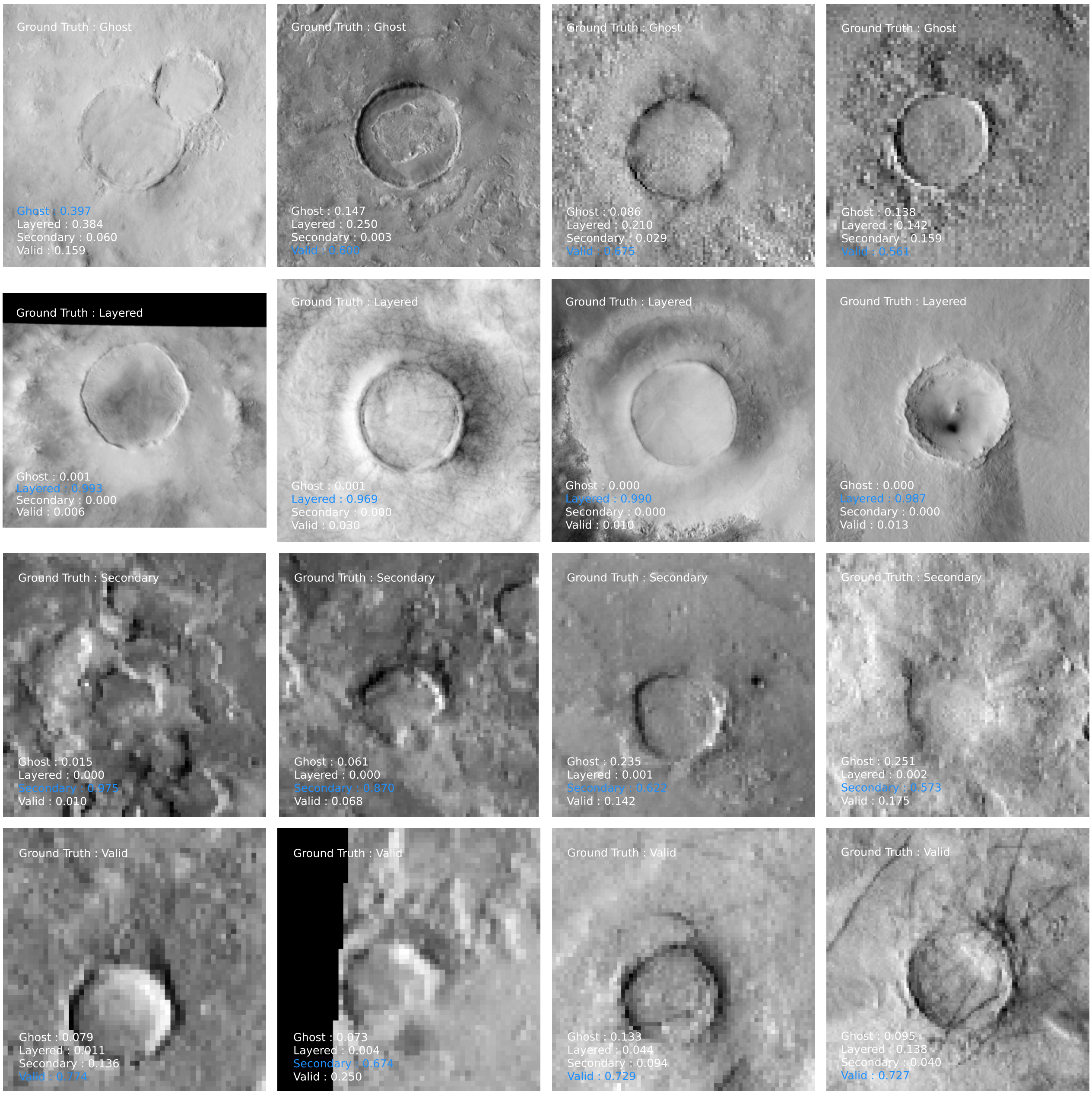

Figure 15: Exemple de 16 cratères présents dans une zone de test comprise entre 108° et 120°E de longitude et 40° à 52°N de latitude, classés de haut en bas comme Fantômes, Stratifiés, Secondaires et Réguliers. Les scores de prédiction sont indiqués en bas de chaque image.

Une possibilité serait d'appliquer notre modèle à la Lune. En raison des différences géomorphologiques significatives entre les surfaces lunaires et martiennes, une telle application nécessiterait un entraînement complémentaire, notamment pour les petits cratères. Comme illustré en Fig. 4.13 du chapitre 4, les cratères *Réguliers* lunaires présentent des caractéristiques morphologiques différentes de ceux de

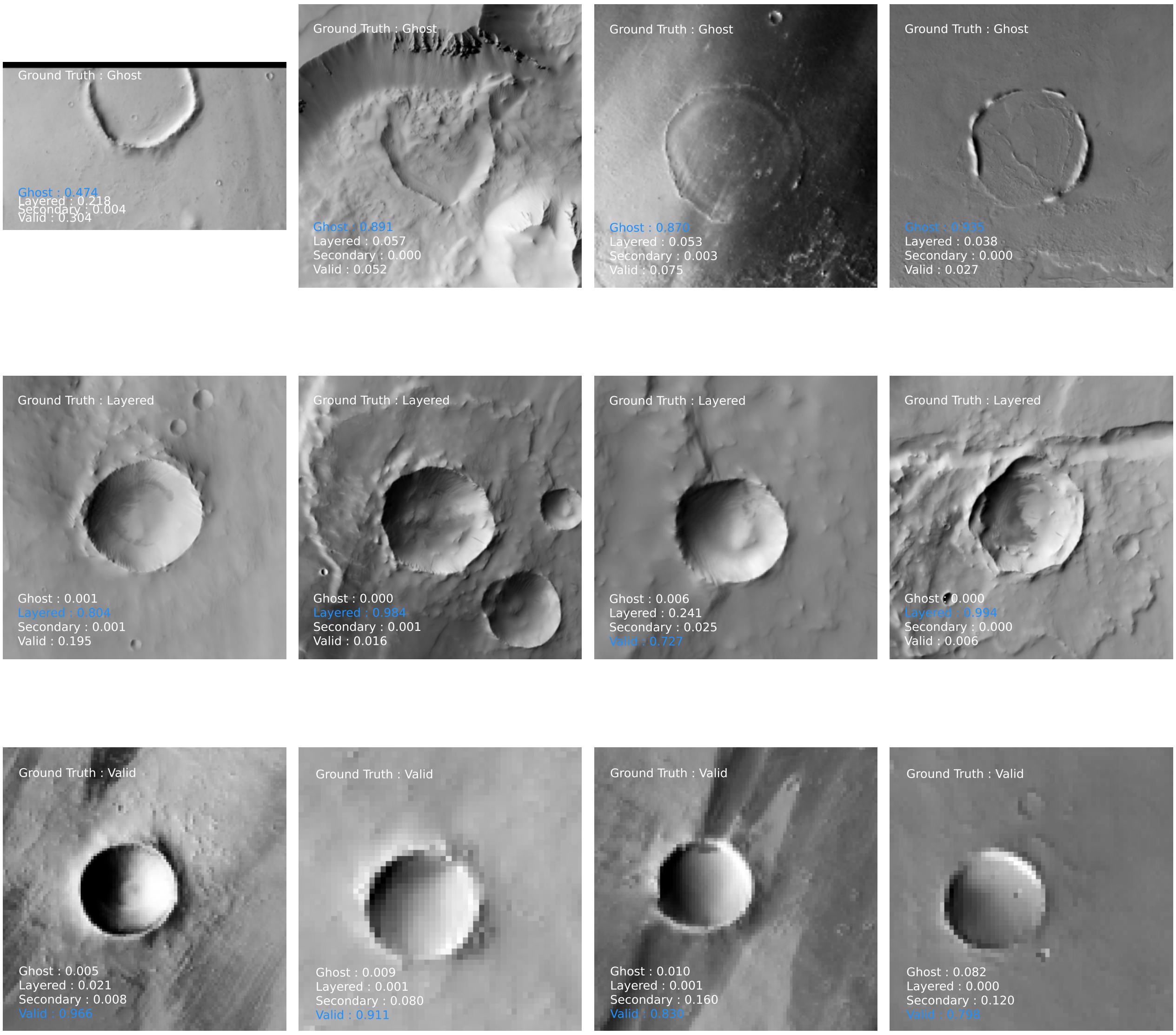

Figure 16: Exemple de 12 cratères présents dans une zone de test comprise entre -100° et -92°E de longitude et 0° à 8°S de latitude, classés de haut en bas comme Fantômes, Stratifiés et Réguliers.

Mars. L'absence d'atmosphère et les effets du vieillissement spatial (*space weathering*) sur la Lune se traduisent par des rebords de cratères plus lissés, érodés et diffus. La morphologie en cuvette typique y est souvent moins marquée, nécessitant soit un entraînement avec des données supplémentaires, soit la création d'une nouvelle classe.

De même, explorer l'applicabilité du modèle à d'autres corps planétaires tels que Mercure ou les lunes glacées comme Europe et Encelade permettrait de démontrer davantage la robustesse et la polyvalence de notre pipeline de *deep learning*. Une telle extension nécessitera toutefois des jeux de données spécifiques, qui ne seront disponibles qu'avec les premières données des missions Europa Clipper et JUICE. Malheureusement, aucune base de vérité terrain n'existe actuellement pour évaluer les performances de notre modèle sur ces corps. En outre, l'usage de techniques d'*apprentissage par transfert* (*transfer learning*) pourrait faciliter l'adaptation de notre modèle à différentes bases de données de cratères et sources d'images. Enfin, une perspective prometteuse de notre méthodologie réside dans l'affinement des techniques de datation des surfaces planétaires. En identifiant et en excluant avec précision les cratères secondaires et fantômes — qui biaisent souvent les mesures de densité de cratères — notre approche automatisée pourrait conduire à des déterminations d'âge plus fiables, améliorant ainsi significativement notre compréhension des chronologies géologiques planétaires. En conclusion, notre algorithme de classification automatique des cratères basé sur le *deep learning* constitue une avancée majeure en sciences planétaires, offrant un outil puissant pour caractériser systématiquement les surfaces planétaires. Le perfectionnement et l'élargissement de cette approche ouvrent des perspectives considérables pour améliorer notre compréhension de l'histoire et de l'évolution géologique de Mars et d'autres corps planétaires.

0.5 - Détermination automatique des ordres de superposition des cratères

Le troisième volet de cette thèse, détaillé dans le chapitre 5, se concentre sur la détermination automatique des ordres de superposition des cratères d'impact martiens à l'aide de techniques de *deep learning*.

La détection des cratères sur les surfaces planétaires est une tâche cruciale, en particulier lorsqu'il s'agit de dater des surfaces dépourvues d'échantillons de roches (Hartmann et al., 2001; Neukum, 1977). Cependant, pour une surface très ancienne, il est impossible d'enregistrer l'ensemble des cratères d'impact, car lorsqu'un impact majeur se produit, il efface les impacts plus petits qui étaient présents auparavant. Ce concept, connu sous le nom de *saturation*, a été généralisé par Hirabayashi et al. (2024) et est désigné comme le "*concept d'équilibre des cratères*". Hirabayashi et al. (2024) présentent cet équilibre comme une condition propre à une surface cratérisée dans laquelle l'équilibre entre la formation et l'effacement des cratères empêche toute augmentation supplémentaire de la population de cratères. Il est donc impossible de connaître le nombre exact de cratères présents dans une population donnée avant un impact majeur. Par conséquent, cela introduit une modification de la courbe de fréquence des cratères, entraînant une sous-estimation des âges par la méthode du comptage de cratères. De plus, la population d'impacteurs dans le système solaire primitif reste mal connue (Morbidelli et al., 2018), et plus particulièrement la période du Grand Bombardement Tardif (LHB), qui, bien quelle demeure encore sujette à débat, est de plus en plus controversée (Hartmann, 2019). Le LHB correspond à une phase de bombardement intense qui aurait pu se produire au début de l'histoire du système solaire et aurait joué un rôle déterminant dans la structuration des surfaces planétaires et lunaires. Connaître le nombre de cratères en fonction de leur taille pourrait ainsi contribuer à reconstituer notre compréhension de l'histoire primitive du système solaire. L'étude des populations de cratères superposés pourrait permettre d'en apprendre davantage sur les cratères effacés par des impacts plus importants. De plus, puisque la distribution des cratères évolue selon une loi de puissance (Fielder, 1961), l'usage d'algorithmes d'intelligence artificielle est fortement requis si l'on souhaite obtenir une classification exhaustive des cratères, notamment à petite échelle. Ainsi, dans le chapitre 4, nous développons, à l'aide d'un algorithme de classification, un modèle capable de détecter si un cratère a été recouvert par un autre, par exemple en fonction de la présence ou non d'un rebord continu. En effet, si un cratère possède un rebord continu, cela signifie qu'il est le plus récent dans la superposition. À l'inverse, s'il ne possède pas de rebord continu, cela signifie qu'il a été partiellement effacé par un impact plus large. Un cratère de plus petite taille peut également se trouver à l'intérieur d'un cratère plus grand et plus ancien. Nous introduisons ci-après de manière précise le concept d'*ordre de superposition*, et proposons un algorithme de *deep learning* destiné à l'estimer. La base de données initiale utilisée pour cette tâche a été construite par Lagain et al., 2021a, comme décrit en section 3. Cette base référence l'ensemble des cratères martiens d'un diamètre supérieur à 1 km. Pour chaque cratère, elle inclut la localisation de son centre ainsi que son rayon. Notre objectif est de nous appuyer sur cette base et d'y ajouter une nouvelle information : les relations de superposition entre cratères. L'objectif de ce chapitre est donc de proposer une méthode permettant d'estimer l'ordre de superposition des cratères au sein d'un regroupement. Cela permettrait de déterminer quel cratère est le plus ancien et lequel est le plus récent dans une situation donnée de superposition. Pour ce faire, nous avons entraîné un modèle de classification par *deep learning*, en utilisant une méthodologie similaire à celle développée en section 4. Dans ce chapitre, nous détaillerons la création d'un jeu de données de référence annoté, les étapes de prétraitement, ainsi que les résultats obtenus pour la détermination de l'ordre de superposition des cratères.

Cette nouvelle base de données de cratères annotée nous a permis d'entraîner un modèle de classification par *deep learning* capable de déterminer l'ordre de superposition des cratères. Le modèle a atteint une précision de 97,5% sur le jeu de validation et a ensuite été appliqué à l'ensemble de la surface martienne afin d'estimer l'ordre de superposition de tous les cratères d'un diamètre supérieur à 2 km. Notre analyse a révélé que l'ordre de superposition dépend fortement de la taille des cratères. Plus précisément, nous avons montré qu'au-delà d'un rayon de 7 km, le nombre de cratères ne présentant aucune superposition chute de manière drastique, indiquant que les grands cratères sont significativement plus susceptibles d'être recouverts par des impacts plus petits. Ce comportement est en accord avec les attentes issues de la population d'impacteurs du système solaire primitif, où les grands impacts étaient plus rares mais avaient la capacité d'effacer un grand nombre de petits cratères. Nous avons également observé que les densités de cratères selon les différents ordres de superposition présentent une relation non linéaire, avec l'émergence de régimes distincts entre les régions de faible et de forte densité. Il est important de souligner qu'une classification aussi détaillée à l'échelle globale aurait été pratiquement impossible sans l'utilisation de l'intelligence artificielle. La combinaison de l'expertise humaine pour l'annotation initiale et de la capacité de passage à l'échelle des méthodes de *deep learning* a rendu possible le traitement efficace et cohérent de millions de cratères. Ces nouveaux résultats ouvrent la voie à des recherches complémentaires basées sur l'ordre de superposition, telles que l'étude de l'anisotropie du cratérisme ou l'estimation du nombre de cratères effacés au cours du temps afin d'affiner les méthodes de datation géologique. En définitive, ces travaux visent à améliorer notre compréhension de l'histoire du bombardement à l'échelle de l'ensemble du système solaire.

0.6 - Conclusion générale

Les chapitres de conclusion 7 et de perspectives 8 sont résumés dans cette dernière section.

L'étude de la chronologie des surfaces planétaires repose sur l'identification, la mesure et l'interprétation précises des cratères d'impact. Les approches traditionnelles, basées sur le comptage manuel des cratères, ont fourni des décennies de données précieuses mais restent intrinsèquement limitées : le processus est laborieux, chronophage et soumis à une variabilité inter-opérateurs (Benedix et al., 2020). Avec l'augmentation exponentielle du volume d'images planétaires à haute résolution, de tels inventaires manuels comme celui de Robbins et al. (2012) sont désormais impraticables à l'échelle globale, rendant le développement de méthodes robustes de détection automatique indispensable.

Au-delà de la simple détection, la classification morphologique des cratères joue un rôle crucial dans la datation des surfaces planétaires. L'exclusion des cratères secondaires, fortement dégradés ou altérés (cratères fantômes), est essentielle pour éviter des biais significatifs dans les estimations d'âge. Alors que cette classification est systématiquement effectuée manuellement dans le cadre du comptage traditionnel des cratères, elle n'a que rarement — voire jamais — été mise en œuvre de manière totalement automatisée et à grande échelle. Cette lacune a limité la fiabilité et la reproductibilité des chronologies dérivées des cratères, en particulier lorsqu'elles sont appliquées à des jeux de données étendus et morphologiquement variés, tels que ceux de Mars ou de la Lune.

De même, la détermination des ordres de superposition des cratères, qui constitue un outil important pour la datation relative, demeure un domaine émergent de la géomorphologie planétaire automatisée. Dans cette thèse, nous avons développé et validé un cadre préliminaire permettant de déterminer automatiquement ces relations. Bien qu'encore exploratoire, cette approche confirme déjà des interprétations issues des courbes de distribution cumulative de fréquence des cratères (CCFDs) et ouvre la voie à des applications plus quantitatives.

En intégrant ces deux piliers méthodologiques — la détection automatique des cratères et la classification morphologique automatisée — ce travail propose une chaîne d'inférence unifiée pour l'analyse des surfaces planétaires. Un tel système *de bout en bout*, capable de traiter de grands volumes d'images à haute résolution et de produire des inventaires de cratères affinés prêts pour l'interprétation chronologique, n'existait pas avant cette étude. L'outil développé ne se contente pas de remplacer un processus autrefois manuel : il améliore également l'objectivité, la reproductibilité et l'évolutivité de la datation fondée sur les cratères. Ce faisant, il offre à la communauté des sciences planétaires un cadre robuste pour produire des chronologies plus précises et plus cohérentes, contribuant ainsi à enrichir notre compréhension de l'évolution géologique des corps planétaires.

1 - General Introduction [1]

Contents

1.1 From Dust and Gaz to Planets . . . 46
1.2 Remote sensing, datation and crater counting . . . 51
  1.2.1 Mosaic and datasets . . . 52
  1.2.2 Absolute Lunar datation using radiometric dating . . . 53
  1.2.3 Relative datation on the Moon using crater counting . . . 54
  1.2.4 Transfer function curves for Mars and other planetary bodies . . . 59
1.3 Example of studies on Impact Craters . . . 62
  1.3.1 Erosion and Degradation of Craters . . . 62
  1.3.2 Origin of Martian Meteorites . . . 66
1.4 Crater detection method: A review of the bibliography . . . 69
  1.4.1 Manual crater Database . . . 69
  1.4.2 Machine learning for crater detection or recognition . . . 70
  1.4.3 Typical methodology to set a machine learning algorithm . . . 77
  1.4.4 Precision, Recall and others : Metric to evaluate a detection and classification . 82
  1.4.5 Deep-learning-based Crater Detection Methods . . . 87
1.5 Problematic . . . 90

---

[1] The notations used in this chapter may vary from one chapter to another

1.1 - From Dust and Gaz to Planets

In the beginning, there was nothing. Nothing? Not exactly. A small part of a giant cloud of molecular gas (Cameron, 1995; Montmerle et al., 2006), with a mass estimated at three times the current solar mass and composed mostly of hydrogen and helium, was collapsing under its own gravity while initiating an inertial movement (Cameron, 1962b; Cameron, 1962a). Over a few million years, gravity continued to compress the gas, and the conservation of angular momentum forced the cloud to spin faster as it contracted. The cloud heated up more and more as it collapsed and the temperature at the center of the cloud reached several million degrees. At this temperature, hydrogen nuclei start fusing into helium. The conservation of angular momentum also causes the cloud to flatten and take the form of a disk around the protostar that would much later become the Sun (Beuther et al., 2014). This model, known as the nebular hypothesis, was first proposed by Emanuel Swedenborg in 1734 (Swedenborg, 1734). In 1755, Immanuel Kant [2] significantly advanced this idea in his *Universal Natural History and Theory of the Heavens*, by proposing that a large, slowly rotating cloud of gas and dust (a "nebula") would gradually contract under self-gravity, spin faster, flatten into a disk, and thereby form the Sun at the center with planets emerging from the surrounding disk (Kant, 1755). Later in 1796, and independently, the french astronomer Pierre-Simon Laplace developed a similar model (Laplace, 1796). The Swedenborg-Kant-Laplace hypothesis describes how protoplanetary disks formed and evolved to build planetary systems but it has some limitations. For example, it does not explain how the material, which is present in the disk, loses its angular momentum during accretion. Later, the works of Alfvén (1977) who suggests that the angular momentum is lost by radial ejection and the work of Cameron (1962b) refine the nebular hypothesis model. With the development of new astronomical instruments, this stellar and planetary formation theory has been confirmed by numerous observations as the one shown in Figures 1.1 and 1.2. The right image from JWST Near-InfraRed Camera (NIRCam) (Fig. 1.1) is probably one of the most detailed and impressive image of proto-planetary disk ever made. We can see the disk edge-on, with a dark lane of dust and gas in the middle. The left image from the Atacama Large Millimeter Array (ALMA) radiotelescope shows the same disk but in the millimeter range, revealing the dust and gas cloud in which protoplanets are forming.

In the disk, mainly composed of gas (Hydrogen and Helium) and dust, the gravitational and electrostatic interactions made the dust particles to accrete to form larger and larger objects (Safronov et al., 1994; Poppe et al., 2000). The first objects to form whithin 1000 years are the planetesimals, which are small solid bodies ranging from a few meters to several kilometers in diameter (Cuzzi et al., 2001; Johansen et al., 2007). These planetesimals will collide and merge to form larger objects called protoplanets. The process of accretion continues until the protoplanets reach a size large enough to reach hydrodynamical equilibrium. Generally, from that point, the disk starts to dissipate it's thermal energy and the protoplanets start to cool down. As we can see in Fig. 1.2, the protoplanetary disk is not uniform, and we can see dark areas in the disk. Those dark areas correspond to the possible positions where the hot gas and dust are not dense enough to be observed in radio wavelenght, potentially because it has already been accreted by a forming proto-planet. This process — defined as "runnaway growth" by Kokubo et al. (1998)— quickly leads to the formation of planetary embryos with a size of several hundred kilometers (Kokubo et al., 2000). Then, follows a period in which the reserve

---

[2] In German, Emmanuel Kant is written Immanuel Kant.

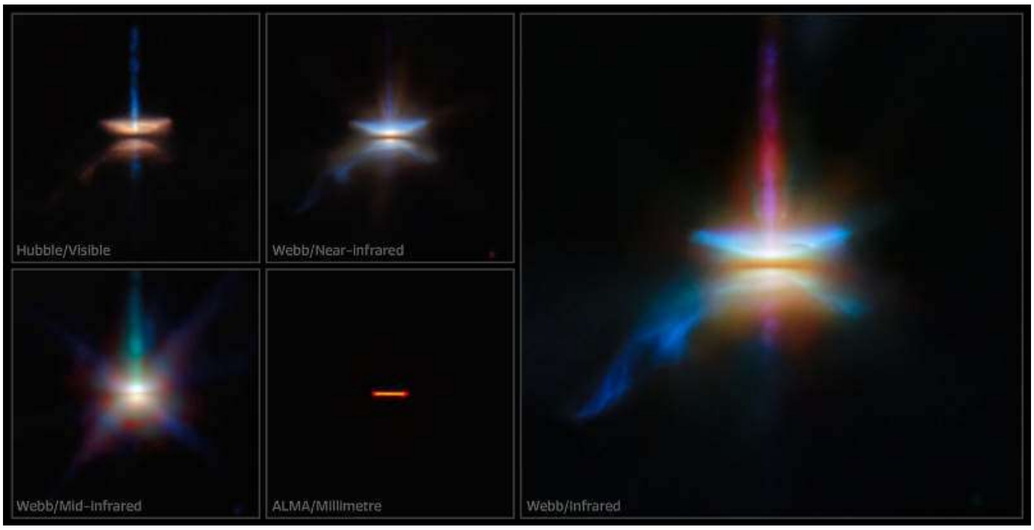

Figure 1.1: Picture from NASA/ESA/CSA James Webb Space Telescope complementing observations from the NASA/ESA Hubble Space Telescope and the Atacama Large Millimeter/submillimeter Array (ALMA). This target call HH30 is an edge-on protoplanetary disc located in the dark cloud LDN 1551 in the Taurus Molecular Cloud. The new observations made with the James Webb Space Telescope were conducted by Tazaki et al. (2025)

of planetesimals in the disk is reduced, leading to a decrease in the accretion rate. It's also during this period that planetary embryos enter in collision producing giant impacts which can lead to the formation of Moons and small bodies in the Solar System (Canup, 2008; Canup, 2012; Ćuk et al., 2012; Mastrobuono-Battisti et al., 2015). This period can last from a few million years to several tens of millions of years, depending on the mass of the disk and the distance from the star (Morbidelli et al., 2012).

In our Solar System, the process of planet formation is thought to have taken place 4 568.2 million years ago (Bouvier et al., 2010). At this time, Earth was a molten mass of silicate rock and metals. It's during this period of time — that geologist called Hadean period — that the heaviest materials such as nickel and iron deposit from meteoritics impacts started to sink under gravity influence (Melosh, 1997; Lherm, 2021). On Mars the process of planet formation was similar. This period of time, which on Earth is called Hadean period, is refered as the Noachian period on Mars (Hartmann et al., 2001). The Noachian period is the oldest geological period of Mars, lasting from about 4.6 to 3.5 billion years ago (Tanaka et al., 2014). Most of the planet's geological activity occurred during this period (Head et al., 2001). Indeed, during the Noachian period, the formation of the crust and the emergence of a magnetic dynamo driven by mantle convection generated a strong, global magnetic field that helped retain a much denser atmosphere than nowadays and protected it from solar wind escape (Solomon et al., 2005). During this period, Mars has known an intense volcanic activity, with the formation of the dome of Tharsis, the largest volcanic region in the Solar System (Carr, 1973). This volcanic activity, combined with the presence of a dense atmosphere, allowed the formation of rivers and lakes on the surface of Mars which was massively documented in scientific literature (Masson et al., 2001; Mangold et al., 2003; Bibring et al., 2006; Carr, 2012; Appere, 2012; Bultel, 2016; Mangold et al.,

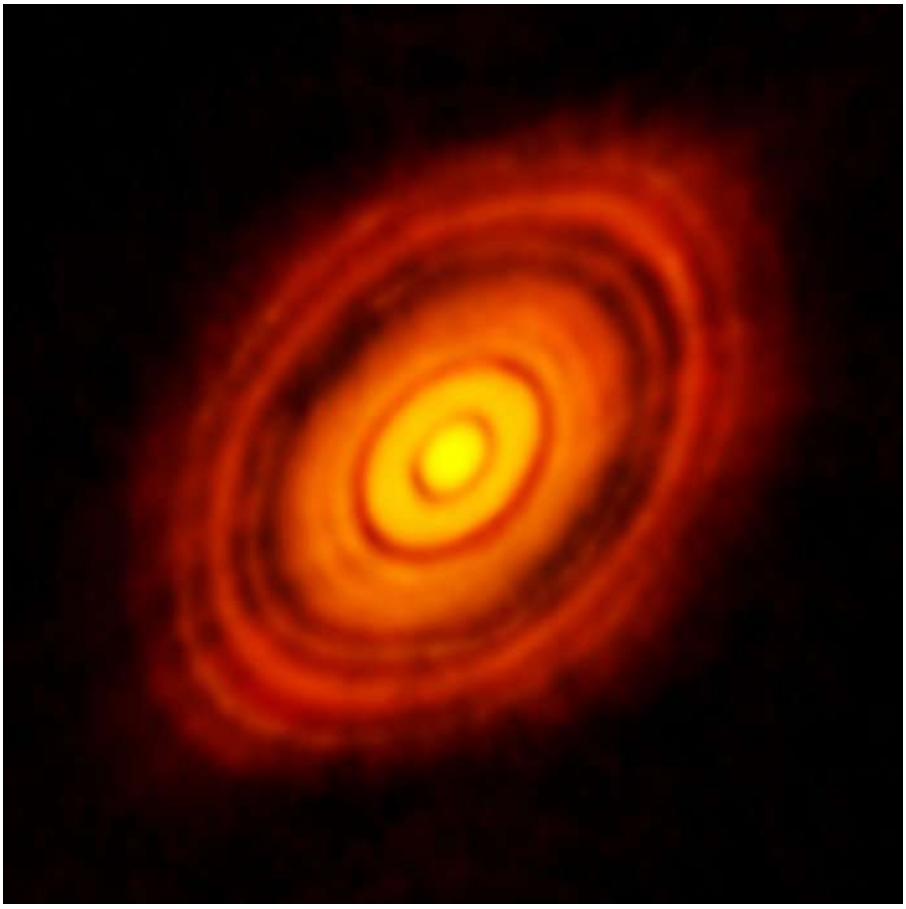

Figure 1.2: Image of a protoplanetary disk acquired by the Atacama Large Millimeter Array (ESO/NAOJ/NRA) at a wavelenght of 1.28mm. This protoplanetary disk is located in the constellation of Taurus, at a distance of about 450 light-years (138 pc) from Earth. The image shows the disk surrounding the young star HL Tauri. These observations reveal substructures within the disk that might be the possible positions of planets forming in the dark patches within the system (Akiyama et al., 2016).

2021; Quantin et al., 2004).

At this point, the development of the primitive Mars is very similar to the primitive Earth. Then, on Earth, things changed drastically: the presence of plate tectonic, and the volcanic activity completely reshaped the planet through time. Because of this, we can not find much trace of the Hadean period on Earth, excepted for some zircons crystals found in western Australia and orthogneiss rocks in northwestern Canada both dated between 4.3 and 4.4 Gy [3] (Bowring et al., 1999; Wilde et al., 2001; Mojzsis et al., 2001). On the Moon, the oldest rock samples which were collected by the astronauts were found during Apollo 16 mission with an age of 4.46 Gy (Norman et al., 2003). It is consistent with the collision hypothesis made by Canup (2008) between the protoplanet Earth and a planetesimal 4.51 Gy ago (Barboni et al., 2017).

The period which follows the Noachian era was defined by Hartmann et al. (2001) as the Hesperian. The Hesperian period is characterized by a significant decrease in volcanic activity and the formation of large impact craters, such as the Hellas basin (Tanaka et al., 2014). The atmosphere of Mars became thinner, and the planet's surface was exposed to more intense solar radiation. This period lasted from about 3.7 By to 2.5 to 2 billion years ago (Tanaka, 1986; Hartmann, 2005) and is likely to coincide with the Earth's early Archean Eon (Carr et al., 2010). The Hesperian period is also marked by the appearance of large outflow channels, which are thought to have been formed by massive floods of water as illustrated in the artist view of Mars from space shown in Fig. 1.3 (Costard, 1989; Schmidt et al., 2022).

The last period of Mars history is called Amazonian period. This period is characterized by a decrease in the rate of meteorite and asteroid impacts (Tanaka et al., 2014; Carr, 2007). The atmosphere of Mars became thinner, and the planet's surface was exposed to more intense solar radiation. This period lasted from about 2.5 to 2 billion years ago to the present day. (Tanaka, 1986). The error bars on the end of the Hespeian period/ the beggining of the Amazonian are extremely large (∼500 million years) and are still suject to discussion in the literature (Hartmann, 2005; Werner et al., 2011). The Amazonian period is also marked by the formation of aeolian features, such as dunes and ripples, which are thought to have been formed by the action of the wind on the surface of Mars. It also may be marked by a recent volcanic activity especially in the Tharsis region and Cerberus fossae region tenth of thousands of years ago (Horvath et al., 2021).

The history of the inner Solar System especially around the period of 3.9 Gy ago was and is already subject to different hypothesis (Hartmann, 2019). For some, the inner Solar System experienced a cataclysmic spike in the cratering rate from 3.9 to 3.7 Gy, commonly referred in the literature during the year 1973-1974 as a "terminal cataclysm" (Turner et al., 1973b; Turner et al., 1973a; Tera et al., 1973; Tera et al., 1974) or also from 1975 as a "Late Heavy Bombardment" (LHB) (Wetherill, 1975). This event is thought to have been triggered by the migration of the giant planets, which destabilized the orbits of countless asteroids and planetesimals, sending them toward the inner Solar System (Gomes et al., 2005; Morbidelli et al., 2001). According to this hypothesis, a large number of high-energy collisions occurred between planetary bodies, proto-planets, comets, planetesimals, and asteroids, dramatically reshaping the surfaces of terrestrial planets (Claeys et al., 2011; Bottke et al., 2017). However, this interpretation has been increasingly challenged. As reviewed by Hartmann (2019), growing evidence from lunar meteorites and asteroid samples suggests a more prolonged and

---

[3] Note that in this thesis, My and Gy are used for 10^6 years and 10^9 years, respectively.

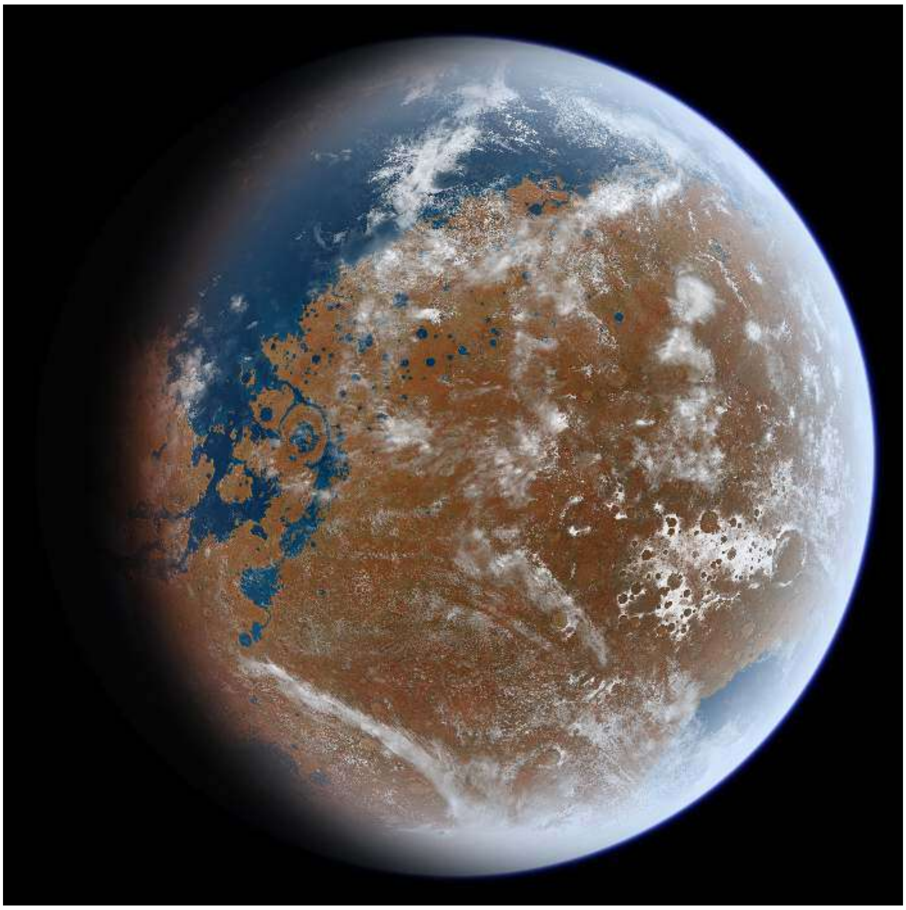

Figure 1.3: Artist's view of Mars during the Late Noachian/ Early Hesperian period. Terrestrial-like geological features such as outflow channels, lakes, canyon, etc... are shown. This does not represent an accurate picture of Noachian Mars, but the overall appearance viewed from space.

continuous bombardment rather than a short, cataclysmic event (Eugster, 2003; Schultz et al., 2016; Cohen et al., 2000; Hartmann et al., 1981). Radiometric dating fails to show a distinct spike at 3.9 Ga, and many impact ages appear spread between 4.2 and 3.5 Ga (Fernandes et al., 2013; Zellner, 2017). Additionally, reinterpretations of Apollo sample ages suggest that multiple basins may not have formed simultaneously (Haskin et al., 1998; Norman, 2009; Huang et al., 2022). Combined with evolving dynamical models, these findings support a more extended decline in impact rates rather than a sharply defined Late Heavy Bombardment (Morbidelli et al., 2018).

In this context, crater counting emerged as a powerful complementary method to radiometric dating, especially for terrains that lack returned samples. The pioneering work of Neukum (1983) introduced a production function which relates the number and size distribution of craters to the surface age of planetary terrains. By comparing observed crater size–frequency distributions (CSFDs) with calibrated flux-versus-time curves, absolute model ages can be inferred for different regions. This approach was then refined with updated impact flux models and cross-planetary comparisons or who applied crater statistics to higher-resolution datasets on Mars, improving age estimates for young surfaces (Neukum et al., 1995; Neukum et al., 2001; Quantin et al., 2004; Quantin et al., 2007; Robbins, 2013). And so, Hartmann's chronologic system (Hartmann, 1972), updated in Quantin et al. (2007) and Hartmann et al. (2007), proposed an alternative crater production function, calibrated using both lunar and martian terrains, and suggested that impact flux continued to decline beyond 3.0 Ga.

In this PhD, we dig deep into the field of planetary chronology using crater counting methods. As developed upper, the datation methods are a keypoint in our understanding of the first few billion years of our Solar System. We focused on one of the main limitations of this datation technique: the ability to accurately and comprehensively identify and count impact craters in a given geological unit. Since the derived model age is directly dependent on the completeness and reliability of the crater counting, any misidentification can significantly affects the resulting chronological interpretation, specially in the big crater size range.

The first part of this introduction in section 1.2 will describe the basics of the datation using crater counting methods and highlight the possible limitations of the actual method. The section 1.3 will illustrate different application of this methodology. The next section 1.4 will present a review of the different approaches proposed to detect craters. Finally, the last section 1.5 will presents the main questions addressed by this PhD.

1.2 - Remote sensing, datation and crater counting

Modern geology is the study of the Earth and other astronomical bodies, focusing on their structure, composition, and both internal and external processes. Like every natural sciences, geology focus on the observation of natural phenomena and the interpretation of these observations. The goal of modern geology is to understand the history and evolution of the Earth and other celestial bodies. In the context of planetary science and exploration, it raises two fundamental questions. In a first hand the morphological and compositional characteristics of the surface (1) (sub-section 1.2.1) and in the other hand the absolute age of every geological units that composes it (2) (sub-sections 1.2.2, 1.2.3 and 1.2.4). Those informations are crucial to understand the geological history of a planet, its evolution, and its current state. In this section, we will focus on the study of Mars and the Moon. We will begin by presenting the various datasets available for investigating their surfaces, then, we will review the key research efforts undertaken to determine the ages of these two bodies.

1.2.1 - Mosaic and datasets

Recent advances in orbital remote sensing have drastically improved image resolution, transforming our ability to detect and interpret small-scale geomorphological features. For Mars, the first surface images acquired by Mariner IV in 1965 had a resolution of approximately 3 km/pixel. The first global mosaic of Mars, produced using images from the Viking Orbiter, had an initial resolution of ∼925 m/pixel, later refined to ∼230 m/pixel (James, 1966; VikingV1, 2001; VikingV2, 2009).

Today, image resolution has improved by more than an order of magnitude. Indeed, the most detailed local imagery available is provided by the High-Resolution Imaging Science Experiment (HiRISE) onboard the Mars Reconnaissance Orbiter, capable of achieving resolutions of 25–30 cm/pixel (McEwen et al., 2007). While HiRISE coverage is spatially limited, it is complemented by the Context Camera (CTX), which has produced the most detailed global mosaic to date, with a resolution around 5–6 m/pixel (Malin et al., 2007; Bell III et al., 2013; Dickson et al., 2024; Planetary Visualization, 2022; Planetary Visualization, 2024). This CTX mosaic now covers 99.5% of the Martian surface from 88°S to 88°N. It's an impressive quantity of data which represent 5.7 Tera pixels (= 5.7 Tera bytes).

In parallel, Europe's contribution came from the High Resolution Stereo Camera on board of Mars Express, which acquired global coverage at ∼12 m/pixel resolution (Michael et al., 2016a; Michael et al., 2025), offering stereo capabilities valuable for topographic analysis. More recently, China's Tianwen-1 mission released a global color mosaic at 76 m/pixel resolution, providing full hemispherical coverage and filling gaps in the existing planetary cartographic archives (Liu et al., 2024).

Although this discussion has focused primarily on Mars, similar datasets exist for other planetary bodies. The Moon is extensively imaged by the Lunar Reconnaissance Orbiter Camera (LROC), at a resolution around 0.5 m/pixel, enabling detailed lunar surface characterization and crater analysis (Robinson et al., 2010). For Mercury, the MESSENGER spacecraft has produced global image mosaics and digital terrain models via its MDIS camera system (Becker et al., 2009), supporting geological interpretations of heavily cratered terrains.

These increasingly detailed datasets enable the identification of small craters, layered deposits, and subtle erosional features that were previously undetectable. Spectroscopic data from the OMEGA instrument have revealed widespread hydrated minerals, offering insights into ancient aqueous processes (Bibring et al., 2006). Mapping of aeolian activity, such as dust devil tracks, has been compiled from orbital monitoring (Conway et al., 2025), while older studies have highlighted the potential role of subsurface volatiles in shaping surface landforms (Costard, 1989). Thermal inertia datasets from the THEMIS instrument also provide valuable information about day and night surface temperature (Edwards et al., 2011). More recently, studies have focused on specific regions such as Oxia Planum (Fawdon et al., 2024), or morphological features like pitted cones, which may signal past degassing or cryovolcanic activity (Mills et al., 2024). Several efforts have also aimed at constructing global crater catalogs using these high-resolution datasets but few of them will be discussed in section 1.4.

In summary, the exponential growth of high-resolution datasets has both revolutionized planetary surface studies and introduced new methodological challenges, particularly in the context of automated geomorphological feature detection and age estimation via crater counting.

1.2.2 - Absolute Lunar datation using radiometric dating

Radiometric dating mesurments technics are the only way that we have to measure the absolute age of rocks and minerals. These techniques, originally developed a century ago, are based on comparing the abundance of a naturally occurring radioactive isotope within the material to the abundance of its decay products, which form at a known constant rate of decay (Boltwood, 1907; McDougall et al., 1999). The recent explorations of the Moon from the 1970's to nowadays enabled astronauts and robotic missions to bring rock samples from various lunar terrains. The Table 1.1 shows the Mission, the location and the total mass of every sample-return mission that has been conduct on the Moon.

Mission	Returned Sample Mass [kg]	Location	Year
Apollo 11	21.6	Mare Tranquillitatis	1969
Apollo 12	34.3	Ocean of Storms	1969
Luna 16	0.101	Mare Fecunditatis	1970
Apollo 14	42.3	Fra Mauro	1971
Apollo 15	77.3	Hadley–Apennine	1971
Apollo 16	95.7	Descartes Highlands	1972
Apollo 17	110.4	Taurus–Littrow	1972
Luna 20	0.055	Terra Apollonius	1972
Luna 24	0.17	Mare Crisium	1976
Chang'e 5	1.731	Mons Rümker	2020
Chang'e 6	1.935	Apollo Basin	2024
Total	385.592		

Table 1.1: Lunar missions that returned surface samples and their respective sample masses and years. Tab from Stöffler et al. (2001), Table 1. The Chang'e mission masses are from Che et al. (2021) and Cui et al. (2024) for Chang'e 5 and Chang'e 6 respectively.

Pioneering studies based on isotopic systems such as Ar-Ar, K-Ar and U-Pb have established that many lunar basins formed between 3.8 and 4.0 billion years ago (Turner et al., 1973b; Turner et al., 1973a; Guggisberg et al., 1979). These studies contributed to defining a temporal framework for the Moon's major geological events, including the formation of the Imbrium, Nectaris, and Serenitatis basins (Norman et al., 2003). Over the following decades, improved analytical techniques have refined these age estimates, reducing uncertainties and enabling a more detailed reconstruction of lunar impact history (Fernandes et al., 2013).

One of the most powerful high–precision techniques is the ^{40}Ar–^{39}Ar method, an advancement of conventional K–Ar dating. In this approach, a sample containing ^{39}K and ^{40}K is irradiated in a nuclear reactor to convert a known fraction of ^{39}K to ^{39}Ar. Upon stepwise heating of the irradiated material, both ^{39}Ar (proxy for ^{39}K) and radiogenic $^{40}\mathrm{Ar}_{*}$ are released and measured in a mass spectrometer. The age of the rock sample is given by the following equation:

$$t = \frac{1}{\lambda} \ln \left[1 + J \cdot \left(\frac{^{40}Ar*}{^{39}Ar} \right) \right] \tag{1.1}$$

where t is the age of the sample, λ is the decay constant of ^{40}K to ^{40}Ar —which is approximately 5.5×10^{-10}year^{-1}, corresponding to a half-life of approximately 1250 Million years—, J is the neutron fluence parameter determined by irradiating a standard of known age, and $\left(\frac{^{40}Ar*}{^{39}Ar} \right)$ is the measured ratio of radiogenic to proxy argon. By analyzing multiple temperature steps ("age spectrum"), one can identify and correct for any argon loss or excess, yielding highly robust crystallization ages.

In recent years, China's Chang'e missions have revitalized the field by expanding the spatial and temporal coverage of radiometric constraints on the lunar surface. Notably, the Chang'e-5 mission returned samples from the Procellarum Terrane, yielding an absolute age of 2.03 Ga for a young mare basalt unit — the youngest lunar rock dated so far (Xiao et al., 2024). In addition, crater size-frequency distributions calibrated on these new dates have confirmed the persistence of volcanic activity on the Moon well after the traditional cessation time inferred from Apollo samples (Xie et al., 2023).

Together, these data points (see Fig. 1.4) provide essential calibration anchors for crater-counting techniques on the Moon and, by extension, for other solid surfaces in the Solar System. However, the limited spatial sampling of returned samples and the reliance on cratered terrains near landing sites remain significant limitations. These constraints highlight the ongoing need to refine lunar chronology using both future sample return missions and high-resolution orbital observations.

1.2.3 - Relative datation on the Moon using crater counting

Relative dating of planetary surfaces by crater counting has its origins in the pre-Apollo era. As early as 1961, Fielder (1961) observed that lunar craters appeared to follow a size distribution described by a power law. He was the first to introduce the concept of the Crater Size-Frequency Distribution (CSFD). Subsequently, this power-law distribution was utilized for the relative dating of planetary surfaces. Indeed, the fundamental hypothesis of this theory is that the older a geological unit is—meaning the region has not experienced resurfacing through erosion, volcanism, or other geological processes—the longer it will have been exposed to bombardment by meteorite projectiles (Hartmann, 1965b; Hartmann, 1965a; Hartmann, 1966). Thus, with the return of the first Apollo and Luna samples, the connection between CSFD and absolute ages of planetary surfaces could be firmly established (Hartmann, 1970; Hartmann et al., 1971; Hartmann, 1972).

In this section, we will discuss the central role the Moon has played in the development of crater-count dating methods. We will particularly explore the work of two researchers, Hartmann and Neukum, who independently studied the correlation between the ages of collected rock samples and their corresponding crater densities since 1975. Their studies yielded similar results, notably a marked decrease in the impact flux between 3.9 and 3.2 billion years ago, as illustrated in Figures 1.7 and 1.8.

Hartmann & Neukum production's function In his work published in 1972, Hartmann linked the crater densities observed around sample collection sites with the ages measured from these samples. He subsequently termed this relationship the "production function." As shown in Fig. 1.5, this production function is defined by three distinct segments. These segments —details with equations

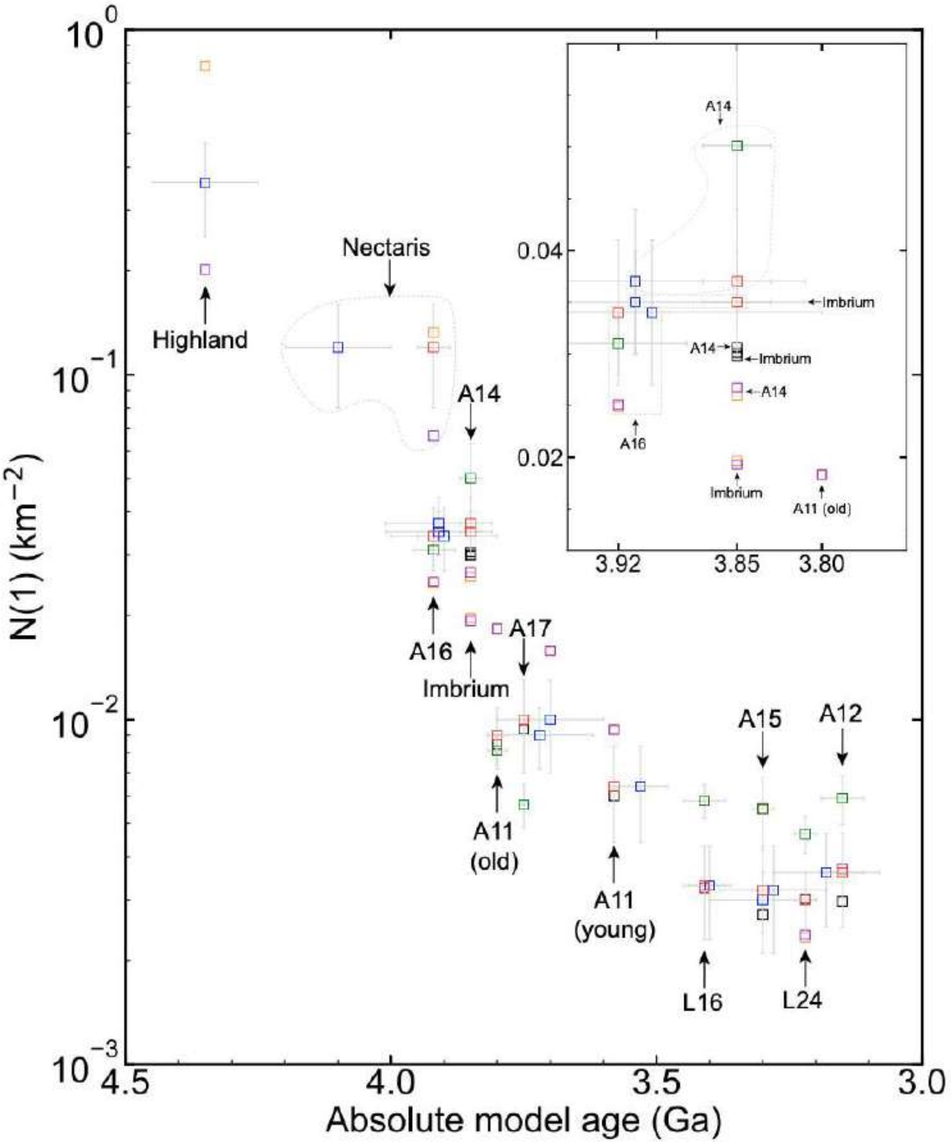

Figure 1.4: From Xiao et al. (2024): Uncertainties of radiometric ages of lunar samples for 14 returned lunar samples from Apollo and Luna missions. This figure shows the N(1) values (number of craters larger than 1 km per km^2) versus the radiometric ages of the corresponding lunar samples.

1.2, 1.3, 1.4— were determined by empirical measurements on a few rock samples whose ages exhibited significant uncertainties. Nevertheless, this work laid the groundwork for a model of relative dating through crater counting.

$$\begin{aligned}
\log(N_H) &= -2.616 - 3.82 \cdot \log(D_L), \text{ for } D_L < 1.41 \text{ km} \qquad (1.2)\\
\log(N_H) &= -2.920 - 1.80 \cdot \log(D_L), \text{ for } 1.41 \text{ km} < D_L < 64 \text{ km} \qquad (1.3)\\
\log(N_H) &= -2.198 - 2.20 \cdot \log(D_L), \text{ for } D_L > 64 \text{ km} \qquad (1.4)
\end{aligned}$$

In his work, Hartmann uses an log-incremental SFD representation with a standard diameter bin size. The number of craters per km^{-2} here is calculated for craters in the diameter bin $D_L < D_L < D_R$, where D_L and D_R are the left and right bin boundary and the standard bin width is $\frac{D_L}{D_R} = \sqrt{2}$.

Parallel to Hartmann's chronology, G. Neukum developed an alternative production function which is cumulative. The Neukum Production Function, introduced in the late 1970s and refined in Neukum et al. (2001), present, as shown in equation 1.5 an analytical formulae which have a form of a 11-order polygon and where the coefficient can be found in Table 1.6, became a standard in many planetary dating applications.

$$\log_{10}(N \geq D) = a_0 + \sum_{i=1}^{11} a_n \left[\log_{10}(D)\right]^n \qquad (1.5)$$

The two systems—Hartmann and Neukum—are broadly consistent for ages younger than 3.2 Gy, but diverge more significantly in older terrains due to different assumptions about early Solar System impact rates and functional forms. Furthermore, because of the crater saturation on ancient highland surfaces, in which every new impact tends to partially erase or overprint an existing crater, the measured crater density ceases to increase linearly with time and instead approaches an equilibrium distribution. As a result, small differences in the assumed production function or in the treatment of secondary craters become amplified, leading to increasingly large age discrepancies for terrains older than $\sim 4.0 Gy$.

Calibration and Use of Apollo Sample Sites The calibration of both Hatmann and Neukum's models relies on crater counts near Apollo and Luna landing sites, where radiometric ages are available from returned samples. These calibration points were used to adjust the isochrons to real geologic timescales as shown in Figures 1.7 and 1.8, notably in works such as Hartmann (2005) and Neukum et al. (2001). However, uncertainties remain, particularly for surfaces younger than 1 Ga or older than 3.9 Ga, where sample constraints are sparse or indirect. Recent work has focused on improving both the statistical basis of crater counts and the modeling of the impact flux. For example, Kneissl et al. (2016) questioned the assumption of spatially homogeneous cratering and introduced methods to model local resurfacing and non-sparse populations. Feuvre (2023) used dynamical simulations to model the flux of impactors in the Earth–Moon system, proposing refined impact rates that inform chronology curves. Lagain et al. (2024) proposed a recalibration of the lunar chronology curve by cross-validating crater-based ages with improved stratigraphy and remote sensing data. Similarly, Bultel et al. (2023) and Werner et al. (2023) reevaluated the ages of key lunar basins, suggesting that several surfaces could be younger than previously assumed.

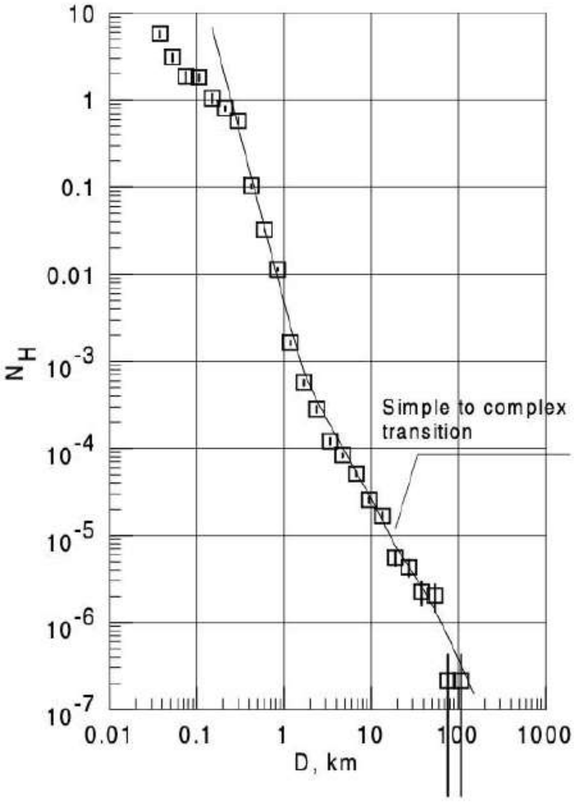

Figure 1.5: From Neukum et al. (2001): Hartmann's production function (HPF). N_H is the number of craters on an "average" mare surface per a $\sqrt{2}$ diameter bin.

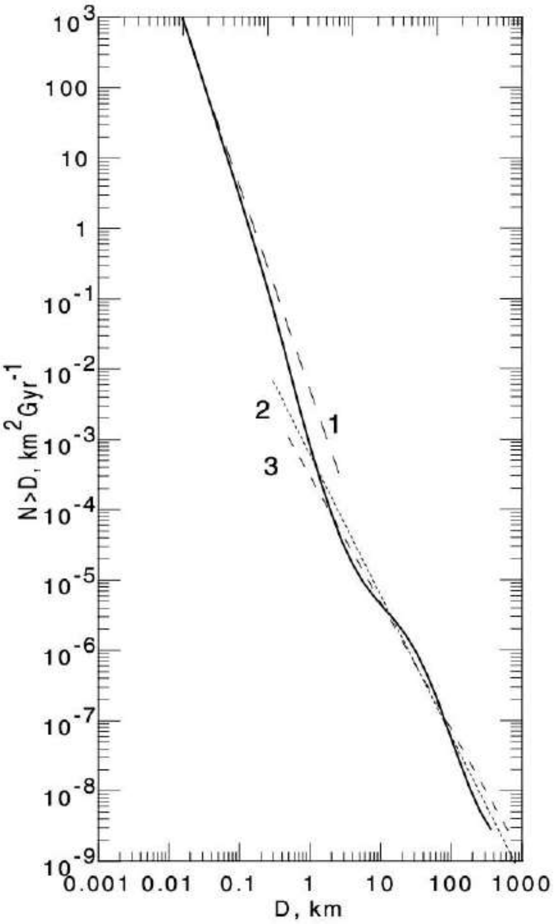

Figure 1.6: From Neukum et al. (2001): Comparison of the Neukums's production function (NPF) with power-law distributions published in the literature: (1) $N \sim D^{-2.9}$ (Shoemaker et al., 1970) ; (2) $N \sim D^{-2.0}$(Hartmann et al., 1971); (3) $N \sim D^{-1.8}$ (Baldwin, 1971; Hartmann et al., 1981)

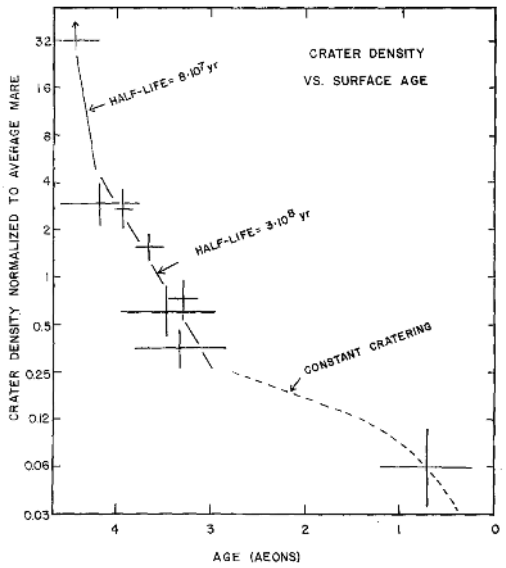

Figure 1.7: From Hartmann (1972): Crater density vs surface age for dated lunar provinces.

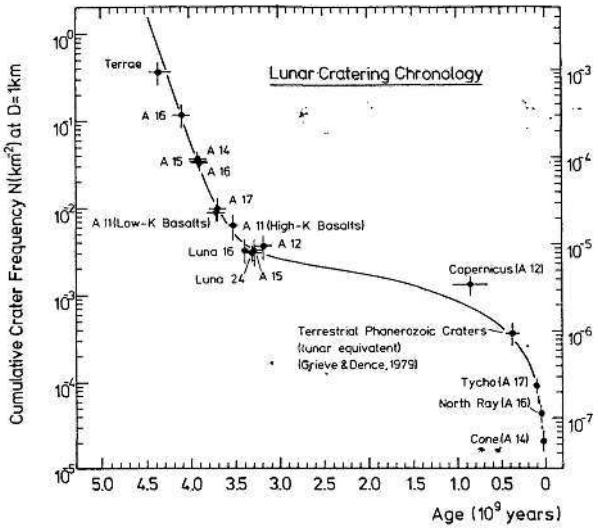

Figure 1.8: From Neukum (1983): Lunar impact chronology. This curve links the cumulative crater frequency for all crater with a diameter > 1 km to the absolute age. It was determined from the radiometric datation made during the post Apollo-era

a_i	"Old" $N(D)$ (Neukum, 1983)	"New" $N(D)$ (Neukum et al., 2001)	"New" $N(D)$ Sensitivity*
a_0	-3.0768	-3.0876	—
a_1	-3.6269	-3.557528	±3.8%
a_2	$+0.4366$	$+0.781027$	±3.9%
a_3	$+0.7935$	$+1.021521$	±2.5%
a_4	$+0.0865$	-0.156012	±1.6%
a_5	-0.2649	-0.444058	±0.88%
a_6	-0.0664	$+0.019977$	±1.3%
a_7	$+0.0379$	$+0.086850$	±0.78%
a_8	$+0.0106$	-0.005874	±1.8%
a_9	-0.0022	-0.006809	±1.8%
a_{10}	-5.18×10^{-4}	$+8.25 \times 10^{-4}$	±5.6%
a_{11}	$+3.97 \times 10^{-5}$	$+5.54 \times 10^{-5}$	±24.1%

Table 1.2: From Neukum et al. (2001): Coefficients of the Neukum Production Function define in the polynomial equation 1.5. (*) The "Sensibility" is the coefficient variation that changes the N(D) value a factor of 2 up and down.

1.2.4 - Transfer function curves for Mars and other planetary bodies

The concept of a crater production function, first extensively developed for lunar surfaces by Hartmann et al. (2001) and Neukum (1983), can be adapted for other planetary bodies, such as Mars or Mercury, by applying appropriate production functions that account for different impact conditions, such as impactor velocity, gravity, and atmospheric effects (Neukum, 1983; Hartmann et al., 2001; Ivanov, 2001; Ivanov, 2008). On Mars, the production curve (or "Mars production function") is crucial as it translates lunar-derived chronology into an absolute Martian chronology, allowing the dating of geological events (Hartmann et al., 2001; Werner et al., 2002; Robbins et al., 2014; Robbins, 2014).

The extension of the crater production function to Mars required adjustments for the proximity of Mars to the asteroid belt, gravitational focusing[4], and notably atmospheric filtering of smaller projectiles, which significantly affects the size-frequency distribution of smaller craters (Neukum et al., 1976b; Neukum, 1983; Ivanov, 2001; Robbins et al., 2014). The most influential adaptations were proposed by Ivanov (2001) and Ivanov (2008), who refined the scaling laws using observed crater populations from different Martian terrains as shown in Fig. 1.9.

Hartmann (2005) independently revised his chronology model by integrating observational constraints from recent orbital missions, notably Mars Global Surveyor (MGS), Mars Odyssey, and Mars Reconnaissance Orbiter (MRO). These missions provided high-resolution imagery, enabling detailed characterization and classification of primary and secondary crater populations on Mars (Hartmann, 2005; Robbins, 2014). Quantin et al. (2004) and Quantin et al. (2007) provided additional observational constraints on the Martian cratering rate by studying landslides in the Valles Marineris region. They highlighted a complex interplay between crater obliteration processes and impacts, emphasizing the necessity of careful chronological calibration. Their findings reinforced the applicability of the refined Martian transfer curve, particularly in terrains with complex resurfacing histories.

Moreover, Bultel et al. (2023) and Werner et al. (2023) recently revisited the lunar cratering chronology, proposing updated calibration points based on an innovative characterization of geological units using spectral observations and analyses. This approach significantly improved the precision of crater counting and, consequently, surface age estimations. As seen in Fig.1.9, the Martian chronology is fundamentally linked to the lunar curve, any refinement in the lunar chronology directly propagates to the absolute dating of Martian surfaces (Werner et al., 2023).

Transfer functions are not limited to Mars and have been successfully applied to other planetary bodies, such as Mercury and icy satellites (Parker et al., 2010; Robbins et al., 2014). On Mercury, for instance, adaptations of the lunar-derived production functions accounted for differences in gravitational acceleration, impact velocity distributions, and surface material properties. Robbins et al. (2014) emphasized the importance of tailoring transfer functions to the specific geological and dynamical contexts of each planetary body.

In summary, the transfer function curves developed for Mars by Neukum, Hartmann, Ivanov, and refined by subsequent observational studies represent a crucial methodological advancement. They enable researchers to establish robust absolute chronologies for Mars and other planetary surfaces by adapting lunar-derived production functions to account for specific impact conditions and geological contexts. Continued refinements based on improved observational data and modeling efforts remain

---

[4] Concept which describes how the gravitational attraction between two objects increases the probability that they will collide

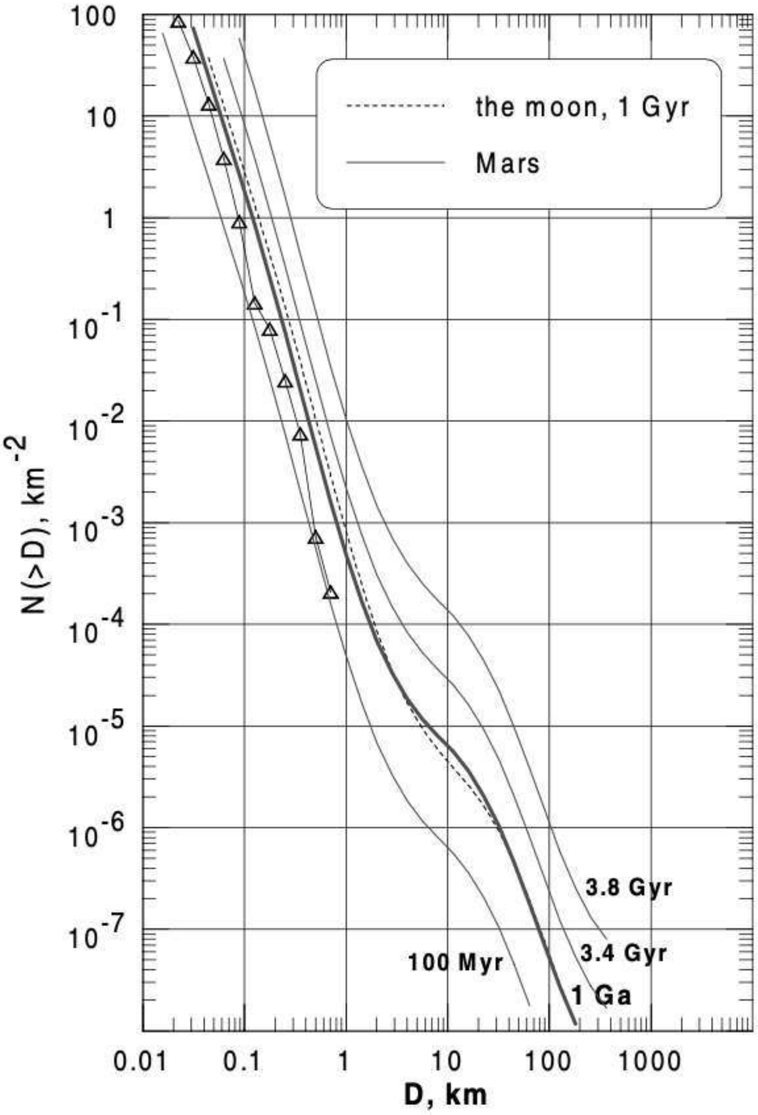

Figure 1.9: From Ivanov (2001): The Martian "isochrones" based on the Neukum Production Function (Model 1) with the gravity/collapse (no strength/gravity transition) scaling of cratering. The dashed line presents the 1 Gyr isochron for the Moon. For more detailed about the Mars-to-Moon comparison, see Fig. 5 of Ivanov (2001).

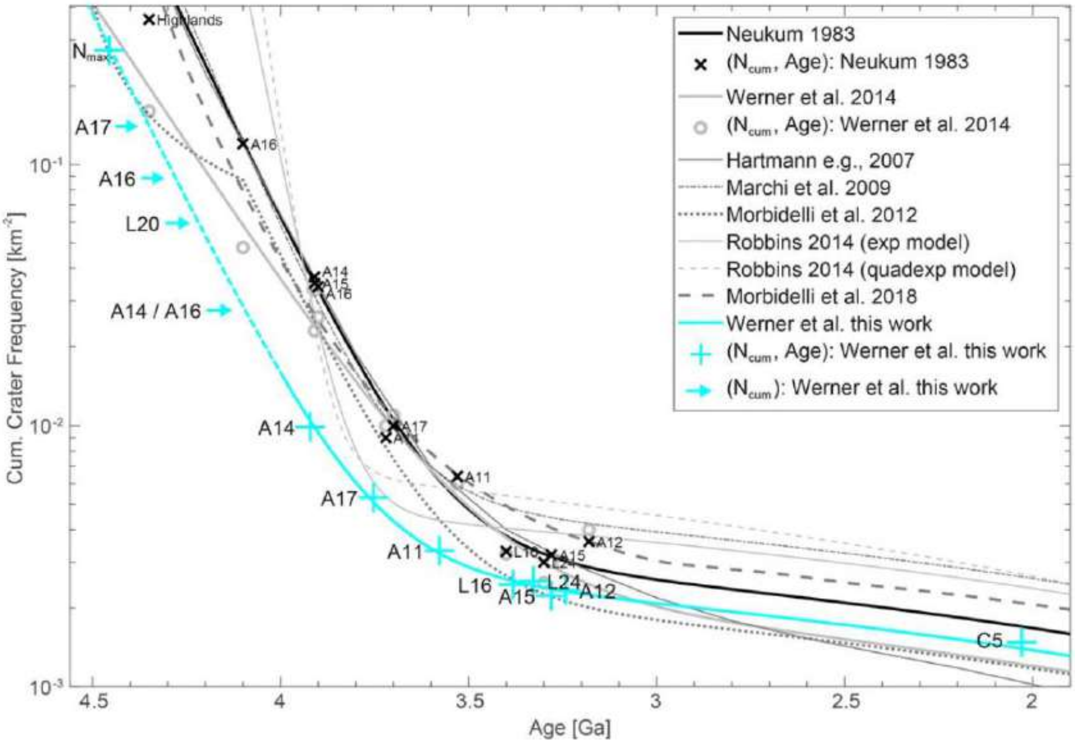

Figure 1.10: From Werner et al. (2023): Overview of the newly proposed calibration pairs and their fitted analytical function for the updated cratering chronology model (cyan). Each calibration point is shown with uncertainties in crater frequency and assigned age, while an upper–lower envelope illustrates the propagated calibration uncertainties. For samples where no direct age assignment was possible, only the corresponding age range is indicated. At younger ages (below 1 Gy), red calibration pairs are taken from Hiesinger et al. (2012). For comparison, the standard chronology model by Neukum (1983) (black) and several more recent models (gray) are also displayed

essential for enhancing the accuracy of planetary chronologies.

Applications and Limitations The lunar crater chronology remains the reference standard for extrapolating ages on other planetary bodies, such as Mars and Mercury (Ivanov, 2001; Ivanov et al., 2007; Quantin et al., 2007). However, the method has intrinsic limitations. First of all, this model is, as described previously in this section, an extension of the radiometric datation made on the lunar samples collected from the Moon. Even if the datations made during the 1970's has been refined, the incertitude remains important and is possibly subject to discussion. Furthermore, the presence of secondary craters, resurfacing events, and preservation biases can affect crater counts, particularly at small diameters (Halim et al., 2024). Additionally, the use of crater counts below 500 m is debated due to uncertainties in distinguishing primaries from secondaries and remains a very hard task since the crater size-frequency distribution follows a power law (Hartmann, 2005; Fielder, 1961).

Despite these challenges, crater counting on the Moon remains a robust tool for reconstructing planetary histories. Ongoing improvements in data resolution and crater classification, combined with dynamical models of the impactor population, are gradually refining the absolute dating of lunar and planetary surfaces.

1.3 - Example of studies on Impact Craters

Impact craters are the most widespread geological landforms in the Solar System. They are observed on nearly all solid-surfaced bodies, including the Moon, Mars, and Earth, but also on Mercury, Venus, the Galilean and Saturnian Moons, and even on small bodies such as the asteroid Vesta and comet 67P/Churyumov–Gerasimenko. While crater populations have been historically used for surface dating, the significance of impact craters in planetary science goes well beyond chronology.

In this section, we review a range of studies that focus on various aspects of impact craters and their scientific applications beyond direct crater counting. These include research into erosion processes, impact mechanics, secondary effects, and their implications for planetary surface evolution. Although not always directly related to age determination, these studies contribute essential knowledge for interpreting planetary histories through the lens of impact cratering.

1.3.1 - Erosion and Degradation of Craters

The first observation of craters on a planetary surfaces is probably the one made by Galileo Galilei when, on the end of November 1609, he turned his telescope in the direction of the Moon. What he described was a surface marked by rugged mountains and circular depressions, a scene later famously referred to by Buzz Aldrin as a "magnificent desolation". However, the origin of these depressions remained a subject of debate for centuries. In his influential work *Micrographia*, Hooke (1665) proposed two possible origins for these circular features: volcanic activity or impacts from projectiles coming from space. Although both hypotheses remained under consideration for a long time, Young (1940) and later Fielder (1961), noticed that the crater distribution on a given surface envolves as a power law which is incompatible with the volcanic hypothesis. The crater morphology but also as mentioned by Hartmann (2003), the crater states of erosion in a given region give important information about the region history. In this section we will start from the very fresh impact and discuss what created the wonderful diversity of martian and lunar landscape by reviewing the literature on crater morphology, erosion, and degradation processes.

Morphology of standard craters, a first step though classification The morphology of the craters was explored by different studies such as Cintala (1977), Cintala et al. (1998), and Melosh (1997) who proposed a classification scheme based on the size and shape of craters. This classification made the difference between simple and complex craters (see Fig. 1.11). Simple craters are typically less than ∼10 km in diameter on Mars and the Moon and are characterized by their bowl-shaped morphology, well-defined rims, and uniform interior slopes. Their depth-to-diameter (d/D) ratio is approximately 1:5, consistent across many planetary surfaces.

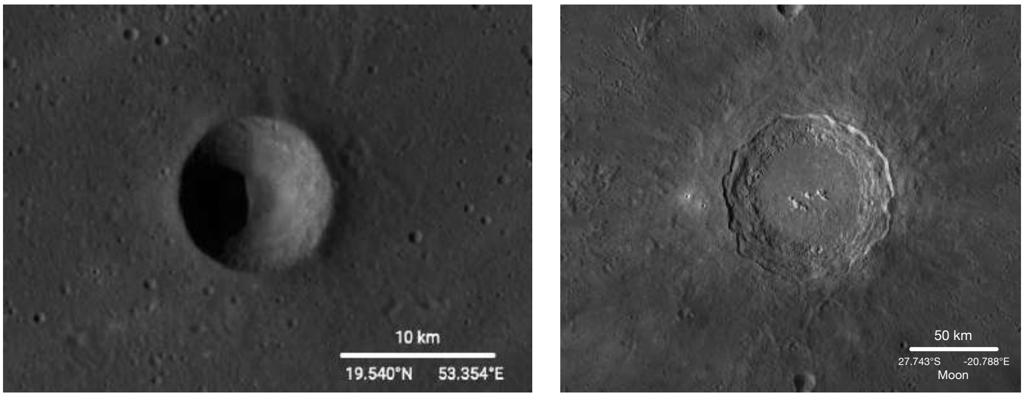

Figure 1.11: Two different craters on the Moon. The one on the left is a simple crater, while the one on the right is a complex crater. The difference between the two is that the complex crater has a central peak and a multiringed structure as described by Chandnani et al. (2019).

According to Pike (1980), these craters display an isometric scaling up to a critical diameter beyond which structural transitions occur. Their ejecta are generally radially symmetric, and in airless environments, these fresh features are often surrounded by high-albedo rays and secondary crater fields. When the energy is higher (i.e.: The mass of the impactor is more important), complex craters begin to form. It happens because the impact energy surpasses a threshold sufficient to induce collapse of the transient cavity. This transition occurs at ∼4–7 km diameter on the Moon and ∼5–8 km on Mars (Pike, 1980). These craters exhibit a range of interior features including central peaks produced by elastic rebound of the crater floor. These morphologies are the result of the interplay between shock wave propagation, target material strength, and post-impact modification (Chandnani et al., 2019; Baker et al., 2011).

Studies such as Baker et al. (2011) have demonstrated the evolution from complex craters to peak-ring basins, which typically form above 100 km in diameter. In these structures, the central uplift collapses into a ring of peaks, potentially due to fluidization of the interior or lithospheric weakening. This transformation is highly sensitive to crustal thickness and rheological layering, making such craters important geophysical probes.

Morphometric analysis has been pivotal in quantitatively differentiating crater types. Parameters such as rim height, crater depth, and central peak elevation are measured via topographic profiles obtained from instruments like LOLA (Lunar Orbiter Laser Altimeter) on the Moon and MOLA (Mars Orbiter Laser Altimeter) on Mars. Cintala et al. (1998) synthesized morphometric data across multiple planetary bodies, establishing scaling relationships and gravitational dependencies. These studies confirm that the transition diameter from simple to complex craters inversely correlates with surface gravity, supporting theoretical models of crater collapse mechanics. Another critical insight comes from temporal imaging studies such as Speyerer et al. (2016), who used LROC NAC images to track the formation of new impact craters on the Moon. Their work improve our understanding of regolith mixing rates, and suggest that small impacts may play a larger role in regolith evolution than previously believed.

Together, these studies demonstrate that crater morphology is a rich source of geologic and geophysical information. The classification and analysis of impact structures—ranging from pristine bowl-shaped depressions to degraded, peak-ring basins—provide valuable insights into surface processes, substrate properties, and the impactor flux through time. As high-resolution datasets continue to grow, automated classification tools and advanced morphometric algorithms will further refine our understanding of the impact cratering process across the Solar System.

Lobate craters and water-ice interaction Another very martian-endemic type of crater morphology is the lobate crater. These craters, present only on Mars, are characterized by the presence of lobes of ejecta extending around the impact site. These lobes are typically wider than the crater itself and can extend for several kilometers. The presence of lobate ejecta is thought to be related to the presence of water or ice in the subsurface, which can facilitate the ejecta flow, creating the characteristic lobate shape (Costard et al., 2001; Head et al., 1999).

Barlow et al. (2000) developed a standardized nomenclature for Martian ejecta morphologies, distinguishing Single Layer Ejecta (SLE) craters, Double Layer Ejecta (DLE) craters, and Multiple Layer Ejecta (MLE) craters shown respectively in Fig. 1.12, **A**, **B**, **C**. Additional ejecta morphologies include pedestal craters (Pd), characterized by a single, elevated ejecta blanket that terminates without a distinct outer rampart (Fig. 1.12, **D**). Circular and unlobed ejecta forms, such as pancake craters (SLEPC), are considered a subtype of SLE craters, with a smooth, rounded ejecta layer (Fig. 1.12, **E**). More recently, Boyce et al. (2015) identified Low-Aspect-Ratio Layered Ejecta (LARLE) craters, which exhibit similar morphologies to SLE, DLE, or MLE craters but are distinguished by a particularly thin and extensive outer ejecta layer. These various morphologies are interpreted as indicators of the presence of subsurface volatiles, such as ice or liquid water, which vaporize during impact and influence ejecta emplacement (Fig. 1.12, **F**).

The presence of ice in the Martian subsurface further supports the hypothesis of an ancient climate favorable to the existence of liquid water on Mars. As early as the 2000s, following the works of Strahler (1957), few works argued in favor of the presence of liquid water on Mars, mostly created by rainfall (Masson et al., 2001). These observations were corroborated by climate modeling studies such as those conducted by Bouley et al. (2016). Even, an ocean has been proposed based on geomorphological analyses (Baker et al., 1991; Head et al., 1999). More recently, Hildenbrand et al. (2023) theorized the possibility that Olympus Mons, which exhibits substantial amounts of hydrated minerals on its flanks, was eroded by liquid water, with comparative analyses with terrestrial analogues supporting this hypothesis (Cornillon et al., 2025).

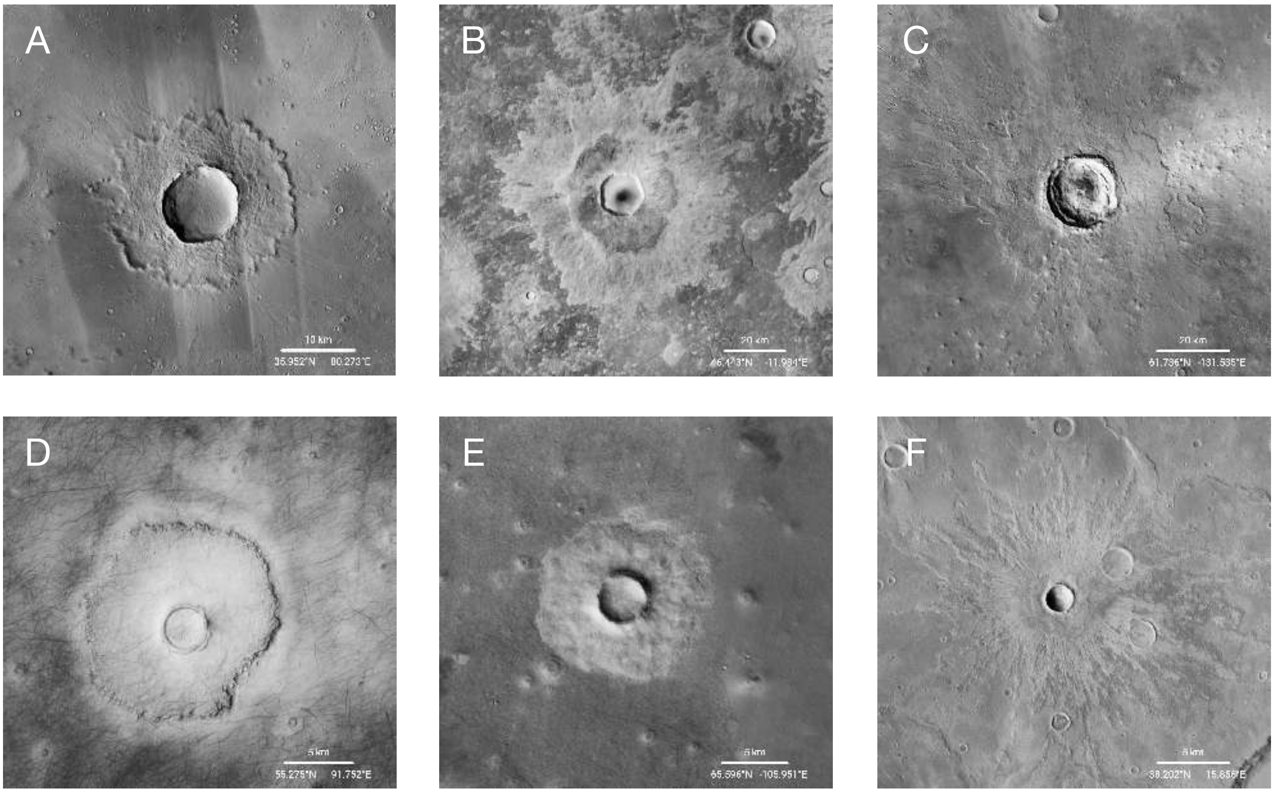

Figure 1.12: Different morphologies of Layered craters identified by Barlow et al. (2000) and Boyce et al. (2015) and imaged with CTX Camera (Dickson et al., 2024): **A**: A single layered ejectas crater (SLE) ; **B**: A double layered ejectas crater (DLE); **C**: A multi layered ejectas crater (MLE) ; **D**: A pedestal crater ; **E**: A Pancake Crater (SLEPC) ; **F**: A Low-Aspect-Ratio Layered Ejecta crater (LARLE)

The presence of lineaments following topographic contours has been interpreted as ancient tsunami traces, further supporting the hypothesis of an ancient ocean on Mars (Costard et al., 2017; Costard et al., 2019) dated 3 Ga. Nevertheless, the climatic conditions on Mars have drastically changed since then (Schmidt et al., 2022). The loss of Mars's global magnetic field, caused by the disappearing of the dynamo effect in the planet's core, allowed its atmosphere to escape into space Solomon et al. (2005). The resultant decrease in atmospheric pressure and temperature made it impossible for liquid water to exist on the Martian surface. However, traces of water ice have been detected in the Martian subsurface, notably by the Phoenix mission Mellon et al. (2009) and Zent (2008) and more recently through observations of morning frost on shaded slopes of impact craters Valantinas et al. (2024).

Erosion and Ghost craters Water and ice in the surface/subsurface do not only contribute to create very specific pattern around the impact site, it also plays a key role in the erosion of impact craters. The presence of water flowing at the surface of Mars has for example contributed to the formation of old paleolakes and river channels (Costard, 1989; Masson et al., 2001; Mangold et al., 2003; Bibring et al., 2006; Carr, 2012; Appere, 2012; Bultel, 2016; Mangold et al., 2021; Nizam et al., 2022). The presence of water in the subsurface also contributes to the erosion of impact craters which can lead to the degradation of the crater path (Breton et al., 2022). As shown in Fig. 1.13 — A, Ghost craters are typically characterized by their shallow depth and wide diameter, and they can be difficult to distinguish from other types of craters (Benedix et al., 2020). Erosion is not only present on Mars. Space Weathering is also a process that affects the surface of the Moon, leading to the formation of ghost craters. Space weathering is caused by the interaction of the lunar surface with solar wind and cosmic rays, which can cause the surface to become more porous and less reflective Shi et al. (2022). We also know that space weathering is more present on planetary surfaces without atmosphere, such as the Moon (see Fig. 1.13 — B) and Mercury (see Fig. 1.13 — C) and it can makes the crater harder to detect Kinczyk et al. (2020).

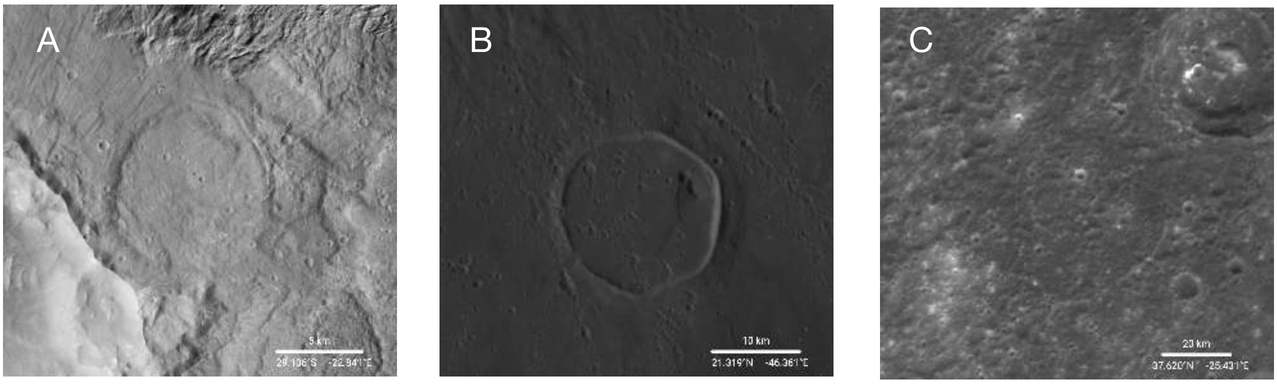

Figure 1.13: Three examples of ghost craters: (**A**) located on the Moon, imaged by the LROC instrument, (**B**) on Mars, observed with the CTX camera and (**C**) on Mercury imaged with the Messenger LOI instrument. These craters are characterized by their subdued topography, with rims and ejecta ramparts that appear shallow, eroded, or partially buried. Their degraded morphology suggests a long post-impact evolution, potentially involving volcanic resurfacing, sediment infill, or other erosional processes that have partially obliterated their original features.

1.3.2 - Origin of Martian Meteorites

Martian meteorites, extract during an impact and projected in the direction of the Earth at subsonic speed constitute the only physical samples of Mars that we can analyze in laboratories on Earth. In his study, Head et al. (2002) showed that the energy released during impacts forming craters as small as 3 km in diameter is sufficient to propel ejecta toward Earth. Martian meteorites are categorized primarily into three main petrological groups: shergottites, nakhlites, and chassignites, collectively referred to as the SNC group, along with a unique orthopyroxenite known as ALH84001 (Werner et al., 2014; Lagain et al., 2021a).

The transfer mechanism of these rocks from Mars to Earth involves high-energy impact events. When large asteroids or comets collide with the Martian surface, some ejecta achieve velocities sufficient to escape Mars's gravitational field, ultimately being captured by Earth's gravitational attraction and landing as meteorites (Lagain et al., 2021a). Identifying the exact Martian source craters for these meteorites remains a critical but also challenging scientific objective, because it requires multidisciplinary fields such as remote sensing, geochemical analysis and so on.

A first attempt proposed the Mojave Crater (Werner et al., 2014), approximately 55 kilometers wide and less than 5 million years old, as the source crater for shergottite meteorites. Mojave's geological context indicates it formed in ancient terrain, dating back roughly 4.3 billion years, suggesting that the crystallization ages of shergottite meteorites, traditionally dated at less than 600 million years based on radiometric dating, may reflect reset ages rather than their original formation ages. This finding potentially recalibrates the chronology models for Martian surface evolution, pushing back the absolute age of Mars's oldest terrains by about 200 million years (Werner et al., 2014).

Significant advancements have recently been made in the research of these source craters, particularly through detailed analyses of secondary cratering patterns and sophisticated crater detection algorithms. A notable contribution is the work of Lagain et al. (2021a), who utilized a convolutional neural network-based Crater Detection Algorithm trained on 5m-resolution CTX imagery to systematically map 90 million impact craters on Mars. By identifying secondary crater fields associated with young primary impact craters, they narrowed down candidate source craters for depleted shergottites, a subgroup of Martian meteorites characterized by their geochemical depletion in rare earth elements (REE). Their findings suggest that the Tooting and 09-000015 craters, both located in the Tharsis volcanic province, are likely candidates for the launch sites of these meteorites. This revelation implies a profound and long-lasting thermal anomaly beneath the Tharsis region, responsible for sampling depleted mantle sources reflective of Mars's early geological history (Lagain et al., 2021a).

The link between Martian meteorites and specific impact craters not only refines our understanding of the geological processes on Mars but also significantly enhances the accuracy of crater-count-based chronologies that are essential tools in planetary geology (Lagain et al., 2021b; Lagain et al., 2021c). By establishing more precise correlations between meteorite samples and Martian terrains, we can better reconstruct Mars's geological timeline, including volcanic, tectonic, and erosional histories.

A complementary perspective on Martian meteorites's origins and their geological context was recently brought by the discovery and analysis of granitic rocks in Martian meteorite NWA 7533 (Malarewicz et al., 2025). This breccia contains quartz-bearing clasts that represent the oldest differentiated lithologies identified on Mars. These clasts, which have granitic mineral assemblages dominated by quartz, potassium feldspar, and plagioclase, indicate significant magmatic differentiation processes on early Mars. The presence of quartz, a mineral indicative of evolved crustal compositions and hydrothermal conditions, suggests that early Martian crust formation involved extensive water–rock interactions, possibly combined with impact melting. Such processes parallel those hypothesized for the formation of Earth's oldest continental crusts, like the Acasta Gneiss Complex, emphasizing the commonalities between early Earth and Mars geodynamic evolutions.

Furthermore, detailed isotopic analyses (O and Si isotopes) on these quartz grains from NWA 7533 have shown signatures indicative of magma mixing with water-altered crustal materials, reinforcing the hypothesis of a significant hydrothermal alteration and impact-melting environment during the early Martian crustal evolution (Malarewicz et al., 2025). Such findings imply that differentiated rocks, similar to those found on Earth's ancient continental crust, formed under analogous conditions involving hydrothermal fluids and impact-induced magmatic processes.

In conclusion, Martian meteorites such as shergottites, and polymict breccias like NWA 7533, not only provide invaluable samples from Mars but also yield critical insights into early planetary crust formation and evolution processes. Continued studies using advanced automated crater counting methods, detailed mineralogical analyses, and isotopic measurements will further refine our understanding of the geological contexts from which these meteorites originated, helping reconstruct the evolutionary history of Mars and, by analogy, that of early Earth.

1.4 - Crater detection method: A review of the bibliography

In this section we will review the literature on crater detection methods, especially since the development on Artificial intelligence based tools to detect and classify geological features on planetary surfaces. We will start to present the manually counted databases that have brought a precious contribution to the field of planetary science. Then we will present the machine learning based methods that have been developed to automatize the detection of craters on planetary surfaces. Finally, we will present the most recent advances in deep-learning based methods that have been developed to detect and classify craters on planetary surfaces.

1.4.1 - Manual crater Database

The first crater databases were manually counted by planetary scientists (and probably a lot of future planetary scientist). These databases were created by manually identifying craters one by one on planetary images. We organised this section by planetary bodies, starting with the Moon, then Mars and finally other bodies.

Moon The first crater databases were created during the Apollo-era. The first lunar crater database was created by Pike (1976) who manually referenced 484 craters with a size range from 400m to 300km on the Moon using topographic and morphometric analyses. This work also included a small Earth database of 22 craters from 10m to 22km in diameter for comparison purposes.

A significant advancement came with the work of Head et al. (2010), who used Lunar Reconnaissance Orbiter Laser Altimeter (LOLA) data to systematically identify and measure over 5 000 craters larger than 20 km across the entire lunar surface. Their study revealed the global distribution of large impact craters and provided new insights into the impactor populations and the resurfacing history of the Moon. Crater densities derived from this dataset enabled stratigraphic correlations across major lunar basins, while also confirming saturation equilibrium in heavily cratered highland regions.

More recently, Robbins (2019) compiled one of the most comprehensive lunar crater catalogs, manually identifying craters larger than 1 km in diameter using images from LROC and Kaguya. This database has become a reference for numerous morphologic and statistical studies of lunar craters.

Also, Renson et al. (2013) contributed a detailed regional database of lunar craters by combining automatic detection with manual verification, focusing on morphometric characterization for dating purposes. Altogether, these datasets helps scientist to perform datation or science on the Moon.

Mars The construction of manually counted crater databases on Mars has followed a similar evolution as for the Moon, but benefited from the increasing quality of orbital imaging. The most influential global Martian crater database is the one of Robbins et al. (2012), later refined in Robbins et al. (2014), which includes 384,343 craters larger than 1 km in diameter. This database, compiled from high-resolution imagery primarily from the Mars Orbiter Camera (MOC) and Context Camera (CTX), has been widely adopted for surface dating and geomorphologic analyses. It provides crater positions, sizes, preservation states, and in some cases classifications into primary and secondary origins.

To evaluate the consistency of this database and to extend its utility, Lagain et al. (2021b) developed a participatory project involving over 56 trained researchers and students. The aim was to systematically classify all craters larger than 1km in diameter based on key morphological attributes, including ejecta morphologies—such as Single Layer Ejecta (SLE), Double Layer Ejecta (DLE), and Multiple Layer Ejecta (MLE) types (see definitions in subsection 1.3.1 and illustration in Fig. 1.12) —as well as degradation state and whether each crater was of primary or secondary origin. Through this effort, over 8,000 entries from the original Robbins catalog were reclassified as invalid crater features, 55,309 craters were identify as secondary craters ; 8,445 craters were classified as "Layered craters" —independantly of their specific morphology (see Fig. 1.12) ; 24,530 were classified as partially or totaly buried craters (see Fig. 1.13) and 288,155 craters were identify as regular craters.

Additional regional surveys have also played an important role. For instance, Robbins et al. (2011a) and Robbins et al. (2011b) performed detailed counts over the Hellas and Isidis impact basins, providing valuable constraints on local resurfacing events and crater retention ages. Other recent efforts such as that of Jia et al. (2020) focus on the accurate classification of small craters using manual techniques supported by high-resolution mosaics, with applications ranging from chronological modeling to landing site analysis.

Taken together, these works have progressively improved both the completeness and reliability of crater inventories on Mars, especially for diameters above 1km. However, smaller diameters still pose challenges due to image resolution limits, detection biases, and the subjective nature of visual identification.

Other bodies Manually compiled crater catalogs also exist for other Solar System bodies, though generally at more limited resolution or coverage. On Ceres, Toyokawa et al. (2022) constructed a database of impact craters using Dawn Framing Camera data, offering insights into crustal processes and resurfacing events. For Vesta, Liu et al. (2018) cataloged craters with special attention to equatorial and polar morphological differences. In parallel, (Bottke, 2000) focused on elliptical impact craters across multiple bodies, providing constraints on low-angle impact mechanics and target rheology.

These planetary-specific catalogs are fundamental for comparative planetology, as they help constrain how impact processes vary with gravity, surface composition, and geological history across different Solar System bodies.

1.4.2 - Machine learning for crater detection or recognition

The application of machine learning technics to crater detection has steadily progressed over the past two decades, transforming from early rule-based systems into more sophisticated ones, including also data-driven models. This evolution has been largely motivated by the increasing availability of high-resolution planetary imagery and the impracticality of manual crater annotation at global scales. In a first part of this subsection we will introduce what Machine learning, deep-learning and Convolutional Neural Network are. Then, in a second time, we will make a literature review of the work that has been done with those relatively new tools.

Definition — machine learning In order to place crater detection within the broader context of artificial intelligence, it is necessary to introduce several foundational concepts. Object detection models are based on machine learning algorithms. Machine learning is a field of artificial intelligence grounded in applied mathematics and statistics. It involves programming an algorithm to learn how to perform tasks based on examples, rather than relying on explicitly defined rules (Bishop, 1995; Mitchell, 1997). Several learning paradigms exist for training a computer:

- **Supervised learning:** This approach consists of training a model using a labeled dataset—i.e., a set of examples for which the correct outputs are known. The model learns from these examples and is then tested on new, unseen data to evaluate its generalization capabilities.
- **Reinforcement learning:** Similar to animal training techniques, this paradigm is based on the principle of rewards. The model receives feedback in the form of a score and learns to maximize this reward as it interacts with its environment.
- **Unsupervised learning:** In this case, the model is exposed to a set of unlabeled data. It learns to identify patterns or similarities within the dataset, which can later be used for tasks such as clustering or dimensionality reduction.

The object recognition algorithms used in this study rely on supervised learning. In other words, during the training phase, the model learns from labeled examples, allowing it to make accurate predictions when applied to new data in the testing phase. In the following sections of this dissertation, we will examine the types of algorithms used for object detection in images. Nevertheless, if the object detection algorithms used in this work operates on the same fundamental principles as traditional machine learning algorithms, they do not rely on the same learning models. The underlying learning process remains **exactly** the same: the system is provided with data, and an optimization algorithm is employed to minimize errors and adjust the model to fit the data.

Definition — deep-learning and neural network In 1943, neurologist Warren McCulloch and mathematician Walter Pitts modeled, for the first time, the functioning of biological neurons by considering that a neuron could be represented as a logical transfer function. To understand their operation, it is useful to first examine the functioning of biological neurons. Neurons are the fundamental cells of the brain. As illustrated in Fig. 1.14, a neuron consists of a body cell, one or more dendrites that receive incoming information, and a single axon that transmits information. To send a signal, the neuron releases small quantities of neurotransmitters. These neurotransmitters are chemical substances that bind to the dendrites of subsequent neurons. The signal received by a neuron can be of two types: excitatory (+) or inhibitory (−).

Artificial neurons are conceived in a manner analogous to biological neurons. As illustrated in Fig. 1.15, they are represented as transfer functions that take input signals x and produce an output y. Such an artificial neuron is called *perceptron*.

This function performs two main steps to transmit information. First comes the aggregation step, which, as shown in Eqn. 1.6, consists of summing the product of the inputs x with a weight coefficient w. This weight coefficient represents synaptic activity (Fig. 1.14) and indicates whether the input signal is excitatory or inhibitory. The coefficient w is a real number between -1 and 1. The bias coefficient b acts as an additional adjustable parameter that allows the activation threshold of the neuron to be shifted independently of its weighted inputs. In biological terms, it can be thought of as an intrinsic level of excitability of the neuron. From a mathematical perspective, the bias enables the activation function to be translated along the input axis, which is crucial to model relationships

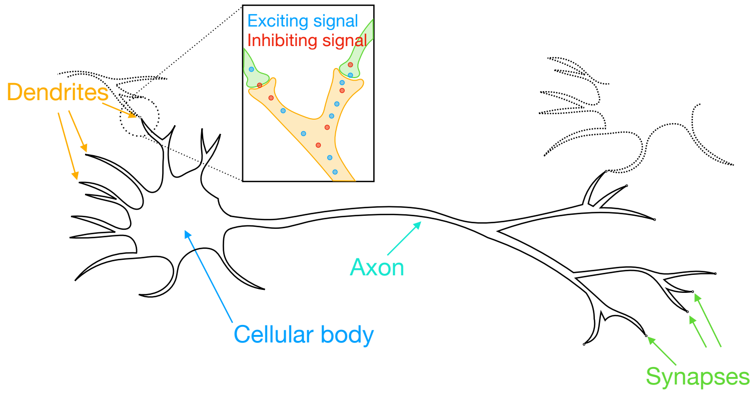

Figure 1.14: Schematic view of a biological neuron

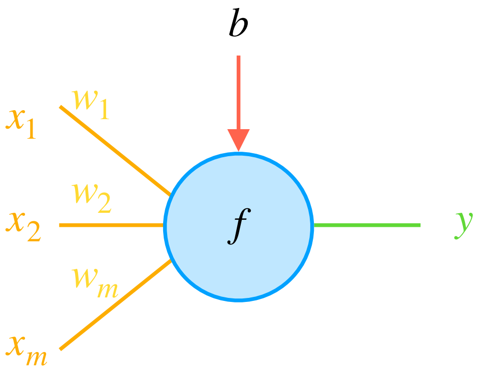

Figure 1.15: Schematic view of an artificial neuron (perceptron). x_m represent the input information and the coefficient w_m is the weight coefficient which represents synaptic activity. The b is a biase coefficient which can be use to offset the result.

that do not pass through the origin. Without a bias term, the neuron's output would be constrained to be zero whenever all inputs are zero, severely limiting the flexibility of the network to fit complex, non-linear patterns.

$$\text{Agregation: } f = \left(\sum_{i=1}^{m} w_i \cdot x_i\right) + b \tag{1.6}$$

The second step is the transfer phase. This function determines whether or not the neuron is activated, based on the result of the aggregation phase. In this work, we have chosen to use the ReLU function (Rectified Linear Unit, Eqn. 1.7), although other functions also exist. Among the most widely used are the hyperbolic tangent and the sigmoid functions.

$$\text{Transfert: } y(x) = \max(0, x) \tag{1.7}$$

In their study, McCulloch et al. (1943) demonstrated that this model could reproduce basic logical operations such as the AND and OR gates. However, the breakthrough of their invention lies in the fact that by connecting the outputs of certain neurons to the inputs of others, it becomes possible to solve problems far more complex than those handled by a single neuron. Fig. 1.16 illustrates a multilayer neural network composed of an input layer with two neurons and an output layer with a single neuron.

Although this model laid the foundations for deep-learning, it has several limitations. For instance, it does not include a learning algorithm; in other words, to use it, one must manually determine the values of the weight coefficients w_i and biases b_i. It is therefore not directly usable in its original

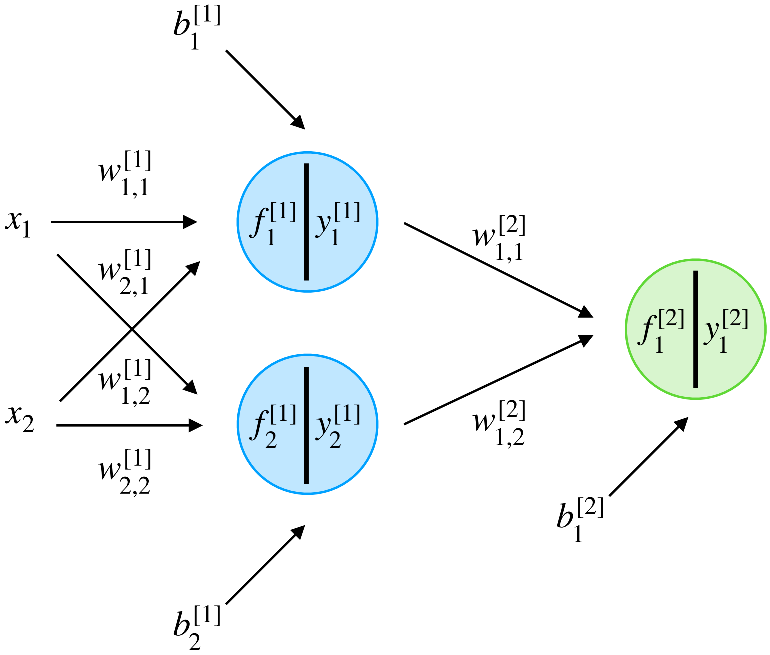

Figure 1.16: Schematic representation of the functioning of an artificial neural network (also called a multilayer perceptron) composed of three neurons arranged in two layers.

form. This limitation was not addressed until 1957, with the work of Frank Rosenblatt on the so-called "multilayer perceptron" (Rosenblatt, 1961), as illustrated in Fig. 1.17. These networks of functions are more commonly referred to as artificial neural networks (McCulloch et al., 1943).

Convolutional Neural Network and basic object detection network In this paragraph, we will describe an object detection/computer vision tool. It should be noted that this deep-learning approach represents only one category among the many available methods.

Convolutional neural networks (CNNs) are a class of neural networks with broad applications in object detection from images or videos. As illustrated in Fig. 1.18, a convolutional neural network is composed of three main types of layers:

- **Convolutional layers:** These layers process a limited portion of the image using a convolution operation.
- **Pooling layers:** These layers aggregate the outputs of the convolutional layers.
- The so-called *fully connected* (FC) layer: This layer is used to classify the input image.

Convolutional layers use filters that scan the input image across its dimensions while performing convolution operations (see Fig. 1.19).

Pooling layers perform an operation aimed at reducing the number of features in the image by subsampling it. Pooling is generally applied after a convolutional layer. Although several types of pooling operations exist, the two most widely used are *max pooling* and *average pooling*.

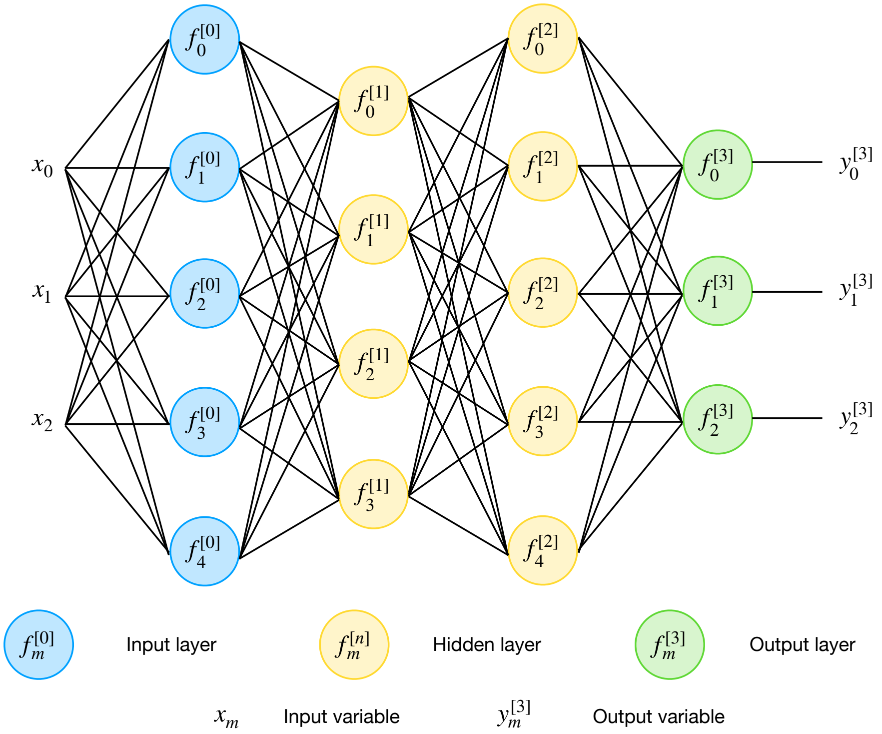

Figure 1.17: Example of a neural network with five layers. **Note:** The notation used to identify neurons within a network is as follows: The aggregation functions are denoted as $f_m^{[n]}$ and the transfer functions as $y_m^{[n]}$, where n represents the layer index and m the index of the perceptron within that layer.

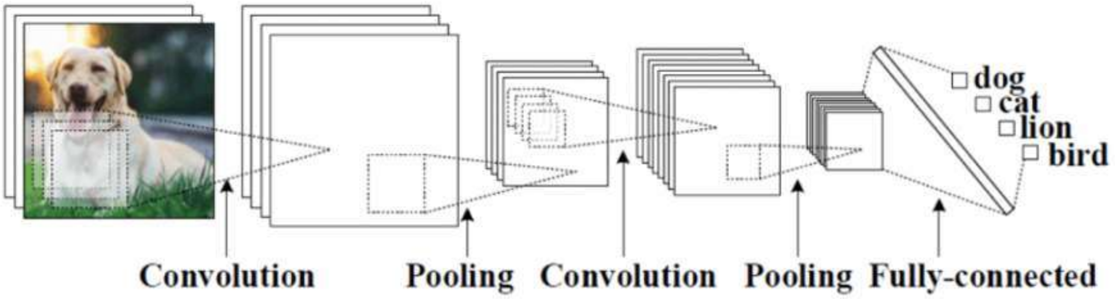

Figure 1.18: Schematic representation of the functioning of a convolutional neural network. Figure source from : Medium.com

.

The *max pooling* operation consists of selecting the maximum pixel value within the filter, as illustrated in Fig. 1.20. The *average pooling* operation, on the other hand, selects the average pixel value within the filter.

Finally, a convolutional neural network typically includes a *fully connected* layer, which can be

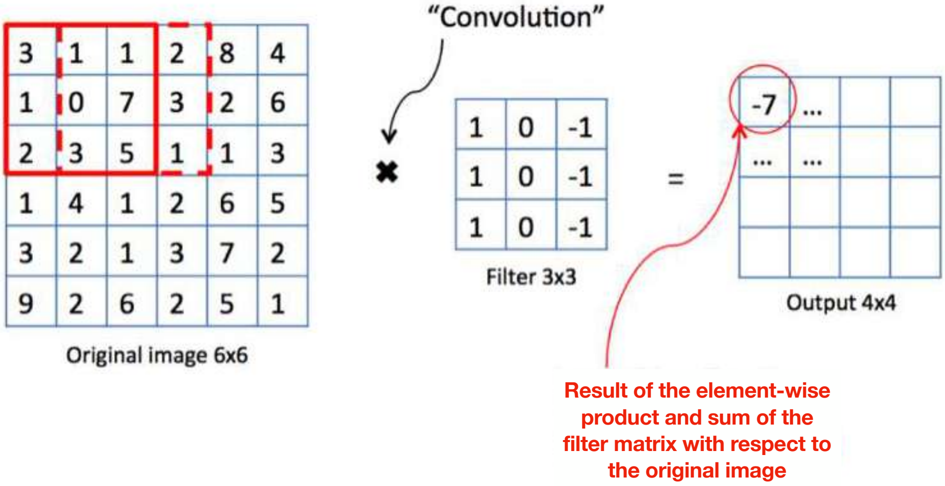

Figure 1.19: Diagram illustrating the convolution operation. Figure source from : Medium.com

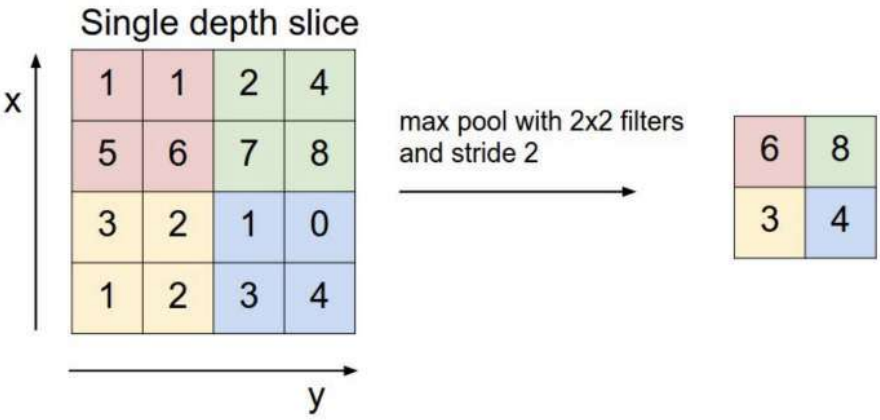

Figure 1.20: Diagram illustrating the pooling operation. Figure source from : Medium.com

used to optimize objectives such as class scores.

Machine learning for crater detection in literature In this paragraph, we will present a chronological overview of the key contributions that have shaped this field.

The first artificial neural networks applied to crater detection using manually extracted features from planetary images has been proposed by Vinogradova et al. (2002).

Although limited in number of artificial neurons and scale, this work laid foundational ideas for using learning-based models over purely algorithmic methods. Shortly after, Wetzler et al. (2005) developed a supervised system to detect small impact craters. By focusing on sub-kilometer features, this approach addressed a scale often neglected by traditional algorithms.

Around the same time, Barata et al. (2004), Bandeira et al. (2007b), and Bandeira et al. (2007a)

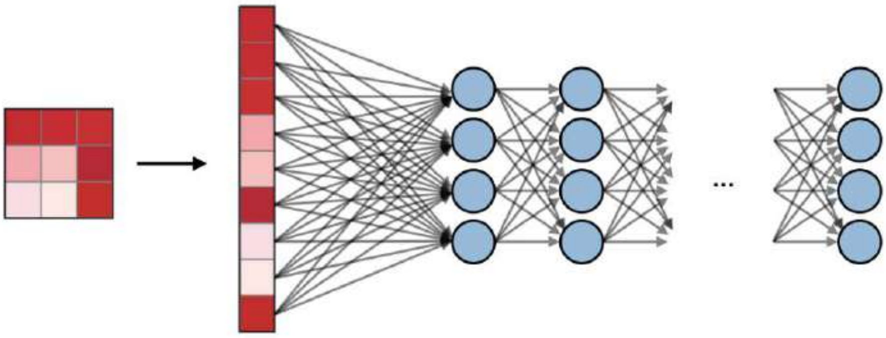

Figure 1.21: Diagram representing the *fully connected* layer. Source: stanford.edu

introduced template matching and pattern recognition methods using Mars Orbiter Camera (MOC) images. These studies pioneered the use of statistical shape descriptors and localized image analysis to identify candidate craters. Bandeira et al. (2008) further advanced this methodology by incorporating texture-based descriptors, notably improving detection robustness in the complex terrain of the Gusev Crater region.

Kim et al. (2005) provided a conceptual outlook on the use of machine learning for planetary science, foreseeing its importance in geomorphological feature analysis. This theoretical grounding was complemented by empirical advancements like those of Martins et al. (2009), who applied k-nearest neighbor (kNN) classifiers to crater detection using texture signatures derived from pixel neighborhoods.

The publication of Bandeira et al. (2012) marked a methodological shift toward more rigorous machine learning frameworks. Their use of Support Vector Machines (SVMs), trained on CTX images with both shape and texture features, introduced quantitative performance assessment through Receiver Operating Characteristic (ROC) curves, establishing new standards for evaluation in the field.

Concurrently, Urbach et al. (2009) implemented boosting classifiers on hand-crafted features, demonstrating the scalability of ML approaches to vast Martian datasets. This line of research was boosted by Di et al. (2014), who introduced a stereo-derived Digital Elevation Model (DEM) pipeline for detecting topographic depressions indicative of degraded craters, thus expanding detection capabilities into the 3D domain.

Efforts to standardize and benchmark crater detection methods were spearheaded by Salamuniccar et al. (2010), Salamunićcar et al. (2011), and Salamunićcar et al. (2012). Their work resulted in the creation of annotated datasets and performance metrics, providing a basis for comparison across different algorithms and facilitating reproducibility.

In more recent years, Matchev et al. (2022) proposed an unsupervised clustering approach to crater identification, offering an alternative to supervised models that require extensive labeled data. This was particularly relevant in the context of planetary exploration, where annotated datasets are scarce.

Addressing methodological transparency, Wagstaff et al. (2022) emphasized modular pipeline design and error quantification. Their work promoted the development of interpretable and reproducible ML-based crater detection systems, reinforcing scientific rigor in the face of increasingly complex models.

Together, these contributions trace the chronological advancement of machine learning techniques applied to crater detection. They demonstrate a field transitioning from early pattern recognition and handcrafted methods to modern supervised and unsupervised learning architectures, thereby setting the stage for the recent explosion of deep-learning methods, discussed in the following section.

Together, these works form the basis for more recent advances in deep-learning, which will be covered in the following subsection.

1.4.3 - Typical methodology to set a machine learning algorithm

In this section, we will detail the general workflow followed when developing a deep-learning model for crater detection, from the preparation of the reference dataset to the evaluation of the final trained model. The process typically begins with the creation of a labelled dataset. The next step is to define the model architecture, which in most crater detection tasks is a convolutional neural network (CNN), although other architectures can be used depending on the specific requirements. The model parameters (weights) are initialised and associated with a loss function, which quantifies the difference between the predicted outputs and the ground truth. A training strategy is then applied to minimise this loss, commonly involving stochastic gradient descent or one of its variants, with weight updates performed in batches to optimise computational efficiency.

Creation of a dataset for AI In order to train an object detection model—whether for crater detection or any other type of target—the first essential step is to build a dedicated dataset. The quality and representativeness of this dataset have a direct impact on the model's ability to learn relevant features and to generalise to new unseen data. In this section, we do not detail the specific pre-processing steps developed in this dissertation, but we provide a general overview of the standard procedure for creating a dataset for AI-based detection tasks.

A dataset is typically split into three distinct subsets. The *training set* constitutes the majority of the data and is used to iteratively adjust the model's parameters during learning. The *validation set* serves to monitor the model's behaviour at each training step (epoch), allowing us to check that learning is progressing correctly. Finally, the *test set* is used only once training is complete, to provide an unbiased statistical evaluation of the model's performance. It is essential that the test set remains completely unseen during training and validation, so that the reported performance reflects the model's ability to handle truly new data.

In our case, we allocated 85% of the available data to the training set, 5% to the validation set, and the remaining 10% to the test set. To ensure scientific relevance, the test set was composed of well-studied Martian sites, including all past and planned landing locations (Fig.1.22a). We also selected regions with contrasting crater densities—for instance, the densely cratered Noachis Terra and the relatively smooth Isidis Planitia—to capture a broad range of geological contexts. The training and validation sets were then populated by randomly assigning the remaining images according to the predefined 85%/5% split. The complete spatial distribution of the dataset is shown in Fig.1.22b.

Definition of the model Once the dataset has been prepared, the next step is to define the model architecture that will be used for crater detection. In most recent studies, this architecture is based on convolutional neural networks (CNNs), which are particularly well suited for image analysis tasks due

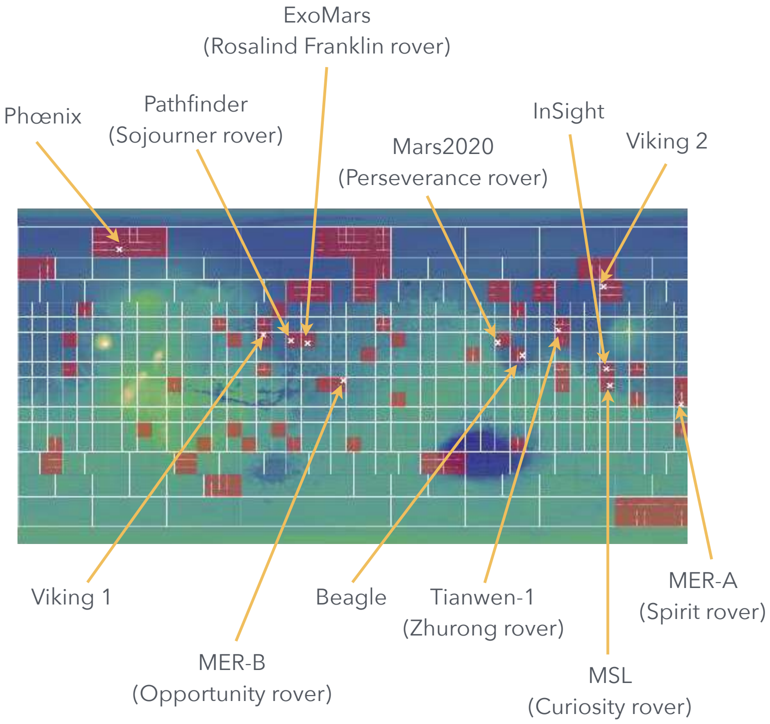

(a) Spatial distribution of the sites included in the test dataset. The selection covers past and future Martian landing sites, as well as regions with contrasting crater densities, such as for exemple, Noachis Terra (high density) and Isidis Planitia (low density).

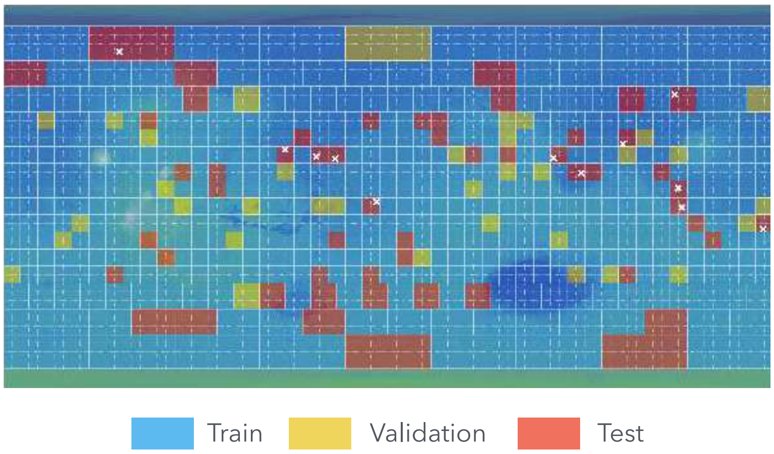

(b) Spatial distribution of the complete dataset used for crater detection model training, validation, and testing. Colours indicate the partition between training (85%), validation (5%), and test (10%) subsets.

Figure 1.22: Spatial distribution of the sites used in the study. (a) Location of the test dataset, which includes past and future Martian landing sites. (b) Distribution of the complete dataset used for model training, validation, and testing.

to their ability to learn spatially localised patterns such as crater rims, shadows, and ejecta blankets. As detailed in section 1.4.2, a CNN is composed of a series of layers—convolutional, pooling, and fully connected—that progressively extract and combine features from raw pixel values to produce a detection output.

Regardless of the chosen architecture, the model is characterised by a set of trainable parameters known as *weights* ($w_i^{[n]}$ in Fig. 1.16). These weights determine the strength and sign of the connections between neurons in consecutive layers. During training, the values of the weights are iteratively adjusted to minimise the error between the predictions and the ground truth, allowing the model to improve its predictions over time. Alongside the weights, *bias* parameters ($b_i^{[n]}$ in Fig. 1.16) are also learned, enabling the model to shift activation thresholds and better fit the data. While CNNs are the most common choice for crater detection, alternative architectures—such as transformer-based models or hybrid approaches—can also be used, depending on the resolution of the input images, the size of the dataset, and the computational resources available.

Loss function and minimisation The loss function is a mathematical expression that quantifies the difference between the model's predictions and the ground-truth labels and bounding boxes. It serves as a guide for the learning process: a lower loss indicates that the model's outputs are closer to the expected results. In crater detection, as in most object detection tasks, the loss function typically combines two complementary objectives.

The first objective is a classification purpose, ensuring that the model correctly identifies whether a region contains a crater or not. In general, for binary classification problems, the function used is the binary cross-entropy loss, which measures the dissimilarity between the predicted probability p_i and the ground-truth label $p_i^* \in \{0, 1\}$ for each sample i:

$$\mathcal{L}_{\text{BCE}}(p_i^*, p_i) = -\frac{1}{N}\sum_{i=1}^{N}\left[p_i^* \log(p_i) + (1 - p_i^*)\log(1 - p_i)\right] \tag{1.8}$$

In Eqn. 1.8, N is the total number of samples. The first term penalises false negatives (when $p_i^* = 1$ but p_i is low), and the second term penalises false positives (when $p_i^* = 0$ but p_i is high).

The second objective concerns localisation precision, ensuring that predicted bounding boxes accurately match crater positions and sizes.

In CNN-based object detection, this regression loss is often computed using the Smooth L1 loss, defined as as shown in Eqn. 1.9:

$$\mathcal{L}_{\text{SmoothL1}}(x) = \begin{cases} 0.5\,x^2 & \text{if } |x| < 1, \\ |x| - 0.5 & \text{otherwise,} \end{cases} \tag{1.9}$$

where $x = p_{ij} - p_{ij}^*$ is the difference between the predicted bounding box p_{ij} and the corresponding ground-truth value p_{ij}^*. This formulation enable a trade-off between an L1 loss for large errors (ensuring robustness against outliers) and an L2 loss for small errors (ensuring stability).

Minimising the total loss is achieved through iterative optimisation algorithms such as stochastic gradient descent (SGD) or its adaptive variants (ADAM), which updates the model's trainable parameters—weights and biases—in the direction that reduces the loss. This process is repeated over many iterations (epochs) until the model converges to a set of parameters that yield the best possible performance on the training data while maintaining good generalisation to unseen data.

An example of such a combined loss is provided by the Faster R-CNN algorithm (Ren et al., 2017), used in our crater detection pipeline (see chapter 3). The total loss $\mathcal{L}$ is defined as the sum of the losses from two components: the Region Proposal Network (RPN), which generates candidate object regions, and the Fast R-CNN detection head, which classifies and refines these proposals. Each component includes a classification loss and a bounding box regression loss:

$$\mathcal{L} = \frac{1}{N_{\text{cls}}} \sum_i \mathcal{L}_{\text{cls}}\left(p_i, p_i^*\right) + \lambda \frac{1}{N_{\text{reg}}} \sum_i p_i^* \, \mathcal{L}_{\text{reg}}\left(t_i, t_i^*\right) \tag{1.10}$$

Here:

- i indexes an anchor (in the RPN) or a Region of Interest (RoI) in the detection head.
- p_i is the predicted probability of the i-th anchor/RoI containing an object, and $p_i^* \in \{0, 1\}$ is the corresponding ground-truth label.
- $t_i = (t_x, t_y, t_w, t_h)$ are the predicted bounding box parameters, and t_i^* are the ground-truth box parameters relative to the anchor/RoI.
- $\mathcal{L}_{\text{cls}}$ is the classification loss, typically the binary or softmax cross-entropy:

$$\mathcal{L}_{\text{cls}}(p_i, p_i^*) = -p_i^* \log p_i - (1 - p_i^*) \log(1 - p_i) \tag{1.11}$$

- $\mathcal{L}_{\text{reg}}$ is the bounding box regression loss, defined as the Smooth L1 loss:

$$\mathcal{L}_{\text{reg}}(t_i, t_i^*) = \sum_{j \in \{x, y, w, h\}} \text{SmoothL1}(t_{ij} - t_{ij}^*) \tag{1.12}$$

- N_{cls} and N_{reg} are normalisation factors for the classification and regression losses.
- λ is a balancing parameter (typically set to 1) controlling the relative contribution of the regression loss.

The multiplication by p_i^* in the regression term ensures that bounding box regression is applied only to positive samples, avoiding unnecessary updates for background regions.

This combined loss function allows the model to learn both to classify regions as containing craters or not but also to refine the bounding boxes as precisely as possible around the detected craters.

Training strategy Once the dataset, model, and associated optimiser are set, a training strategy is required to coordinate the entire process and define how the model parameters are iteratively updated to minimise the loss function and achieve optimal performance. At the core of this process is the optimisation algorithm, which adjusts the weights and biases in the direction indicated by the gradient of the loss with respect to these parameters.

In our experiments, optimisation is performed using the adaptive algorithm ADAM, which dynamically adjusts the *learning rate* for each parameter based on the first and second moments of the gradients (Kingma et al., 2014). The *learning rate* is a key hyperparameter that determines the magnitude of each step during training (i.e. it enable us to control the "distance traveled" in parameter space at each step of gradient descent). If the *learning rate* is too large, the optimisation may overshoot the minimum of the loss function, leading to instability. If it is too small, convergence will be excessively slow, and the model may become trapped in local minima. ADAM's adaptive nature allows it to modify the *learning rate* individually for each parameter, leading to faster convergence and greater robustness to initial hyperparameter settings compared to standard stochastic gradient descent (SGD) with momentum (Ruder, 2016).

The training process is organized into *epochs*, which is when the training processes the entire training dataset once. An epoch is further divided into smaller subsets of data (image + labels) called *batches*. Instead of updating the model after seeing all the data at once (which can be slow and memory-intensive) or after each individual example (which can make the optimization unstable), the batch enable to make a trade-off. It allows the model to update its parameters more frequently while keeping the gradient estimates stable, often leading to faster and more reliable convergence. A key hyperparameter in this process is the *batch size*, which determines the number of images in each batch and directly affects both the stability of the optimization and the memory requirements during training.

Weight initialisation and regularisation techniques such as weight decay or dropout are also employed to improve convergence and reduce overfitting. Throughout training, model performance is periodically evaluated on the validation set to monitor progress, and guide hyperparameter tuning. This iterative process continues until the model converges to a satisfactory trade-off between detection accuracy and generalisation capability.

With the model fully trained following this strategy, the next step is to rigorously assess its performance using appropriate evaluation metrics.

1.4.4 - Precision, Recall and others : Metric to evaluate a detection and classification

In this section, we will introduce the metrics used to evaluate the performance of an object detection algorithm. We will first define the metrics, then explain how they are computed with examples, and finally discuss their interpretation in the context of crater detection.

Precision and Recall To evaluate the performance of an object detection algorithm, we introduce two metrics: **precision** and **recall** (also referred to as sensitivity) (Buckland et al., 1994). In this subsection, we describe the method for computing these metrics, followed by a discussion of their interpretation.

Precision and recall, respectively defined in equation 1.13 and 1.14, are used to assess the performance of classification models. Both metrics are based on the confusion matrix (Fig. 1.23), which records all possible combinations of outcomes.

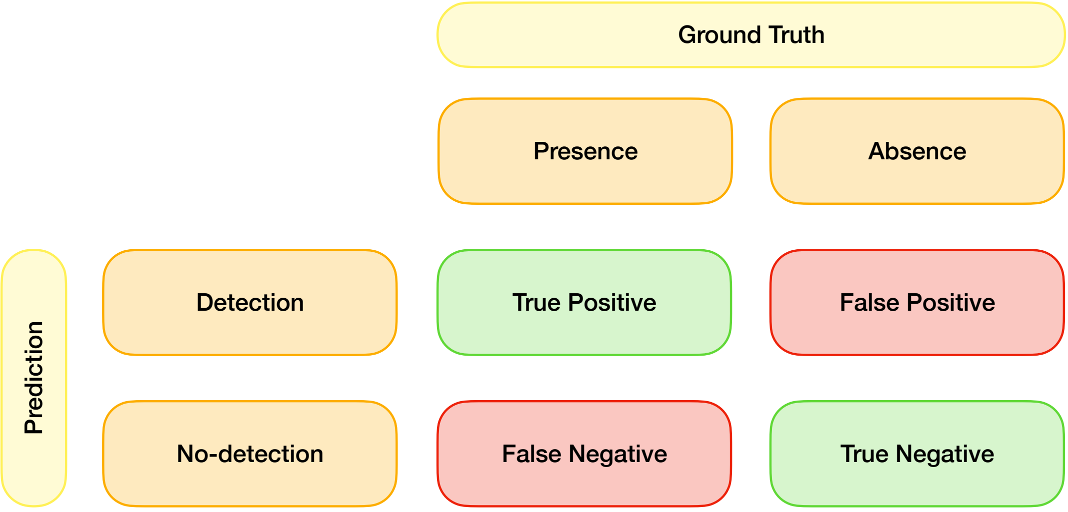

		Ground Truth	
		Presence	Absence
Prediction	Detection	True Positive	False Positive
	No-detection	False Negative	True Negative

Figure 1.23: Confusion matrix for a binary problem: *crater detected* or *no crater detected*.

To illustrate the functioning of this matrix, we take a binary example: testing our algorithm on an image of Mars. The ground truth is provided in the form of a label file containing relevant information such as the number of craters and their positions. For a given detection, four cases are possible during testing:

- **True negative** (TN): The image contains no craters, and the algorithm correctly detects nothing.
- **True positive** (TP): The image contains a crater, and the algorithm correctly detects it.
- **False negative** (FN): The image contains a crater, but the algorithm failed to detect it.
- **False positive** (FP): The image contains no craters, but the algorithm detects one.

Let us now consider an image containing seven craters. Each crater is enclosed within a *bounding box* whose coordinates are recorded in the ground-truth label file. To assess how accurately the detection model has localized a given crater, we compute the Intersection over Union (IoU) between the predicted and ground-truth bounding boxes, as illustrated in Fig. 1.24. Fig. 1.24 and 1.25 show that the IoU measures the degree of overlap between the bounding boxes.

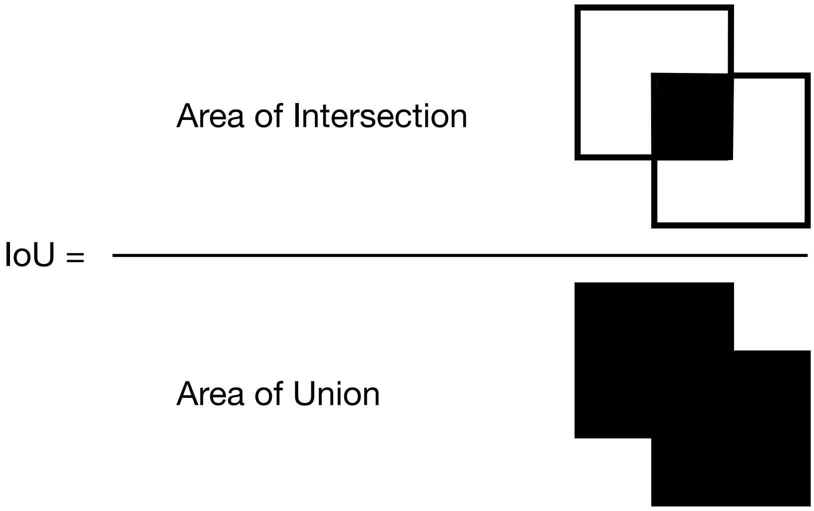

Figure 1.24: Computation of the Intersection over Union (IoU).

If the predicted box is far from the ground truth, the intersection—and thus the IoU—will be zero. Conversely, if the predicted and ground-truth boxes perfectly overlap, the IoU will be equal to 1. To determine whether a detection is considered valid, a threshold must be set above which the detection is accepted.

In Fig. 1.26, eight craters are confirmed by the ground truth (green boxes). The model also detected eight objects (red boxes), including one that does not correspond to any crater (false positive). One crater was missed (false negative). Applying a detection threshold of $\mathrm{IoU}_{thr} > 0.5$, the shaded cells in the table indicate objects with IoU values below the threshold, leading to three additional craters being classified as non-detections.

Using the confusion matrix define in Fig. 1.23 would enable us to calculate precision and recall for this image:

$$\mathrm{P}_{IoU_{thr}} = \frac{TP}{TP + FP} \tag{1.13}$$

$$\mathrm{R}_{IoU_{thr}} = \frac{TP}{TP + FN} \tag{1.14}$$

where TP are the true positives detections, TN true negatives detections, FP false positives detections, and FN false negatives detections.

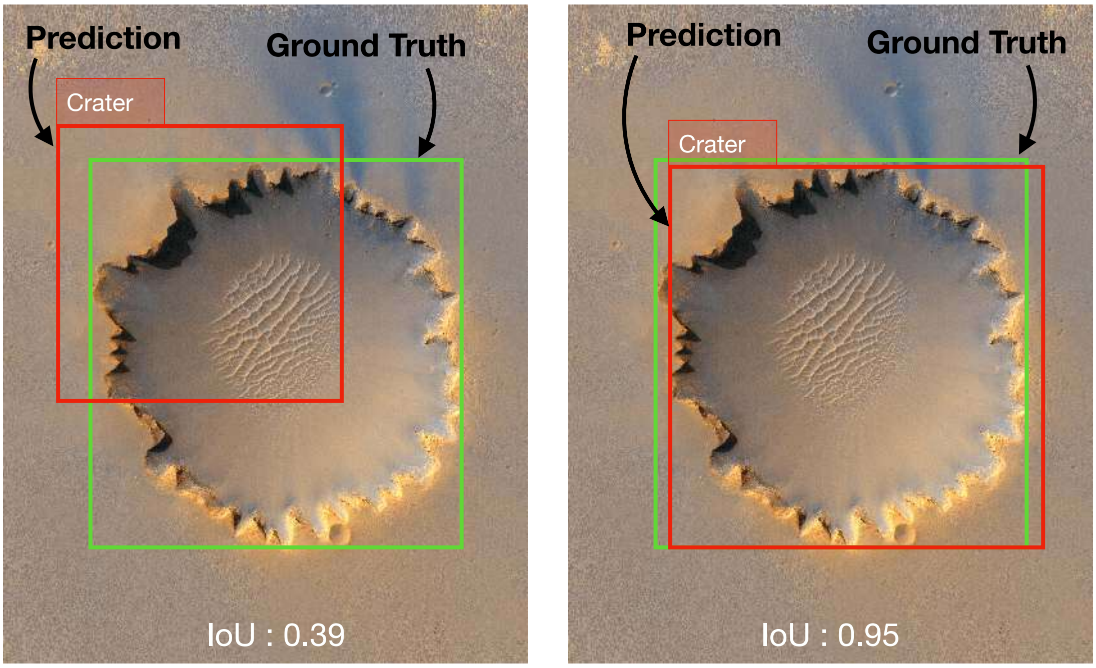

Figure 1.25: Exemple of 2 different detections. On the left the IoU of the prediction and ground truth boxes is 0.39. Meanwhile on the right image it is 0.95. With a threshold set to $\text{IoU}_{thr} = 0.5$, the left case will conduct to a False positive detection while the right case will be a true positive one.

We observe that the IoU_{thr} threshold value influences both precision and recall. For example, with the Fig.1.26 situation, if the detection threshold is set to 0.5, we obtain four true positives, four false negatives, one false positive, and zero true negatives. This results in $P_{0.5} = 0.5$ and $R_{0.5} = 0.80$.

In theory, a perfect detector would achieve a precision and recall of 1. In other words, it would correctly detect all craters in the image (recall) and make no false detections (precision). In practice, such performance is unattainable, primarily because of the intrinsic limitations of real-world data and model generalization. Indeed, crater images often exhibit variability in illumination, resolution, and degradation state, while overlapping or partially buried craters introduce further ambiguity. Moreover, the presence of noise, artefacts from image acquisition, and the imperfect nature of human-generated ground truth annotations make it impossible for any algorithm to perfectly match all true craters without also introducing false detections. Our goal is therefore to design a detector with the highest possible precision and recall. A detector with high precision but low recall is likely to produce correct detections when it does identify an object, but will miss many craters (high false negative rate). On the contrary, a detector with high recall but low precision will detect many craters, but the detections will include a significant number of false positives.

Precision–Recall Curve Since that dealing with two metrics to mesure a single phenomena is not something very intuitive, we decided in this PhD project to use the precision and recall metrics to build what is called in literature the **Precision–Recall curve** (PR curve) (Saito et al., 2015). This curves, is very useful to evaluate the performance of our crater detection algorithms (see Fig. 1.27 for

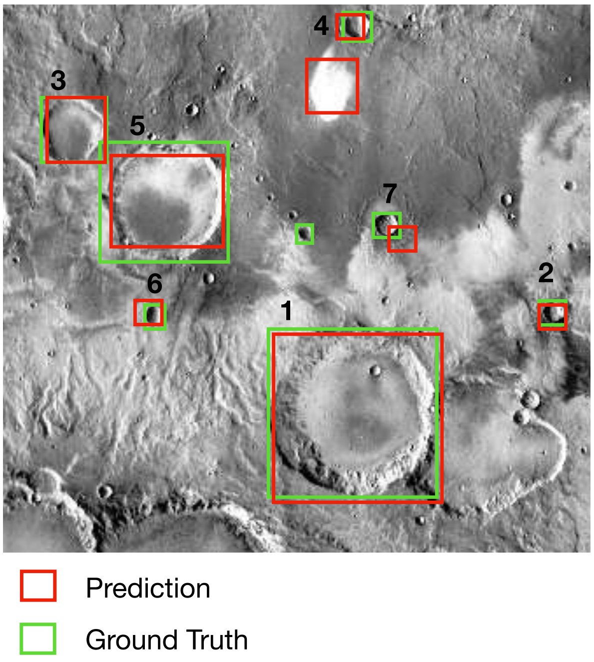

Figure 1.26: Example of a region of Mars where certain craters have been annotated as ground truth.

Crater ID	IoU
1	0.95
2	0.83
3	0.75
4	0.60
5	0.45
6	0.36
7	0.12

Table 1.3: List of detected craters in Fig. 1.26 with IoU threshold > 0.5. Shaded rows correspond to non-detections.

an exemple). The PR curve enable to visualize the trade-off between precision and recall at different confident score thresholds, allowing us to assess how well our model balances these two metrics across a range of operating conditions.

As illustrated in Fig. 1.27, each point on the precision–recall curve corresponds to a specific threshold applied to the confidence score assigned to each detection. In simple terms, the predictions are ranked according to their confidence score, and for each threshold the corresponding precision and recall values are computed. Lowering the threshold allows the model to detect more objects, which typically increases recall but also raises the number of false positives, thereby reducing precision.

A perfect detector would have a precision–recall curve with a square shape (as seen in Fig. 1.27, purple curve), since it would correctly identify for example every crater in the scene and each detection would correspond to a true crater. In practice (as seen in Fig. 1.27, blue curve), such a detector does not exist: real models inevitably face trade-offs between precision and recall due to image resolution limits, noise, and the inherent variability of crater identification methods. The precision–recall curve therefore provides a useful way to visualize and quantify these trade-offs, and is widely used to evaluate and compare the performance of object detection algorithms.

mean Average Precision mAP In a binary case, the overall performance of a detector can be summarised by the area under the PR curve (mean Average Precision, mAP), where higher values indicate a better balance between precision and recall. In our crater detection problem, the PR curve provides us an intuitive way to evaluate how a model performs under different operating conditions,

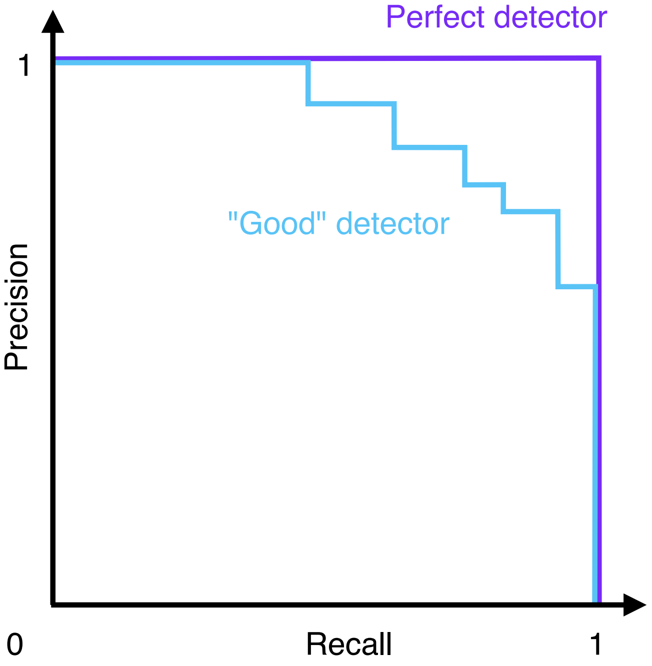

Figure 1.27: Two theoretical examples of precision–recall curves: one corresponding to an ideal (perfect) detector, and the other illustrating a more realistic, physically representative case.

and to select the threshold that best suits the scientific objectives.

F1 Score Another metric which is commonly used in object detection literature is the F1 score. It is a single metric that also combines *precision* and *recall* into their harmonic mean, providing a balanced measure of a model's accuracy when both false positives and false negatives are important. It is particularly useful for comparing models or configurations when a single value is desired instead of examining the entire precision–recall curve. The F1 score is defined as followed in Eqn. 1.15. Again, a perfect detector would have an F_1 score of 1, while a score close to 0 indicates a poor performance in at least one of the two metrics.

$$F_1 = 2 \cdot \frac{\text{Precision} \cdot \text{Recall}}{\text{Precision} + \text{Recall}} \tag{1.15}$$

Accuracy In the domain of *classifiers*, a commonly used metric is *accuracy*, which measures the proportion of correctly classified instances over the total number of instances. In the context of crater detection and classification, it corresponds to the fraction of craters that are correctly predicted by the model. Formally, it can be defined as:

$$\text{Accuracy} = \frac{TP + TN}{TP + TN + FP + FN} \tag{1.16}$$

where TP are the true positives detections, TN true negatives detections, FP false positives detections, and FN false negatives detections.

Limitations and inconsistencies in the use of precision and recall While precision and recall are widely adopted metrics for evaluating object detection algorithms, their use in crater detection studies has often been inconsistent. In the literature, there is no universally accepted evaluation protocol: authors may employ different Intersection-over-Union (IoU) thresholds, use distinct definitions of what constitutes a true positive, or even omit recall in favour of alternative measures. Furthermore, variations in ground-truth datasets, image resolutions, and preprocessing steps introduce additional biases, making direct comparison between studies problematic. As a result, benchmarking crater detection methods across publications is challenging, since performance values reported under differing conditions are not necessarily comparable. This lack of standardisation highlights the need for a common evaluation framework in the planetary science community to ensure reproducibility and facilitate fair performance assessments. Establishing such a unified evaluation framework would not only improve the reproducibility of crater detection studies, but also provide a robust basis for comparing new algorithms with existing approaches, thereby accelerating methodological advances in the field.

1.4.5 - Deep-learning-based Crater Detection Methods

As explained in subsection 1.4.2, deep-learning is a subset of machine learning that relies on multi-layered artificial neural networks to automatically learn hierarchical feature representations from raw data. In the context of image analysis, and more specifically crater detection, deep-learning models can extract complex spatial patterns such as crater rims, shadows, and ejecta structures directly from pixel values, without the need for manually engineered features. This ability to jointly optimize feature extraction and classification within a single architecture has made deep-learning, and particularly convolutional neural networks (CNNs), the state-of-the-art approach for high-resolution planetary image interpretation.

In recent years, deep-learning has emerged as a transformative approach in planetary surface analysis, and particularly in the field of automatic crater detection. While machine learning techniques rely on human-engineered features that are manually designed and selected to represent crater shapes, textures, or contextual cues, deep-learning models learn to extract these features automatically from raw data. This is typically achieved through neural network architectures composed of multiple hierarchical layers that capture increasing levels of abstraction. The fact that multiple *deep* layers are able to handle complex tasks where simple neural network fails is simply due to the number of degrees of freedom. This revolution, handled numerically with Graphics processing Units (GPU) requires more training datasets than usual machine learning methods. The other key advantage of deep-learning over traditional machine learning lies in its ability to learn complex spatial patterns directly from data with minimal preprocessing, which makes it especially well-suited to planetary datasets that are often noisy, large-scale, and heterogeneous.

In crater detection, this shift has enabled a new class of algorithms that are not only more accurate and scalable, but also more adaptable to different types of planetary surfaces and instruments.

deep-learning models can be trained end-to-end, meaning they can ingest raw optical or topographic inputs and directly output crater locations, sizes, and shapes. They have shown particular strength in identifying degraded or partially buried craters, and in generalizing across terrains with different geological contexts.

In this section, we organize the literature on deep-learning-based crater detection by major methodological themes: the evolution of the neural network architecture (e.g., CNNs, U-Nets, transformers), the application using optical imagery or topography. For each category, we highlight representative studies and summarize key performance metrics to provide a comparative benchmark.

Model Architectures and Innovations Deep-learning models for crater detection can be broadly divided into two main families, depending on the nature of the output they produce: *detection/localisation models* and *segmentation models*.

Detection and localisation models, such as Faster R-CNN, YOLO (You Only Look Once), or RetinaNet, are designed to predict the position of objects within an image by enclosing them in a *bounding box* and assigning a class label to each (Ren et al., 2017; Redmon et al., 2016). These models focus on identifying the approximate location and category of each object rather than its exact pixel-level outline. Architectures such as ResNet or EfficientNet are often used as what we call the *backbone* of these detectors (such as in FasterRCNN), acting as powerful feature extractors. In Fig. 1.28a and Fig. 1.28b you will respectively see a schematic overview of Faster R-CNN framework and the YOLOv11 model, which illustrate the two object detection models applied in this thesis.

More recent advances have introduced attention mechanisms (e.g., Transformers) to better capture long-range spatial dependencies, which can help detect craters with diffuse or degraded rims (Vaswani et al., 2017).

Segmentation models, by contrast, aim to predict a dense classification for each pixel in the image, producing detailed *masks* that outline object shapes. In *semantic segmentation*, all pixels belonging to the same class (e.g., “crater”) share the same label, while in *instance segmentation*, each individual object is assigned a separate mask. U-Net, originally designed for biomedical imaging, has become a widely used architecture for planetary science due to its encoder–decoder design, which captures context at multiple scales while preserving fine spatial details. Mask R-CNN extends Faster R-CNN by adding a parallel branch that generates segmentation masks for each detected object, thus combining object detection and instance segmentation in a single framework (He et al., 2017). More recently, models like the Segment Anything Model (SAM) have introduced prompt-based segmentation, where a user can guide the segmentation process interactively using points or bounding boxes, enabling rapid adaptation to new datasets without retraining (Kirillov et al., 2023).

In summary, detection models provide faster and more compact object localisation, making them efficient for large-scale crater surveys, while segmentation models deliver more precise shape information, which can be valuable for morphological analysis. The choice between these approaches depends on the scientific objectives, the resolution of the imagery, and the computational resources available.

Detection model for crater detection in literature Early deep-learning models for crater detection employed standard CNN classifiers or simple segmentation architectures. Over time, more sophisticated models have emerged. Chen et al. (2018) and Zhou et al. (2018) applied Mask R-CNN

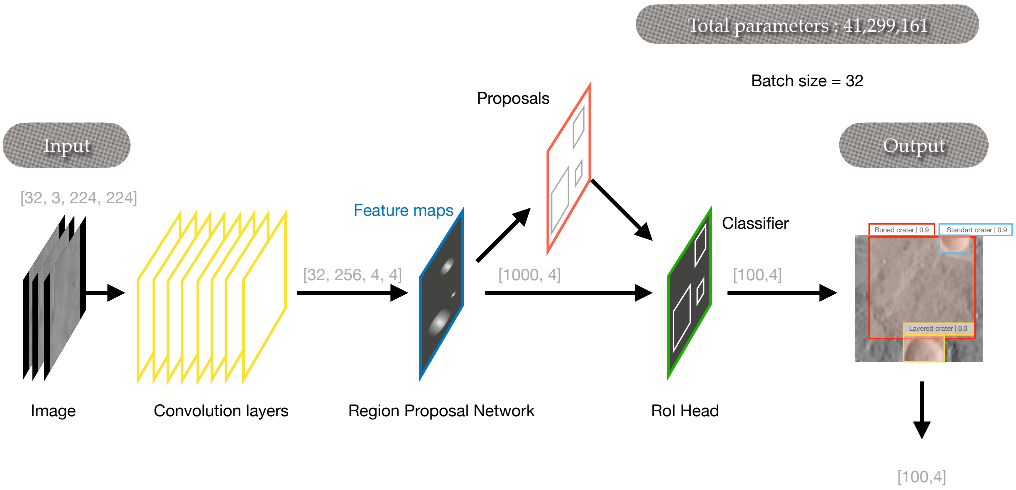

(a) Schematic representation of the Faster R-CNN architecture. This two-stage detector first generates region proposals through a Region Proposal Network (RPN), and then classifies and refines bounding boxes to identify crater candidates.

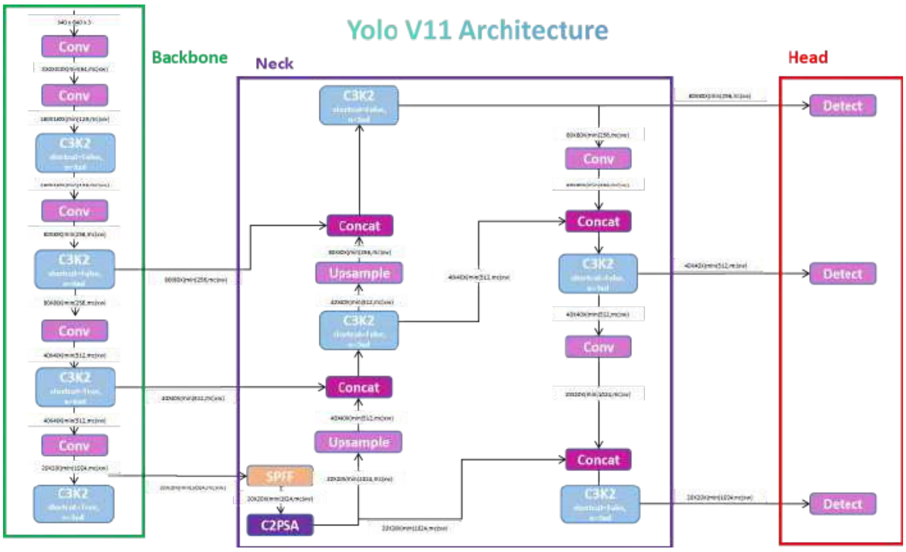

(b) Schematic representation of the YOLOv11 architecture. This single-stage detector directly predicts bounding boxes and crater classes from feature maps, offering high efficiency and real-time detection performance.

Figure 1.28: Comparison of deep-learning architectures applied to crater detection. (a) Faster R-CNN, a two-stage region-based approach, and (b) YOLOv11, a single-stage detection framework optimized for speed and efficiency.

for instance segmentation of lunar and Martian craters, enabling fine-grained boundary delineation. Ali-Dib et al. (2020) and Ali-Dib (2022) explored weakly supervised learning, using image-level labels and region proposals to detect crater candidates at scale, with precision above 85%.

Recently, transformer-based architectures have been introduced. Su et al. (2023) implemented a Vision Transformer backbone in a crater segmentation task, outperforming baseline U-Net and ResNet models on both IoU and F1 metrics. Giannakis et al. (2024) demonstrated that the Segment Anything Model (SAM), a foundation model pretrained on Earth data, can be fine-tuned to detect craters with strong generalization performance. This opens the path to universal pretraining strategies for planetary surfaces.

Detection from Optical Imagery Many deep-learning-based studies operate on high-resolution visible imagery from instruments such as CTX, HiRISE, or HRSC. Silburt et al. (2019) pioneered the use of convolutional neural networks for crater detection on CTX imagery, training a sliding-window classifier that achieved over 90% precision and 80% recall for craters larger than 50m. Benedix et al. (2020) adapted the YOLO object detection framework, enabling real-time inference and demonstrating high detection performance with mean Average Precision (mAP) above 85%. Their model facilitated detection of both primary and secondary craters over large regions.

Lagain et al. (2021a) and La Grassa et al. (2023) proposed regional-scale crater mapping using Faster-RCNN architectures trained on Mars imagery. Their approaches achieved mAP values ranging from 72% to 89% depending on the resolution and crater size range. Lee et al. (2021) achieved near-human performance with a deep ensemble of detection and classification networks, reporting F1-scores above 0.9 on a manually curated HiRISE benchmark. A follow-up comparative study by Lee (2023) evaluated several CNN-based and transformer-based detectors, concluding that data augmentation and resolution-normalized training significantly impact performance across scales.

Detection from Topographic Data (DEM) Topographic inputs provide geometric robustness and enable detection of eroded or buried structures. Emami et al. (2019) used shaded-relief images derived from DEMs with a U-Net architecture and achieved recall rates up to 93% on test regions of Mars. Tao et al. (2021a) and Tao et al. (2021b) introduced an attention-enhanced U-Net architecture trained on HRSC-derived DEMs. Their models yielded IoU scores above 0.75 for craters larger than 200m, demonstrating robustness to noise and topographic variation. Qiua et al. (2024) proposed a YOLO-derived model based on tensorial calculus that they call TYOLO, a lightweight hybrid model leveraging both visual and DEM-based cues, reporting 91.6% recall and mAP of 88.2% on test datasets.

1.5 - Problematic

The accurate and robust detection of impact craters on planetary surfaces is fundamental for establishing precise chronological frameworks through crater counting methods. Despite significant advancements in crater detection techniques—from manual cataloging to recent deep-learning algorithms—several critical challenges persist, motivating this PhD thesis.

Firstly, achieving robust crater detection across all latitudes remains a major challenge, particularly on Mars. Variations in illumination conditions, surface morphology, and the presence of volatile-rich substrates introduce significant biases and uncertainties in the identification process. For these reasons, image pre-processing plays a critical role, as it directly influences the quality of the detection results. For instance, as illustrated in Fig. 1.29, the performance of Benedix et al. (2020) shows a marked decline at latitudes higher than 45° north and south. This limitation may stem from the fact that the authors did not appear to reproject their images, which could present deformation due to high-latitude datasets. Furthermore, the use of comprehensive data augmentation—encompassing a broad range of image transformations—might have helped the model capture the full complexity and diversity of crater morphologies across different terrains and illumination conditions.

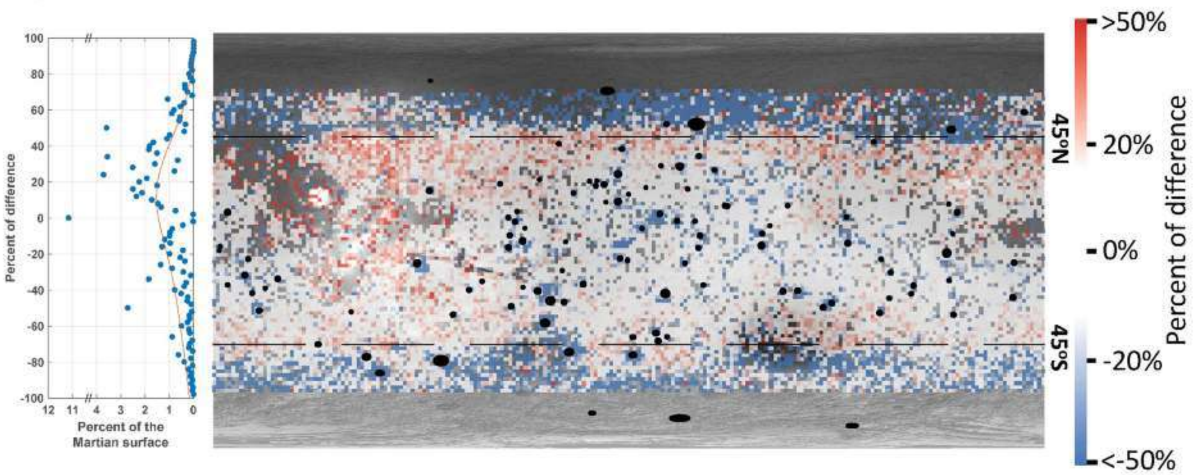

Figure 1.29: Figure from Benedix et al. (2020): Difference between manual (Robbins et al., 2012) and automatic datasets. Red areas correspond to areas where the CDA counts more, whereas blue areas indicate where the CDA counts fewer craters than the manually compiled database.

While deep-learning approaches have greatly improved detection performance, their robustness and generalization capability across diverse terrains, from equatorial volcanic plains to polar ice-rich regions, have yet to be thoroughly validated. Therefore, a critical aspect of this work will involve developing and rigorously testing crater detection algorithms capable of maintaining high accuracy and reliability across all latitudes and diverse geological contexts, validated against independent, manually verified datasets.

Secondly, a significant obstacle in crater-based dating methods arises from distinguishing primary from secondary craters. Secondary craters, resulting from ejecta impacts, complicate the chronological interpretation as they artificially inflate crater density estimates. Thus, an essential component of this research will involve developing advanced classification methods to reliably distinguish secondary craters. This classification is critical for ensuring the accuracy of surface age estimations and for refining our understanding of planetary bombardment history. This aspect is an innovation proposed in this thesis.

Lastly, crater superposition poses another intriguing challenge. Traditional crater-counting methods largely rely on identifying and counting discrete, isolated craters. However, many surfaces feature extensive crater overlap due to prolonged bombardment and resurfacing processes. The correct interpretation of such overlapping craters is essential for accurately reconstructing chronological sequences of geological events. Therefore, this thesis will explore novel methodological approaches to interpret crater superposition relationships, potentially redefining standard crater counting techniques. These innovations may lead toward a new, more nuanced approach to planetary surface dating that better accounts for complex geological histories. This theme is another innovation proposed in this PhD.

In summary, this PhD thesis addresses three key challenges: (1) achieving robust crater detection across all planetary latitudes, scales, validated on independent datasets; (see chapter 3) (2) reliably classifying secondary craters to enhance dating precision (see chapter 4); and (3) accurately interpreting crater superposition to refine chronological frameworks (see chapter 5). By addressing these problems, the proposed research aims to significantly improve the accuracy and reliability of crater-based chronologies, providing deeper insights into planetary evolution processes. In addition, the dataset preparation is described in chapter 2 and the full pipeline in chapter 6. The manuscript ends with conclusions and perspectives in chapter 7. Each chapter should be considered independent in terms of notation since most of them are related to a scientific publication.

2 - Crater database improvement using automatic circle detection [1]

Contents

2.1 Introduction . . . 94
2.2 Data . . . 95
  2.2.1 Re-projection and database cutting . . . 95
2.3 Method: Automatic crater circle improvement . . . 96
  2.3.1 Edge detection . . . 96
  2.3.2 Hough transform . . . 98
  2.3.3 Best circle selection . . . 100
2.4 Results and evalution . . . 104
  2.4.1 Examples . . . 104
  2.4.2 Evaluation . . . 108
  2.4.3 Final dataset . . . 109
2.5 Conclusion . . . 112

---

[1] The notations used in this chapter may vary from one chapter to another

The construction of a reliable crater database is a fundamental step in planetary surface dating, as the accuracy of subsequent analyses—such as morphological classification (chapter 4) or superposition order determination (chapter 5)—depends directly on the precision of crater measurements. Existing manually compiled databases, while invaluable, often suffer from geometric inaccuracies in crater positions and sizes, particularly for small and degraded features. In this chapter, we address these limitations by implementing an automatic circle detection approach based on the Hough transform, with the aim of refining crater coordinates and radii across the dataset.

We begin by introducing the context and limitations of the current reference database, highlighting the main sources of geometric errors and their implications for scientific analysis (section 2.1). We then present the methodology for applying the Hough circle transform to high-resolution imagery, detailing the pre-processing steps, detection parameters, and validation criteria (section 2.2). Next, we describe the strategy used to integrate these improved measurements into the existing database, including criteria for accepting or rejecting corrections (section 2.3). Finally, we evaluate the improvements brought by this approach, both quantitatively and qualitatively, and discuss their impact on subsequent crater-based studies (section 2.4).

2.1 - Introduction

The task of crater detection on planetary surfaces can be solved using a machine learning method, or a deep-learning model (like in our case). In any case, the learning process rely on a precise database to learn shared patterns and features associated to craters in the image in order to identify those features in Region Of interest (ROI). The method will then assign an index, interpreted as a detection probability and a bounding box to each ROI, effectively marking the location of a potential crater. It's important to note that for the detection model to perform optimally, it must be trained on a diverse and representative set of images, along with their corresponding ground truth data.

This ground truth data, which consists of annotated images indicating the presence and location of craters, is crucial for the the detection model to learn how to accurately detect craters. The quality of the input data, specifically its precision and sensitivity, plays a crucial part in the performance of the detector. In essence, the more representative and diverse the training dataset is, the more accurately the detection model will be able to detect craters on any given planetary surface. Furthermore, to be precise in the detection, the ground truth database has to be precise.

In order to verify the precision of the ground truth database, we examined several images. As seen in Fig. 2.1, the localisation and radius of crater which are registered in the ground truth database (green circles) do not overlap the crater in a satisfying way. We observe that the craters are often shifted in a random direction and that this difference becomes more noticeable as the size of the crater decreases.

In this chapter we will propose a solution to improve the accuracy of the ground truth data. Our ultimate goal is to develop a more precise ground truth database, which will enable us to train the detection model more effectively and achieve better performance in crater detection tasks on planetary surfaces.

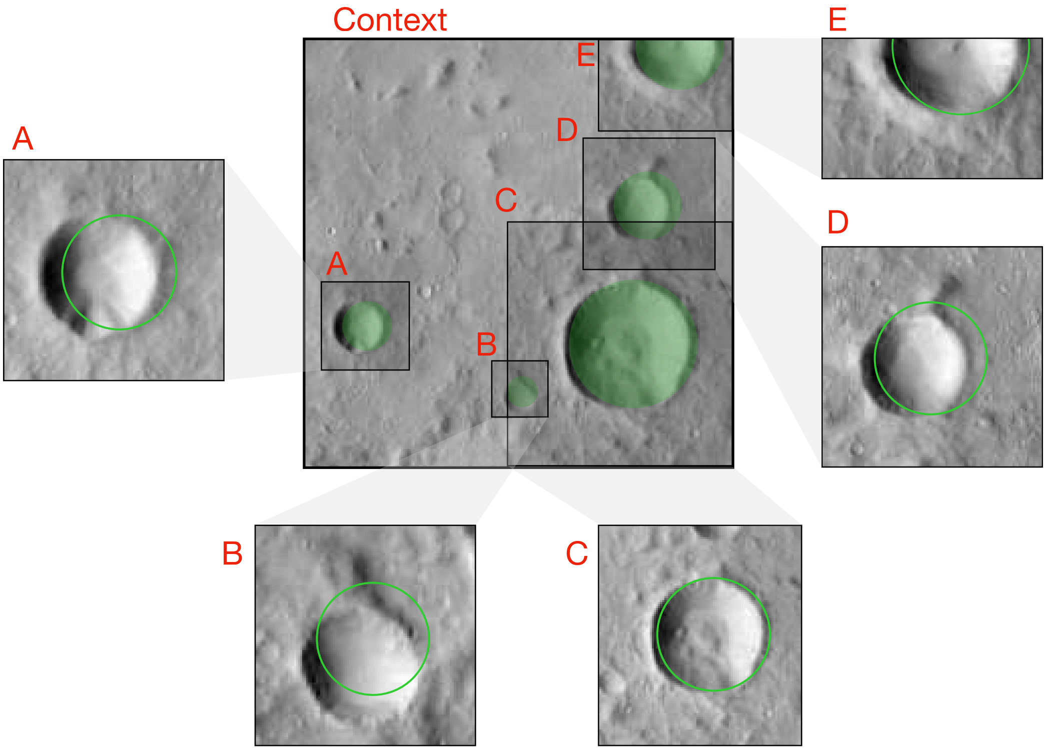

Figure 2.1: Initial crater database (Lagain et al., 2021a) in green superposed with CTX images of Mars (Malin et al., 2007; Dickson et al., 2024). The position and radius are nearly correct but an improvement is required.

2.2 - Data

We used image data record by Mars Reconnaissance Orbiter's ConTeXt camera (CTX) as a reference image dataset. This instrument is designed to provide a context image of the surface of Mars and can be used to study the geology of the planet, including the composition and structure of the surface. It has a resolution of 6 meters per pixels and take images in a pushbroom mode with a ground swath of 30 kilometers at the Martian surface (Malin et al., 2007). Since the beginning of MRO's mission, CTX has covered 97.3% of the planet (from 88°N to 88°S). We used a global CTX map of mars made by The Bruce Murray Laboratory for Planetary Visualization (Dickson et al., 2024). This mosaic is distributed per quadrangle with its own stretch in 8 bits. It is thus not possible to easily combine data from different quadrangles. We naturally choose to process the data on a quadrangle basis.

The initial crater database contains all Martian craters larger than 1 km in diameter. This database made by Lagain et al., 2021a, manually validating the database from Robbins et al., 2012. It contains 376,417 craters with information about their localisation, radius and morphology.

2.2.1 - Re-projection and database cutting

The CTX mosaic was divided into 3960 quadrangle in equirectangular projection, each covering a latitude/longitude portion of $4 \times 4°$. The first step will be to reproject each quadrangle to avoid deformation. Indeed, during their processing, Dickson et al., 2024 use an equidistant cylindrical projection which conserve distances with respect to the meridians but not angles. In other words, the circular shape of the craters will be flattened when approaching the poles (see Fig. 2.2). Maintaining the true circular geometry is crucial to detect a proper center/radius.

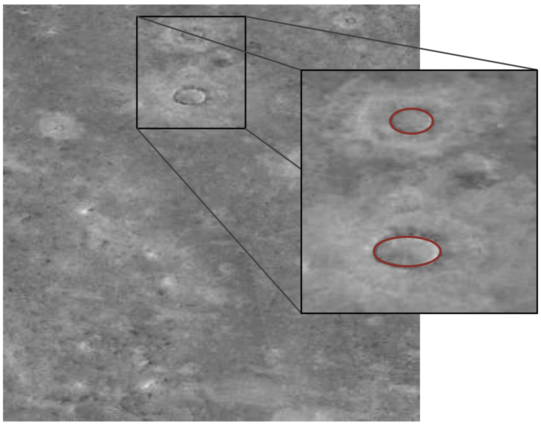

Figure 2.2: Elliptical crater shape in the quadrangle at 56°N/156°E due to the equidistant cylindrical projection.

The first step will be to reproject all the quadrangle in a local stereographic projection which has no local deformation (Fig. 2.3).

A second step will be to trim the whole 384,582 crater database in order to create a smaller database that only includes crater within the quadrangle.

So in the end we will have 3960 reprojected quadrangles associated with as many small crater database.

2.3 - Method: Automatic crater circle improvement

One of the distinctive features of craters are their circular shape. To improve the accuracy of our crater database, we propose to implement an automated circle detection method and estimate the best crater circle, nearby the initial ground truth. To do this we will first have to generate an edge map of the image and then, we will perform a Hough transform in the edge of the image. The Hough transform is an elegant technique that requires only a few parameters to identify circles in an image. In this section, we will detail our approach to boundary detection, which aims to enhance the accuracy of our crater database.

2.3.1 - Edge detection

The first step in order to perform an edge map of the image. This edge map is a binary image, each non-null point of the edge map will be considered as part of a potential circle. To create this edge map, we used a Canny edge filter implemented in the python scikit-image library (Van der Walt et al., 2014). It calculates a gradient intensity using a Gaussian derivative filter.

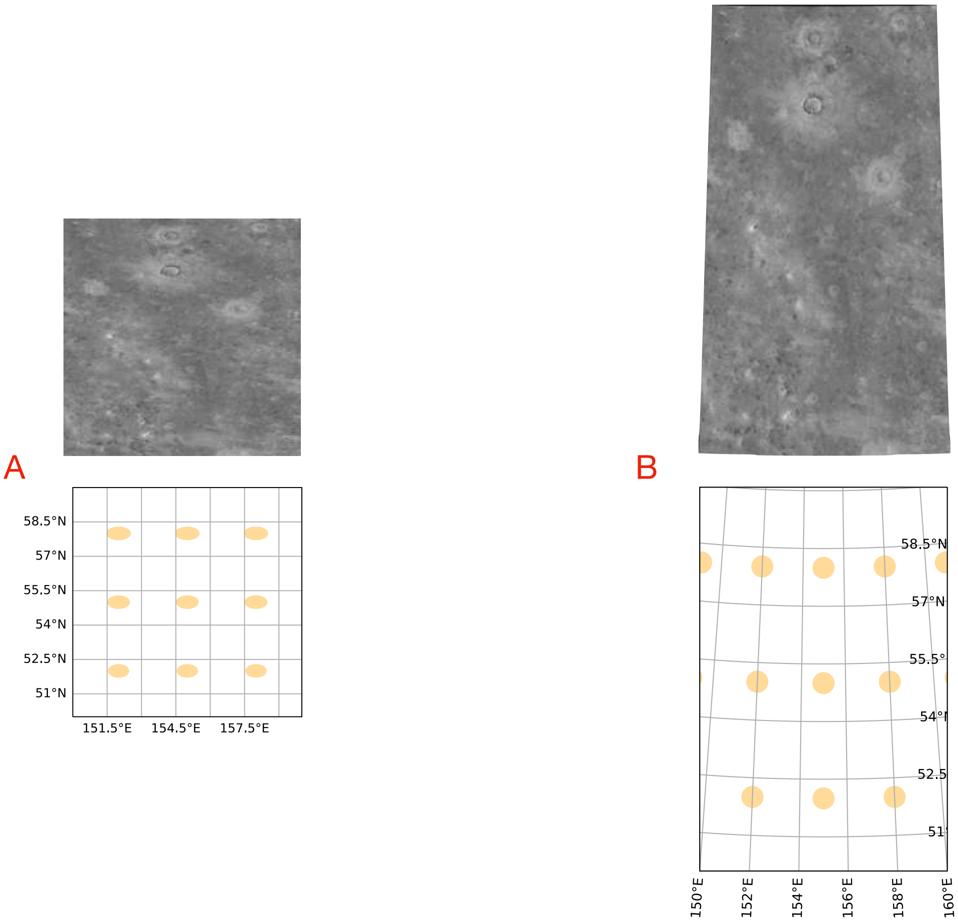

Figure 2.3: Effect of reprojection on the quadrangle at 56°N/156°E from a equidistant cylindrical projection (A) to local stereographic projection (B).In principle, circles appear increasingly elongated in the north–south direction when moving away from the equator due to projection distortions. However, in this example, which spans only from 50° to 60° at mid-latitudes, the deformation is not significant enough to be visually apparent, so the craters still appear nearly circular.

As a preprocessing, we cut the image around the target crater and resampled it in agreement with its crater diameter. Indeed, as we cut the image around the craters, we notice that edge map of more than 80 pixels in radius craters contained many parasitic edges which doesn't belong to the crater edge that we wanted to fit. Those edges misled our algorithm and thus, it increases considerably the computation time. We also stretch the image to a mean value of 128 and standard deviation varying depending on the type of crater. Indeed, we notice that some of the most eroded craters are more difficult to see in the images. In order to make them visible we perform a different treatment for this specific crater category. For those eroded or buried craters that we will call "ghost" craters, we put the standard deviation stretching parameter to 15. On every other crater type we put the standard deviation to 9.

The Canny edge filtering is described hereafter and has two threshold tuning parameters. Edges which have a gradient intensity higher than the high threshold are considered as sure edges. In the same way, edges which have a gradient intensity lower than the low threshold are not considered as edges and so they are discarded. For edges with a gradient intensity between high and low threshold, they are considered as edges if they are connected to "sure edge". Otherwise they are discarded. As we said before, we perform a different treatment for some of the most eroded craters compared to the others. For ghost craters we put the low threshold to 30 and the high threshold to 45. For others, we put the low and high threshold respectively to 35 and 40.

We can see in Fig. 2.4 a picture of the surface of Mars with it's correspondent edge map.

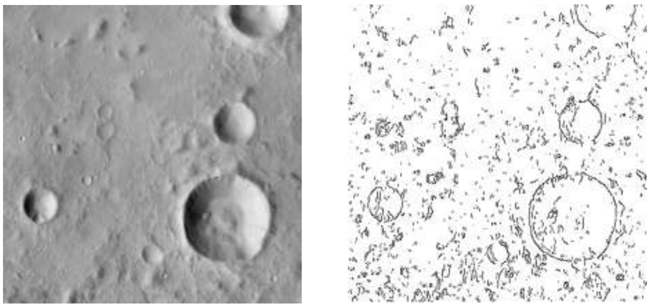

Figure 2.4: Canny edge filtering. On the left we can see a CTX image of the surface of Mars. On the right the binary image produced by the Canny edge filtering. Each black point is considered as a potential crater circle boundary.

2.3.2 - Hough transform

The next step is to estimate all circles present in the edge binary map. Detecting circle from images as as Fig. 2.4 poses three major problems. First, we need to know which point really corresponds to the circle that we want to fit. Then we will also have to deal with incomplete data due to a missing/corrupted part of the image but also due to incorrect edge filtering. This later case could happen in some areas where there is no gradient variation in the image. Finally, we will have to deal with the noise that can appear in the edge map.

The Hough transform is a standard solution to deal with these three problems in one shot (Hough, 1962) and gives a very powerful way to detect simple geometry such as straight line but also circles in the images. The Hough transform works by transforming each point in the "image space" into a parameter space that represents circles.

Indeed a circle, i.e. all points (x, y) in the circle, can be described by the following equation:

$$(x - x_h)^2 + (y - y_h)^2 = r_h^2 \tag{2.1}$$

with:

- (x_h, y_h) as the coordinate of the center of the circle that we want to fit from edge map
- r_h as the radius.

Subscript $_h$ denotes the crater after Hough transform (updated circle) and $_0$ denotes the initial position.

The Hough algorithm aims to identify the optimal values of the circle's center coordinates (x_h,y_h) and radius r that best fit the edge pixels in the image, thus allowing us to pinpoint the location and size of the craters. As shown in Fig. 2.5, the Hough transform algorithm works by transforming each point in the image space into a parameter space that represents circles.

Firstly, the algorithm updates an "accumulator" *Acc* array that keeps track of all the circles that could be present in the image. This array have a three-dimensional shape can be seen as a numerical parameter space. It will be indexed by three values: the (x_h,y_h)-coordinate of the center of the circle, and the radius r of the circle.

Then, for a given radius, for each pixel in the binary edge, the algorithm add a vote in all the position of the center of circles (x_h,y_h). By repeating this step for all radius, each possible circle that passes through all current edges will add a vote accumulator array.

After all the edges have been processed, the best circles are the ones with highest *Acc*, i.e. the highest number of votes in the accumulator array. We can see this accumulator array as a score. The higher the accumulation score is, the higher circles fit the craters path in the edge map. The main step of the process are illustrated in Fig. 2.5.

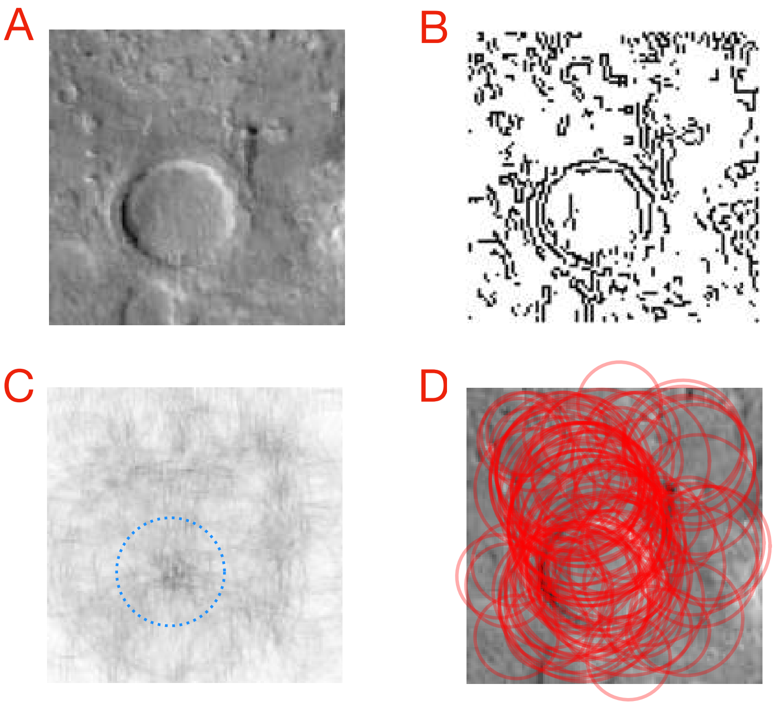

Figure 2.5: Hough circle detection perform on crater n° 06-002993 from quadrangle E108/N40. Main Hough transform process steps. (A): reference image (B): edge-map ; (C): accumulation in grey level (darker for higher accumulation) of the center location at a given radius, indicated by the blue circle. (D): Plots of the 100 best accumulations, i.e. the 100 best circles in the initial image space, each one with an accumulation score.

As we can see in Fig. 2.5 (D) the circle algorithm detects a lot of crater candidates in an image which is very small. In order to make the algorithm work for every crater, we perform it on small patch images centered around each of the database craters. If we perform an Hough transform algorithm on a big region of the planet, a lot of edges will be identified and so a lot of crater candidates. The computation will be long and worst, neighbouring crater could also be interpreted as candidate craters. In order to make the algorithm work for every crater, we perform it on small patch images centered around each of the database craters as shown for example in Fig. 2.8.

2.3.3 - Best circle selection

As we saw in the sub-section 2.3.2, the Hough transform algorithm does not give us a unique solution but a list of circles that all fit more or less the target crater. Indeed, we want our correction to be "not so different" of the database value. In other words, we trust the original database but we just want to apply a small correction. Also we want to have the best possible circle, that maximizes the circularity score. The aim will now be to select the best circle solution.

In order to select the optimum crater, we need to build a new score which would be a combination of different information:

- The candidate center should be close to the reference center.
- The candidate radius should have a radius close to the reference radius.
- The candidate circle should have the best accumulation score.

We express those information in form of probability that will be combined.

Center distance probability In order to advantage candidate which are closer to the reference center, we introduce distance factor which could be interpreted as a pseudo-probability with a maximum normalized to 1, based on the distance Δ_d between the reference center and the candidate center. We propose a Gaussian-like function with a standard deviation σ_d representing the acceptance error around the reference center (see the plot of this Gaussian function in Fig. 2.7).

$$P_d(\Delta_d, \sigma_d) = exp\left(-\left(\frac{\Delta_d}{\sigma_d}\right)^2\right) \tag{2.2}$$

We used defined the local acceptance on the center, using the initial radius with:

- Δ_d: the list of distance between each candidate center and reference center as shown in eq. 2.3
- σ_d: the characteristic distance deviation as described in eq. 2.4

$$\Delta_d = \sqrt{(x_h - x_0)^2 + (y_h - y_0)^2} \tag{2.3}$$

$$\sigma_d = \begin{cases} 40 & \text{if } r_0 < 20 \text{ pixel} \\ 2 \times r_0 & \text{otherwise} \end{cases} \tag{2.4}$$

In this way, $P_d(\Delta_d, \sigma_d)$ will give less weight to the center candidates furthest from the reference center during the selection process.

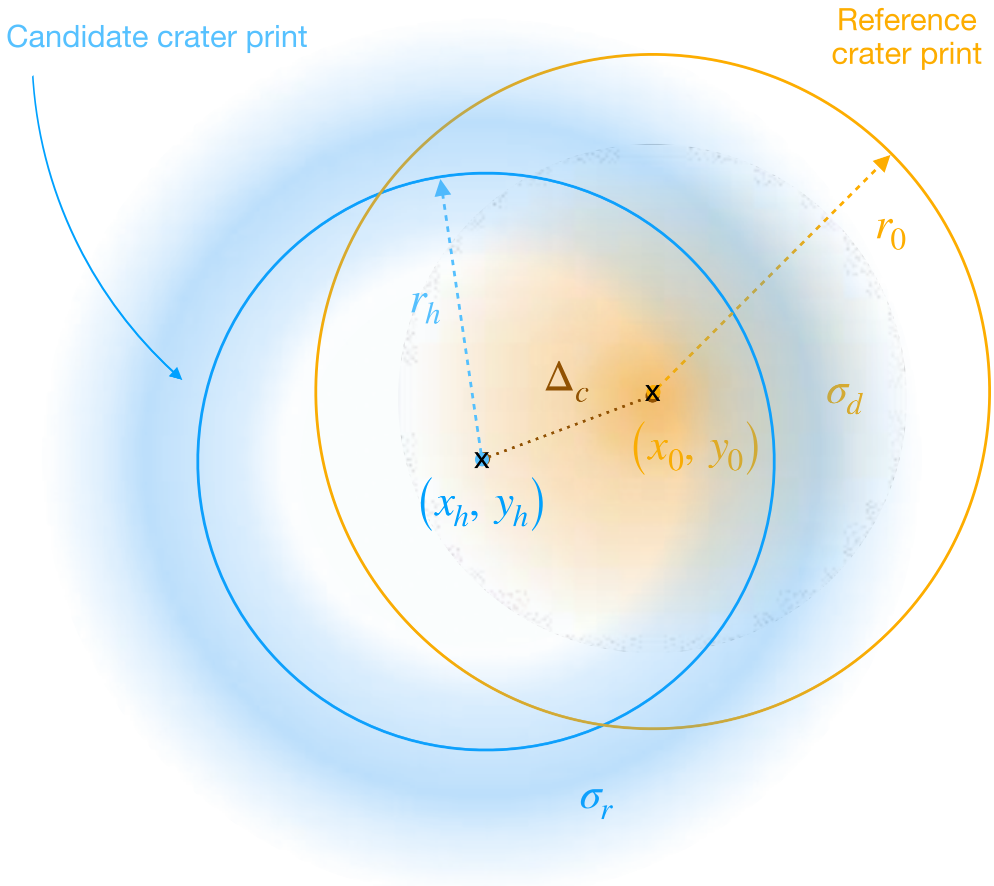

Figure 2.6: Schematic view of the problem. In blue we have the candidate crater with it's center position (x_h,y_h) and it's radius r_h. In orange we have the reference crater with it's center position (x_0,y_0) and it's radius r_0. The halo represents the probability decreasing when going away from the reference.

Radius distance probability In order to advantage candidate which have a closer radius to the reference radius, we introduce radius factor which could be interpreted as a pseudo-probability with a maximum normalized to 1, based on the difference Δ_r between the reference radius and the candidate radius. We also propose a Gaussian-like function with a standard deviation σ_r representing the acceptance error around the reference radius (see the plot of this Gaussian function in Fig. 2.7).

$$P_r\left(\Delta_r, \sigma_r\right) = exp\left(-\left(\frac{\Delta_r}{\sigma_r}\right)^2\right)$$

We used defined the local acceptance on the center, using the initial radius with:

- Δ_r: the list of differences between each candidate radius and reference radius as shown in eq. 2.5
- σ_r: the characteristic distance deviation as describe in eq. 2.4

$$\Delta_r = |r_0 - r_h| \tag{2.5}$$

$$\sigma_d = \begin{cases} 15 & \text{if } r_0 < 7.5 \text{ pixel} \\ \frac{r_0}{2} & \text{otherwise} \end{cases} \tag{2.6}$$

In this way, $P_r(\Delta_r, \sigma_r)$ will give less weight to the radius candidates furthest from the reference radius during the selection process.

Circularity distance Then we introduce a third factor to advantage the quality of the circle detection. This factor is gave by the *Acc* score value, that can be interpreted as a pseudo-probability with a maximum normalized to 1:

$$P_c = Acc \tag{2.7}$$

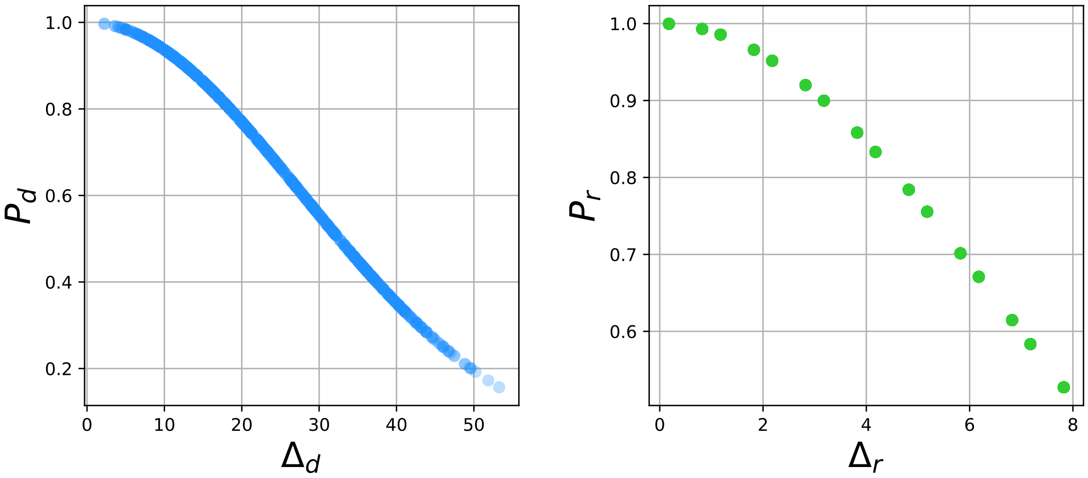

Figure 2.7: Left: Center distance probability ; Right: Radius distance probability.

The higher this score will be, the better the candidate circle will fit a circular shape in the edge map.

Best score We use a combination of this three pseudo-probability by the product of them:

$$P = P_d \cdot P_r \cdot P_c \tag{2.8}$$

In this way, the probability score that we obtain is a compromise between probability to be as close as possible of the original result: to have a center and a radius as close as possible compared to the original crater and an accumulation score as big as possible. The selected solution is the circle which have the highest trade-off probability.

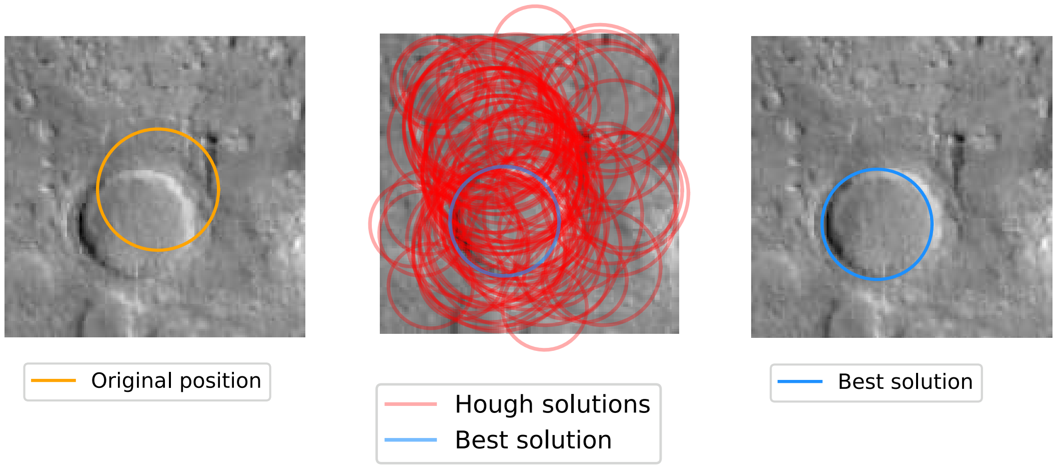

Figure 2.8: Hough circle detection performed on crater n° 06-002993 from quadrangle E108/N40. Left: Crater Initial crater. Middle: We plot the 100 candidate craters from the Hough transform. Right: best candidate crater, using Eq. 2.8

Limits In some cases, no image is available for a given crater (e.g., in CTX no-data value gaps or in the edges). In such situations, the detection process cannot be applied. The original database values for position and radius are therefore kept unchanged. This ensures that missing data do not alter the crater catalogue.

2.4 - Results and evalution

In this section we will show some typical result that we obtain and we will explain how we evaluate our method.

2.4.1 - Examples

Fig. 2.9 to 2.11 represents typical results for 3 craters. In most of the cases, the proposed algorithm significantly improves the crater position and radius. Since we don't have any absolute ground truth, the evaluation has to be done manually with individual validation for each crater.

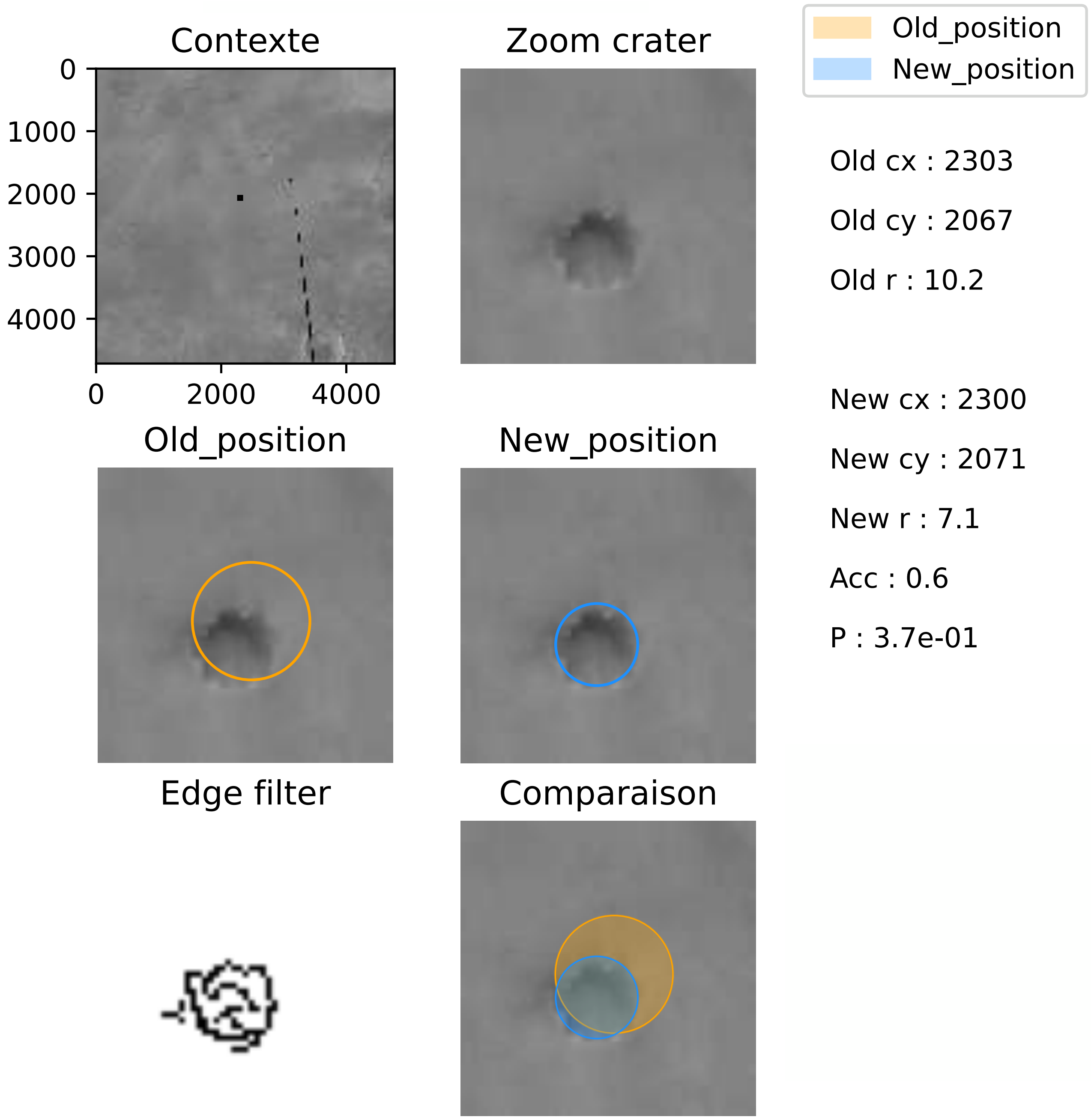

Figure 2.9: Correction perform on crater 19-019982. The upper left image shows us the position of the crater in the quadrangle E-004/N-04. The upper right image is the cut centered around the crater. Center images show the best candidate (left) and reference crater (right). The bottom left image is the edge map. The bottom right image shows the superposed new and old position. The difference between reference and best candidate radius Δ_r is 3.1 pixels and the distance between reference and best candidate center position Δ_d is 5 pixels.

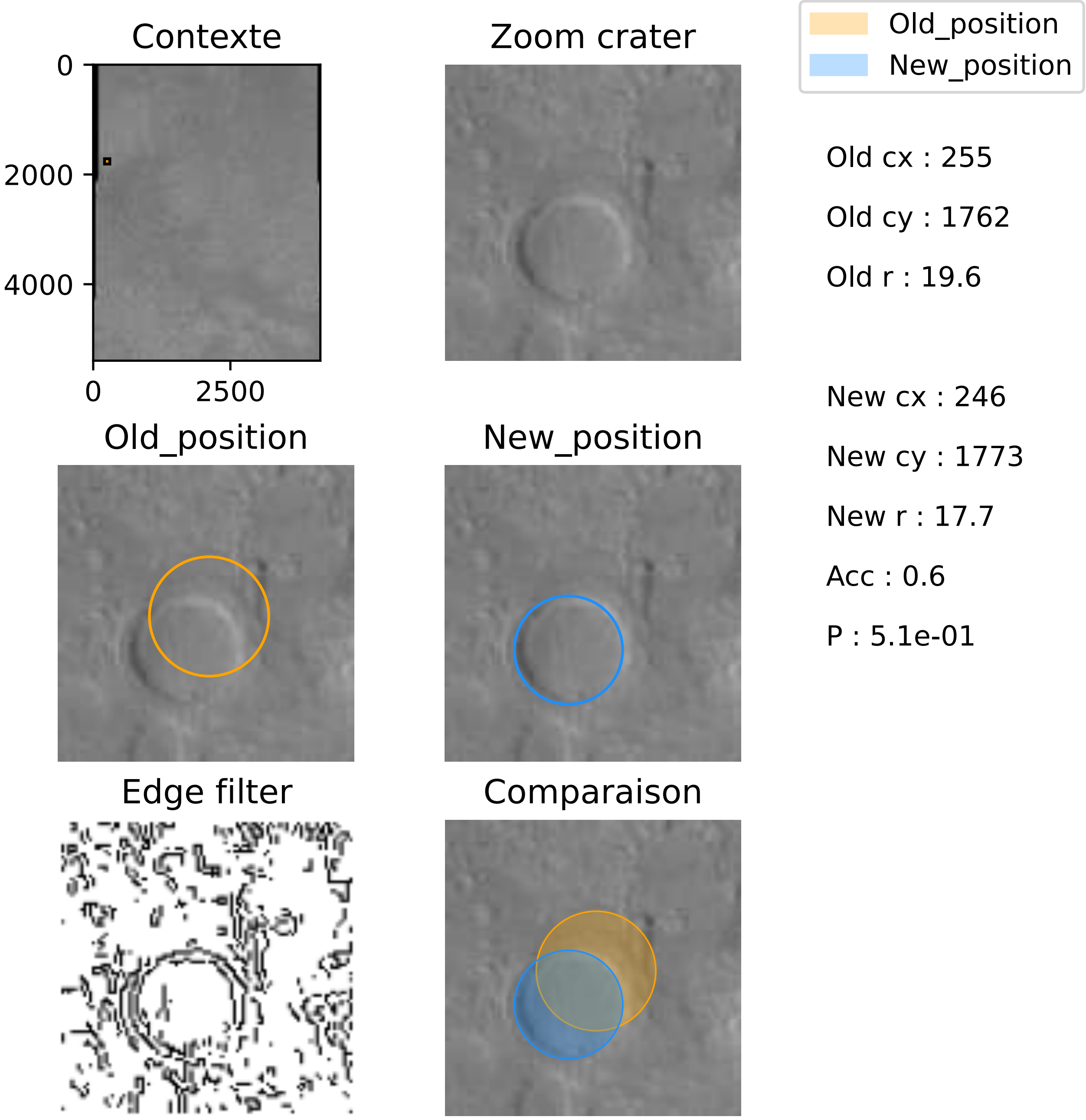

Figure 2.10: Same as Fig. 2.9 on crater 03-002993 from quadrangle E108/N40. The difference between reference and best candidate radius Δ_r is 1.8 pixels and the distance between reference and best candidate center position Δ_d is 14 pixels.

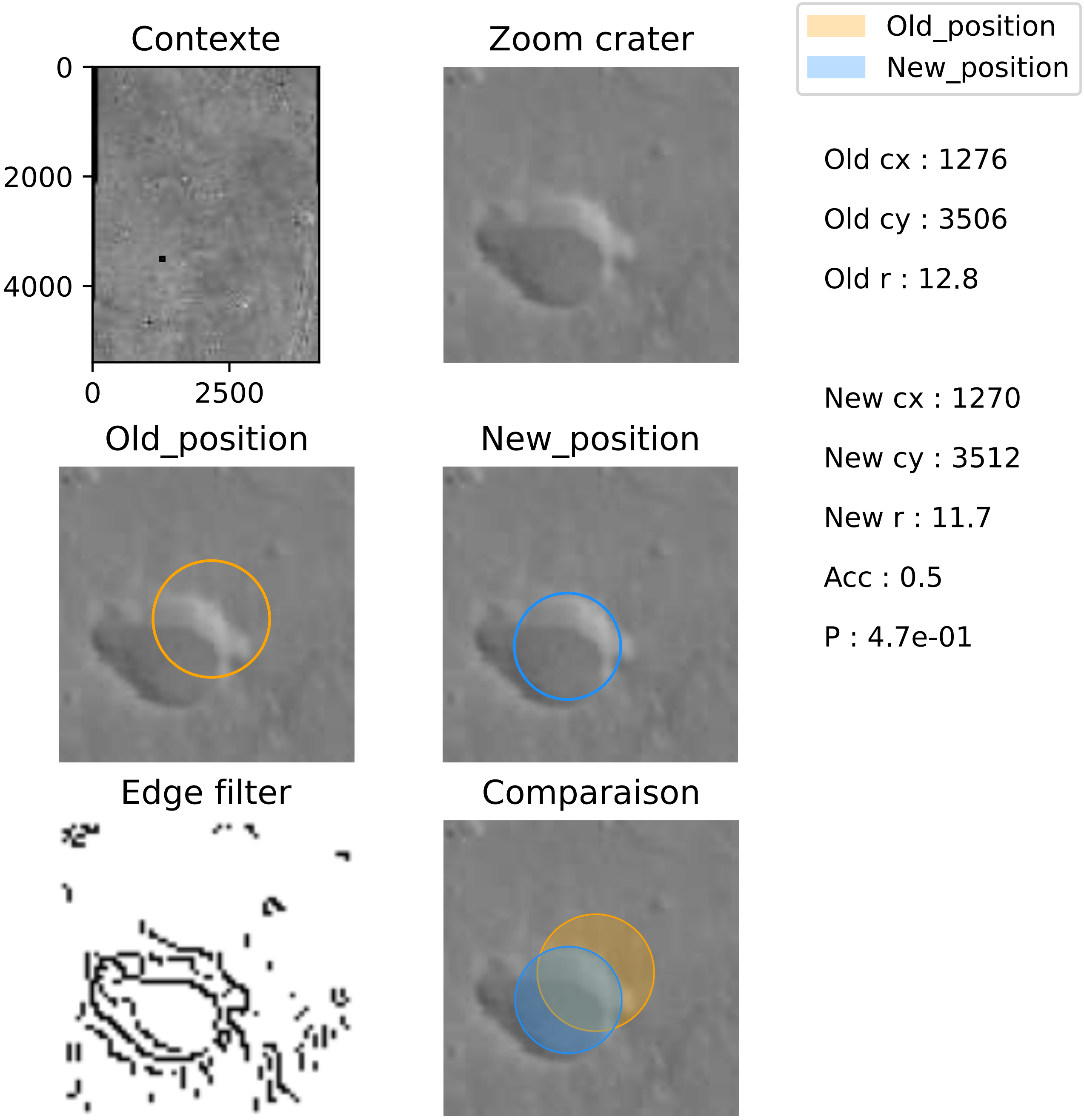

Figure 2.11: Same as Fig. 2.9 on crater 03-006313 from quadrangle E-108/N40. The difference between reference and best candidate radius Δ_r is 1.1 pixels and the distance between reference and best candidate center position Δ_d is 8 pixels.

2.4.2 - Evaluation

In order to verify the accuracy of our crater database algorithm, we perform an exhaustive visual verification. We consider all craters from 7 different quadrangles, representative of Mars, ranging from all latitudes and including terrains of different ages, from Noachian to Amazonian.This corresponds to 639 craters as shown in table 2.1. Among this 639 craters, 479 were qualified as "Valid" craters by Lagain et al., 2021a, 101 as "secondary", 36 as "ghost" craters (i.e: eroded craters) and 23 as "layered" craters as summarized in table 2.2. We can see in this table that we took quadrangles from various region of Mars, at various latitude/longitude/surface age. We can also see in Fig. 2.12 that our sample have a characteristic crater size-frequency distribution which make it representative of the crater population of Mars.

verification dataset information			
Longitude	Latitude	Region	Number of crater
108-112 °W	40-44 °N	Alba Patera	54
168-172 °W	48-52 °S	Arcadia Planitia	120
20-24 °E	44-48 °S	Noachis Terra	139
40-44 °E	12-16 °N	Noachis Terra	196
96-100 °E	60-64 °N	Vasistas Borealis	39
108-112 °E	40-44 °N	Utopia Planitia	66
144-148 °E	44-48 °N	Utopia Planitia	25

Table 2.1: Localisation of the quadrangles $4° \times 4°$ that we used in order to verify that our circle detection algorithm work

We divided the result into four categories:

- **Correct, improved**: It means that the final crater is correct and it has been improved by the algorithm.
- **Correct, no change**: It means that the final crater is correct but was not improved since the initial reference position and radius were already correct.

Type	Count
Valid	479
Secondary	101
Ghost	36
Layered	23
Total	639

Table 2.2: Crater count by type in our verification sample

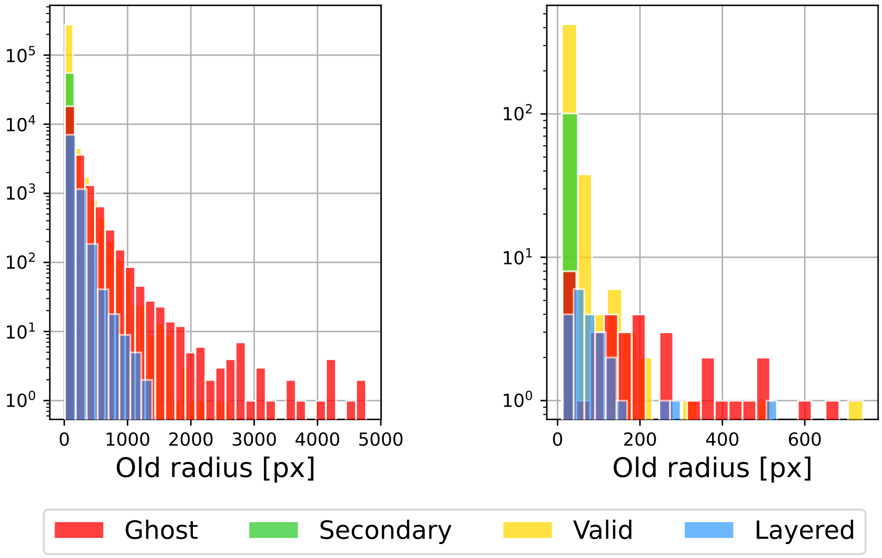

Figure 2.12: **Left**: Distribution of the craters with respect to their radius and their crater status as defined by Lagain et al., 2021a for the whole planet ; **Right**: Same distribution but for our sample.

- **Incorrect, degraded**: It means that the circles detected in the image are not correct craters and so it will degrade the database.

- **Algorithm failed, no data**: It means that the algorithm failed due to the lack of data. It could happen when there is a significant area filled with no data value. Also, for a crater position near the bounds of the quadrangles, it could be when the crater is located too far outside the quadrangle. In this case, we leave values from Lagain et al., 2021a untouched.

Our results are presented in table 2.3 and Fig. 2.13 suggests that when data is available, the algorithm proposes correct positions and radii for a large majority (96.8%) of the craters. The crater description is improved for 87.6% of cases. In some case, the algorithm failed due to no data (3.8% of the total amount of craters).

As we can see in Fig. 2.13, there is no particular crater size in which our algorithm failed more since it follows the initial crater-size distribution 2.12.

In Fig. 2.13, we plot the statistics on each categories in order to determine if there is a particular population of crater on which our algorithm doesn't work. It seems that the position of craters identified as "ghost" craters are a little bit more difficult to detect. This is expected because ghost craters are well eroded. As a reminder, to improve the detection of this class of craters, we used a specific image pre-processing as explained in section 2.3. We also can see that of craters identified as "secondary" craters are sometimes difficult to detect because their shape can significantly differ form a circle.

2.4.3 - Final dataset

We now have a crater database which is able to improve our database in a satisfactory way. So we compute the algorithm on every CTX quadrangle of Mars that we have. It represents 3960 quadrangles

Correct, Improved	539	84.3%	87.6%
Correct, no change	56	8.8%	9.1%
Incorrect, degraded	20	3.1%	3.3%
Algorithm failed, no data	24	3.8%	
Total	639	100%	100%

Table 2.3: Results for each category

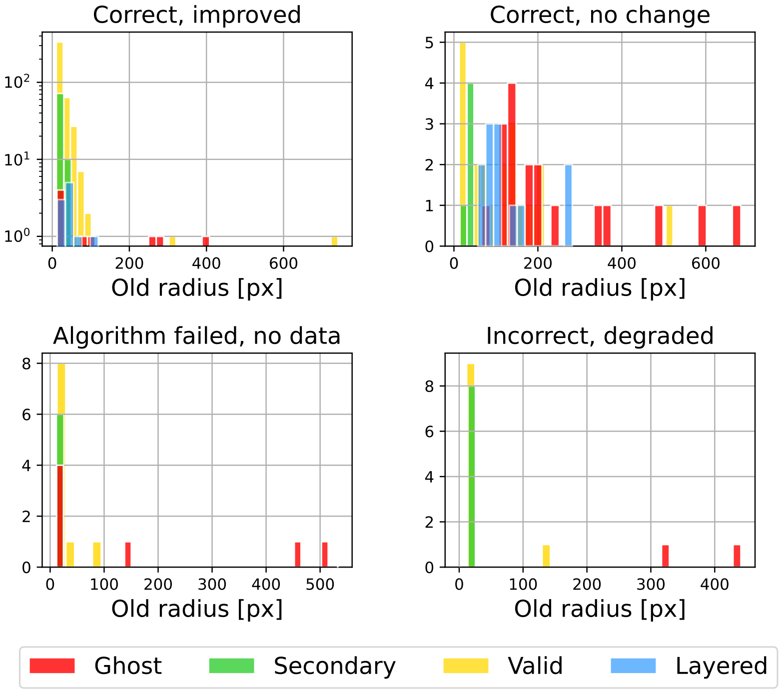

Figure 2.13: Histograms showing the result of our manually checked verification on 639 craters. The "**Correct, improved**" category put together craters in which the algorithm improve the database. The "**Correct, no change**" category put together crater on which the algorithm worked but which not improve noteworthy the database. The "**Incorrect, degraded**" category put together crater on which the proposed crater is incorrect and degrades the database. The "**Algorithm failed, no data**" category put together crater on which the algorithm failed because of no data. We discriminate each crater category define by Lagain et al., 2021a

with 376,417 craters. We run our algorithm on the full dataset, representing approximately 100 hours of computation on a single CPU Intel® Xeon® processor E5-2690 V4 2.6GHZ.

Algorithm failed, no data As described in subsection 2.3.3, some craters cannot be treated because the algorithm failed since they are located within an area without CTX data. The number of crater in this case is 8,218 which represents 2.1% of the full dataset.

Table 2.4: Table listing the number of crater missed per quadrangles. All in all, our algorithm missed 1003 craters.

Crater missed Due to the quadrangle basis of the CTX dataset, we select only craters that are significantly inside the quadrangle. Indeed, as seen in Fig. 2.14, if a crater has a radius $r > r_{max}$, it will be ignored by our algorithm and we copy the initial values from Lagain et al., 2021a. The maximum radius of a crater (in meters) is defined as:

$$r_{max} = \frac{N_x \cdot S_x}{2.5 \cdot 2} \tag{2.9}$$

with:

- N_x: Image width (in pixels) in the direction of longitude. N_x changes with latitude of the quadrangle.
- S_x: Pixel size for the given quadrangle.

As we can see in Fig. 2.15, the N_x in Eq. 2.9 decrease with respect to the latitude and so as we shift to the high latitudes, we will miss more craters. In tab. 2.4, we show r_{max} for each latitude range and then we count how many craters are larger than r_{max}. Our algorithm missed 1,003 craters in the whole dataset, which represent $\approx 0.27\%$ of the dataset, due to quadrangle structure of the CTX dataset.

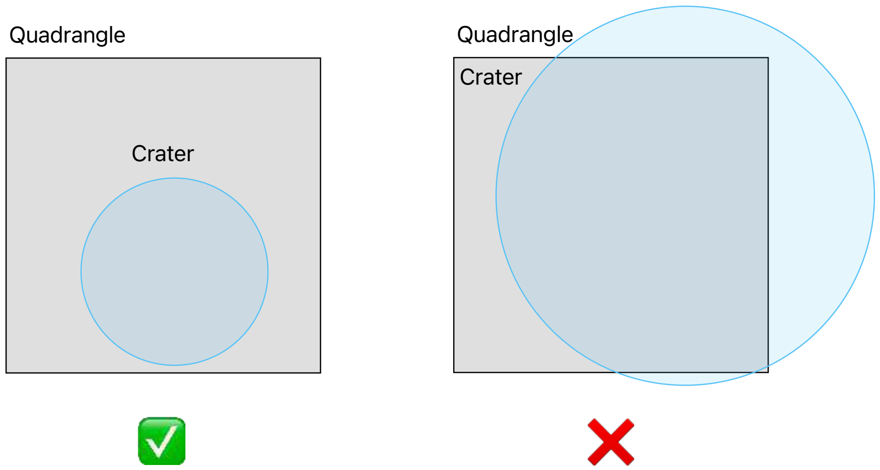

Figure 2.14: schematic view explaining that if a quadrangle is smaller than a crater, it will not be treated by our algorithm.

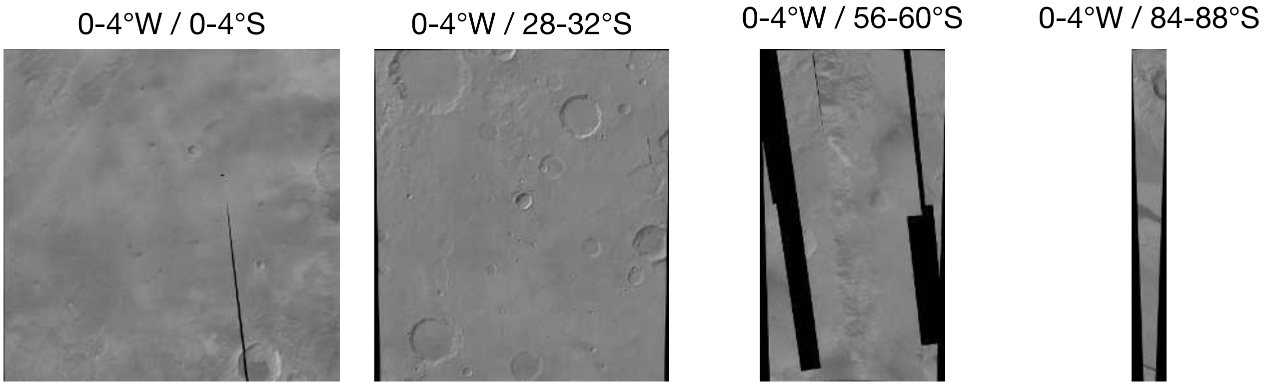

Figure 2.15: Evolution of the quadrangles size with respect to the latitude in local stereographic projection

Fusion of crater duplicated After running our improvement algorithm, we notice that 81 craters located near the boundary of two quadrangles are considered for both quadrangles and thus treated two times. In this case, we fused the data based on the probability score (see Eq. 2.8), noted P_1 and P_2 respectively. To make the selection, our algorithm faced three different situations:

- $P_1 = P_2 = 0$: *No correction.* This case appends for 19 craters when our algorithm failed due to nodata in both quadrangles. In this situation, both solutions are exactly the same because no correction of the crater position and radius occurs. In this case we simply remove the duplicated.
- $P_1 >> P_2$: *Correction with one dominant* This situation is when the ratio of probability is lower than 0.01. In this situation concerning 28 craters, there is a highest fraction of the crater in one quadrangle than in the other. And so we selected the solution with the highest probability score.
- $P_1 \approx P_2$: *Correction with no dominant* In this case concerning 34 craters, both solutions are relevant. The final crater characteristics are the averages weighted by the two probability score P_1 and P_2 of the 2 solution for the position of the center but also for the radius.

In the end, after this fusion process, we removed the 81 duplicated craters in the database which gave us a final database of **376,417 craters**.

2.5 - Conclusion

In this chapter we present a tool to improve the location/size of the crater database construct by Lagain et al., 2021a. This algorithm is valid for 96.8% of the cases but it has some limitations.

Indeed, this algorithm will be able to detect every circular features on planetary surfaces but it will not be able to make the difference between craters, calderas, cinder cones, etc... If non-crater are located nearby a real crater, our algorithm could be blurred. Nevertheless, this situation is unlikely because the score decreases when moving away from the initial crater characteristics.

Here we used the CTX mosaic created by Dickson et al., 2024 in addition with the global crater database made by Lagain et al., 2021a but our algorithm can be used for other dataset for example on the moon. This will require to adapt the parameters of the algorithm, for instance the canny edge filter from the image.

More generally, this algorithm might be used to improve any database of circular shape objects such as planets or moons in an astronomical image.

In addition, one has to note that if this algorithm succeeded to improve the database, it cannot be used alone to detect circles because it requires a reference circles database.

3 - Robust automatic crater detection at all latitudes on Mars with Deep-learning[1]

Contents

3.1 Abstract . . . 116
3.2 Introduction . . . 117
3.3 Data and Methods . . . 118
  3.3.1 Input Images . . . 118
  3.3.2 Improved ground truth crater database . . . 119
  3.3.3 Preprocessing . . . 119
3.4 Crater Detection Algorithm . . . 121
  3.4.1 Faster-RCNN . . . 121
  3.4.2 Training . . . 122
  3.4.3 Evaluation metrics . . . 123
3.5 Results . . . 125
  3.5.1 Global crater detection . . . 125
  3.5.2 Size dependence . . . 126
  3.5.3 Latitude/illumination dependence . . . 126
  3.5.4 Crater-like feature . . . 127
  3.5.5 Miss-classification . . . 128
  3.5.6 Test on other planets . . . 132
3.6 Discussion . . . 132
3.7 Conclusion . . . 136

---

[1] The notations used in this chapter may vary from one chapter to another

This chapter corresponds to an article submitted to *The Planetary & Space Science* journal on the 4th of December 2023 and published on the 11st March 2025. It was written in collaboration with F. Andrieu[2], F. Schmidt[2,3], H. Talbot[4] and M. S. Bentley[5]. The article is available online at `https://doi.org/10.1016/j.pss.2025.106053`.

The ability to reliably detect impact craters across the entire surface of Mars, regardless of latitude or illumination conditions, is essential for constructing complete and unbiased crater inventories. Such inventories form the foundation for planetary surface dating and geological interpretation. In this chapter, we present a deep-learning-based crater detection pipeline designed to operate robustly under a wide range of imaging conditions and surface morphologies. This work builds upon the database refinement approaches described in chapters 2 and acts as a basis for an automatic pipeline of crater detection and classification describe in chapter 6.

We begin by introducing the datasets used for training and validation, detailing the sources of imagery, the preprocessing steps, and the annotation process (section 3.3). We then describe the model architecture, the training strategy, and the data augmentation techniques implemented to improve robustness across varying latitudes and illumination angles (section 3.4). The performance evaluation section presents both quantitative metrics and qualitative visual assessments of the detections, comparing results across different latitude ranges and surface types (section 3.5). Finally, we discuss the implications of these results for planetary surface chronology and outline perspectives for extending this approach to other planetary bodies (section 3.6).

3.1 - Abstract

Understanding the distribution and characteristics of impact craters on planetary surfaces is essential for unraveling geological processes and the evolution of celestial bodies. Several machine learning and AI-based approaches have been proposed to detect craters on planetary surface images automatically. However, designing a robust tool for an entire complex planet such as Mars, is still an open problem. This article presents a novel approach using the Faster Region-based Convolutional Neural Network (Faster R-CNN) for such a detection. The proposed method involves the pre-processing, training and crater detection steps, which are especially designed for robustness regarding latitude and complex geomorphological features. The objectives of this studies are to (i) be robust at all latitudes (ii) for all ≥ 1 km diameter crater sizes, and (iii) to propose an open-source and re-usable algorithm that (iv) only needs an image to run. Extensive experiments on high-resolution planetary imagery demonstrate excellent performances with an average precision $AP_{50} > 0.82$ with an intersection over union criterion $IoU \geq 0.5$, irrespective of crater scale. For mid and high latitudes (higher than 48° north and south), performance decreases down to $AP_{50} \sim 0.7$, which is still better than the current state of the art. Loss of performance is mostly due to strong shadowing effects. Our results also highlight the versatility and potential of our robust model for automating the analysis of craters across different celestial bodies. The automated crater detection tool presented in this article is publicly available as

---

[2] Author from Université Paris-Saclay, CNRS UMR8148, GEOPS, Orsay, France

[3] Author from Institut Universitaire de France (IUF), France

[4] Author from CentraleSupelec – Paris-Saclay University – Inria, Gif-sur-Yvette, France

[5] Author from European Space Astronomy Centre, Villanueva de la Canada, Madrid, Spain

open-source[6] and holds great promise for future scientific research of space exploration missions.

3.2 - Introduction

Planetary surfaces undergo constant evolution driven by geological phenomena such as impacts (Leighton et al., 1965) or volcanic eruptions (Carr, 1973). By analysing the distribution and the density of craters using the “crater counting approach, it is possible to estimate the age of the planetary surface (Hartmann et al., 2001; Neukum et al., 2001). This age is a valuable insight into the geological history and evolution of planetary surfaces (Benedix et al., 2020). Understanding the distribution of impact craters is thus crucial for comprehending the geological processes (Hartmann, 2005), including tectonic deformation, volcanism, erosion, transport, and impact cratering itself (Hartmann et al., 2001).

Historically, crater detection has relied on manual analysis. For Mars and the Moon, in particular, several manuals databases exist (Head et al., 2001; Robbins, 2019; Robbins et al., 2012). Even with corrective analysis (Lagain et al., 2021a), manual databases are all subject to human limitations. Indeed, studies have shown that human attention to repetitive tasks, such as crater counting, rapidly decreases after 30 minutes (See et al., 1995), inducing errors. Moreover, human crater counting has other limitations such as subjectivity and limited scalability. These limitations can be overcome by employing approaches based on Machine Learning (ML).

For this reason, crater detection using computer vision methods has been widely explored in the last decade or so. A proof of concept was described in Vinogradova et al. (2002), achieving good results limited by the image resolution. Some studies tried to use the geometry of the problem as a criterion for detection such as Salamuniccar et al. (2010) and Galloway et al. (2014). This method is interesting because it does not require much computational resources but it gives rise to two problems. The first is that while it can be accurate to detect relatively fresh craters, it remains a challenging task to detect eroded craters (Salamuniccar et al., 2010). Secondly, these methods cannot make the difference between a crater and another geomorphological circular such as calderas or scoria cones that are present at the surface of Mars (Head et al., 2001). Other methods have been suggested using digital elevation models (DEM) such as Di et al. (2014), Zhou et al. (2018), Chen et al. (2018), Lee (2019), and Wang et al. (2019). These methods provided valuable benefits for the community, but require a complex pre-processing step to first create the DEM, requiring multiple views and the use of stereo-vision methods ; and/or lidar/radar measurements. In this article, we focus on crater detection from single images. Salamunićcar et al. (2011) identified 77 different works, categorised into image-based and DEM-based approaches. Since then, many more have been proposed, particularly with the advent of deep-learning based algorithms such as R-CNN (Girshick et al., 2014) or YOLO (Redmon et al., 2016) or even simpler models such as pyramidal networks (Yang et al., 2022). These have enabled ground-breaking performance in detection, such as in Benedix et al. (2020) and La Grassa et al. (2023). These news studies have surpassed the previous generation in performance but some limitations with robustness still remain. In particular, detection rates in latitude higher than 45° north and south have been poorer, as well as in the global planetary scale evaluation. However, these recent techniques are relevant for our objectives, offering the advantage of versatility in detecting a variety of features on planetary surfaces. Notably, deep learning algorithms have been successfully applied to identify linear surface features on

---

[6] Our algorithm is available here: `https://doi.org/10.14768/ae042dbb-37c3-4a98-b72c-02d2a191f53b`

Europa (Haslebacher et al., 2023), to detect rockfalls on Mars (Bickel et al., 2020), and to detect ice block falls on the Martian polar caps (Su et al., 2023). Segmentation-based approaches have also been tried, using models such as the U-Net architecture proposed in Ronneberger et al. (2015), originally for bio-medical imaging. We can for example cite Silburt et al. (2019), Downes et al. (2020), Latorre et al. (2023) or Ali-Dib et al. (2020) which use a Mask-RCNN architecture developed by He et al. (2017) for this task. Another proof of concept was presented in Giannakis et al. (2024) where authors show that it is possible to use Meta's SAM (Segment Anything Model) (Kirillov et al., 2023) to detect craters. These examples highlight the adaptability and effectiveness of deep-learning based methods across diverse planetary environments and geologic contexts.

This research project focuses on the development of a computer vision algorithm specifically designed to automatically detect craters in planetary surface images in a robust manner. Our algorithm has been designed to adapt to different latitudes and potential false positive geomorphological features, ensuring consistent performance across a range of planetary bodies. In previous such work (Benedix et al., 2020), it was shown that the crater detection algorithm efficiency decrease drastically with an increasing latitude. This problem can be either due to geographical reprojection (equatorial projection strongly affects polar features) but also to variation in illumination condition (due to lower solar elevation near the poles). The difficulties associated with illumination conditions are even more important for sun-synchronous platforms, since each latitude is observed at the very same local time. In this case latitude and solar elevation bias combine.

Furthermore, our algorithm is designed to distinguish craters from other circular features present on planetary surfaces such as calderas (Masson, 1984; Williams et al., 2007), scoria cones (Brož et al., 2014), and lava tunnels (Warner et al., 2003) thanks to a global scale learning dataset.

Finally the scale of the crater seems also a key point that induces bias into the detection algorithm. For instance Benedix et al. (2020) only focus on size 1.5 -10 km range for their training database. We propose here a tool to detect craters of $>$ 1km in diameter.

3.3 - Data and Methods

In order to detect and classify craters precisely, our machine learning algorithm needs suitable input data. In this section we will describe the various data used to conduct this study and we will describe the preprocessing steps.

3.3.1 - Input Images

We built our training dataset using surface images of Mars. Indeed, the complexity and the overall diversity of crater morphologies is unrivalled anywhere else in the Solar System. Thus, by building a crater detection model trained on Mars, we aim to be able to detect craters in every planetary surface in the Solar System such as Mercury and the Moon as shown respectively in Fig. 3.13 and 3.12. The second reason why Mars is a privileged planet is that it is one of the most explored extraterrestrial body. Indeed, since the Mariner IV probe first imaged the Martian surface in 1964, the planet has received around fifty more visits.

We used a dataset of high-resolution images of Mars provided by the Context Camera (CTX) onboard the Mars Reconnaissance Orbiter (MRO) (Malin et al., 2007). CTX images the surface of

Mars at a pixel resolution of approximately 5 meters, enabling detailed observations of the Martian surface. The CTX mosaic used covers 99.5% of Mars from 88°S to 88°N (Dickson et al., 2024).

Above latitudes of 80° north and south and beyond, we encountered significant challenges in our crater detection efforts. This area presents a unique set of obstacles, primarily due to the pervasive presence of a seasonal and permanent ice caps and clouds, even during the summer months (Appere, 2012; Schmidt et al., 2009; Langevin et al., 2007). These features make the image mosaic of the surface less reliable. In addition, the global crater database contains almost no craters in this region.

Given these challenges we made the deliberate decision to limit our focus to the area between 76°N and 80°S within the CTX mosaic.

3.3.2 - Improved ground truth crater database

With learning-based object detection we need to provide a reliable list which references the ground truth positions of objects that we want to detect. For Mars there are already several manual crater databases which classify craters. Among them we use here the (Lagain et al., 2021a) database, which was improved by manual checking from the Robbins and Hynek database (Robbins et al., 2012). This database is based on the THEMIS global mosaic (Edwards et al., 2011) and consists of the exhaustive list of the 384,343 craters $>$ 1 km diameter on Mars.

By superposing the CTX images with the crater position and radius from this database, we noticed that a relatively large number of craters appeared to be shifted from their expected location, probably due to the relative errors of pointing between CTX and THEMIS. We improve the Lagain et al. crater position and radius using the Hough transform in order to better point the crater with respect to our images. This method enables us to improve the database precision in 96% of the cases.

3.3.3 - Preprocessing

Our preprocessing pipeline was inspired by our precedent work on the THEMIS dataset (Van den Bossche et al., 2018). We placed significant emphasis on data preprocessing because training on poor-quality data, which contains biases or inaccuracies, would result in the model incorporating these biases, thereby adversely affecting its performance. To facilitate data download, the CTX mosaic was divided into 3,960 quadrangles. Each quadrangle covering a latitude/longitude range of 4 × 4°. The CTX mosaic is available online (Dickson et al., 2024) in the equidistant cylindrical projection. This projection does not preserve geometry, so the circular shape appear flatten at high latitude. In our study we choose to reproject our data to a local stereoscopic projection in order to conserve crater circularity and to ensure that the model has to learn only a single shape. In addition, maintaining a circular geometry is crucial to detect a proper center/radius and it might enable us to correct the issue raised by Benedix and collaborators, 2020, concerning the fact that they observe many false negative detections above 45° in latitude (Benedix et al. (2020), Figure 1).

A second step of our prepossessing pipeline was to cut the whole-quadrangle datasets into smaller patches of images of size 224×224 pixel width, for compatibility with our neural network architecture (Ren et al., 2017). In order to be able to detect only crater above 1km in diameter, we set up a maximum resolution of 200m per pixel. To include the widest variety of crater sizes, we also downsampled the quadrangles into 400 meters and 800 meters per pixel patches, which effectively increased the amount of terrain covered within each patch while maintaining the required pixel dimensions. In the end, we obtain 97,423 patches of images that we split into three different datasets:

- Training dataset : 82,874 images (85%)
- Validation dataset : 4828 images (5%)
- Testing dataset : 9721 images (10%)

The training dataset is the one used to train the deep-learning method. The validation dataset is used to monitor the learning phase. The testing dataset is completely independent of the learning phase and is only used to evaluate the performance of the trained algorithm.

We attributed a class (Training, Validation, Testing) randomly to the 3960 quadrangles in a way that all latitude and all geological units are represented in the 3 datasets (see Fig. 3.1). This ensures a robust training and learning to discard potential false-positive features. In addition, all latitude are present up to 76°N and 80°S, ensuring a robustness to illumination conditions.

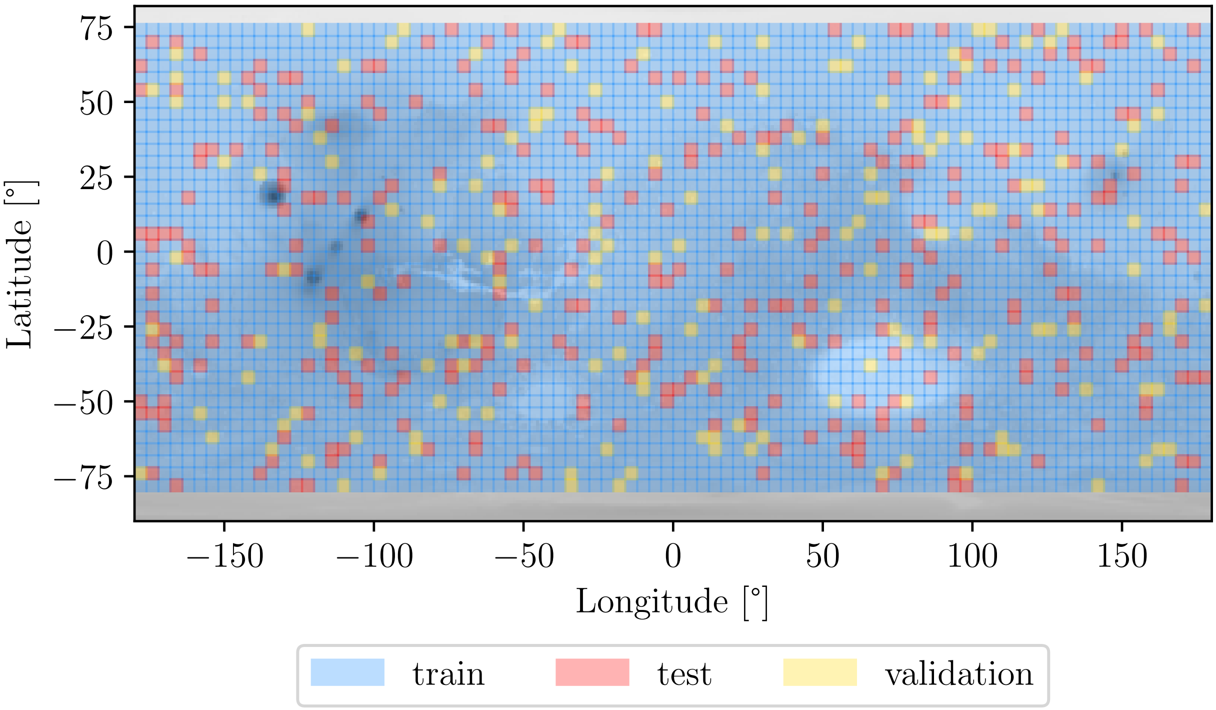

Figure 3.1: Localisation of the 3960 quadrangles attributed to train, validation and test datasets

In order to design a detector robust to varying illumination and acquisition conditions, we performed a data augmentation step by randomly performing the following transformations, which are implemented using the albumentations library, which is a popular library for image augmentation in machine learning (Buslaev et al., 2020):

- Flip : horizontal, vertical or both flips with a probability of 0.5.

- Random Rotate : rotation by 90, 180 or 270 degrees, with a probability of 0.5
- Motion blur : motion blur with a random-sized kernel, with a probability of 0.2
- Median blur : median blur with a random aperture linear size, with a probability 0.1

Deep learning algorithms are well-suited for object detection across multiple scales, allowing them to identify objects of varying sizes within an image. However, in practice, it is essential to establish a minimum scale threshold. This is due to the fact that even in the highest-resolution images, there exist craters smaller than 1 kilometer in diameter, which are not included in our ground truth database. Thus, we theoretically exclude all craters that are smaller than 10 pixels in diameter from the training dataset. This size criterion has been consistently applied during the inference phase as well.

This 10-pixel size constraint is motivated by the fact that craters are generally detected via their rim. Experiments with state-of-the art detectors for thin features such as vessels (Xiuqin et al., 2019) have shown that lines thinner than 3 pixels cannot be detected reliably. Therefore, for a circle, a 9 or 10-pixel diameter should be seen as an absolute minimum. In practice, we notice that our algorithm is much more performant with a size criterion around 20px. By implementing this constraint, we aim to strike a balance between capturing the diversity of crater sizes and maintaining the practical relevance of our detection. It allows us to concentrate our algorithm's training and evaluation on craters of substantial scientific interest while mitigating potential noise from smaller features. As a result, our approach provides a more accurate and relevant assessment of crater detection performance across a range of scales.

3.4 - Crater Detection Algorithm

In this subsection we provide some details about the deep-learning model that we used for the detection task. Then, we explain the training process and give the result of the test step which is essential to evaluate the performances of our algorithm.

3.4.1 - Faster-RCNN

Faster-RCNN is a popular object detection algorithm used in many computer vision tasks (Ren et al., 2017). More recent algorithm, such as YOLO (Redmon et al., 2016), are faster for detections since they are designed for video analysis but not necessarily more accurate. Since computation time is not a limiting factor in this study, we chose Faster-RCNN, which demonstrated better performance in object detection in exchange for a longer computational time (Zaidi et al., 2022). Its main goal is to accurately identify and localize objects within an image. To understand how this object detection algorithm works, it can be decomposed into three stages (see Fig. 3.2) :

1. **Backbone** : A residual Convolutional Neural Network (CNN) is used for the backbone. the first component of Faster-RCNN is a Resnet50 CNN backbone. This model will process the entire input image set and extract high-level features. The CNN backbone typically consists of multiple convolutional and pooling layers with skip connexions, which progressively learns to recognize complex patterns and objects in the image. The purpose of the CNN backbone is to encode the image into a set of feature maps that preserve spatial information (Lecun et al., 1998).

2. **Region Proposal Network (RPN)** : The second step of Faster R-CNN involves generating potential Regions Of Interest (ROI) in an image that are likely to contain objects. This is done using a RPN which takes an input image and scans it with a set of predefined anchor boxes. These anchor boxes with different sizes and aspect ratios could be considered as local projections. For each anchor box, the RPN predicts whether it contains an object or not, as well as adjusts its position and size to tightly fit the object, if it is present. The RPN generates a set of proposed ROI, called region proposals, based on these predictions.

3. **Detector : ROI Head** This part makes the ROI Classification and Bounding Box Regression: The final step involves classifying the proposed ROI and refining their bounding boxes. The feature maps generated by the CNN backbone are used to extract the features for each proposed region. These features are then fed into two separate fully connected layers: one for object classification (determining if the object is a crater) and the other for bounding box regression (refining the location and size of the bounding box). The classification layer produces an index that can be interpreted as a likelihood of membership to an object class for each region proposal, while the regression layer predicts adjustments to the initial bounding box coordinates.

Our Faster-RCNN implementation has 41,299,161 parameters to estimate. For more information, please refer to (Ren et al., 2017). It outputs the final set of detected objects: bounding box coordinates and likelihood index.

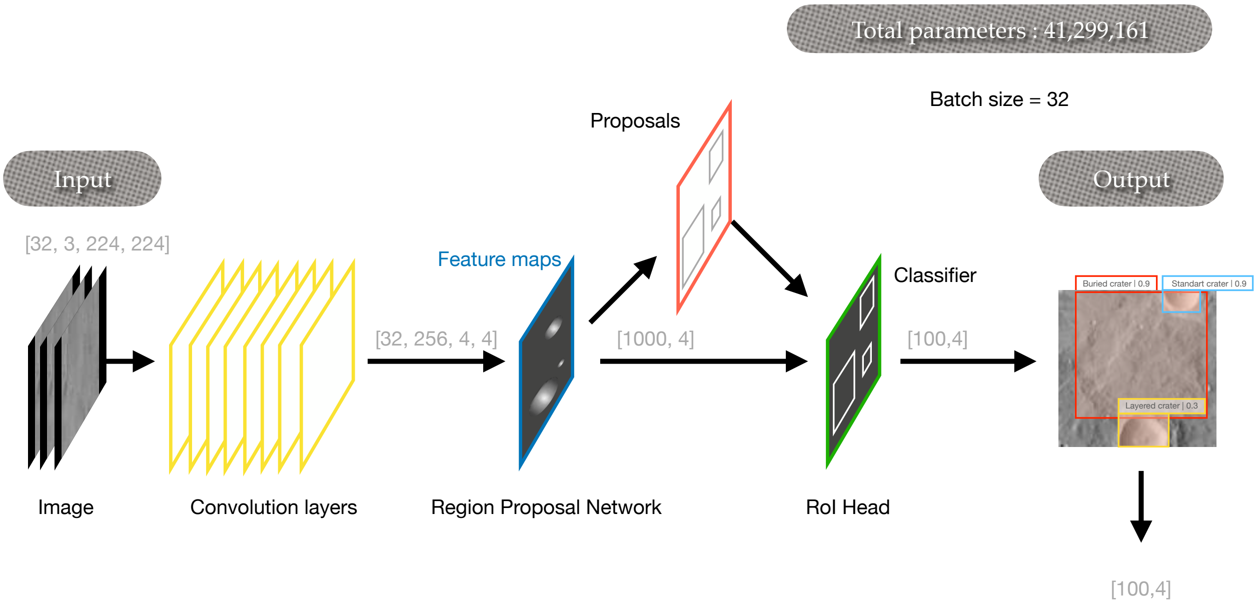

Figure 3.2: Faster R-CNN architecture as described by Ren et al. (2017) with our image configuration.

3.4.2 - Training

The general idea of this training process is to teach the model how to recognize craters in images. Each time the model sees a batch of images, it compares its prediction to the ground truth and calculate an error materialized as a loss function. The aim of the training is to optimize the model parameters by minimizing this loss through a gradient descent.

The loss function L is a sum of regression and classification losses. The regression loss (first term) assesses the precision of bounding box adjustments, while the classification loss (second term) measures the accuracy of crater predictions :

$$L(p_i, t_i) = \frac{\lambda}{N_{reg}} \sum_i p_i^* L_{reg}(t_i, t_i^*) + \frac{1}{N_{cls}} \sum_i L_{cls}(p_i, p_i^*) \tag{3.1}$$

Where: p_i is the predicted probability of anchor i being an object, p_i^* the ground-truth label (1 if the anchor is positive, else 0), t_i^* the ground-truth box associated with a positive anchor, t_i is a vector representing the four coordinates of the predicted bounding box, $L_{cls}(p_i, p_i^*) = -p_i^* log(p_i) - (1 - p_i^*) log(1 - p_i)$, $L_{reg}(t_i, t_i^*) = L_1^{smooth}(t_i - t_i^*)$, $\frac{1}{N_{reg}}$ and $\frac{\lambda}{N_{cls}}$ have the same value. This way, the two terms of the equation are equally weighted.

To train the RPN, the goal is to assign ROI in such a way to minimize the regression loss value. Anchors are local projections at varying scales and multiple aspect ratios. We used typically $N_{reg} \approx 2400$ anchors. ROI are computed for each anchor together with a score.

In a training phase, anchors are learned using the ground-truth box using the following scheme:

- Anchors are assigned a positive class label (object) if they meet one of two conditions: (i) They have the highest Intersection-over-Union (IoU) overlap with a ground-truth box. (ii) They have an IoU overlap higher than 0.7 with any ground-truth box (A single ground-truth box might assign positive labels to multiple anchors.).

- Negative Anchors: Anchors are assigned a negative class label (not an object) if they are not positive and their IoU ratio with all ground-truth boxes is lower than 0.3.

- Neutral anchors: these anchors belong neither to an object or to the background and are not taken into account during training.

Then, the classifier learns the class by minimizing the classification loss value, to ensure that the predicted p_i^* is close to the real p_i classification.

The training process is influenced by several hyper-parameters that can affect the loss function or the gradient descent process. In this study, we apply the same weight to every component of the loss function. For the gradient descent, we use the ADAM stochastic optimization algorithm, primarily controlled by the learning rate (LR). The LR, which defines the step size for each iteration, is kept constant at 10^{-5}. This is a critical factor because a learning rate that is too large can cause the algorithm to learn quickly at first but fail to converge to a relevant minimum of the loss function. On the other hand, a too small learning rate can significantly prolong the training time and may cause the algorithm to become stuck in an irrelevant local minimum.

3.4.3 - Evaluation metrics

In order to evaluate our algorithm, we will use the usual precision and recall metrics.

The choice of the evaluation metrics was enlightened by Vinogradova et al. (2002). Indeed, in this study, the authors state that "*Many pattern recognition algorithms could be applied to this problem* *[i.e.:detecting craters in an automated way] but a systematic validation process is required to select the best method for each scientific application and to determine its reliability for scientific use."* This is a point which was as it was also underlined by C. Lee in his comparison between Benedix et al. (2020) and Lee et al. (2021) : "*The apparent performance of automatic crater detection algorithms is sensitive to the choice of metric used to gauge the performance.*". Indeed, in all those study, authors fine-tune Machine Learning tools and thus a fair comparison of the results require the use of the same training and evaluation method. In our study we decided to take the same evaluation metrics as in previous studies (Benedix et al., 2020; La Grassa et al., 2023; Ali-Dib et al., 2020; Silburt et al., 2019).

The precision P measures the proportion of correctly identified craters among all the objects classified as craters (Eqn. 3.2):

$$P = \frac{TP}{TP + FP} \tag{3.2}$$

True Positives (TP) refers to the number of correctly identified craters, while False Positives (FP) indicates the number of non-crater objects mistakenly classified as craters.

The recall R or the sensitivity measures the proportion of correctly identified craters among all the actual craters present in the dataset (Eqn. 3.3) :

$$R = \frac{TP}{TP + FN} \tag{3.3}$$

False Negatives (FN) represent the number of craters that were not detected by the algorithm.

Since it is also commonly used in the literature, we have calculated the F_1 score, which is the harmonic mean of precision and recall:

$$F_1 = \frac{2 \cdot \mathrm{AP}_{50} \cdot \mathrm{AR}_{50}}{\mathrm{AP} + \mathrm{AR}} \tag{3.4}$$

To specify true positive (TP) vs. false negative (FN) detections, we use the Intersection over Union (IoU) criteria. IoU is a measurement of the overlap between the predicted bounding box and the ground truth bounding box. If the IoU value is greater than a threshold fixed by the user (usually 0.5), the detection is considered a TP, else it is a FN. This IoU threshold is an important criterion because the higher it is, the more stringent we are in considering what a TP is. The figure Fig. 3.3 show the evolution of the Average Precision (AP_{50}) and the Average Recall (AR_{50}) at IoU 50 with respect to the training steps. We also added the F_1 score.

In order to evaluate the global performances, we measure the precision and the recall for all images and calculate the average precision and the average recall on the whole testing dataset. Since the IoU threshold commonly used in the literature for evaluating computer vision model is 0.5, we will use average precision and recall with IoU $= 0.5$ (AP_{50} and AR_{50}). It is necessary to use these two metrics to evaluate our algorithm since they assess different aspects of the model's performance. In summary, precision measures the proportion of true positives among all detections, while recall evaluates how comprehensively the model identifies relevant instances. It is always possible to improve one metric to the detriment of the other. To integrate these together, we calculate the Precision-Recall (PR) curve and introduce a new metric based on the work of Saito et al. (2015), which indicates that the Area Under the PR Curve (AUPR) is an effective way to combine precision and recall. Additionally, it states that for binary classification problems, the AUPR is equivalent to the Average Precision (AP) (Saito et al., 2015).

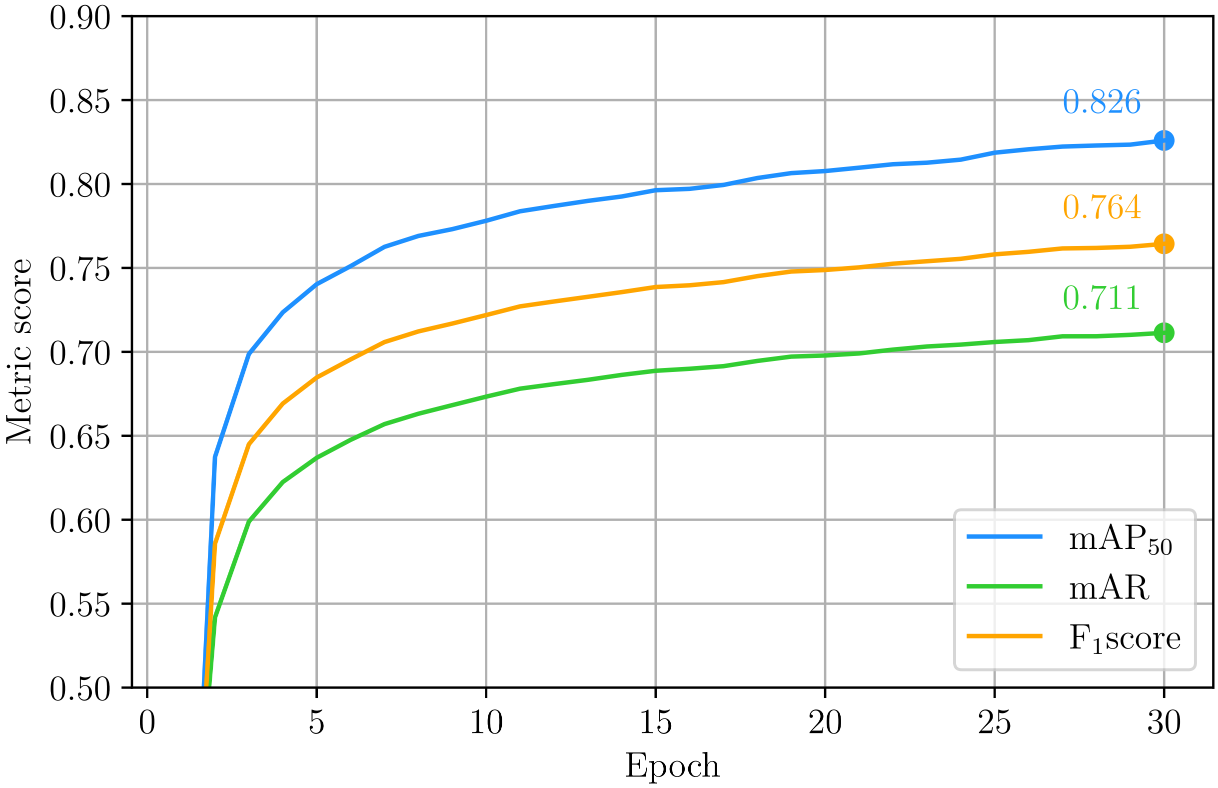

Figure 3.3: Evolution of the AP$_{50}$, the AR$_{50}$ and the F_1 score during the training phase.

3.5 - Results

3.5.1 - Global crater detection

As introduced in sub-section 3.4.3, Fig. 3.4 is a graph called Precision vs Recall Curve (PR curve) that depicts how precision changes as the recall varies(and the likelihood index) at various Intersection-over-Union (IoU) thresholds. In this way, we can observe the performance of the algorithm across different levels of detection. As expected the curves appear better as the IoU threshold decreased. On the contrary, when the threshold varies from 0.7 to 0.9, i.e. when being more demanding on how well the bounding boxes must fit the craters, the performance decreases.

In order to achieve a comprehensive and precise performance metric, we calculated the area under the Precision vs Recall curve. This area gives us the mean Average Precision (mAP), which summarizes the algorithm's ability to accurately detect objects across various precision-recall trade-offs. A higher mAP indicates better detection performance. Figure 3.5 shows the computed mAP values corresponding to different IoU thresholds. The algorithm is robust from IoU 0 to ~ 0.7 with a $mAP > 0.8$ but drastically decreases above IoU > 0.7. We obtain a mAP at IoU $= 0.5$ (AP_{50}) of 0.82 which is in the range of the best values from the literature for crater detection on Mars (Benedix et al., 2020). We note however that our value is achieved on the entire planet.

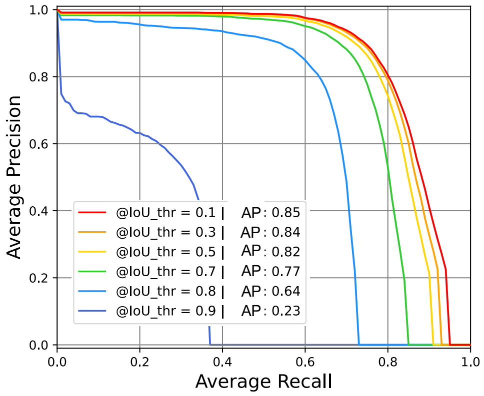

Figure 3.4: Precision as a function of recall for six different IoU thresholds.

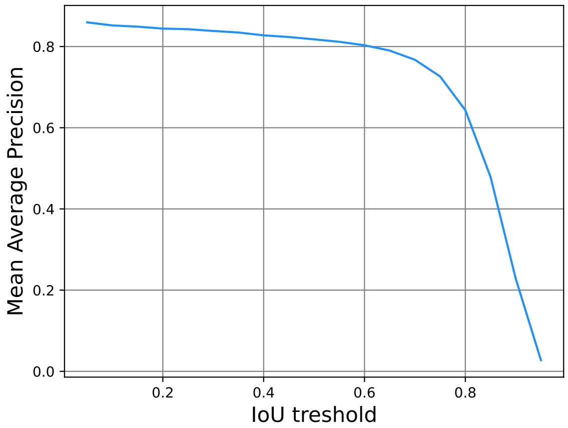

Figure 3.5: mAP as function of IoU threshold

3.5.2 - Size dependence

Crater distributions on planetary surfaces are close to a power law (Hartmann et al., 2001) with a -2 slope, meaning that there are 100 times more craters > 1 km than craters > 10 km. To accurately evaluate the performance of our detection algorithm across this wide range of sizes, we perform the same evaluation (at IoU threshold $= 0.5$) on three different bounding boxes size range with limits of 32^2 and 96^2 pixel size. We can see in Fig. 3.6 that our algorithm is robust to crater scale because the AP_{50} scores are equally good.

3.5.3 - Latitude/illumination dependence

To assess the robustness of our crater detection algorithm across different latitudes/illumination conditions, we conducted experiments using subsets of the test dataset. The images were categorized into ten latitude groups as shown in Fig. 3.7, all evaluated using the standard metrics AP_{50} described above.

The experimental results demonstrate that our crater detection algorithm exhibits robustness across different latitudes, with varying degrees of performance. The algorithm achieved excellent performance in equatorial regions (from 48°N to 48°S), accurately identifying a significant number of craters with AP_{50} up to 0.86. At higher latitudes, the algorithm maintained an acceptable level of performance with $\mathrm{AP}_{50} >\sim 0.7$.

In Fig. 3.8, we present an example image from the mid-latitude in old Noachian terrain, demonstrating the effectiveness of our algorithm. Despite the presence of challenging surface features and illumination conditions, the algorithm successfully identifies all the craters within the image. This case is an example of perfect detection (AP_{50}=1). Figure S2 shows another example with AP_{50}=0.9,

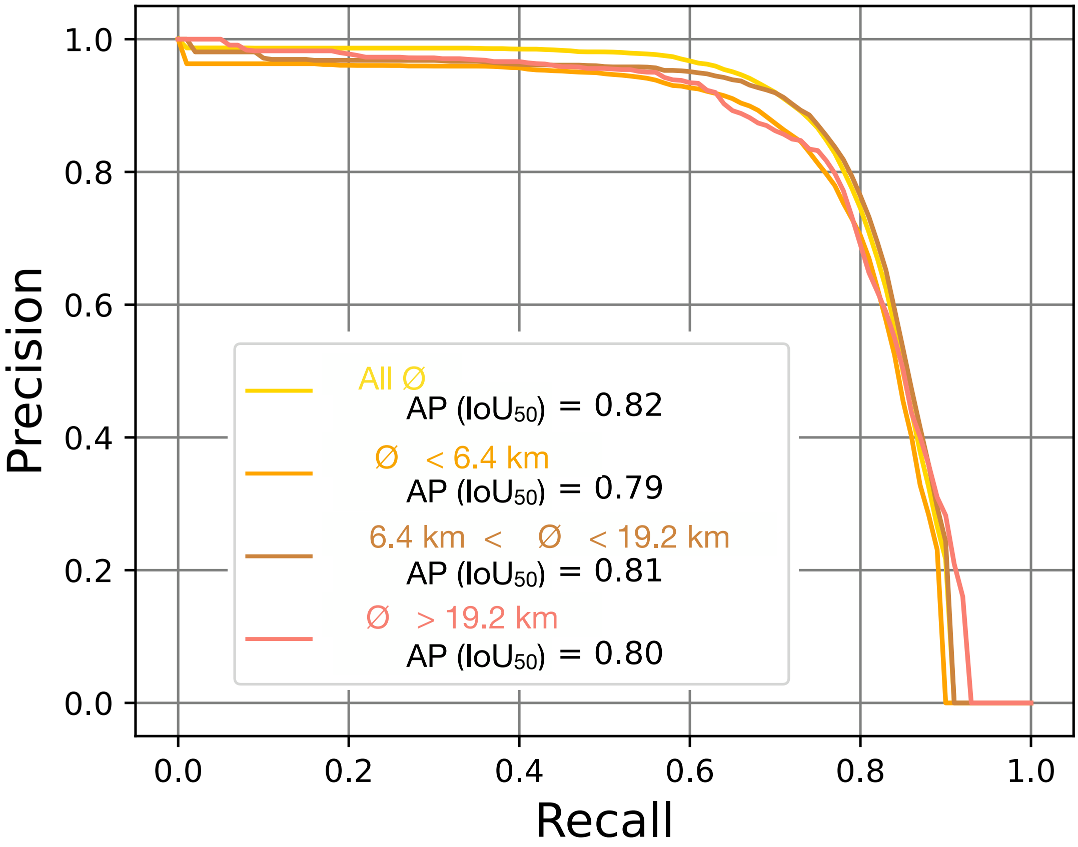

Figure 3.6: Precision vs Recall curves for an IoU = 0.5 and for different bounding box sizes of the test dataset. Each curve represents the precision with respect to the recall for three bbox size. The orange curve corresponds to bbox with a size of 32px^2 which corresponds to every craters with a diameter of lass than 6.4 km. The brown curve corresponds to bbox with a size between 32px^2 and 96px^2 which corresponds to a diameter size between 6.4 and 19.2 km. The red curve corresponds to bbox size of more than 96px^2 which corresponds to a crater size of more than 19.2km in diameter.

more representative of the global results. Figure 3.11 shows a case with relatively apparent poor result (AP_{50}=0.5) and will be discussed in the next section.

3.5.4 - Crater-like feature

In this subsection we will investigate the ability of our model to distinguish craters from other geomorphological circular features commonly found on planetary surfaces. This analysis aims to determine the algorithm's robustness in detecting craters, rather than miss-classifying non-crater circular features.

We evaluate special cases with other circular features, such as scoria cones, (Fig. 3.11), calderas (see Fig. 3.9), or lava tubes (see Fig. 3.10). Results show that our detector do not detect circular morphological features which are not craters, as expected. For the image in Fig. 3.11, none of the

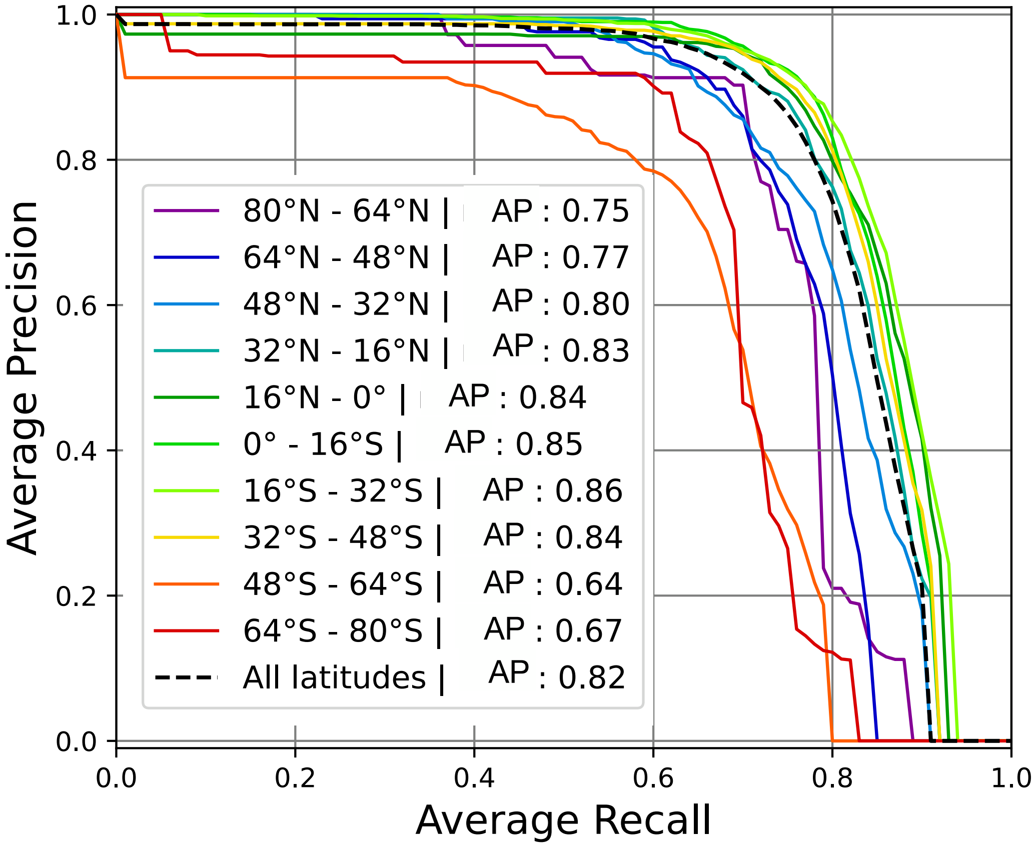

Figure 3.7: Precision vs recall curve at IoU = 0.5. Each curve represents the precision with respect to the recall for a given latitude range.

numerous scoria cones are detected as crater.

This results means that we have gained valuable robustness on many of those features. However, as we can see in Fig. 3.9 challenges arise when distinguishing calderas and, to a lesser extent, lava tubes from craters. One may note that caldera are circular hole features that can be hard to distinguish from crater, even for planetary scientist. Additionally, small errors in recognizing lava tubes highlight a need for further refinement, even though the model generally performs well in this regard.

This finding highlights the algorithm's effectiveness in capturing the unique characteristics and morphology associated with craters.

3.5.5 - Miss-classification

For the image in Fig. 3.11, mAP50 is 0.5 with the ground truth filtered at 10 pixels (100 meters). Unfortunately the proposed crater F (with a confident score of 0.992) is actually a real one but the ground truth crater is not present in the crater database because its size is below 1 km in diameter (below 10 pixels). Our method estimates crater features with minimum 10 pixels radius. By including crater F, the mAP increases to 0.8, which is representative of the average results error. This effect

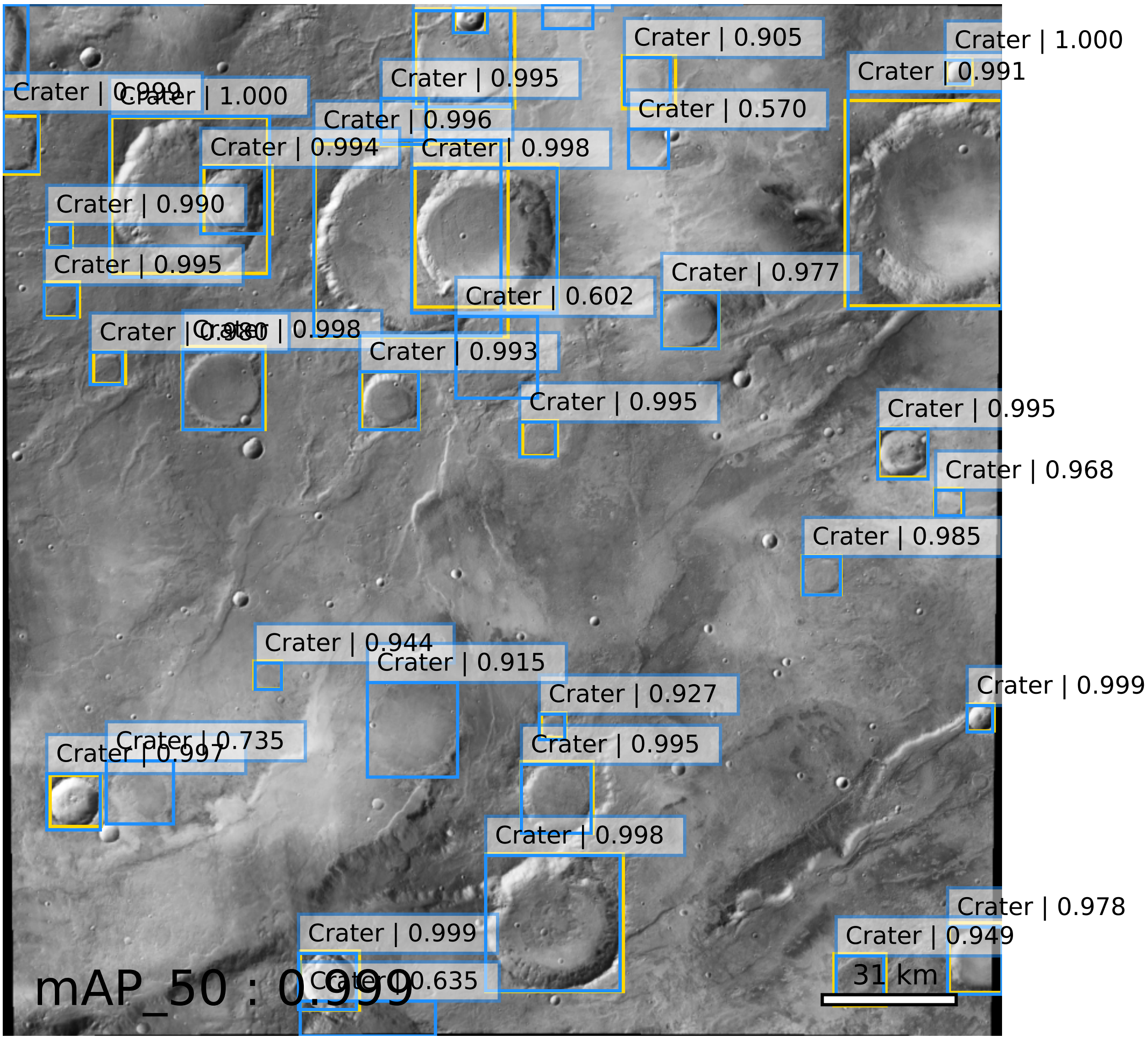

Figure 3.8: Inference in Noachis Terra region (Mars). The lower right corner of this 4°×4° quadrangle is located at 44°W, 20°S. The yellow boxes represent the ground truth information and the blue boxes the predictions ones. The mAP for this image is 0.999. Please note that crater smaller than 10 pixels in diameter are ignored.

of size threshold (correct detection but classified as incorrect) could decrease the score, making our algorithm not as good as it actually is.

Another source of miss-classification is due to interpretation of complex geological features. For

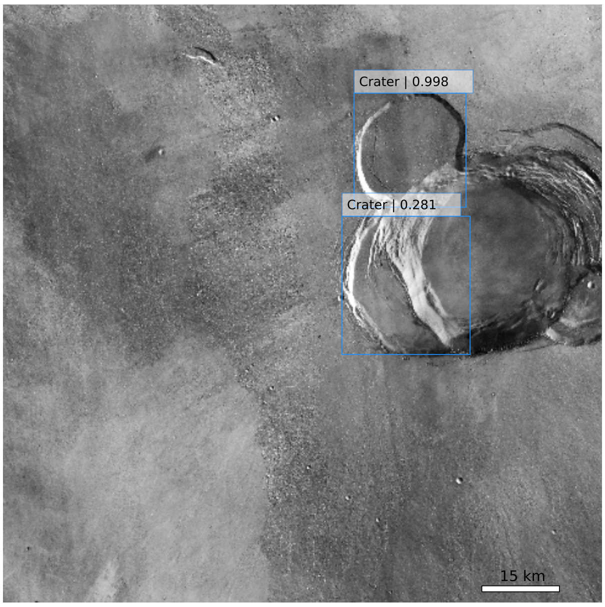

Figure 3.9: Inferences on Arsia mons's volcanic caldeira. The lower right corner of this 2°×2° images is located at 106°W, 10°N. Here, the model is predicting a crater where there is not, demonstrating the limit of it's robustness.

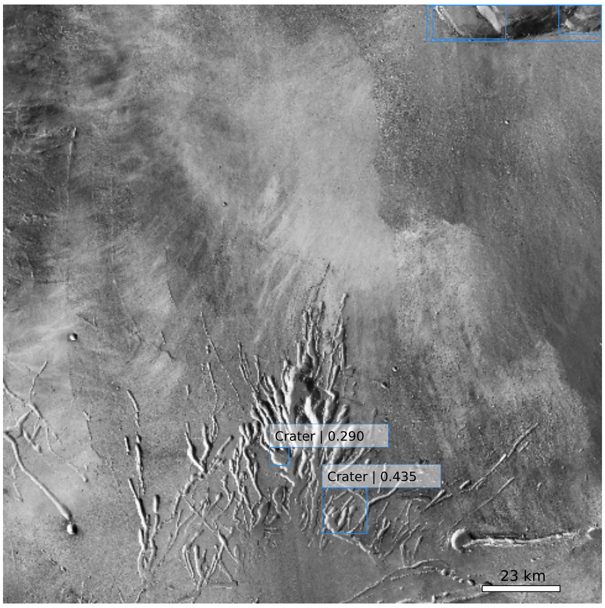

Figure 3.10: Inferences on a Martian region in which we can see lava tubes in the lower part of the image. The lower right corner of this 3°×3°quadrangle is located at 107°W, 08°N on Arsia Mons slopes. Here, the model is not predicting crater demonstrating its robustness.

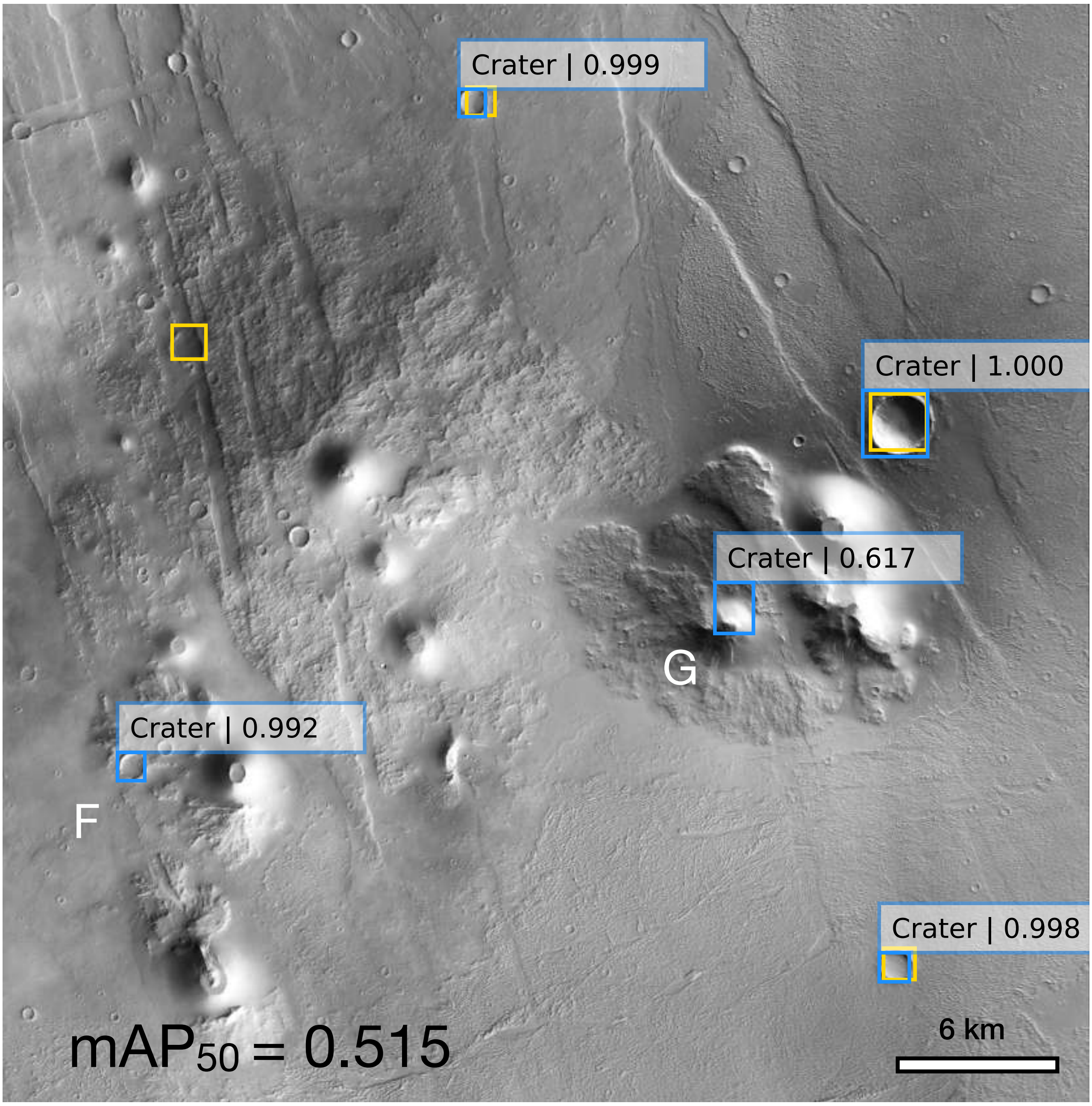

Figure 3.11: Inferences on Ulysses scoria cones region (Mars). Some volcanic cones are present in the center of image. The lower right corner of this 0.8°×0.8° quadrangle is located at 122°24'W, 05°24'N on Arsia Mons slopes. Here, the model is not inferring crater where there is no crater demonstrating its robustness. Proposed craters F and G are discussed in section 3.5.5

instance, the proposed crater G (with a confident score 0.617) has no equivalence in the ground truth. This apparent incorrect detection is debatable because there is indeed a circular shape in the North East of the scoria cone but it's interpretation is difficult at this spatial resolution. Is it a real crater in the hummocky terrain covered by the cone formation? Is it a part of the scoria cone? This case typically illustrates the limitation of the ground truth interpretation due to human interpretation.

3.5.6 - Test on other planets

In this subsection, we endeavor to extend the applicability of our model to planetary surfaces beyond Mars. In this study, the aim is not to build a complete database of the whole solar system but more to demonstrate the robustness of our crater detector applying it to different bodies. Specifically, we turn our attention to two celestial bodies, Mercury and the Moon, both of which offer comprehensive mosaic datasets for our evaluation. For the lunar surface assessment, we leverage the Wide Angle Camera (WAC) dataset obtained by the Lunar Reconnaissance Orbiter (LRO) mission (Robinson et al., 2010). This dataset provides high-resolution imagery with a remarkable level of detail, boasting a resolution of 100 meters per pixel. In the case of Mercury, we employ the MESSENGER global mosaic dataset (Becker et al., 2009). MESSENGER, the Mercury Surface, Space Environment, Geochemistry, and Ranging mission, has contributed a wealth of data, including imagery at a resolution of 166 meters per pixel.

Our aim is to apply our raw crater detection model without any optimization to these distinct planetary surfaces, each presenting its own unique geologic characteristics and challenges. By doing so, we seek to assess the model's versatility and its potential utility in automating crater detection tasks on multiple celestial bodies. On each images we built handmade database in order to measure the precision of our algorithm.

As can be seen in Figures 3.12 and 3.13, our algorithm is also able to detect crater in an efficient way on other planetary bodies with scores. Results on Mercury are excellent ($AP_{50} = 0.92$) and on the Moon the performances are similar to those on Mars ($AP_{50} = 0.78$). Both these surfaces are very old, much more cratered than Mars, with overlapping and buried craters that are well detected. Buried craters correspond to ≈6% of the training database (Lagain et al., 2021a), a better transfer learning may improve this performance. Crater overlap makes the detection harder because their shape is not always fully circular. Nevertheless, our detection model is able to detect craters on the Moon and Mercury in a satisfactory way.

3.6 - Discussion

Our findings concur with the observations made by Benedix et al. 2020. In their work Benedix et al. (2020), suggests that detecting craters becomes notably more challenging beyond 45° latitude. In response, we have endeavored to enhance our model by implementing a specialized re-projection technique within a local stereoscopic projection and by taking special care to include high-latitude samples, with extreme illumination condition, in the training phase. These modifications improved our algorithm's detection performance, especially in regions where traditional methods encounter difficulties.

As the latitude increases, cast shadow become larger in the observations, making the detection slightly more difficult. The overall decrease in performance with latitude that can be seen on Fig. 3.7 is expected. This effect is limited and the performance of the detector remain good even at high latitudes. In the southern hemisphere, 3.14 (B), shows a high concentration of eroded crater in the

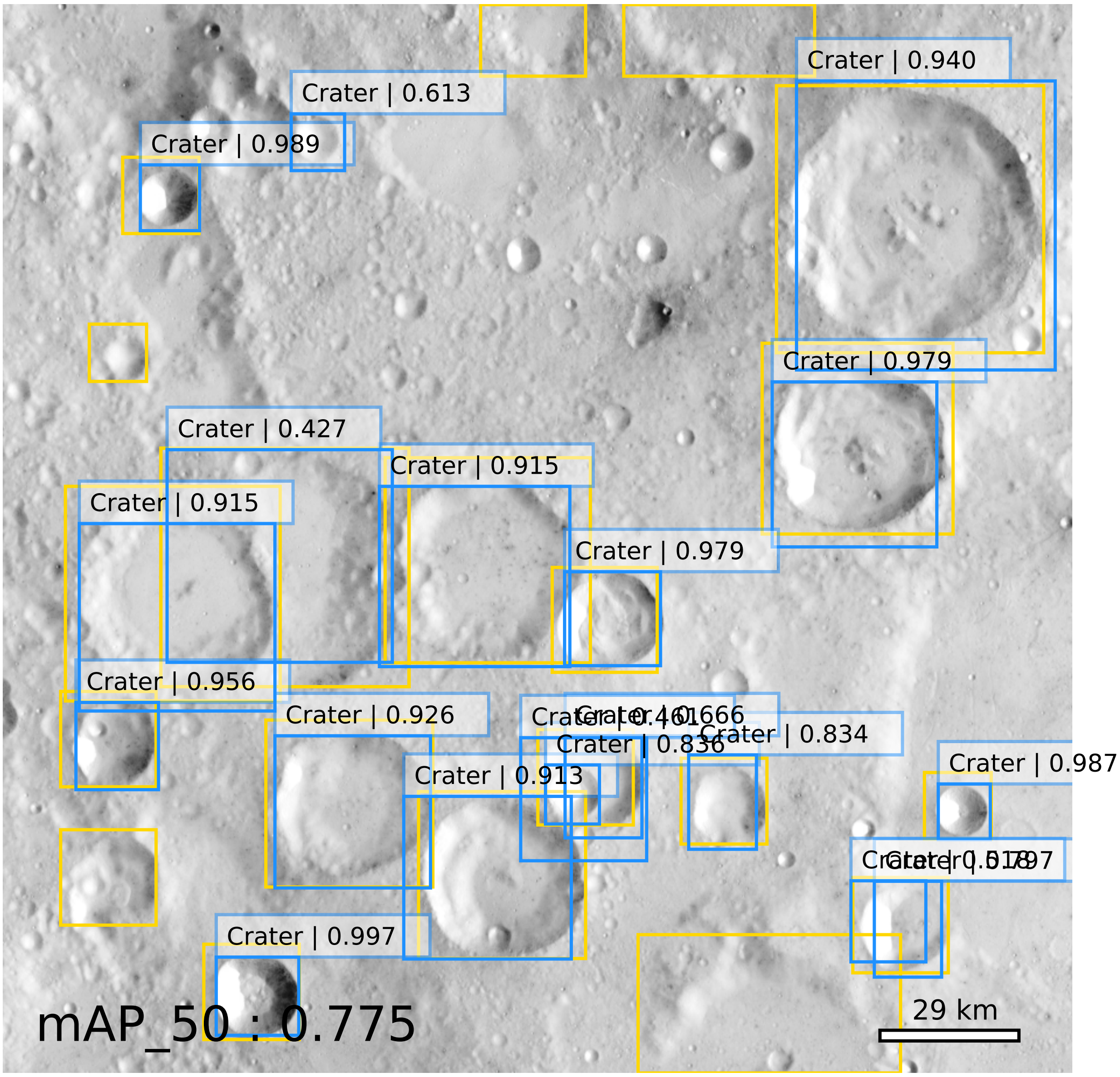

Figure 3.12: Example on the Moon. The lower right corner of this 8°×8° quadrangle is located at 77,78°E, 4,24°S near mare Smythii (in the eastern part of the Moon). The yellow boxes represent the ground truth information and the blue boxes the predictions ones. The mAP for this image is 0.775. Please note that crater smaller than 10 pixels in diameter are ignored.

whole -30°/-60° latitudinal band. These older terrains, i.e.: in the Noachian geologic terrain more present in the south hemisphere of Mars, also have a high density of craters as seen on Fig. 3.14 (A), and thus a high number of superimposed craters. Knowing this, we expect our detector to exhibit

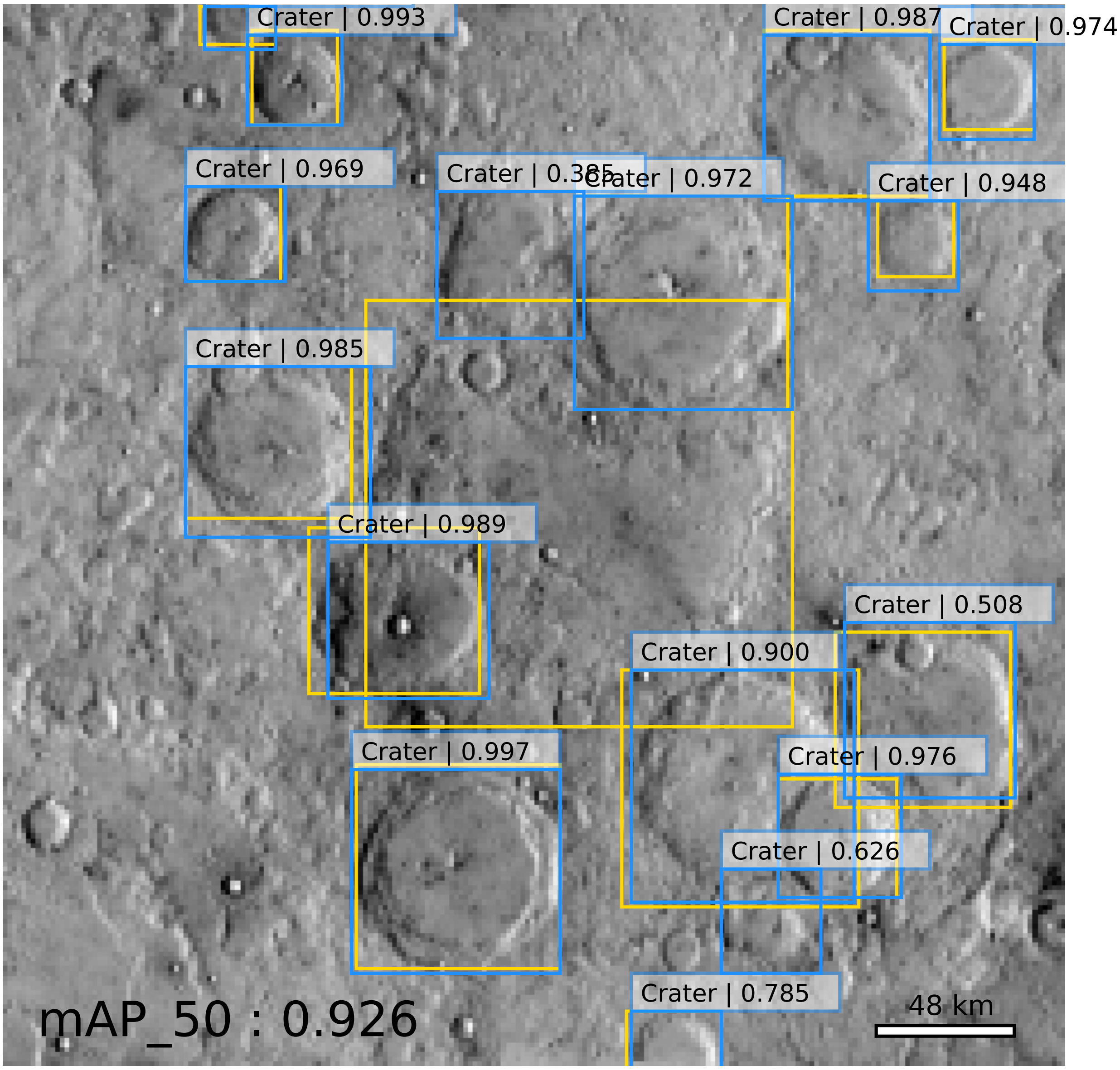

Figure 3.13: Example on Mercury. The lower right corner of this 9.5°×9.5° quadrangle is located at 121°W, 5°S near Verda-Da-Silva Crater (Beethoven, quadrangle, Mercury). The yellow boxes represent the ground truth information and the blue boxes the predictions ones. The mAP for this image is 0.926. Please note that crater smaller than 10 pixels in diameter are ignored.

lower performance in these areas where the craters significantly more difficult to detect, which is the case for the 48°/ -64° in Fig.3.7. This highlights the fact that working on eroded and superimposed craters would be a key to significantly improve the performances of future detectors.

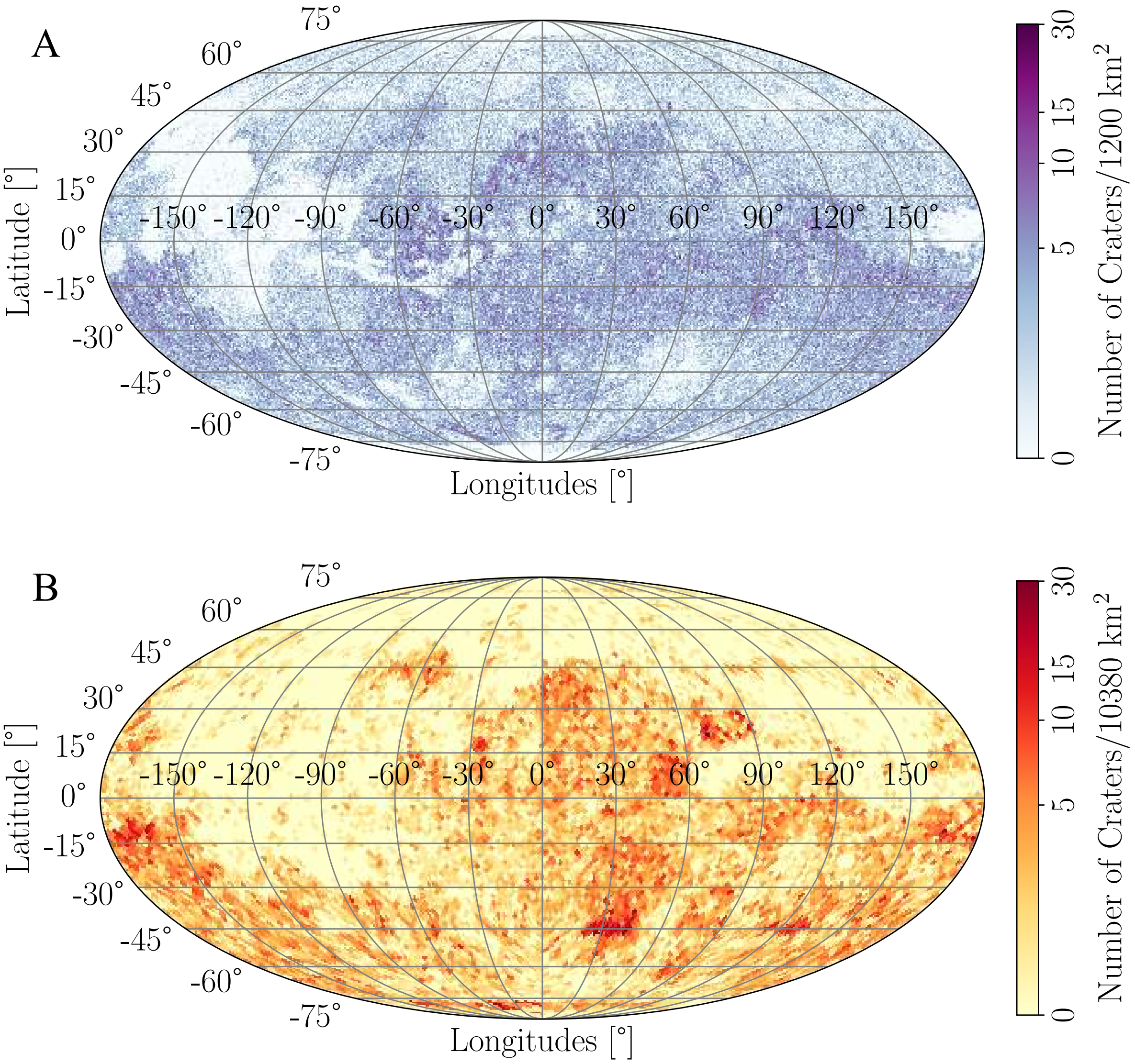

Figure 3.14: Crater density map of (A) All craters classified as 'Valid' by (Lagain et al., 2021a) and (B) the craters classified as 'Burried/Eroded' by (Lagain et al., 2021a). This crater density map is built with healpix polygons of respectively 1200 ^{2} and 10,380km^2 each for (A) and (B).

One other notable contribution of our research lies in the algorithm's ability to differentiate between craters and other circular geomorphic features such as scoria cones. Although our results indicate some success in this regard, we recognize that refining this capability is an ongoing endeavor. In particular, distinguishing craters from calderas remains a challenge that requires further attention and development. In practice, this limitation is not crucial since calderas are very uncommon in the Solar System.

The findings of our study underscore the potential and limitations of employing a Faster-RCNN model for automated crater detection on a planetary scale. The application of this computer vision algorithm has delivered promising results, particularly in its ability to perform well across various latitudes, crater scales, and to distinguish craters from other circular geomorphologic features. However, as illustrated in the inferences shown in Fig. 3.15, the detection process can be compromised when a crater is incomplete within the image frame, excessively eroded, or smaller than the 10-pixel threshold required for detection.

3.7 - Conclusion

The successful development and evaluation of a robust computer vision algorithm for automated crater detection on global scale planet marks a significant achievement in our study. Leveraging a state-of-the-art model, we embarked on a comprehensive assessment of the algorithm's performance across varying latitudes, crater scale and its capacity to discriminate craters from other circular features. The insights gained shed light on both the algorithm's effectiveness and the remaining challenges, propelling us toward valuable avenues of further research and improvement.

Since the algorithm is open-source, future development would be a more comprehensive and fair comparison with other algorithms.

Looking ahead, our work lays the foundation for the development of next-generation algorithms capable of cross-instrument, cross-planetary body, and cross-observation condition crater detection. In conclusion, while our Faster RCNN-based crater detection algorithm represents a significant step forward, it also highlights the complexities and ongoing challenges in the field. Continued research and collaboration are essential for overcoming these challenges and furthering the capabilities of automated crater detection systems.

Data availability

The raw training dataset used for our analysis is available online, as detailed in the publication by Dickson et al. (2024). For further information and access to the dataset, please refer to the following : link.

Additionally, the source code developed for this study will be made publicly available on GitHub open acceptance.

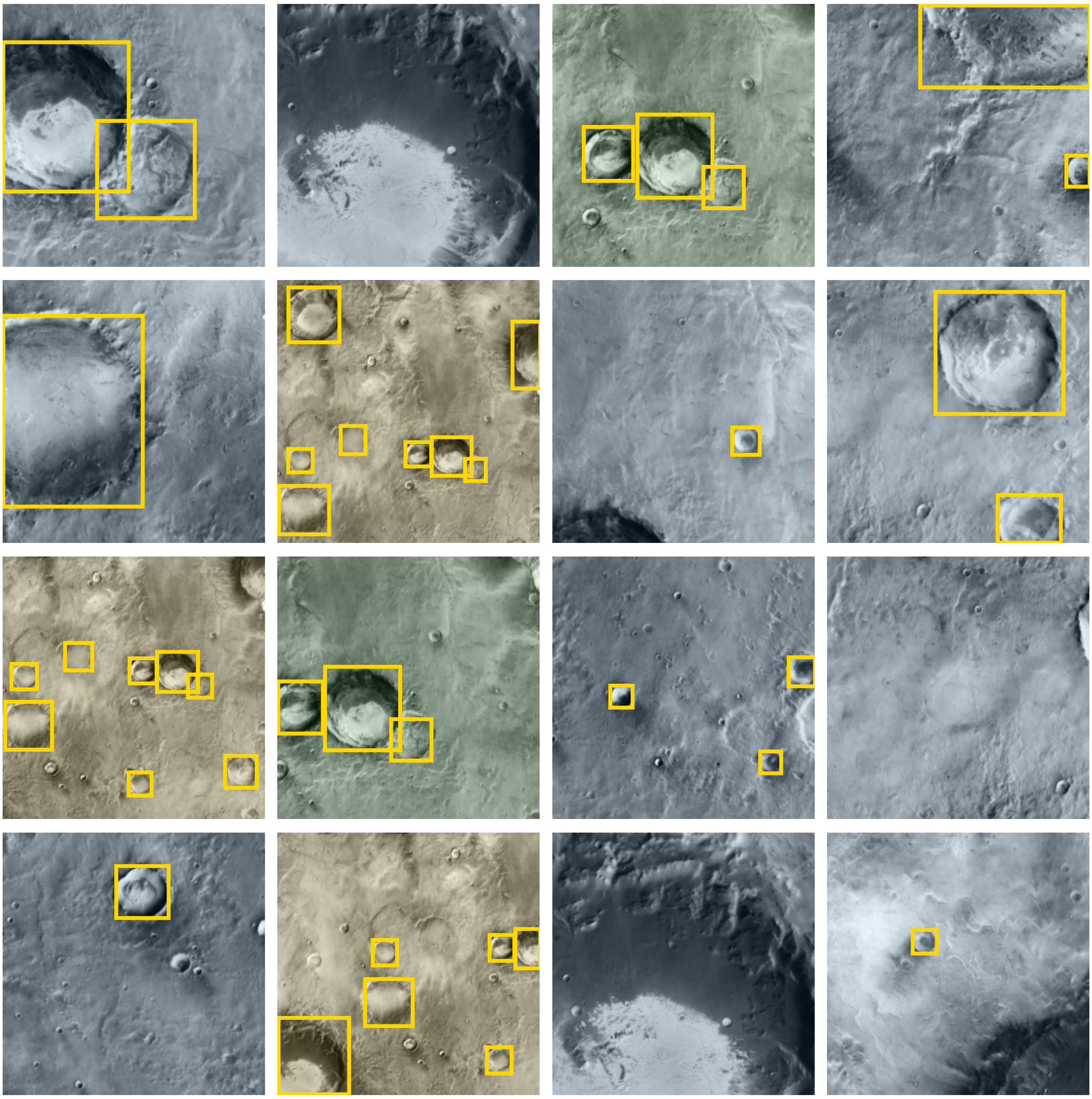

Figure 3.15: Some crater detection inference conducted on CTX images of the Arabia Terra region on Mars, specifically located at 04°W, 08°S. These images were examined at various zoom levels and corresponding downsampled resolutions. Each image patch has a dimension of 224 × 224 pixels. The blue images represent a resolution of 100 meters per pixel (m/px), the green images have a resolution of 200 m/px, and the yellow images are at 400 m/px resolution.

4 - Automatic Crater Classification Using a Deep-learning-based Pipeline[1]

Contents

4.1 Abstract . . . 140
4.2 Introduction . . . 141
4.3 Data . . . 142
  4.3.1 The most complete classified crater database on Mars . . . 142
  4.3.2 CTX V01: A New Global Mosaic . . . 143
4.4 Pre-processing . . . 145
  4.4.1 Crater bounding-box improvement using Hough Circle detection . . . 145
  4.4.2 Data Preparation . . . 146
  4.4.3 System Setup . . . 148
4.5 Method . . . 149
  4.5.1 Classifier . . . 149
  4.5.2 Metrics . . . 149
  4.5.3 Training . . . 151
  4.5.4 Validation . . . 151
4.6 Results and Discussion . . . 152
  4.6.1 Global Performances . . . 152
  4.6.2 Application : Dating and analysis of an Early Amazonian Terrain . . . 153
  4.6.3 Discussion . . . 154
4.7 Conclusion . . . 156

---

[1] The notations used in this chapter may vary from one chapter to another

This chapter corresponds to an article submitted to the *Journal of Geophysical Research: Machine Learning & Computation* on the 14th of April 2025. The first round of review was made on the 14th of November 2025 and it is still under review at the moment I wrote those lines. It was written in collaboration with F. Andrieu[2], F. Schmidt[2,3] and M. S. Bentley[4]. The article is under review with manuscript ID: 2025JH000737.

The morphological classification of craters plays a key role in planetary geology, as it allows distinguishing between primary craters, secondary craters, and degraded or buried structures—each carrying different chronological significance for surface dating. Building on the improved crater database presented in chapter 2, this chapter focuses on the development of a deep-learning-based approach to automatically classify craters according to their geomorphological characteristics. Such classification aims to improve the reliability of crater counts by filtering out features that should not be included in chronological analyses. It is also a part of our automatic pipeline of crater detection and classification described in chapter 6.

We start by describing the preparation of the labelled dataset, including the definition of the morphological classes, the image extraction process, and the annotation strategy (section 4.3). We then present the convolutional neural network (CNN) architecture selected for this task, together with the associated training strategy, loss functions, and optimisation techniques (section 4.4). The evaluation metrics used to assess the model's performance are also discussed. Next, we detail the results of the classification on both the validation and test datasets, highlighting class-specific performance and typical misclassification cases (section 4.6). Finally, we discuss the implications of this classification for crater-based dating methods and propose potential improvements for future work (section 4.6.3).

4.1 - Abstract

Identifying and classifying impact craters on Mars is crucial for understanding the planet's geological history and surface evolution. Traditional crater classification relies on manual annotation methods, which are often limited by human biases and the difficulty of interpreting geomorphological features. Classifying crater is both necessary and challenging. This task is necessary because planetary surfaces ages are estimated by crater density, but some crater types have to be discarded from the analysis to avoid large estimation errors. For instance, secondary impact craters or buried craters should not be counted for a given surface unit. This task is also challenging because all craters have a circular shape and the different crater classes share a lot of common features. In this study, we present a robust deep-learning approach for automated crater classification on Mars. Our method employs a YOLOv11 architecture trained on downsampled (50 m/pixel) images derived from high-resolution Context Camera dataset —ensuring both computational efficiency and large-scale coverage— and a human-made crater database encompassing every crater bigger than 1 km in diameter. Additionally, we incorporate a pre-processing refinement step to reduce false positives and improve classification consistency. We both train and test at the global Martian scale (on separate datasets). Our results demonstrate that the proposed model achieves 76.5 % of accuracy, providing a reliable tool for large-scale planetary sur-

---

[2] Author from Université Paris-Saclay, CNRS UMR8148, GEOPS, Orsay, France

[3] Author from Institut Universitaire de France (IUF), France

[4] Author from European Space Astronomy Centre, Villanueva de la Canada, Madrid, Spain

face analysis. The developed pipeline represents a significant advancement in planetary geosciences by enabling systematic crater classification based on geomorphological features. Our findings contribute to ongoing efforts to automate planetary geomorphology and highlight the potential of deep learning in planetary exploration.

Plain Language Summary

In this work, we developed an AI-based tool to assist planetary scientists in classifying impact craters on Mars. Craters provide valuable insights into the age of planetary surfaces; however, not all craters are suitable for dating, as some are secondary or predate the current surface. Traditionally, distinguishing between crater types has been done manually—a process that is both time-consuming and prone to human error.

Our approach leverages a deep learning model trained on 50km per pixel Martian imagery to automatically classify each crater into one of four categories. The model was evaluated on unseen data from various regions of Mars and achieved an accuracy of 76.5%. Additionally, we enhanced the spatial accuracy of thousands of craters using a shape-detection algorithm, improving the reliability of the dataset.

This tool offers a more efficient and objective method for crater analysis, ultimately contributing to more accurate surface age estimations. Beyond Mars, our approach may be used for automated geological mapping on other planetary bodies, such as the Moon or icy moons like Europa, with further model adaptation and training.

4.2 - Introduction

Impact craters are among the most prominent geomorphological features found on solid planetary surfaces (Leighton et al., 1965). Their morphology, spatial distribution, and degradation states provide crucial insights into the geological history, surface processes, and relative and absolute age of planetary terrains (Neukum et al., 2001; Hartmann et al., 2001). Moreover, crater counting is the only dating method available for planetary surfaces for which a sample return has not yet been achieved. So far, only a few locations on the Moon and two asteroids can be absolutely dated using the radiochronology method. Mars, on the other hand, has been extensively dated by the crate-density method (Neukum et al., 1976c; Benedix et al., 2020). Over the past decades, various automatic crater detection algorithms have been proposed, particularly for Mars. These approaches typically fall into three categories: (1) template matching methods (Salamuniccar et al., 2010), (2) digital terrain model (DTM)-based algorithms using topographic derivatives (Zuo et al., 2016; Chen et al., 2018; Lee et al., 2021; Tao et al., 2021a), and (3) modern machine-learning or deep-learning methods (Benedix et al., 2020; La Grassa et al., 2023; Martinez et al., 2025). Machine learning techniques can also be use to detect other geomorphological features such as ice sheet (Su et al., 2023), pitted cones (Mills et al., 2024) or rockfalls (Bickel et al., 2020). Recently, the application of convolutional neural networks (CNNs) and object detection models has significantly improved crater detection accuracy, particularly when leveraging high-resolution datasets such as CTX V01 Mosaic which provides a 5 m/pixel resolution.

Despite these advances in crater detection, the classification of craters based on their morphological state or origin remains a relatively unexplored area. A notable exception is the work by (Lagain et al., 2021a), who manually classified more than 376,000 Martian craters larger than 1 km into four categories: *regular*, *layered*, *ghost*, and *secondary* craters. However, this classification relied entirely on manual inspection, which is inherently time-consuming, subject to human bias, and difficult to scale. Moreover, studies such as (See et al., 1995) have demonstrated that repetitive tasks like manual annotation lead to performance degradation after only short periods of concentration.

In this study, we introduce the first fully-automated crater classification pipeline based on deep learning, capable of distinguishing crater morphologies using high-resolution CTX imagery. Our approach is built upon the YOLOv11 architecture—a state-of-the-art object detection framework—trained to assign each crater into one of four classes (Lagain et al., 2021a): regular, ghost, layered, and secondary. By incorporating a pre-processing step based on Hough circle detection (Duda et al., 1972) to refine crater bounding boxes, our method enhances the alignment between the visual features and the label annotations, reducing misclassifications.

To the best of our knowledge, this is the first attempt to classify Martian craters using a deep-learning approach, moving beyond detection to enable automated geomorphological interpretation at the planetary scale. Here, we develop a method to only classify the crater and decide not to combine classification and detection to simplify the problem. We evaluate our model's performance using a test set distributed across various quadrangles of Mars at global scale, providing insights into regional variations in classification accuracy. Furthermore, we discuss how such classification could be extended to other planetary bodies and ultimately contribute to more accurate surface dating by filtering out misleading features such as secondary and degraded craters.

4.3 - Data

4.3.1 - The most complete classified crater database on Mars

The Mars Crater Database presented by Lagain et al. (2021a) provides one of the most comprehensive classifications of Martian craters to date. Using imagery predominantly from THEMIS mosaics at a resolution of 100 m/px, this crater database classifies 376,419 Martian craters larger than 1 km in diameter into four distinct categories: *Regular* (noted as *Valid* in the initial database), *Layered*, *Ghost* and *Secondary* craters. It comprises respectively 288,155 *Regular* craters (76.5%), 8,445 *Layered* craters(2.3%), 24,530 *Ghost* craters (6.5%), and 55,309 *Secondary* craters (14.7%), highlighting the diverse morphologies present on the Martian surface. In this study, we adopt the terminology "*regular*" to refer to ordinary craters, consistent with their classification. In this work there is no question about the validity of the crater (detected or not): all objects are truly craters and the purpose of the tool is to classify them. This comprehensive classification facilitates refined analyses, such as surface age dating, by clearly delineating morphological characteristics across a wide range of crater sizes and types.

Each of the crater categories present in the Lagain et al. (2021a) is further defined below:

1. Secondary: Crater formed by the ejecta of a primary impact event. Secondary craters tend to be aligned radially around a primary crater. They are characterized by a much smaller size than the primary crater. Their shape can be more irregular compared to primary craters because of

lower impact velocities. Several studies have explored this subject (Quantin et al., 2016; Robbins et al., 2011a; Robbins et al., 2011b). The authors state that secondary craters should not be considered in the dating process, as their formation is not directly related to the primary impact flux and can lead to an overestimation of surface ages.

2. Ghost craters: Primary craters that are characterized by significant degradation and are partially or completely buried, distinguishing them from eroded craters (Robert A. Craddock, 1997). Importantly, as secondary craters, they shall not be considered in dating processes, as their formation predates the surface being dated.
3. Layered: Primary impact craters, which present a continuous rampart of ejectas blanket. They are characterized by fluidized ejecta patterns around the crater, suggesting that the material had a mud-like flow during impact (Costard, 1989; Barlow et al., 2000)
4. Regular: Craters categorized as regular are the ones which could not be assigned to any of the three previous categories (assigned as "Valid" in the initial Lagain database).

It is important to note that a minimum crater size was arbitrarily set through manual inspection (Lagain et al., 2021a). Consequently, threshold issues may arise near the 1 km limit. Because the labeling was done manually, some craters slightly larger than 1 km may be missing from the database, while others slightly smaller than 1 km might be included. To address this issue, we filter the database to only keep craters with diameters greater than 1.2 km.

Other possible crater classes Another common morphological classification which can be made is the distinction between *simple* and *complex* craters based on their structural features. Complex craters are generally defined by the presence of central peaks, terraced walls, or flat floors, while simple craters lack these features and typically exhibit a typical bowl-shaped morphology (Cintala, 1977; Cintala et al., 1998; Kalynn et al., 2013; Pike, 1980; Baker et al., 2011; Robbins et al., 2012).

In this study, we deliberately chose not to include this distinction. Indeed, identifying simple and complex craters does not necessitate sophisticated deep-learning techniques. Furthermore, complex craters are not numerous since only the largest craters have these characteristics (Herrick et al., 1998; Chandnani et al., 2019). They may very easily manually checked by geomorphologist. On Mars, the transition between simple and complex craters occurs at diameters between about 3 and 8 km (Pike, 1980; Croft, 1985). Furthermore, integrating such a classification would add unnecessary complexity, as craters categorized as *Regular* or *Layered* could simultaneously belong to either the simple or complex morphological types, complicating the training and evaluation of our deep-learning model, while being useless for dating purposes.

4.3.2 - CTX V01: A New Global Mosaic

The CTX V01 Mosaic is the latest version of the global mosaic compiled by the Bruce Murray laboratory from images captured by the CTX instrument aboard the Mars Reconnaissance Orbiter (MRO) (Malin et al., 2007; Dickson et al., 2024)[5]. It encompasses more than 100,000 individual

---

[5] `https://murray-lab.caltech.edu/CTX/tiles/`

panchromatic image patches, which have been combined to create a mosaic with a total size of 5.7 trillion pixels, covering 99.5% of Mars from 88°N to 88°S. For practical reasons, the Bruce Murray Laboratory team reprojected the mosaic into an equirectangular projection and divided it into 3,960 tiles, each covering an area of 4° × 4°.

For the purpose of this study and the previous one about crater detection (Martinez et al., 2025), we excluded the polar ice sheets and seasonal caps by using only the tiles between 80°N and 80°S. Additionally, since the smallest crater in the database is 1 km in diameter, we automatically down-sampled the tiles to a resolution of 50 m/px to avoid detecting craters that smaller than the ground truth database (1km in diameter).

Quadrangle repartition At this stage, we had 3,600 image tiles at a resolution of 50 m/px. The next step was to ensure that all craters retained their circular shape. Indeed, with the native projection of the mosaic, the higher the latitude is, the more craters will appear with an oval shape. To correct this distortion, we reprojected the tiles — as done in our previous study (Martinez et al., 2025) — into a local stereographic projection centered at the midpoint of each tile. One issue encountered during this processing step is that a 4° × 4° tile in the polar regions covers a significantly smaller surface area than at the equator. Also the numerous tiles boundaries in the polar areas could create difficulties when learning and merging all results. In order to avoid this effect, we decided to merge adjacent tiles in the mid/high latitude regions to create larger "quadrangles", ensuring a more consistent coverage. The table 4.1 shows the quadrangle size and surface with respect to the latitude range ; Fig. 4.1 shows the selected quadrangle grid merged from CTX Tiles.

Latitude range	Quadrangle size	Surface [Km^2]
80° - 64°	16° × 40°	689 884
64° - 52°	12° × 20°	444 276
52° - 40°	12° × 12°	349 434
40° - 32°	8° × 8°	181 055
32° - 24°	8° × 8°	197 601
24° - 16°	8° × 8°	210 300
16° - 8°	8° × 8°	218 906
8° - 0°	8° × 8°	223 251

Table 4.1: Definition of the quadrangle as a function of latitude (applied to both North and South latitudes). The surface represent the image surface once projected in local stereographic projection, to avoid projection distortion.

The next step was to split our global, reprojected dataset into three distinct subsets. As is standard in deep learning workflows, we required one subset for training, another for validation (to monitor the training process), and a third for testing, which is used exclusively to evaluate the model's final performance. The latter is never used during training and is therefore ideally suited for a fair and unbiased assessment. We divided the dataset into training (70%), validation (15%), and test (15%)

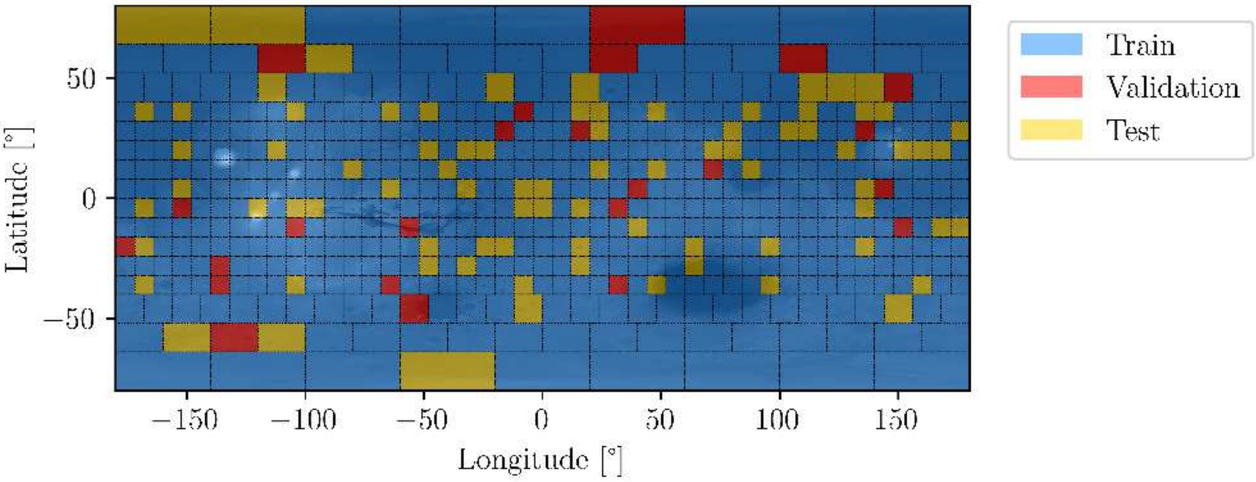

Figure 4.1: Definition of the quadrangle and their attribution for the Train, Validation and Test subsets. The partitioning was performed randomly for the training and validation subsets, ensuring that latitude, illumination, and geological diversity were equally represented, following a stratified approach. The test subset was also composed of randomly selected tiles, but not exclusively: we deliberately included tiles that have been extensively studied in the literature, most of which cover well-known landing sites and thus serve as valuable reference areas for comparison (Quantin-Nataf et al., 2021; Parker et al., 2010; Hynek et al., 2017).

4.4 - Pre-processing

4.4.1 - Crater bounding-box improvement using Hough Circle detection

In order to verify the precision of the ground truth database, we examined several images. As seen in Fig. 4.2, the localisation and radius of craters which are registered in the ground truth database (green circles) do not perfectly overlap the crater seen in the image. We observe that the craters are often shifted in an apparently random direction and that this difference becomes more significant as the size of the crater. One plausible explanation for these shifts is the errors and uncertainties on the initial THEMIS mosaic dataset in comparison with our CTX dataset. Another possibility may be uncertainties in the crater position and size from Lagain et al. (2021a), initially from Robbins et al. (2012), simply because they were done manually.

In 2, we propose a pre-processing step based on the Hough algorithm (Hough, 1962; Duda et al., 1972) that improves the match between the crater database center and size and the actual image. This step is designed to build a more precise ground truth database, which will enable us to achieve the goal of 0.77 in accuracy obtain by ultralytics in their classification performance benchmark on ImageNet Large Scale Visual Recognition Challenge (`https://docs.ultralytics.com/fr/tasks/classify/#models`).

4.4.2 - Data Preparation

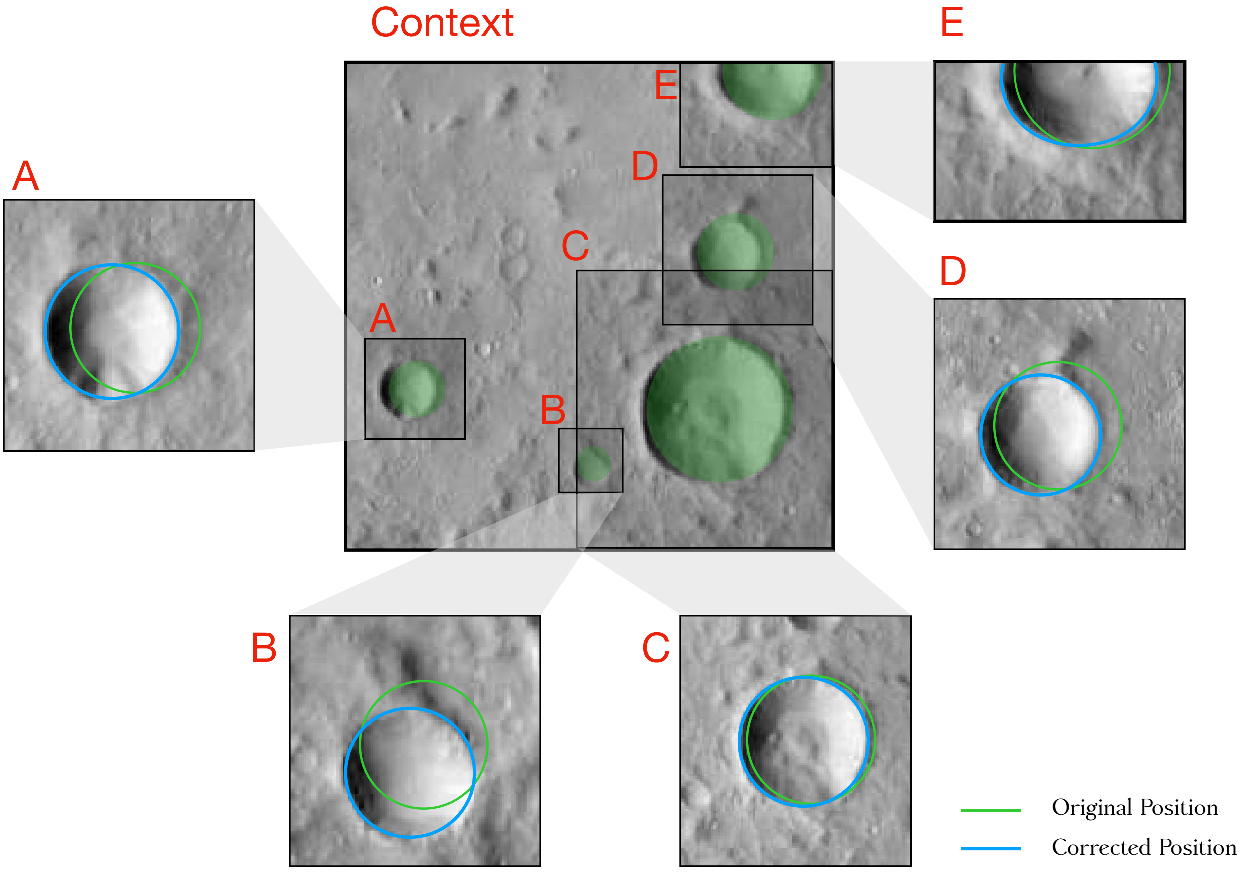

Figure 4.2: Initial crater database (Lagain et al., 2021a) in green superposed with CTX images of Mars. The position and radius are nearly correct but an improvement is required. The original position appear in green and the improved position appear in blue.

For each crater listed in the ground truth database, we extracted a square image patch from the corresponding CTX tile. The size of each patch was set to four times the crater radius and centered on the crater's coordinates. These patches were then saved into folders corresponding to their crater class.

Subdataset: coherent crater class and size sampling Due to the very large number of craters in the global database (376,419 entries) and the highly heterogeneous crater repartition through the different classes (described in 4.3.1). In order to balance the different classes to increase the robustness of the learning process we limited our selection to a balanced subset of approximately 20% of the total dataset (see 4.2).

This new dataset will be called the "subdataset". Tab. 4.2 illustrates the total number of crater image patches we have in the training, test and validation databases for each category and in total. This sampling allowed for a more efficient training phase and ensured that each class was equally represented to avoid class imbalance during model learning. This sampling strategy significantly improved training efficiency while preserving diversity across classes. However, due to the strict requirement of balancing the dataset across all classes, the requested number of craters per class occasionally exceeded the available entries in the original dataset—especially for *Layered* crater classes. As a result, the final proportions may slightly differ from the ideal theoretical distribution. Nevertheless, our selected subdataset maintains a realistic distribution of crater sizes, as confirmed by its alignment with the Cumulative Crater Frequency Distribution Curve (CFDC), shown in Fig. 4.3.

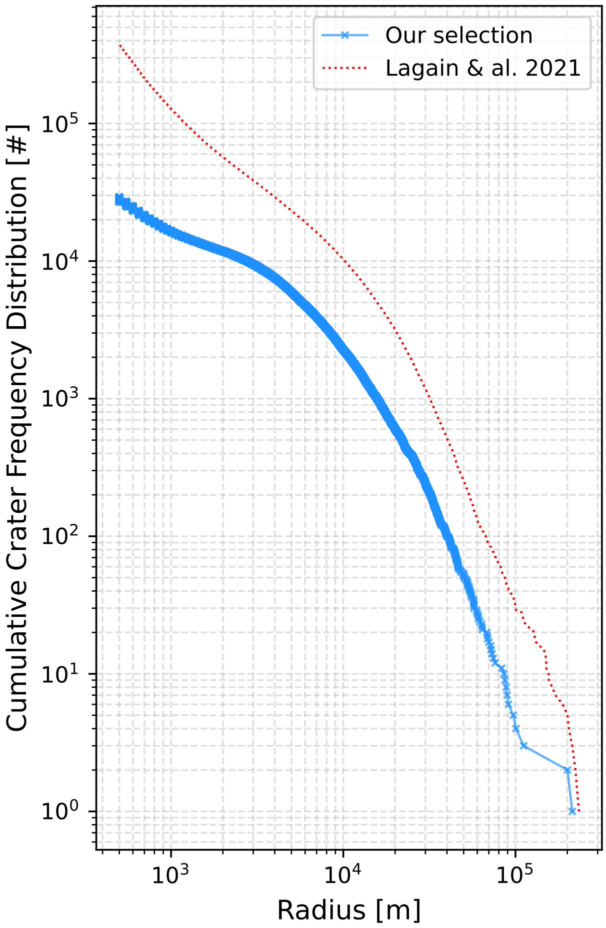

Figure 4.3: Cumulative Crater Frequency Distribution Curve of our training dataset compared to the full crater database.

We had to limit our training dataset to a smaller subset to equally represented classes. In order to be able to use a sufficiently large model, we now want to increase the size of our subdataset, ensuring the best accuracy as possible and to prevent overfitting, we applied two systematic data augmentation strategies.

Data augmentation to increase the total number of images For each image patch, we generated seven additional versions by applying a series of geometric transformations: rotations of 90°, 180°, and 270°, as well as horizontal and vertical flips of both the original image and the 90°-rotated image. These operations were chosen because, due to the circular nature of craters, they preserve the relevant features while introducing diversity in illumination and orientation. With this approach referenced in Tab. 4.2, every original image comes with a total of 8 augmented images, effectively expanding the dataset size and enabling the use of deeper classification models.

This augmentation strategy was deliberately limited to this complete but minimal set, as it already covers all combinations of rotations and flips, making further transformations redundant. It was only also done for the train and validation dataset since we wanted the test dataset to obey to realistic condition so the test dataset encompass all craters of the Lagain et al. (2021a) dataset present in the test area.

Data augmentation to increase robustness The YOLO pipeline includes a comprehensive series of data transformations that are crucial for enhancing both the robustness and performance of the model. These transformations introduce variability into the training data, allowing the model to better generalize to unseen examples and reducing the risk of overfitting (Aquino et al., 2017).

To build a more reliable classifier, we applied a diverse set of augmentations that simulate various image dynamics, such as changes in contrast, brightness, and noise. These augmentations help the model learn more invariant features and improve its ability to handle real-world variations.

For example, real images may contain pixels flagged as "no data", often resulting from gaps in observation during the mosaicking process. To account for this and train a model resilient to such artifacts, we introduced a data augmentation step that randomly adds black patches to training images, simulating missing data in a controlled way.

	Regular	Ghost	Secondary	Layered	**Total**	**Total augmented**
Lagain et al.	288 155	24 530	55 309	8 445	376 419	—
Train	7 000	7 000	7 000	6 729	27 729	221 832
Validation	1 500	1 500	1 500	1 250	5 770	46 160
Test (from Lagain et al.)	35 166	3 373	6 563	1 270	46 372	—

Table 4.2: Total number of crater images in the initial database and in our subdataset used to train, evaluate and test the model.

4.4.3 - System Setup

In this study, we parallelized the training on 8 NVIDIA GeForce GTX TITAN X GPU boards. The GPUs are installed within a single server equipped with two Intel Xeon E5-2690 v4 @ 2.60GHz 28 core processors and 756 GB of RAM. The server ran Ubuntu 20.04.6 LTS. A Python environment containing TensorBoard (version 2.17.0), PyTorch (Paszke et al., 2019) (version 1.13.1), and Ultralytics (Jocher et al., 2025) (version 8.3.79) was used to implement, train, and visualize the networks. The typical computation time for training is 3.6 minutes per epoch with 417 batches of a 512 images batch size (Fig 4.5 and 4.6) and 12 ms for a batch of 4 images at inference on CPU.

4.5 - Method

4.5.1 - Classifier

We chose to use the classification model of the YOLO-v11 medium-sized architecture. Yolov11 is the lastest model in the YOLO series. It was presented in September 2024 at the YOLO Vision conference YV24. The network architecture, presented in fig 4.4, introduces a number of improvements compared to previous versions such as C3K2 blocks (Cross Stage Partial with kernel size 2), SPFF (Spatial Pyramid Pooling Fast), and advanced attention mechanisms like C2PSA (Convolutional block with Parallel Spatial Attention) which contribute to improved model performances in several ways, such as enhanced feature extraction (Khanam et al., 2024).

The loss function used in the YOLOv11 model in the classification task is a cross entropy loss function. This component measures the divergence between predicted class probabilities and the ground truth labels. It is based on cross-entropy principles, which are effective for classification tasks by penalizing incorrect class predictions and rewarding correct ones (He et al., 2024).

At inference, this classifier proposes a score for each class and the class is attributed to the highest class score.

Several studies have demonstrated that while increasing the model size beyond the medium variant can lead to marginal gains in precision, these gains come at a significant computational cost. For instance, Jegham et al. (2025) showed that larger models yield diminishing returns in accuracy improvements compared to the substantial increase in inference time and resource consumption. Consequently, we determined empirically that the medium model provides the best trade-off between accuracy and speed, making it ideally suited for our application.

These improvements are particularly relevant for crater classification, where objects are small, low-contrast, and morphologically diverse. The enhanced feature fusion and attention mechanisms of YOLOv11 allow the model to better capture subtle rim and ejecta morphologies, while the multi-scale detection architecture ensures robustness across a wide range of crater sizes and illumination conditions. Furthermore, the improved training stability and regularization strategies make YOLOv11 well suited to the limited and heterogeneous labeled datasets typical of planetary imagery.

4.5.2 - Metrics

The metric used during the evaluation and testing included is the common classification metrics call: accuracy.

$$\text{Accuracy} = \frac{\text{Correct predictions}}{\text{All predictions}} \tag{4.1}$$

As described in equation 4.1, accuracy refers to the percentage of correct predictions among all predictions. In order to explain how the accuracy score is calculated, let's consider a region with 4 classes of craters and the associated predictions. We then divide all correct predictions by the total number of predictions.

To have a better insight into the model's intra-class error, we also calculate a confusion matrix. This diagnostic tools provides a detailed estimation of the model's performance by showing the rate of true positives with respect to misclassified identifications. This helps assess misclassification patterns

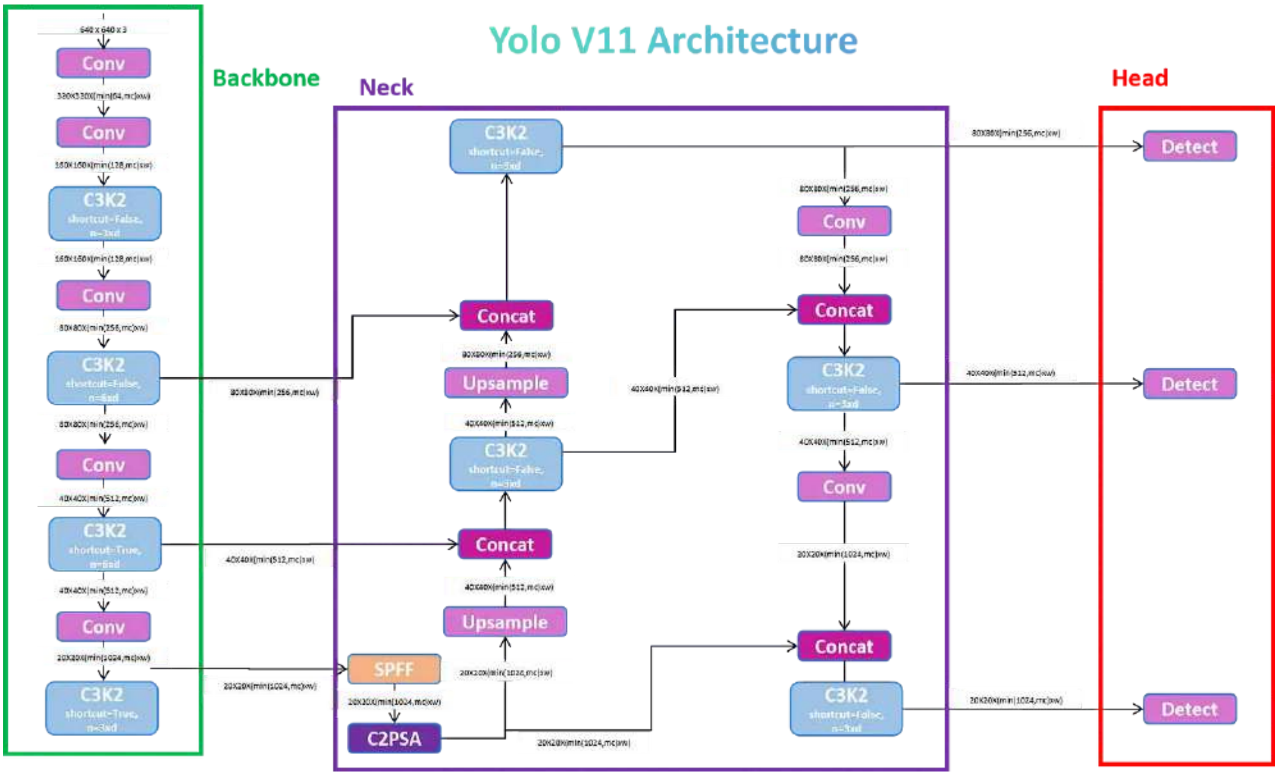

Figure 4.4: Yolov11 architecture as presented by S. Nikhileswara Rao on https://medium.com/@nikhil-rao-20/yolov11-explained-next-level-object-detection-with-enhanced-speed-and-accuracy- and as resumed from Khanam et al. (2024).

and overall classification reliability. The confusion matrix summarizes the performance of the classifier by comparing predicted and true labels. Each row corresponds to the actual crater class, and each column to the predicted class. Values along the diagonal represent correctly classified samples, while off-diagonal entries indicate misclassifications between classes (e.g., a regular crater predicted as secondary). This structure allows direct visualization of which classes are most frequently confused and forms the basis for computing derived metrics such as accuracy, precision, and recall.

4.5.3 - Training

During the training process, the model was trained from scratch (random initialization of the weight) for 31 epochs, incorporating a learning rate warmup over the initial 5 epochs, followed by a cosine learning rate decay, as shown in Figure 4.5. This strategy is designed to enhance model convergence and performance.

Learning Rate Warmup : The warmup phase gradually increases the learning rate from a lower starting value to the initial target learning rate over the first 5 epochs. This approach helps stabilize the training process and prevents issues like unstable updates or divergence early in training (Goyal et al., 2018; Kalra et al., 2024).

Cosine Learning Rate Decay : After the warmup phase, a cosine annealing schedule is applied to decrease the learning rate smoothly over the remaining epochs. This method reduces the learning rate following a cosine curve, which allows the model to make finer adjustments to the weights as training progresses, potentially leading to better generalization and performance. The cosine decay strategy is known for its effectiveness in achieving smoother transitions in learning rates compared to linear decay methods (Gotmare et al., 2018).

The combination of these techniques—learning rate warmup and cosine decay—result in an optimized training process by initially allowing large updates for rapid learning and gradually refining the model parameters for improved accuracy and stability.

During the learning phase we set the batch size to 512, to improve the computational efficiency and stabilizing the training process. The batch size value is a crucial hyperparameter. Indeed, from our experience larger batch sizes can lead to more accurate gradient estimates, facilitating smoother convergence and this value is the maximum possible with our GPU architecture.

We also implemented a Multi-Scale Training: The model was trained on images of varying sizes, improving its robustness to objects at different scales. This approach randomly resizes input images during training, helping the model generalize better across diverse object dimensions.

4.5.4 - Validation

At the end of each training epoch, after the model has processed the entire training dataset, it evaluates its performance by calculating the top-1 accuracy on the validation dataset. This evaluation allows us to monitor the learning progress, as depicted in Figure 4.6.

4.6 - Results and Discussion

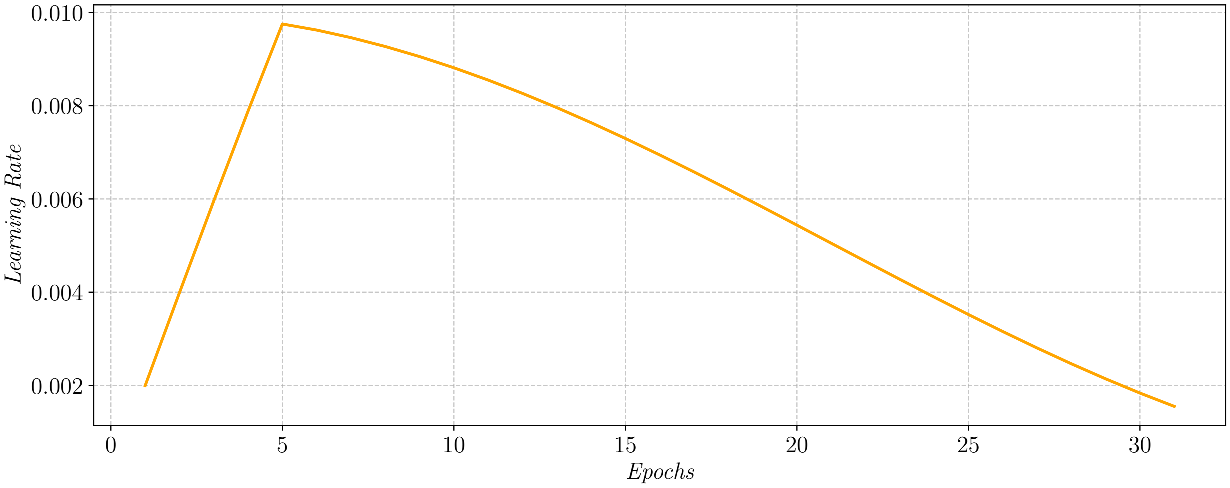

Figure 4.5: Learning rate variations used during training

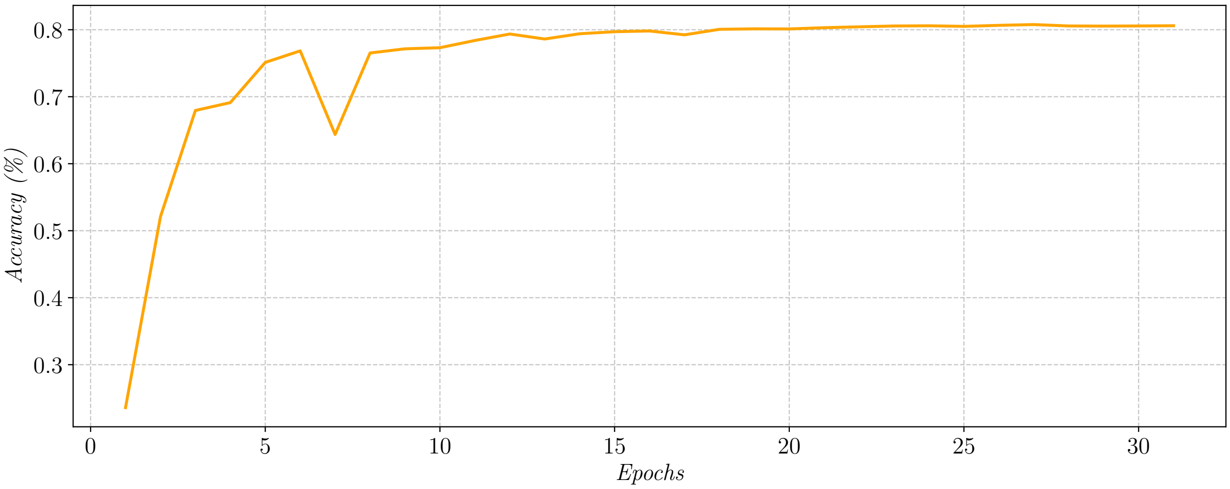

Figure 4.6: Validation accuracy with respect to learning epochs

4.6.1 - Global Performances

After training, we use our subdataset to test the model on images never seen before. We then measure the confusion matrix, as shown in Figure 4.7.

The distribution of correct and incorrect classifications reflects the trends seen during validation, reinforcing the reliability of our trained model. This consistency suggests that the model has effectively generalized to unseen data, with minimal overfitting or unexpected deviations.

We conducted an evaluation of our trained model across all quadrangle regions present in the test dataset, resulting in the accuracy map shown in Figure 4.8. This geographical testing is critical as it allows us to assess the spatial consistency and robustness of the classifier across diverse terrains,

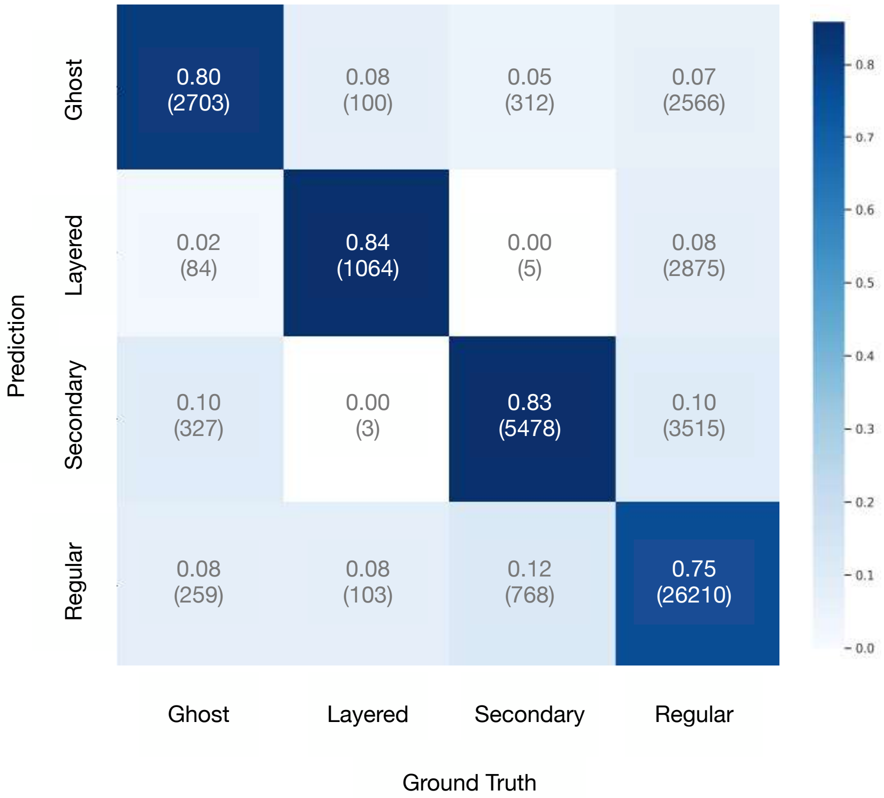

Figure 4.7: Confusion matrix made on the test subdataset. These results show for instance that 80% of true Ghost crater — 2703 craters — were correctly classified, and 2% of them (84 craters) where misclassified as Layered. Overall, the performance is excellent. The regular crater appears slightly more difficult to classify, most probably due to human misclassification (see section 4.6.3)

illumination conditions, and morphological features. By analyzing accuracy at the quadrangle scale, we can detect potential biases due to the latitude.

4.6.2 - Application : Dating and analysis of an Early Amazonian Terrain

The Zhurong rover, part of the Tianwen-1 mission, landed on 14^{th} May 2021 in southern Utopia Planitia (25.066° N, 109.925° E) within the Amazonian lowlands of Mars. This region is characterized by relatively smooth terrains, interpreted as resurfaced plains, with a sparse population of large craters but abundant small features such as secondary craters and pitted cones. Previous studies based on crater size–frequency distribution (CSFD) analysis have suggested resurfacing ages ranging from early to middle Amazonian, with significant variability depending on the chosen count area and interpretation of crater morphologies (Tanaka et al., 2014). Our study about crater retention age is part of a broader geological analysis of this region (Zhang et al., 2025).

In our analysis, we applied our deep-learning–based detection and geomorphological classification

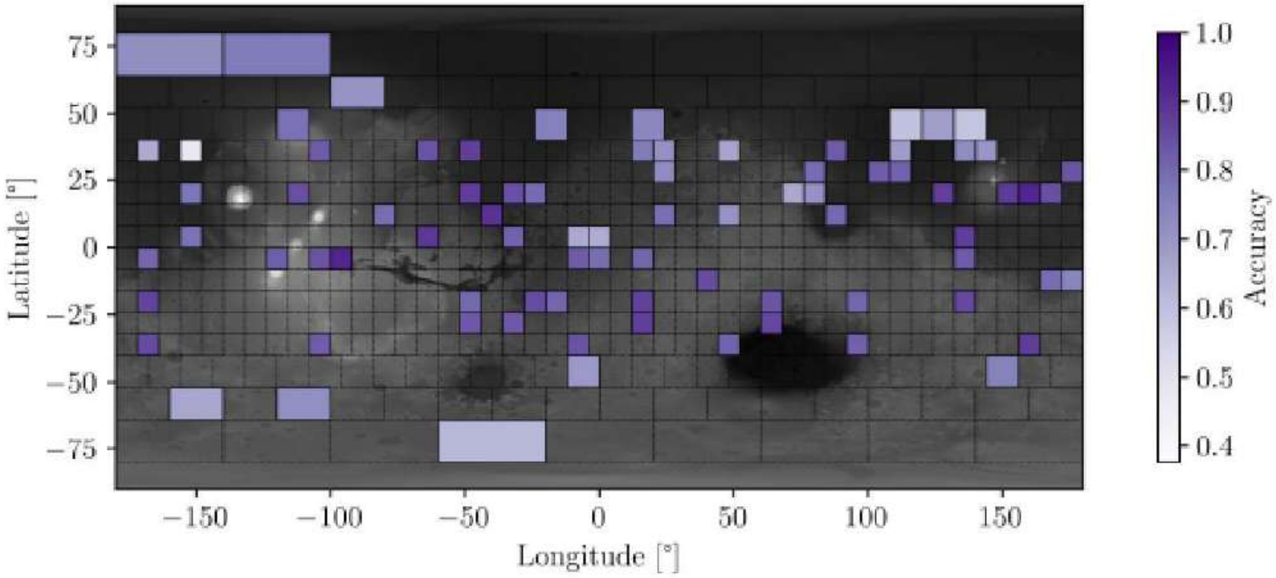

Figure 4.8: Global accuracy on each quadrangle of the test database which contain 46,372 craters as describe in Tab. 4.2

pipeline (Martinez et al., 2025). We restricted the count area to the CTX quadrangle presented in Fig. 4.9, focusing on craters with diameters above 100 m to ensure robust detection and minimize classification uncertainties. The resulting inference map is presented in Fig. 4.9. The cumulative CSFD curve shown in Fig. 4.10b was fitted using the (Hartmann, 2005) chronology model to estimate the model surface age.

Our CSFD for Zhurong's surroundings yields to an over-estimation in comparison to manual counting (Zhang et al., 2025) when using all detected crater (see Fig. 4.10a). When filtering out *Secondary* and *Ghost* crater, this effect is significantly decreased and the density curve better follows the theoretical curve (see Fig. 4.10b).

The absolute model age $\sim 3.04\ ^{+0.087}_{-0.11} Gy$ (Early Amazonian) we estimate is consistent with the lower end of the range proposed by Wu et al. (2022), who reported ages $\sim 3.01\ ^{+0.23}_{-0.47} Gy$ on a manually crater counted analysis. Notably, our results reinforce the interpretation that the plains in southern Utopia Planitia underwent significant resurfacing during the Amazonian, most likely through processes such as mud volcanism, ice-related sediment mobilization and volcanic flooding, which effectively reset the small-crater population while preserving larger, older impact structures.

4.6.3 - Discussion

Performance As shown in Fig. 4.8, some regions present a significantly lower accuracy scores compared to others. For instance, in the area between 108° and 120°E longitude and 40° to 52°N latitude, the accuracy drops to around 0.598. In this region, where we can count 233 *Regular* craters, 40 *Secondary*, 18 *Layered* and 18 *Ghost*, many craters were classified as *Ghost* when they actually appear to be *Regular*. Indeed, in Fig. 4.11, on the first line, three out of four craters which were classified as ghost do not clearly exhibit characteristics typical of ghost craters. Their classification as ghost

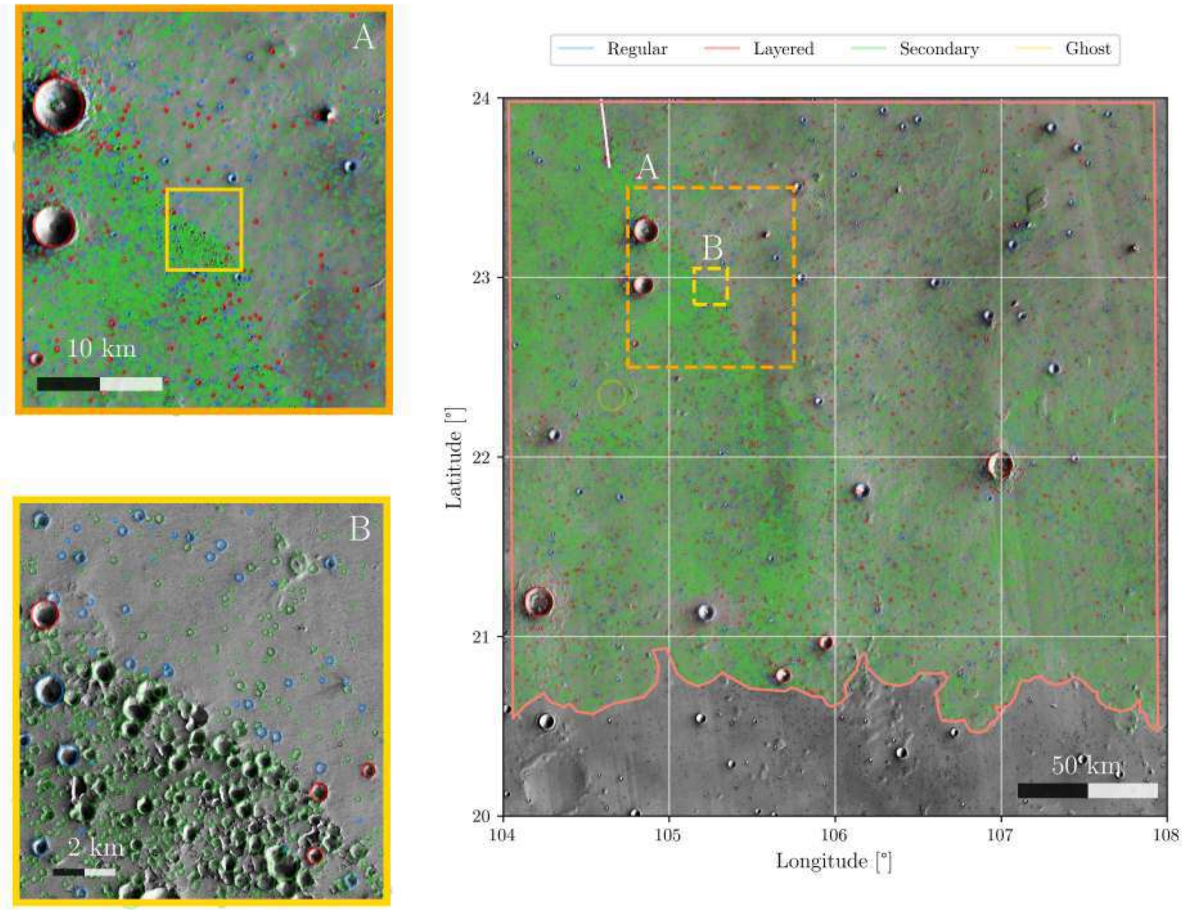

Figure 4.9: Inferences made in a 4° × 4° quadrangle in Utopia Planitia (in equi-rectangular projection, lower right coordinate : 20°N, 104°E). All craters have been detection using Martinez et al. (2025). Blue squares represent the *Regular* and *Layered* craters classified by our algorithm, that are kept for surface datation. Orange squares represent *Secondary*, and *Ghost* craters, removed from the datation. The A and B zones are zoomed area.

crater is subject to human interpretation. Moreover, the original crater classification database (Lagain et al., 2021a), was done manually by more than 60 different human operators. In the light of this, we interpret these quadrangles with a notably low score as due to "outliers" in human classification.

We can also see in Fig. 4.8, that certain regions exhibit notably higher classification accuracies, such as the quadrangle defined by longitudes -100° to -92°E and latitudes 0° to 8°S, where the accuracy reaches 0.924 (see Fig. 4.12). In this quadrangle, Lagain and his collaborators identified 185 *Regular* craters, 10 *Layered* craters, 4 *Ghost* craters, and no *Secondary* craters. The exceptional performances observed here is largely attributed to the predominance of *Regular* craters, which constitute 93% of the craters in this region. Furthermore, among the predictions made for this crater class, 93% were correctly identified as *Regular* craters.

While a manually classified global catalog (Lagain et al., 2021a) already exists, its resolution is limited to craters larger than ∼1 km and was generated through time-consuming visual inspection. The present work provides a complementary, automated solution capable of classifying approximately six craters per second, including those smaller than 1 km, with consistent accuracy and reproducibility. This new capability greatly accelerates crater-based geological analyses and extends the accessible size range for age estimation, thereby enhancing our understanding of surface evolution on Mars and other planetary bodies.

Sources of apparent errors and regional variability Beyond isolated labeling inconsistencies, a substantial fraction of the apparent "errors" reflects geomorphological under-determination: for degraded rims, layered ejecta, or clustered small craters, multiple labels can be reasonably defended by experts, which makes the decision boundary inherently fuzzy. In our experiments we did not observe a consistent, dataset-wide penalty attributable to class imbalance, image quality, shadowing, or topography once the stratified split and standard augmentations were applied. Accuracy drops in the lowest-performing quadrangles are not driven by a single cause, but rather by local combinations of resurfacing history and low-contrast textures that increase ambiguity. One clear failure issue, however, is the presence of missing-data areas in the CTX mosaics (pixels flagged as no-data), which can induce spurious assignments; this behavior is consistent with our robustness tests and with the explicit augmentation that injects black patches. Altogether, these effects confirm that the classifier can be regarded as a robust quick and first-level filtering tool, while manual validation remains advisable for high-precision dating studies, particularly in geologically complex regions.

Discussion about application Although the classifier achieves overall accuracies between 75% and 84% (Fig. 4.7), the confusion matrix reveals class-dependent misclassifications that may influence crater count–based age estimations. For instance, in the context of dating analyses, the objective is to remove secondary and ghost craters. Misclassifications between regular and secondary or ghost craters can therefore lead to minor under/over-estimation of crater densities. However, as shown in previous section and Fig. 4.10b, these misclassifications have only a limited effect on the crater density and on the resulting age estimate.

4.7 - Conclusion

In this study, we presented an innovative deep-learning approach using the YOLOv11 architecture for automatic crater classification on Mars. Our methodology use high-resolution imagery from the Mars Reconnaissance Orbiter's CTX camera and a refined crater database. The classification targeted four geomorphological crater categories defined by Lagain et al. (2021a): *regular*, *ghost*, *layered*, and *secondary*. A notable pre-processing step using Hough Circle detection significantly enhanced the alignment between the ground truth and observed crater features, improving the quality and reliability of the classification model.

The proposed YOLOv11-based model achieved a robust overall accuracy of 76.5%, demonstrating its capability to reliably classify various crater types on a planetary scale. We observed, however, geographic variations in accuracy, particularly noticeable in the latitudes ranges 40° to 52°N and longitudes 108° to 120°E, highlighting areas requiring further refinement and analysis.

Our methodology sets a precedent for fully automated planetary surface analyzes, significantly reduces human subjectivity and saves time compared to manual annotation techniques traditionally used in planetary geomorphology. This automated classification not only accelerates the process but also provides consistent and reproducible results that can be systematically applied to large datasets.

To go further with the capabilities of this classification tool, several ideas might be developed in the future. One possibility would be to apply our model to lunar craters. Due to significant geomorphological differences between the lunar and martian surfaces, applying the model to the Moon may require additional targeted training, particularly for small craters. As illustrated in Fig. 4.13, *regular* lunar craters display different morphological characteristics compared to those on Mars. The absence of atmosphere and the effects of space weathering on the Moon result in much smoother, more eroded and diffuse crater rims. The typical bowl-shaped morphology is often less defined, and a specific configuration should be developed, either by training with supplementary data, or by creating a new class.

Similarly, exploring the model's applicability to other planetary bodies such as Mercury or icy moons like Europa and Enceladus would further demonstrate the robustness and versatility of our deep-learning pipeline. Such expansion may require the usage of customized datasets that we will only have after the first light from the Europa Clipper and JUICE missions. Unfortunately, no existing ground truth database are available to assess the performance of our model.

Additionally, the use of transfer learning techniques could substantially help to adapt our model to different crater databases and imaging sources.

Lastly, an exciting potential future application of our methodology lies in refining planetary surface dating techniques. By accurately identifying and excluding secondary and ghost craters, which tend to bias crater density measurements, our automated classification approach could lead to more precise age determinations, thereby substantially advancing our understanding of planetary geological chronologies.

In conclusion, our deep-learning-based automatic crater classification algorithm represents a major advancement in planetary geosciences, providing a powerful tool to systematically characterize planetary surfaces. The continued refinement and expansion of this approach hold considerable promise for improving our understanding of the geological history and evolution of Mars and other planetary bodies.

Data availability

The raw image dataset used for our analysis is available online, as detailed in the publication by (Dickson et al., 2024). For further information and access to the dataset, please refer to the following : `https://murray-lab.caltech.edu/CTX/tiles/`. The crater database used for this study is available to the following Github project: `https://github.com/alagain/martian_crater_database.git`.

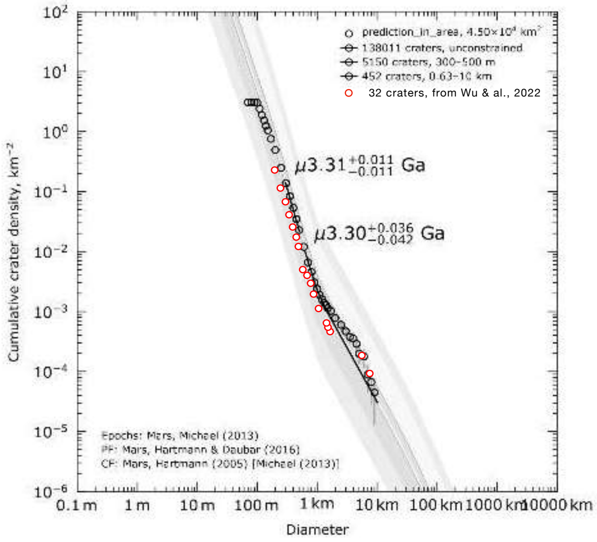

(a) Crater size–frequency distribution (CSFD) and age determination derived using our crater detection algorithm presented in Martinez et al. (2025) in comparison with Wu et al. (2022) (Red dots) in a neighboring region near the Zhurong landing site. Between 2 and 10 km diameter, the data are not fitting the model age and the density is systematically higher than Wu et al. (2022).

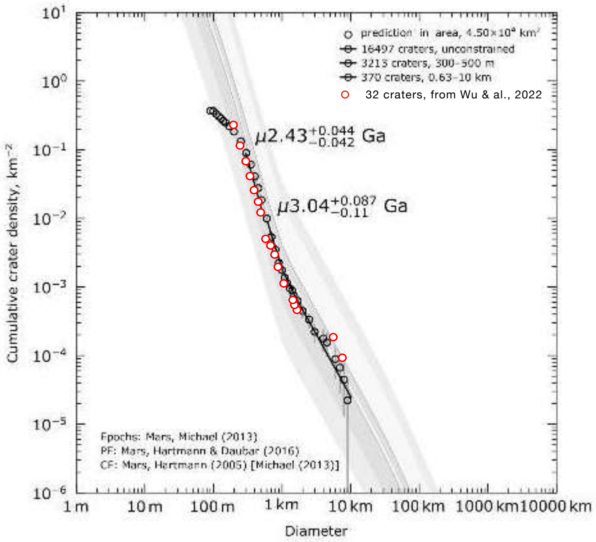

(b) Same as Fig. 4.10a except that neither *ghost* nor *secondary* craters, as detected by our algorithm are included. The crater density here is close to Wu et al. (2022) (Red dots) and the over-density between 2 and 10 km diameter disappears.

Figure 4.10: Comparison between crater count–derived ages obtained in the geological unit define in Fig. Fig. 4.9 before (a) and after (b) geomorphological classes filtering.

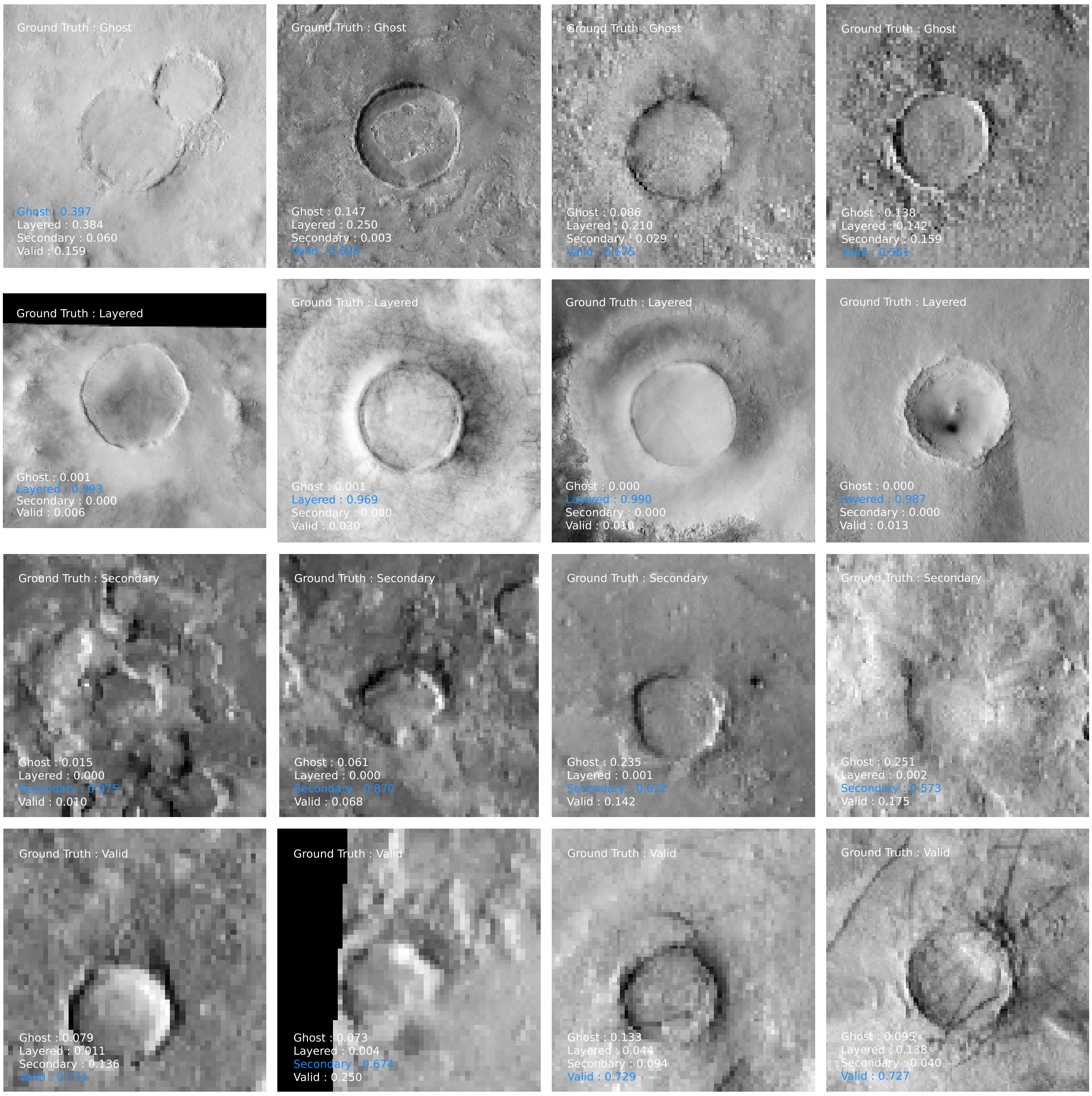

Figure 4.11: Illustration of the lowest accuracy case. Example of 16 crater present in a test area between 108° and 120°E longitude and 40° to 52°N latitude, which were, from top to bottom, classified as Ghost, Layered, Secondary and Regular in the reference dataset. The prediction scores are written at the bottom of each images. The first line illustrates the limitation of the human classification since the last three craters may also be classified as valid from their geomorphological characteristics (no obvious crater fill and well defined rim), as proposed by our algorithm. The same discussion could also be raised for the second example of the valid crater, that may be secondary since the rim is not complete.

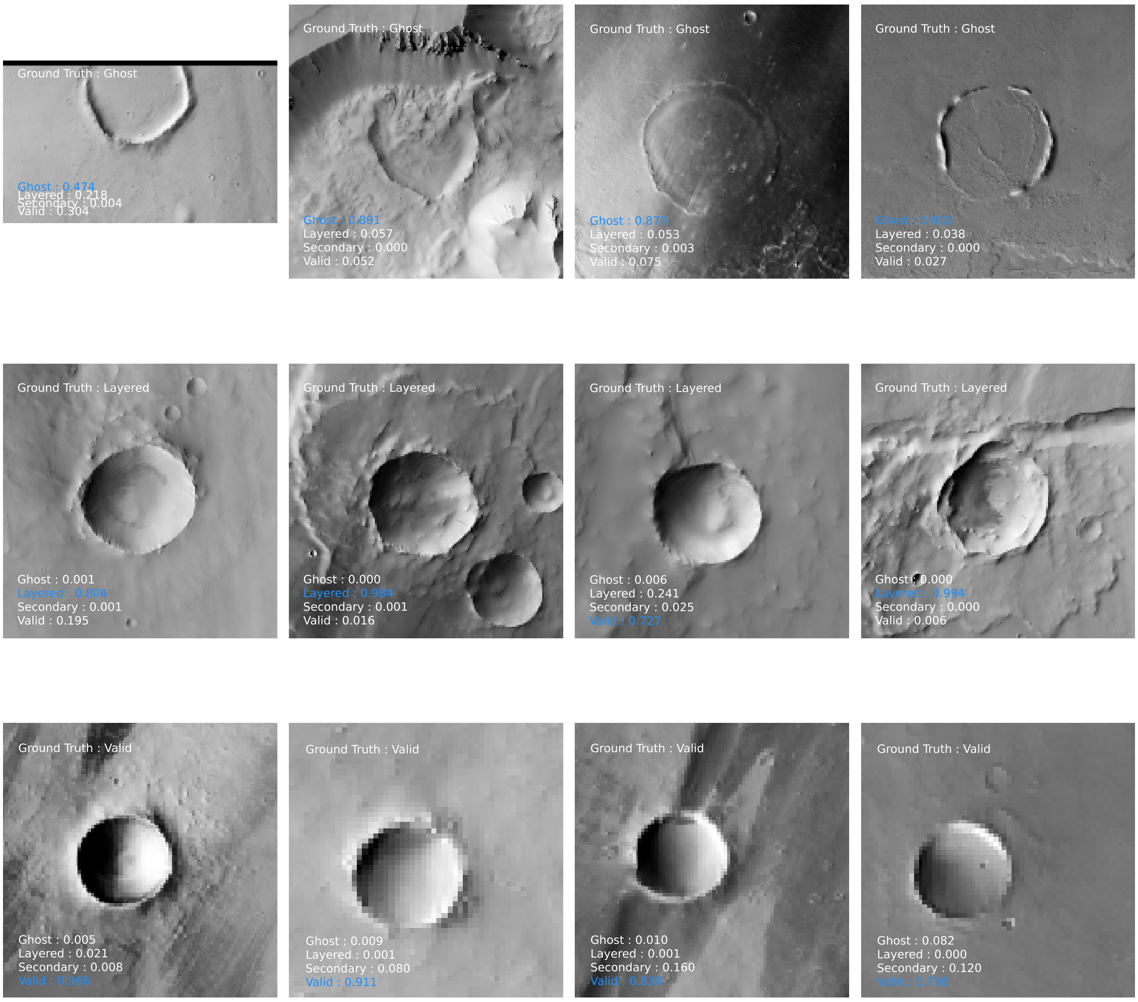

Figure 4.12: Illustration of the highest accuracy case. Example of 12 crater present in a test area between -100° and -92°E longitude and 0° to 08°S latitude, which were, from top to bottom, classified as Ghost, Layered and Regular. Here all the crater are well classified except the 3rd case of the layered class.

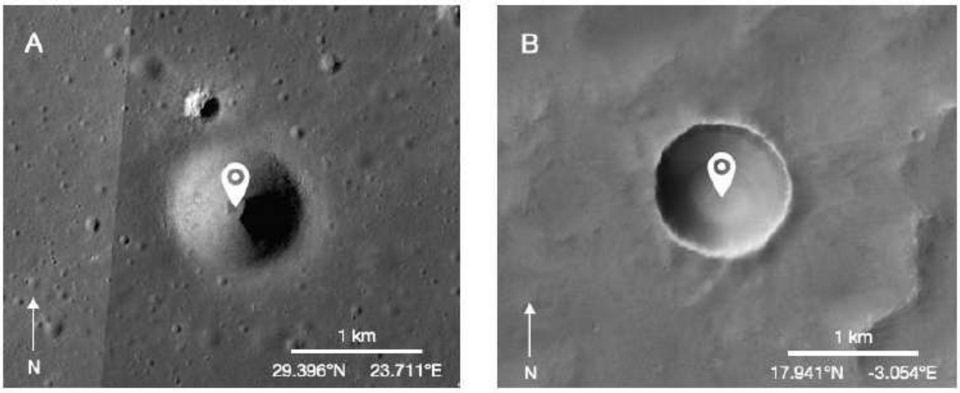

Figure 4.13: Comparision between two 1km size crater on the Moon (A) and on Mars (B)

5 - Detection of crater superposition order using a classification approach[1]

Contents

5.1 Introduction . . . 164
5.2 Crater superposition order definition . . . 165
  5.2.1 Crater superposition order definition . . . 165
5.3 Building a reference dataset : collaborative labellisation approach . . . 166
5.4 Deep-learning processing . . . 170
  5.4.1 Training . . . 170
  5.4.2 Evaluation . . . 170
  5.4.3 Global scale crater superposition order . . . 173
5.5 Results discussion . . . 174
  5.5.1 Example . . . 174
  5.5.2 Cumulative crater frequency distribution analysis . . . 174
  5.5.3 Crater density maps analysis . . . 174
5.6 Conclusion and perspectives . . . 180

---

[1] The notations used in this chapter may vary from one chapter to another

The dating process of planetary surfaces using crater counting relies on the ability to identifying and reference the craters that remain visible in remote sensing imagery. However, when a large impact occurs, it can erase or obscure pre-existing craters, thereby altering the observed crater population. In the previous chapters, we focused on the automatic detection (chapter 3) and geomorphological classification of craters (chapter 4). We now turn to a completely different but complementary problem of determining the relative superposition order between overlapping craters, which provides valuable chronological information for surface dating.

In this chapter, we first describe the theoretical basis for establishing crater superposition relationships, including the geological principles and the inherent limitations of visual interpretation (section 5.2). We then present the dataset preparation process, detailing the selection of crater pairs and the labelling strategy adopted to define superposition cases (section 5.3). Next, we introduce the deep-learning approach developed for this task, including the model architecture, training strategy, and evaluation metrics (section 5.4). Finally, we present and discuss the results, assessing both the performance of the method and its potential applications for planetary chronology studies (section 5.5). The content of this chapter is based on an article currently in preparation.

5.1 - Introduction

The detection of craters on planetary surfaces is a crucial task, especially when it comes to dating surfaces without rock samples (Hartmann et al., 2001; Neukum, 1977). However, for a very old surface it is impossible to record all impact craters because when a large impact occurs, it erases the smaller impacts that were present before the event. This concept, known as "saturation", has been generalized by Hirabayashi et al., 2024, is known as the "crater equilibrium concept". Hirabayashi's team present it as a condition on a cratered surface in which the equilibrium between crater formation and erasure prevents any further increase in the crater population. It is therefore impossible to know the exact number of craters per crater population that were present before a large impact. Consequently, it introduces a change in the crater frequency curve which will lead to age underestimation using crater counting. Furthermore, the impactor population in the primitive solar system is not well known (Morbidelli et al., 2018) and most specifically, the late heavy bombardment (LHB) period is still a matter of debate (Hartmann, 2019). The LHB is a period of intense bombardment that may have occurred in the early solar system, and it is believed to have played a significant role in shaping the surfaces of planets and moons. Knowing the number of craters per crater size might help us to reconstruct our understanding of the primitive solar system history.

Studying the population of superposed craters might help us to learn more about the craters that were erased by larger impacts. Furthermore, as the crater distribution evolves as a power law (Fielder, 1961), the use of artificial intelligence algorithms is highly required if we want an exhaustive classification of craters, especially at small scales. Thus, in this chapter, we build, using a classification algorithm, a model capable of detecting whether a crater has been recovered by another, for instance if it has a continuous rim or not and not. Indeed, if a crater has a continuous rim, it means that it is the most recent in the superposition of craters. If it does not have a continuous rim, it means that it has been erased by a larger impact. Also a smaller crater can lay inside an older larger crater. Hereafter, we introduce precisely the "superposition order" concept, and propose a deep-learning algorithm to estimate it.

The initial crater database that we used for this task made by Lagain et al., 2021a, which has been described in section 3. This database references every Martian craters of a size larger than 1 km in diameter. For each craters, it encompass the center location and the radius of the crater. Our aim is to built up on this database and add a new information: which crater superposes each other. The objective of this chapter is to propose a method to estimate the superposition order of craters in a cluster. It would enable us to know which crater is the oldest and which is the youngest in a given crater superposition situation. In order to do that, we have trained a deep learning classification model, with a similar methods as developed in 4. In this chapter we will explain how we create a reference labelised dataset, the preprocessing and the results of our crater superposition order determination.

5.2 - Crater superposition order definition

5.2.1 - Crater superposition order definition

The concept of *crater superposition order* provides a simple and systematic way to describe the relative chronological relationships between impact craters in a given area. In our approach, the definition is as follows:

- ⇒ Any crater that is not superposed by any other crater is assigned an order $N = 0$.
- ⇒ If a given crater is superposed by a crater of order N, then the first crater is assigned an order $N + 1$.

This hierarchical classification draws inspiration from the work of Strahler (1957), who introduced the widely known *Strahler order* to describe branching river networks. In both contexts, the ordering system captures the topological relationships between elements whether they are channels in a fluvial network for Strahler or geological features in our study. Within this framework, all craters assigned to a given order N are treated as contemporaneous, within the temporal resolution allowed by the method. Conversely, any crater of a higher order $N' > N$ must be older than those of order N, as it would have existed before their formation and later been superposed by them. It is important to note that this definition is inherently dependent on the spatial resolution of the imagery and the minimum crater size considered in the analysis. Indeed, the small craters identification in particular, is constrained by the pixel size of the dataset. In this work, and throughout the remainder of this chapter, we restrict our analysis to craters with diameters larger than 1 km, in order to ensure reliable detection and reduce uncertainties introduced by sub-pixel or marginally resolved features. An illustrative example of crater superposition order is shown in Fig. 5.1. In this schematic representation of a crater cluster, each crater is colour-coded and numbered according to its superposition order as defined in our model. This simplified case demonstrates how the ordering system can be applied in practice to quantify relative ages within a cratered landscape.

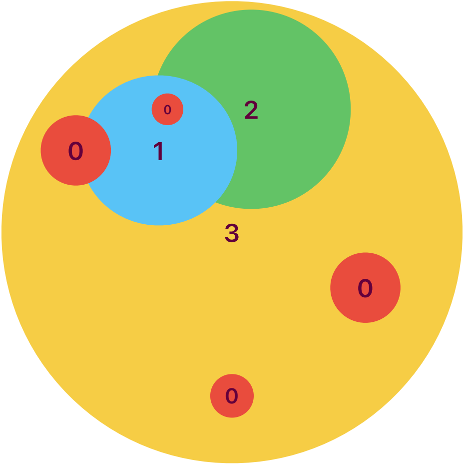

Figure 5.1: Schematic example of a crater cluster. Colours and numbers indicate the crater superposition order as defined in our model, with $N = 0$ corresponding to the youngest craters.

5.3 - Building a reference dataset : collaborative labellisation approach

The first step in our approach was to create a sufficiently representative dataset to train, evaluate and test our classification tool.

Cluster For that purpose, we have to manually define the superposition order of a certain number of craters by hand. This approach was inspired by the work of Lagain et al., 2021a, who proposed a method to labellise craters in a collaborative way with multiple operators. To do that we first determine "crater cluster", which is the complete set of craters that are superposing each other. To be more precise, inside a cluster there is an intersection link through all other craters (see Fig. 5.2). The clusters were selected using the refined Lagain crater database (see chapter 2), and more precisely, by using the crater center coordinates and their radius, we were able to define a shapely polygon (Gillies et al., 2007) for each craters and then to select only the polygones which intersect with each other.

Manual labelling Then, we created a program to show all the craters from all the clusters of craters previously created, to a human operator. The mission of the operator was then to evaluate the superposition order of each craters in the cluster. As illustrated in Figure 5.2, crater labeled 3 was the first to be formed, followed by crater order 2, and so on, up to crater labeled 0. Crater order 0 has a continuous rim, whereas craters with higher superposition order may not have. Our team labelled a part of the dataset, but we also included this work in an internship at the Paris-Saclay University where four bachelor students joined the project to help us labellised the craters during 8 sessions of 4 hours each.

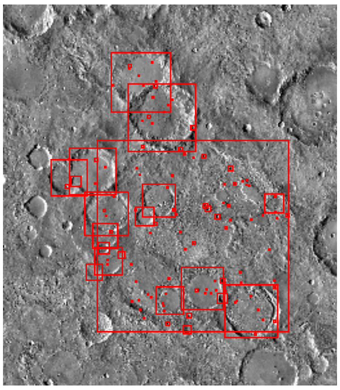

Figure 5.2: Contextual image of a complex crater cluster with the bounding box of every craters. The objective for the operator is to set the crater superposition.

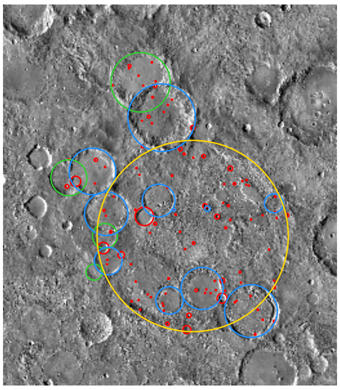

Figure 5.3: Same cluster as in Figure 5.2 but with the craters ordered according to their superposition order. The color code is the same as Fig. 5.1 (0:red, 1:blue, 2:green, 3:yellow). The crater labeled 3 is the oldest, and the crater labeled 0 is the youngest.

First-draw dataset In the end, the operators has provided a superposition order for each craters in the cluster as shown in fig. 5.3. Labellised quadrangles are distributed between 52° and -52° latitudes as it can be shown un Fig. 5.4. This labellisation process was done for 18115 craters as shown in the table 5.1. We can see in this tab that the representation of each class of craters with respect to its crater order N decrease exponentially. Consequently, for order N>2, the number of craters is very low and this will lead to difficulties for the classification algorithm. In addition, the most important information lay in order 0, 1 and 2, so we decided to group all craters with a superposition order of 2 or more into a single class called *Order 2 and More* which encompass 862 craters. This dataset is sufficient to train a small deep learning classification tool to determine the superposition order of craters. But in order to get better results with a bigger model, we will, as explained in the next paragraph, process transformations in order to increase the number of images.

Data augmentation To increase the size and diversity of the dataset, we implemented a data augmentation strategy. For each crater image (see Fig.5.5b), a series of geometric transformations was applied to generate additional samples. These transformations included rotations of 90°, 180°, and 270°, horizontal (left–right) and vertical (up–down) flips, translations, and various combinations of these operations. In total, this process yielded 19 transformed images per crater from a single original image.

However, as illustrated by the augmentation matrix in Fig.5.5a, many of these transformations are redundant. For example, a vertical flip followed by a horizontal flip is equivalent to a 180° rotation, and similar equivalences exist among other combinations. Fig.5.5b presents all transformations applied to a single crater image, revealing that only seven of them are truly unique. Consequently, these seven augmented versions, together with the original image, allow us to increase the dataset size by a factor of eight.

Superposition Order	Number of Craters
0	12 950
1	4 260
2	711
3	134
4	13
5	4
6	0
≥2	862

Table 5.1: Number of craters per superposition order in the labeled dataset.

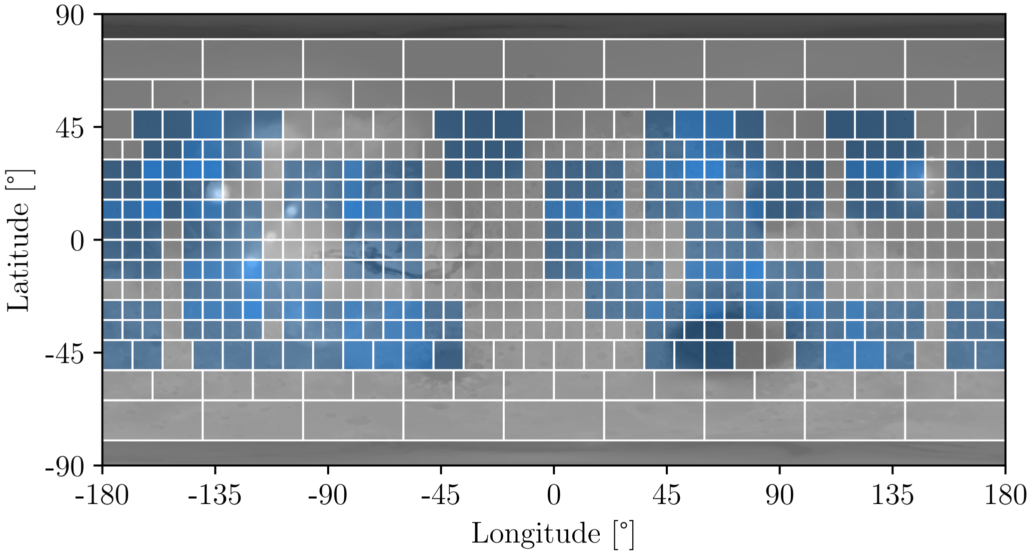

Figure 5.4: Map of Mars showing the distribution of labelled quadrangles used in this study. Blue quadrangles correspond to regions manually treated by operators for crater superposition order labelling, overlaid on the Mars Orbiter Laser Altimeter (MOLA) shaded relief background (Zuber et al., 1992).

Final dataset As we have seen in the chapter 4, the model we are using is a YOLOv11 convolutions neural network developed by ultralytics and specifically made for classification purpose (Jocher et al., 2025). In order to train it, we needed to prepare the data in a way that the model can learn from it. We applied exactly the same development as described in the chapter 4 unless than the ground truth classes are not *regular*, *secondary*, *layered*, *ghost* anymore but *Order 0*, *Order 1* and *Order 2 and More*. The model was trained on the same hardware as the one used in the chapter 4, section with the same hyper-parameters. The only difference is that we used a smaller batch size of 128 instead of 512

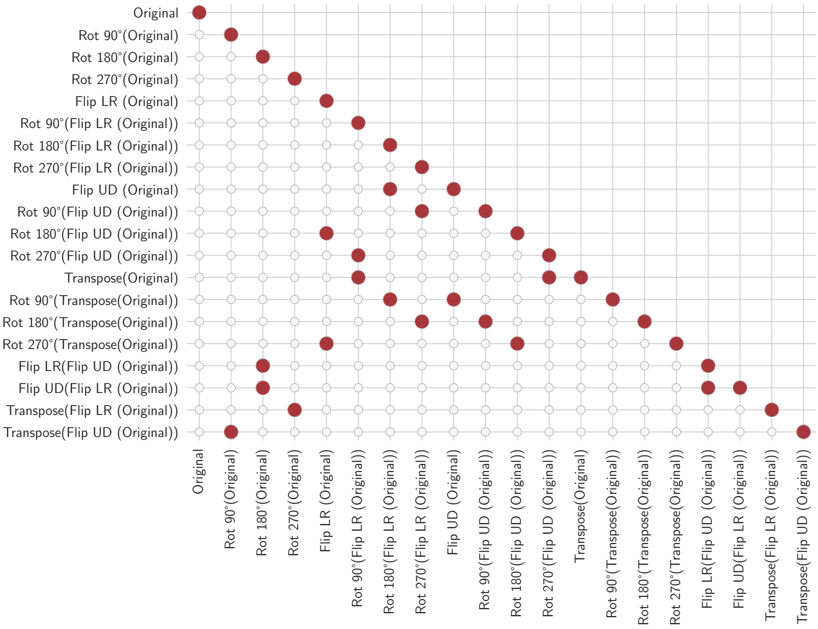

(a) Correlation matrix of transformed crater images.

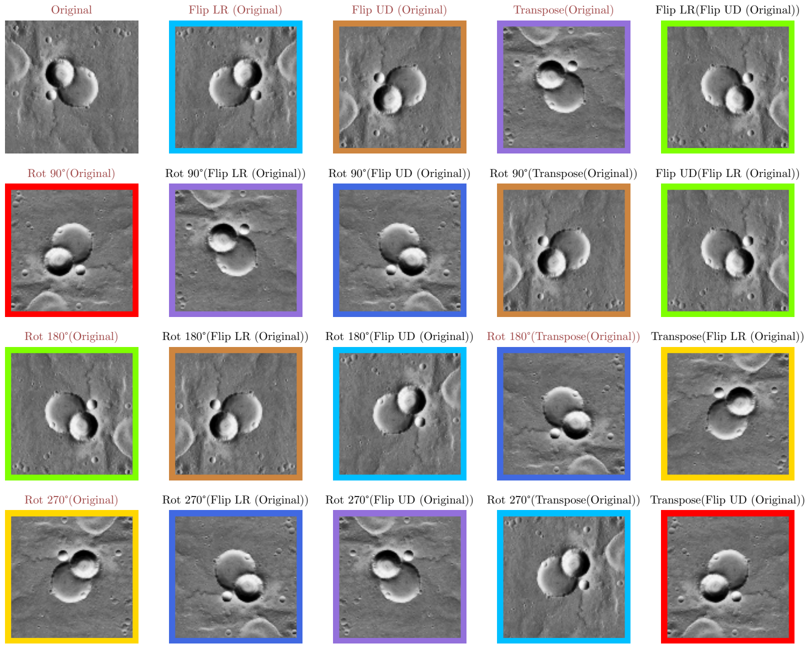

(b) Examples of geometric transformations applied to a crater image.

Figure 5.5: Data augmentation strategy applied to crater images. Various geometric transformations (rotations, flips, transpositions, and combinations) were applied to generate augmented data. The correlation matrix (a) shows that many transformations are redundant—e.g., a vertical and horizontal flip is equivalent to a 180° rotation. Only seven transformations, along with the original image, are geometrically unique. Panel (b) illustrates how these selected transformations are applied to a crater image, expanding the dataset size by a factor of eight.

because of the size of the dataset. The training was done for 150 epochs, which is sufficient to reach a good accuracy on the validation set.

As shown in tab. 5.2, the training dataset after the augmentation process described below is now composed of 127,953 images contained into the three classes: *Order 0*, *Order 1* and *Order 2 and More*. The validation dataset is composed of 7,946 images and the test dataset is composed of 15,810 images.

	0	1	≥ 2	Subtotal
Train	86 696	32 814	8 443	127 953
Val	5 264	2 071	611	7 946
Test	10 669	4 020	1 121	15 810
Subtotal	102 629	38 905	10 175	151 709

Table 5.2: Répartition des données par ensembles et par classes.

5.4 - Deep-learning processing

5.4.1 - Training

The model is trained during 2 periods of time as represented with fig. 5.6b and in fig. 5.6a. In a First time, we choose to train the model during 100 epochs but, as it is shown in fig 5.6b and in fig 5.6a it was not sufficient. Indeed, in the accuracy curve, we suspect the initial training phase to still grow. In the losses curve, we see that the loss of the initial training phase definitely doesn't reach the attended minimum. So we did a second reinforcement training (royal blue curve) which lead to this very good accuracy of 0.975.

5.4.2 - Evaluation

A the end, the model is able to reach an global accuracy of 97.5% on the validation dataset, completely independent from the training/testing dataset, which is an excellent result. The results are shown in Figure 5.7. We can see that the model is able to classify the craters with a continuous rim and the craters with a discontinuous rim almost perfectly (99% accuracy). The result of the test is still excellent when the model has to make the distinctions between the craters with a superposition order of 1 and other classes, misclassifying only 6% of them (4% order 0 and 2% order 2 and more). For an order of superposition of 1, the model is able to classify it with an accuracy of 97% and in 2% of the cases, it classifies it as a crater with a superposition order of 0. For a superposition order of 2 or more, the model have a little harder time, classifying, in the vast majority of the cases, the craters as a superposition order of 2 but misclassified mostly for order1 (13% cases). The fig. 5.6b

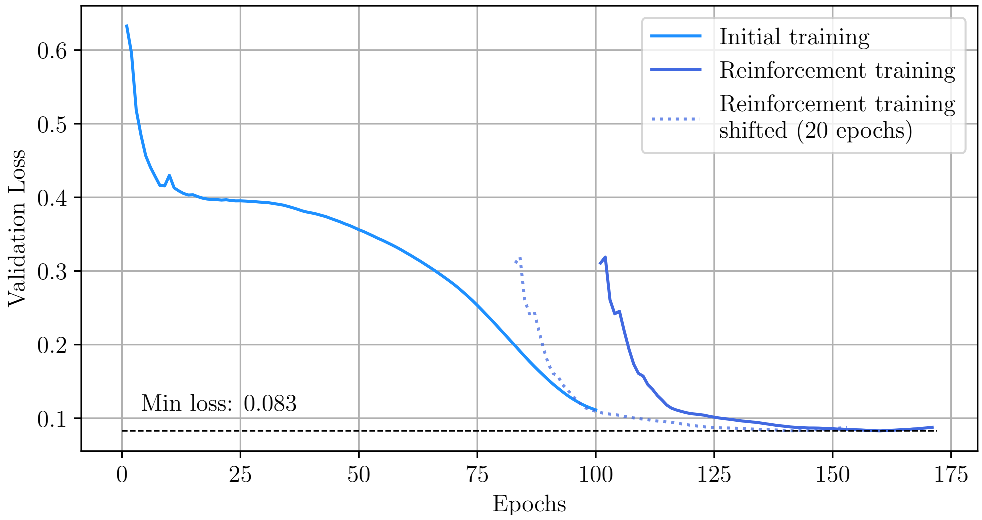

(a) Validation losses of the deep learning crater classification model as a function of training epochs. The losses were calculated on the validation set during training.

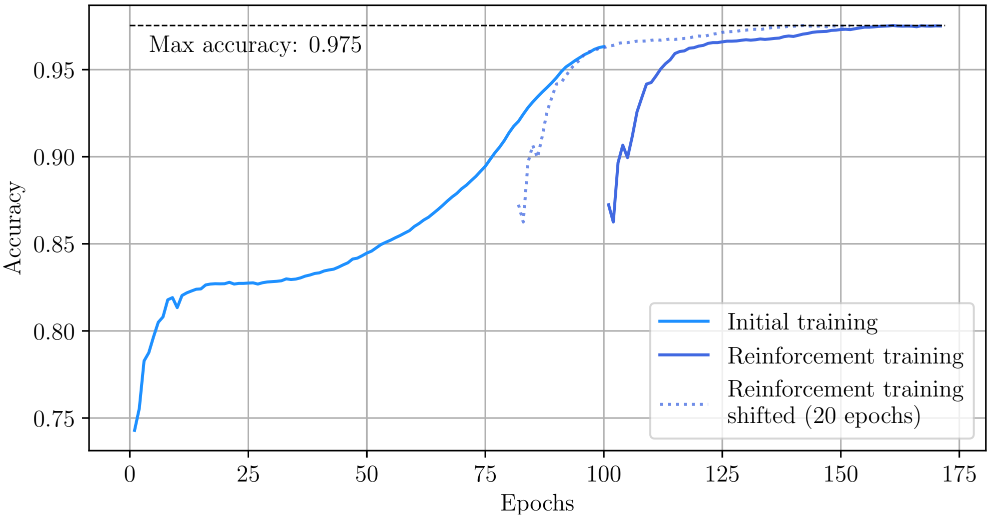

(b) Validation accuracy of the deep learning crater classification model as a function of training epochs. Accuracy was computed on the validation set during training.

Figure 5.6: Training performance of the deep learning crater classification model. Subfigure (a) shows the evolution of the validation losses, while subfigure (b) shows the corresponding validation accuracy. Both metrics were computed during training, which was carried out in two phases. The observed drops between the two phases are linked to a 20-epoch warmup period applied at the start of the second phase. While learning rate warmups are generally used to stabilize the training process, it was not necessary to apply one in the second phase.

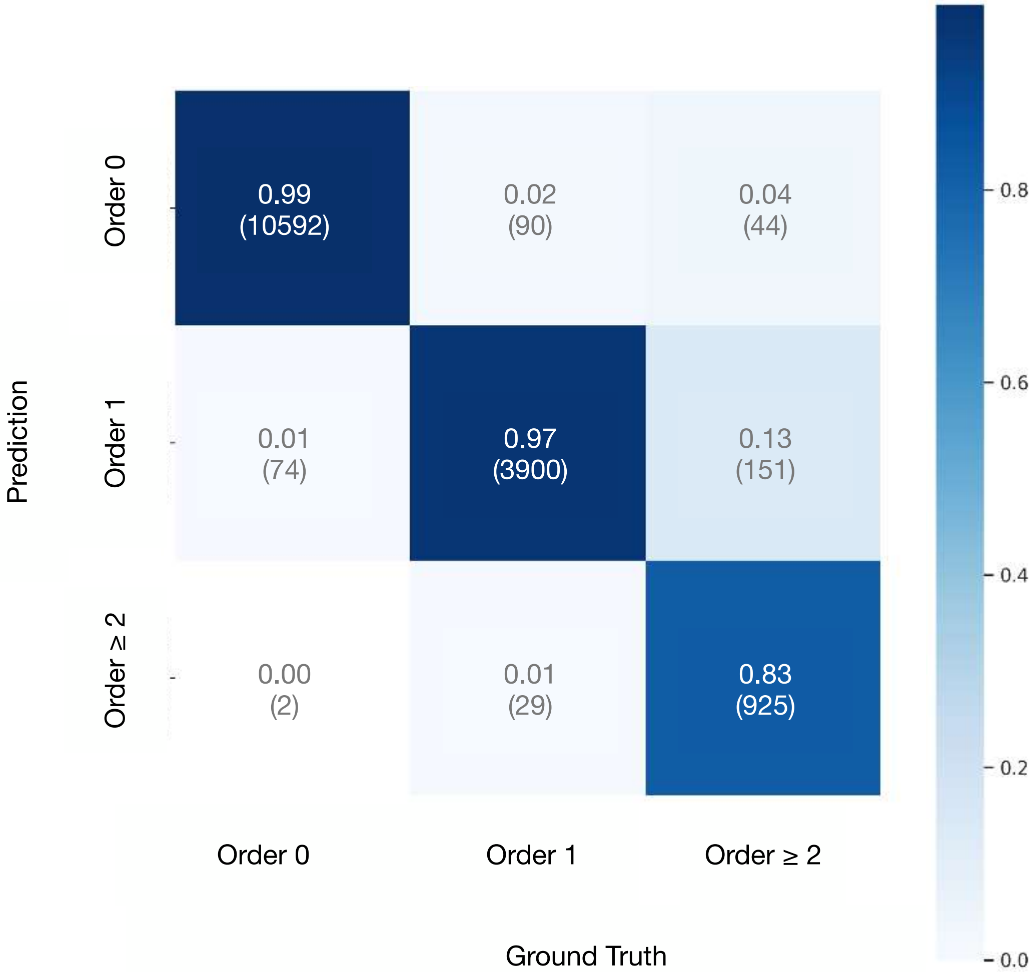

Figure 5.7: Confusion matrix of the crater superposition order classification model. True classes are in lines, estimations are in rows. A perfect match would be 100% in the diagonal. Here the results are excellent for order 0 (99% of good predictions), and very good for order 1 (97%) and order 2 (83%). Non diagonal elements represent mis-classificatied craters. The worst case is 13% of order 2 crater that are mis-classified as order 1.

5.4.3 - Global scale crater superposition order

Now that our model has been satisfactorily trained and validated, we apply it on the data of the entire planet Mars. The goal is to determine the superposition order of all craters to draw statistics at global scale. To do this, we use the database published by A. Lagain and collaborators in 2021 (Lagain et al., 2021a) which encompass more than 376 000 craters of a size larger than 1 km in diameter. As well, we used the V01 mosaic version of CTX images processed by the Bruce Murray Laboratory (Dickson et al., 2024) and which cover the surface of mars at a resolution of 5m per pixels from 88.5°N to 88.5°S. We used the aligned dataset as defined in chapter 2. For the purpose of this study we downgraded the images in order to only work with 50 m / pixel images. Thus, the smallest objects in the database have a size of 20 pixels, which is more than sufficient to characterize the craters.

For this analysis, we proceed as follows: first, we had to create a database of crater image patches. Each image patch has a size of 2x the crater diameter, which allows us not to include too much context around each crater, as this could bias the characterization. In addition, in order to avoid problems related to craters which would be on the image patchs egdes, each image are extracted from all the quadrangle images that intersects the crater of interest. In the majority of cases it represents a single quadrangle but in some cases it's more. When it's more, every images involved are merged to have all of the craters on the image. Then, each image is reprojected into a local stereographic reference frame, which, as explain in chater 3, prevents distortions related to image projection. Finally, the reprojected quadrangle is cropped with a size 2×2 crater diameter, centered on the crater center coordinates.

Once this database is created, we are able to apply the classification model. For pre-processing time reasons, we removed craters < 2 km in diameter. Indeed, craters of this size are often very young and therefore most likely all of them classified with order 0. Moreover, their large number would make the pre-processing time significantly higher. Thus, we were able to apply the classification model to the remaining 127,217 craters. After a relatively long pre-processing time (about 28 hours) and a pretty fast inference time, we obtained the classification results for each crater.

5.5 - Results discussion

5.5.1 - Example

In order to illustrate the capabilities of our approach, we show here examples, out of the training dataset. In Figure 5.8 and 5.9, we can see that the model is able to detect the superposition order of craters with an excellent confident score and without any error in the 2 situations.

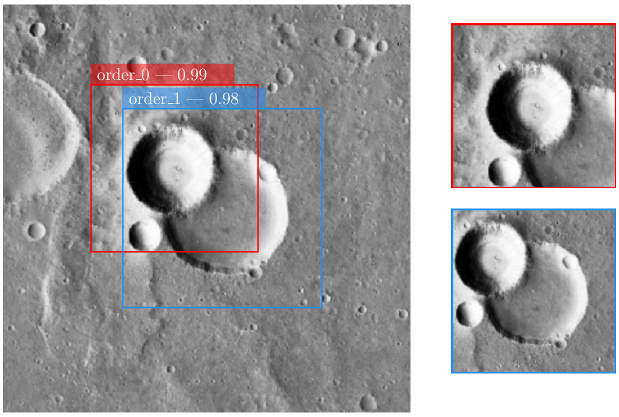

Figure 5.8: Inference made by the model on a two crater cluster.

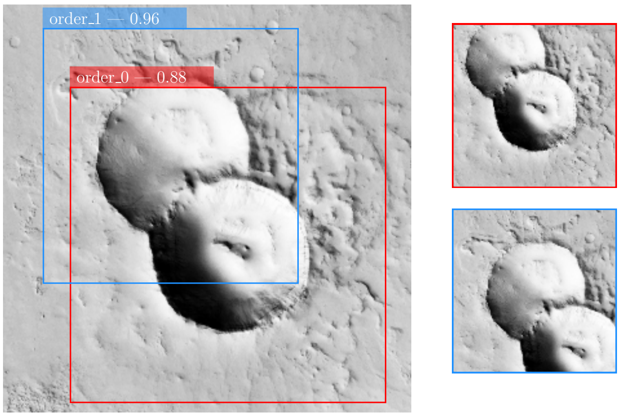

Figure 5.9: Inference made by the model on a two crater cluster.

5.5.2 - Cumulative crater frequency distribution analysis

The global-scale results can be summarised as cumulative crater frequency curves, as a function of crater superposition order, as shown in Figure 5.10. If we consider every crater with a diameter larger than 2 km, there are approximately five times more *Order 0* craters than *Order 1* craters, and ten times more *Order 1* craters than *Order 2 or higher* craters. This trend is expected because, by construction, the existence of an *Order 1* crater requires an *Order 0* crater beneath it, and similarly, an *Order 2* crater requires an *Order 1* crater beneath it.

However, for craters with diameter $>$ 7 km, the number of *Order 1* craters exceeds the number of *Order 0* craters. This inversion reflects the relative cratering rates on Mars. The impact frequency of craters larger than 7km is much lower than that of smaller craters. Consequently, if a large (>7km) crater exists, it is statistically more likely to have been overlaped by one or more smaller impacts after its formation, producing overlapping smaller craters and thereby increasing its superposition order. This result can therefore be interpreted as a signature of the size-frequency distribution of impacts on Mars. Indeed, the same phenomenon is observed for the *Order 2 and more* craters for radius $>$ 70 km, which are more numerous than the *Order 1* craters because the frequency of crater larger than 1km on Mars is very low.

5.5.3 - Crater density maps analysis

Local results could be discussed in density maps. The crater density maps are computed using HEALPix polygones (Gorski et al., 2005) which is a way to pave the total surface of a sphere into equal surface polygones. For our maps we divided the surface with 1200 polygones of equal surface. It

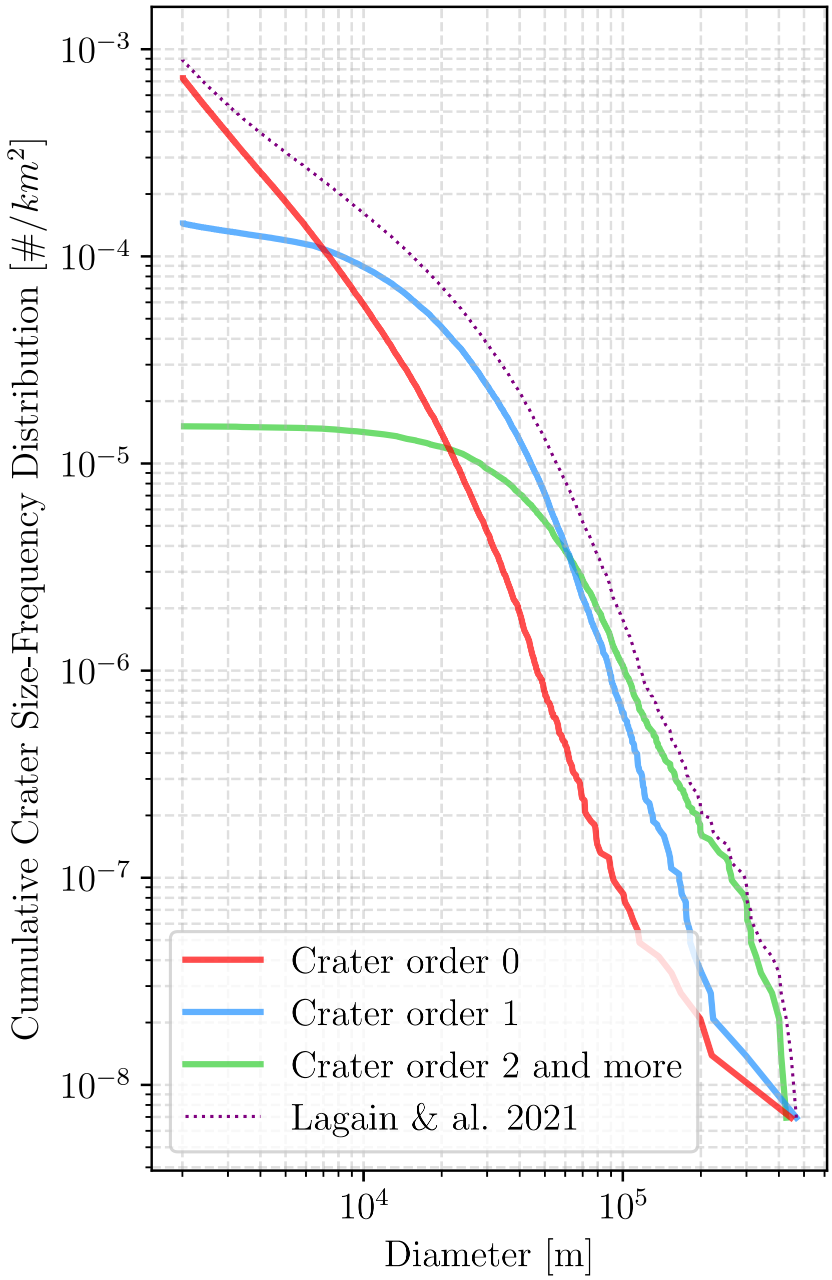

Figure 5.10: Cumulative crater frequency distribution of the superposition order of craters larger than 1km in diameter. The *Order 0* craters —red curve— are never superposed, the *Order 1* craters —blue curve— are superposed by at least one crater of order 0, and the *Order 2 and more* craters —green curve— are superposed by at least one crater of order 1

generates healpix with a surface of 129 990 km^2 which represent around a square of around 345 × 345 km. We chose this value in order to make a compromise between the map resolution and the statistical significance. Indeed, we needed cells wider than the biggest craters of our dataset. The density maps are computed by counting the number of craters in each healpix polygon and then dividing it by the area of the polygon. The results are shown in Figure 5.12a, 5.12b, 5.12c and can be compared to the global mars crater density map represented with Figure 5.11a. For comparison, we also made a topographic map of Mars with HEALPix using the median altitude of the MOLA global map in each HEALPix(see in Figure 5.11b).

Figure 5.12a presents the same map as Figure 5.11a but for superposition order of 0 only. At first order, both maps share the same pattern. The two following maps represented by Figure 5.12b and 5.12c show the density of craters with a superposition order of 1 and 2 or more respectively. As we can see, the density of craters with a superposition order of 1 is much lower than the density of craters with a superposition order of 0. The majority of the craters with a superposition order of 1 are located in the oldest heavily cratered regions (Neukum et al., 2001; Hartmann et al., 2001; Tanaka et al., 2014) as expected.

When comparing the different maps, two distinct regimes emerge rather than a single linear correlation. In the low-density regime, regions with few *Order 0* craters also tend to have few *Order 1* (or *Order 2*) craters, consistent with the expectation that a low crater density limits the probability of superposition. In contrast, in the high-density regime — corresponding to the most ancient terrains — *Order 1* (and to a lesser extent *Order 2*) craters become much more abundant. This does not necessarily imply a strong statistical correlation between densities at different orders in this regime, especially for *Order 1* vs. *Order 2*, where dispersion is larger. Instead, this behaviour reflects the increased likelihood of superposition in heavily cratered landscapes, where the high frequency of impacts over geological time ensures that many craters have been partially overprinted by younger ones.

This interpretation highlights that the transition from low to high densities for higher-order craters is better understood as a consequence of the cratering history, rather than being directly quantified by a correlation coefficient.

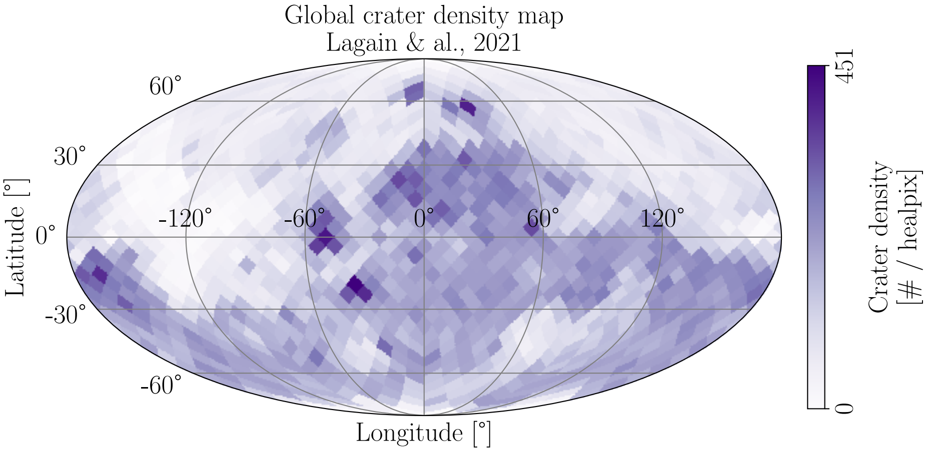

(a) Global martian crater density map. The map made with healpix with a surface of 129 990 km^2, shows the density of craters larger than 1 km in radius. This map is built from Lagain et al., 2021a refined by our work (see section 2). The color scale is logarithmic. The map is centered on the equator and covers the entire surface of Mars.

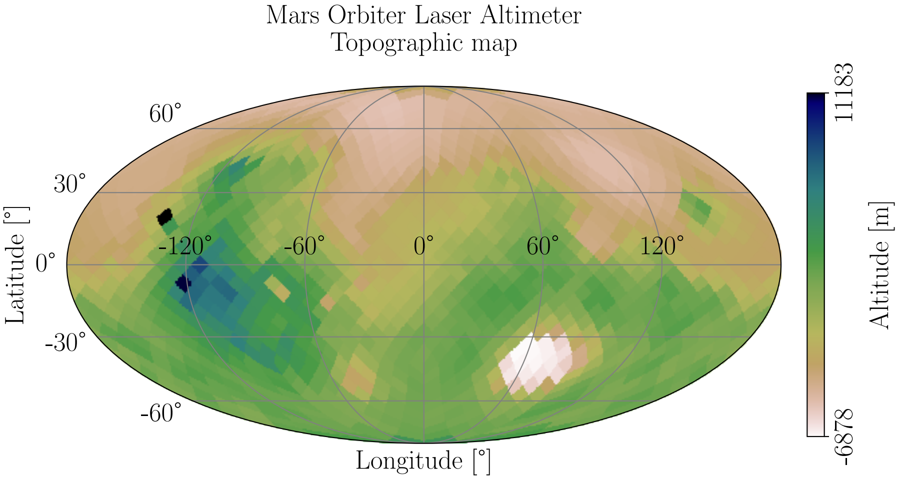

(b) Healpix topography derived from the Mars Orbital Laser Altimeter (Zuber et al., 1992). The map is made with healpix with a surface of 129 990 km^2. The color scale is logarithmic. The map is centered on the equator and covers the entire surface of Mars.

Figure 5.11: Useful maps of global martian crater density and MOLA topography for comparison and discussion.

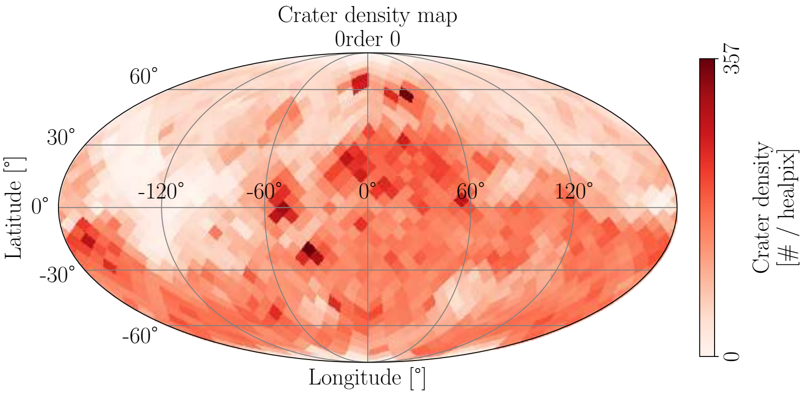

(a) Superimposition order 0.

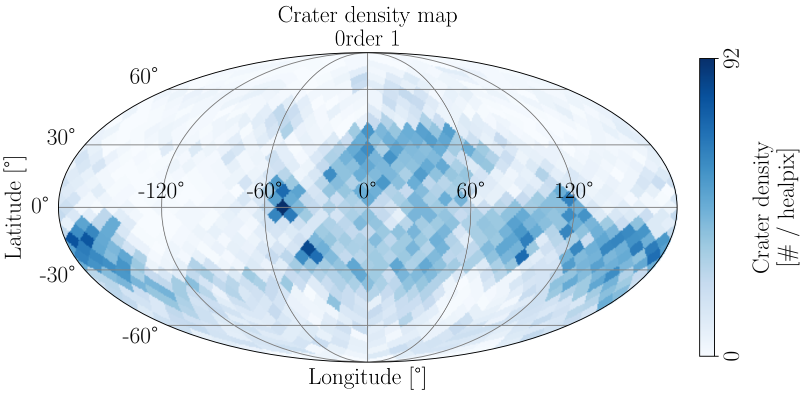

(b) Superimposition order 1.

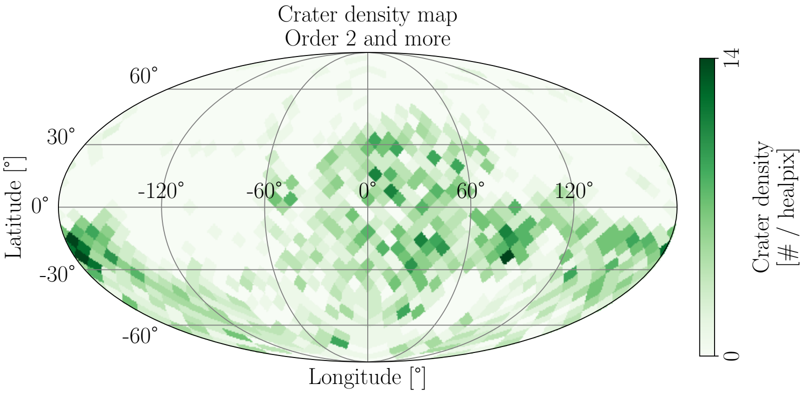

(c) Superimposition order ≥2.

Figure 5.12: Global Martian crater density maps by superimposition order. Each map is produced with HEALPix using a per-pixel area of 129,990 km^2.

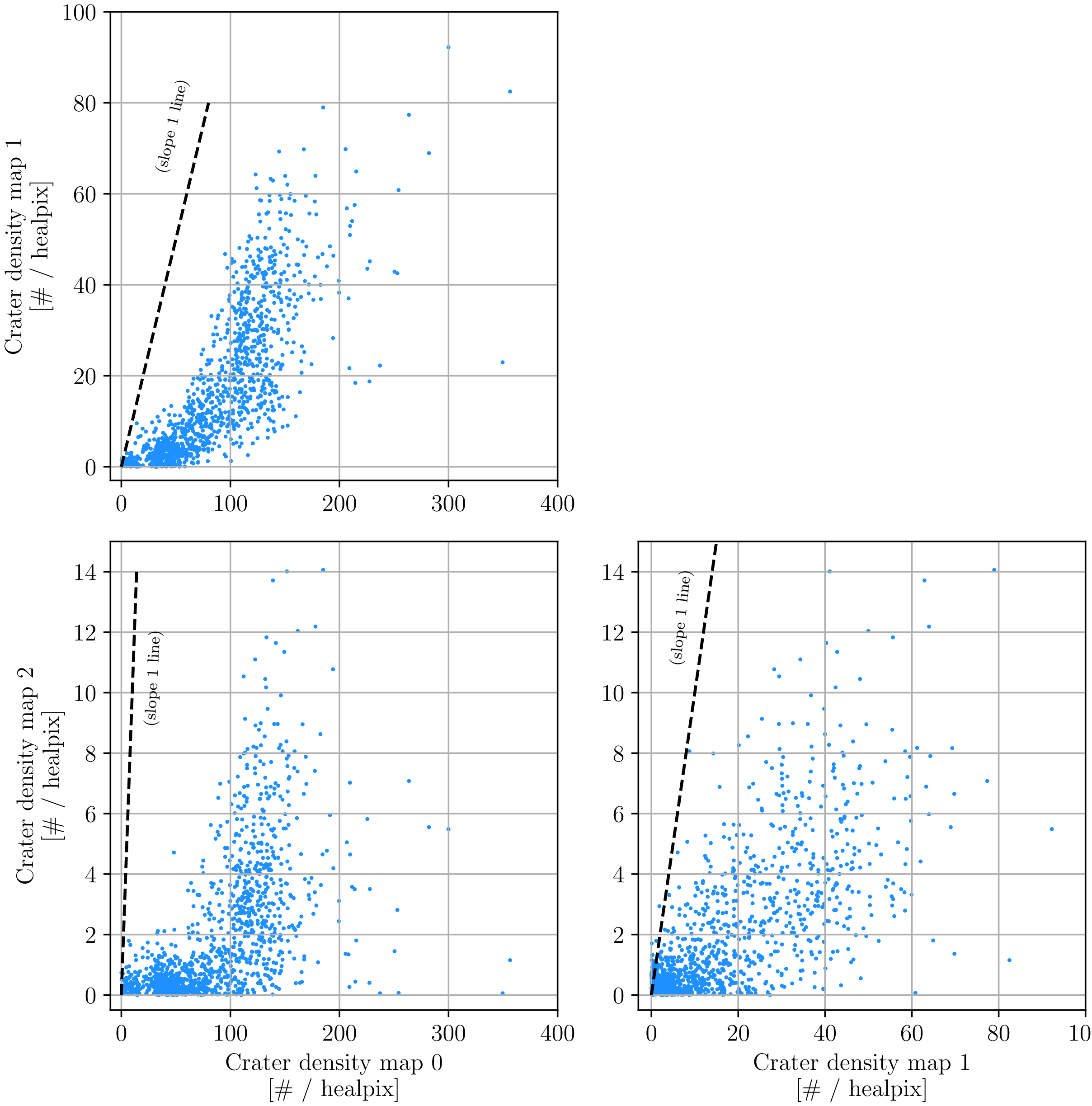

Figure 5.13: Scatter plots comparing crater densities between different superposition orders. (Top left): Order 0 vs. Order 1 densities. (Bottom left): Order 0 vs. Order 2 or higher densities. (Bottom right): Order 1 vs. Order 2 or higher densities. Each point represents a HEALPix cell of equal area (129 990 km^2), and dashed lines indicate the 1:1 slope. Points lying below the line correspond to the expected regime where lower-order craters are more numerous than higher-order ones. Two regimes are visible: in low-density regions, higher-order craters are rare, while in high-density regions, their occurrence increases much more, reflecting greater probabilities of superposition events.

5.6 - Conclusion and perspectives

In this chapter, we have presented a method to automatically classify craters superposition order. With the help of few motivated students, we labelled more than 18 000 craters per order of superposition.

This newly created labelled crater database enabled us to train a deep learning classification model capable of determining the superposition order of craters. The model achieved an accuracy of 97.5 % on the validation dataset and was subsequently applied to the entire Martian surface to estimate the superposition order of every crater larger than 2 km in diameter. Our analysis revealed that superposition order depends strongly on crater size. Specifically, we found that above a radius of 7 km, the number of craters showing no superposition drops drastically, indicating that larger craters are significantly more likely to be overlapped by smaller ones. This pattern aligns with expectations from the impactor population of the early Solar System, where large impacts were rarer but had the capacity to erase many smaller craters. We also observed that crater densities across different superposition orders exhibit a non-linear relationship, with distinct regimes emerging between low- and high-density regions.

It is important to note that such a large-scale, detailed classification would have been practically impossible without the use of artificial intelligence. The combination of human expertise for initial labelling and the scalability of deep learning methods made it possible to process millions of craters efficiently and consistently.

These new results open the way for further research based on superposition order, such as investigating the anisotropy of cratering or estimating the number of craters erased over time to refine geological dating. Ultimately, these studies aim to improve our understanding of the bombardment history throughout the Solar System.

6 - Automatic Age Estimation using ACDC [1]

Contents

6.1 Dataset . . . 182
6.2 Age estimation algorithm . . . 183
  6.2.1 Images reprojection and multiscale cutting . . . 183
  6.2.2 Crater detection . . . 185
  6.2.3 Merging duplicated detection . . . 185
  6.2.4 Improvement of our detection . . . 187
  6.2.5 Restriction to a geological unit . . . 188
  6.2.6 Classification . . . 189
  6.2.7 Age determination . . . 190
6.3 Results — datations . . . 191
  6.3.1 Mars . . . 191
  6.3.2 Moon (Kaguya-based analyses) . . . 195
6.4 Discussion and conclusion . . . 196

---

[1] The notations used in this chapter may vary from one chapter to another

This chapter presents the Automatic Crater Dating and Characterization (ACDC) toolbox developed during this PhD, designed to estimate the age of planetary surfaces from remote sensing data. The method builds on the crater detection and refinement approaches described in the previous chapters, integrating them into a complete age-dating workflow. We first described the required datasets and input formats (section 6.1), including image sources, georeferencing requirements, and crater catalogues used for validation. We then detail the age estimation algorithm (section 6.2), which is structured into sequential steps: image reprojection and multiscale cutting (subsection 6.2.1), crater detection using our pretrained deep learning model (subsection 6.2.2), merging of duplicated detections via non-maximum suppression (subsection 6.2.3), refinement of crater geometry with the Hough-transform-based circle detection (subsection 6.2.4), restriction to specific geological units (subsection 6.2.5), optional morphological classification (subsection 6.2.6), and final age determination using crater size–frequency distribution analysis (subsection 6.2.7). The performance of the ACDC pipeline is then illustrated through several case studies (section 6.3) using CTX, HiRISE, and HRSC imagery, as well as lunar datasets. We conclude with a discussion of the limitations and perspectives for future improvements (section 6.4). The content of this chapter is based on a dedicated user guide and application examples prepared during the thesis.

6.1 - Dataset

As seen in chapter 3 and 4 we developed and trained a tool for crater detection and characterization, that is designed to be robust to any kind of image dataset. Of course, since the training was made on the CTX image mosaic, the application will be more suited for this particular dataset. In order to detect craters, we need an image which covers the geological unit of interest. Any wavelength is in principle possible but we focus here on the visible domain. A prerequisite for inclusion in this analysis is the presence of a georeferenced header accompanying the planetary data. This geo-referenced header, often called CRS for Coordinate Reference System defines a set of parameters that allows for accurate mapping and georeferencing of spatial data. It includes information such as coordinate units, map projection methods, and datum transformations, which are essential for correctly aligning the digital representation of the Martian surface with its actual geographic features.

Mars mosaic — CTX For the purpose of this section, we used the mosaic processed by the Bruce Murray Laboratory for Planetary Visualization (Dickson et al., 2024). Data products are available on their website.

Mars crater database The ground truth data were provided by the collaborative crater database made by Lagain et al. (2021a) which encompasses more than 376 000 crater larger than 1km in diameter. The Fig. 6.5 shows inferences made on the random image patches which were presented in Fig. 6.4.

Moon mosaic — Kaguya We also applied our model to the Moon surface to show that we can apply this crater detection tools on a planetary surface which has not been trained on the model. The data we use for that purpose are data aquired by the Kaguya/SELENE mission (Kato et al., 2007). Images have a 100m resolution

6.2 - Age estimation algorithm

As described in the opening paragraph, this section will give details about the global organisation of our automatic datation algorithm which will be organised as follow :

1. Images reprojection and multiscale cutting (see: subsection 6.2.1)
2. Crater detection (see: subsection 6.2.2)
3. Merging duplicated detections (see: subsection 6.2.3)
4. Improvement of the detection (see: subsection 6.2.4)
5. Restriction to a geological unit (see: subsection 6.2.5)
6. Classification (optional) (see: subsection 6.2.6)
7. Age determination (see: subsection 6.2.7)

This algorithm requires as input:

- The referenced image file (preferred .tif format).
- A neural network checkpoint file which encompasses all the weight and bias parameters that were adjusted during the training phase of the model (see: chapter 3).
- An input shapefile of the geological unit in the referenced image file (optional).

The code returns as output the age of the geological unit present in the images plus the crater database which encompass all the detections present in the area.

6.2.1 - Images reprojection and multiscale cutting

A critical aspect of our preprocessing pipeline lies in ensuring that the inference algorithm is exposed to the full diversity of crater sizes present in the dataset. This step is essential to correct a common source of error in most crater detection workflows: when a single image is directly fed to the model without scale adaptation, small craters may remain undetected because their apparent size falls below the model's minimum detection threshold -which for us is around 20px— while large craters may be missed because they extend beyond the image boundaries and cannot be fully captured. To address this issue, we implemented a multiscale cutting strategy that reprojects and crops the original images at different spatial scales, ensuring that both small and large craters are presented to the algorithm in an optimal size range for detection. This principle is illustrated in Fig. 6.1, where the limitations of a single-scale approach are evident.

The first step of our algorithm is to perform the usual pre-processing as discussed in chapter 2 and 3 is to reproject the image in a non-deformed realistic projection: the local stereoscopic projection. This would ensure that every crater on the image has a round shape.

Then, in order to make good detections on our images, we have to deal with the "no data values" present in our images. There is no universal strategy applicable to all kind of data to deal with the

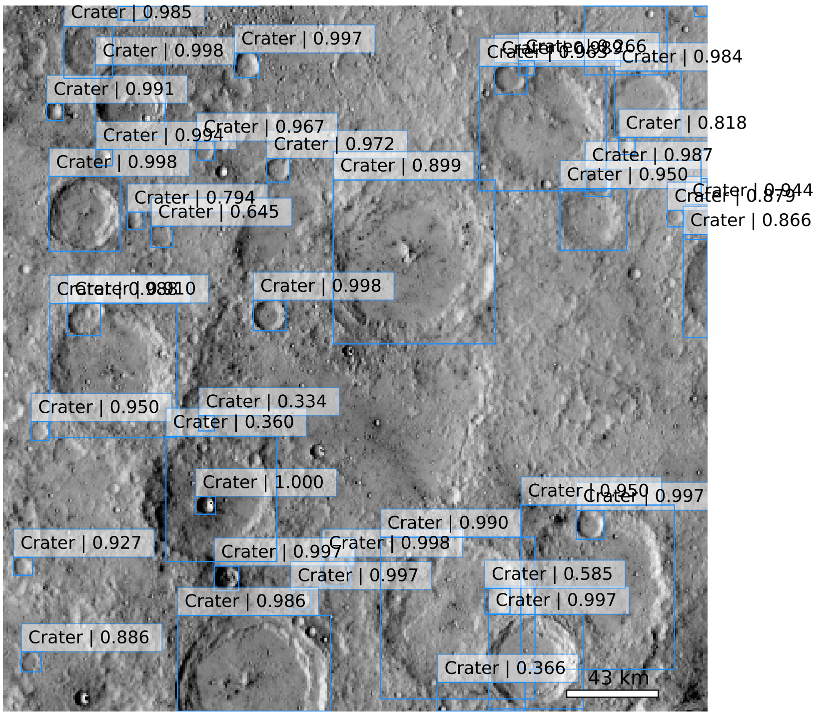

Figure 6.1: Inference made on a 166m resolution of Mercury Messenger imager. The lower right corner of this 9.5°×9.5° quadrangle is located at 121°W, 5°S near Verda-Da-Silva Crater (Beethoven, quadrangle, Mercury). The blue boxes represent the predictions made. We can note that crater smaller than 20 pixels in diameter are ignored.

no data values but in our pipeline we suggest two solutions. The first one is to ignore them by doing inferences on no-data values. In most cases, the model is able to deal with the no-data values if, as shown in Fig. 6.2, the no-data band is thin. But it is not a 100% reliable solution so we implemented an other way of doing it. This other solution is what we called the largest included valid rectangle. As shown in Fig. 6.2, that solution implies to find the largest rectangle with correct data in our image. We will then consider this rectangle as our region of interest and we will only make inferences in this area. It's a pretty radical solution which protect us from boundary false detections due to the presence of no data values in the middle of our image.

As a result, a band in the top of the image will not be considered.

Last, in order to be able to detect the whole diversity of crater size, we will have to split the image into small patches of equal size but at different resolution. As shown in fig 6.3, our algorithm will barely not be able to detect big craters at full image resolution (left) because they might be bigger than the image. But after few zoom levels, it will start to be possible to detect big crater. In the meantime, small craters will have a sizes under the detection level of our algorithms. Furthermore, to be sure that we have not missed any craters, we will split our image into patches which overlap from

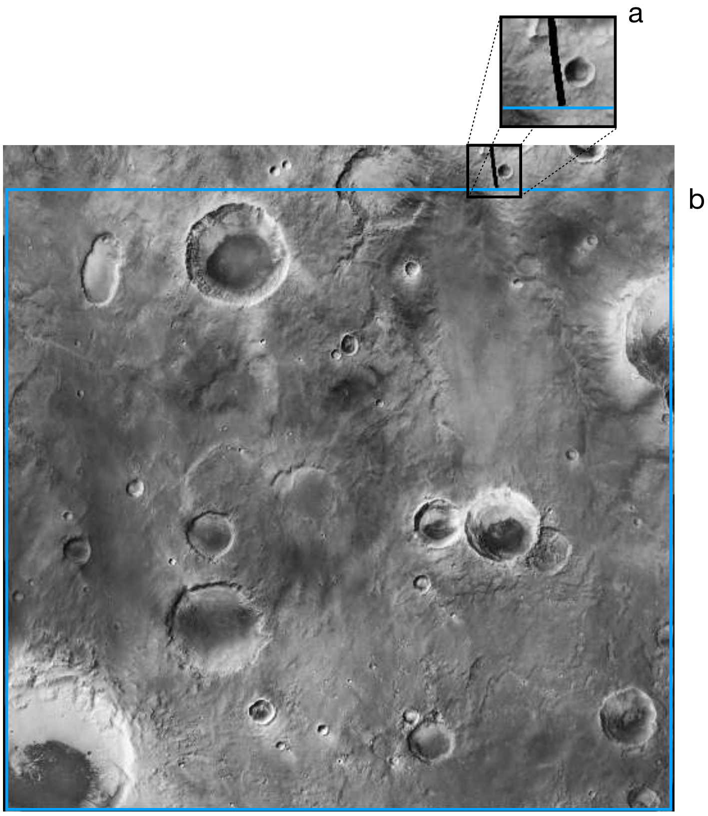

Figure 6.2: Stategy employed with no data value. (a) Band of no data value in the image. (b) "Area of work" which is the largest included rectangle without no data value in the image.

each other. Figure 6.3 illustrates the cut-out template of every image patch with a color indicating the level of downsampling.

The fig. 6.4 shows us some patches, at different scale, randomly chosen in the set of image patches.

6.2.2 - Crater detection

In this second step, we will make inferences on every image patch that we have. In order to do this we load our pre-trained FasterRCNN deep-learning model which will enable us to detect crater (see detail in the specific chapter of this PhD about it 3).

Then, as seen in fig 6.6 we change the coordinates of each bounding boxes of each path to express them in the original image reference frame. At this stage, we collect the predictions made by our model in a dataframe that must be merged. Indeed, as we can see in figure 6.6, that when we put back all the detections on the image, we have further detection for one single object.

6.2.3 - Merging duplicated detection

In this step we will have to merge our predictions dataframe in order to have only one detection per crater. This is very important in order to make the dating algorithm accurate because if we have too many detections in a given geologic area, we will overestimate the age.

The good point with our way of splitting the images is that we are absolutely sure that we have

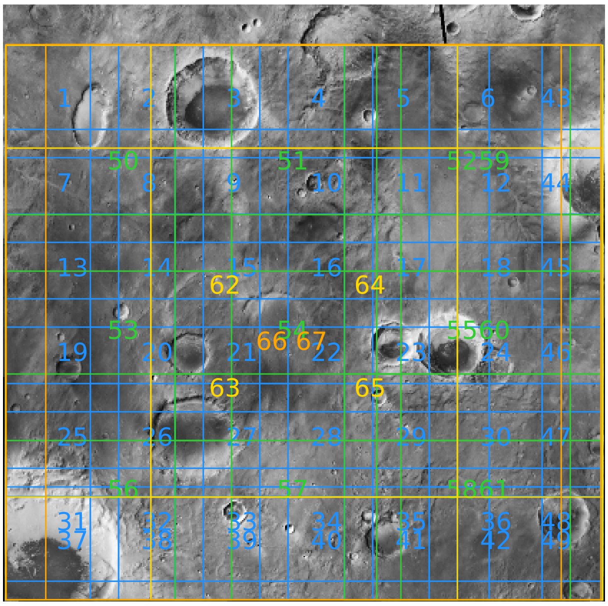

Figure 6.3: Image patches made on our original image. Each image patch has a size of 224×224 pixels. Blue patches correspond to the resolution of the original image, green patches to twice the resolution, and yellow patches to four times the resolution.

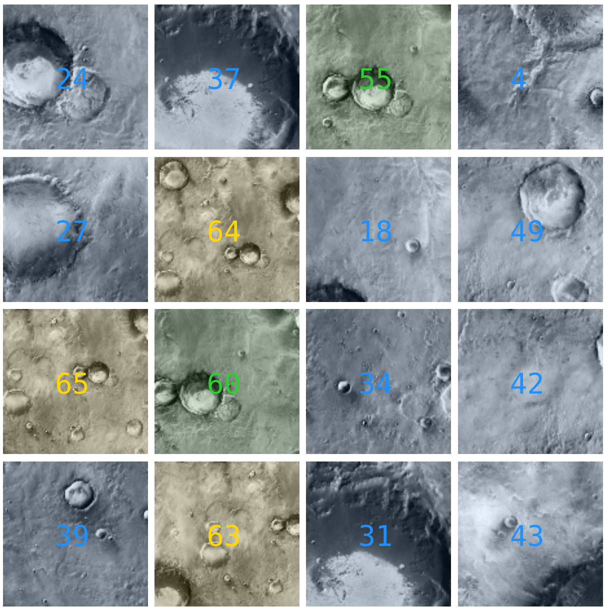

Figure 6.4: Random example of image patches at different downsampling levels (see Fig. 6.3). Blue patches correspond to the resolution of the original image, green patches to twice the resolution, and yellow patches to four times the resolution.

not missed any craters since every image patches overlap with each of its closest neighbours and with the higher resolution image patch (fig. 6.3). The problem with that way of doing is that every crater on the overlap zone will be potentially detected more than 1 times. In order to attribute one detection for a crater we will use an algorithm call Non-Maximum Suppression (NMS) algorithm (Hosang et al., 2017). This technique is commonly used in object detection tasks, and is even part of the latest computer vision algorithms such as Yolo v8 (Jocher et al., 2023). Its purpose is to eliminate redundant or overlapping detections, ensuring that only the most relevant and accurate detections are retained.

NMS addresses the multiple detection issue by iteratively selecting the detection with the highest confidence score (i.e., the likelihood that the detection is correct) and suppressing any other detections that significantly overlap with it. The process typically involves the following steps:

1. *Sort Detections*: First, the algorithm sorts the detections based on their confidence scores in descending order.

2. *Select the Highest Confidence Detection*: The detection with the highest confidence score is selected as the starting point.

3. *Suppress Overlapping Detections*: For each remaining detection in the sorted list, if its overlap (measured using metrics like Intersection over Union) with the selected detection exceeds a certain threshold (0.5 for us), it is suppressed or discarded.

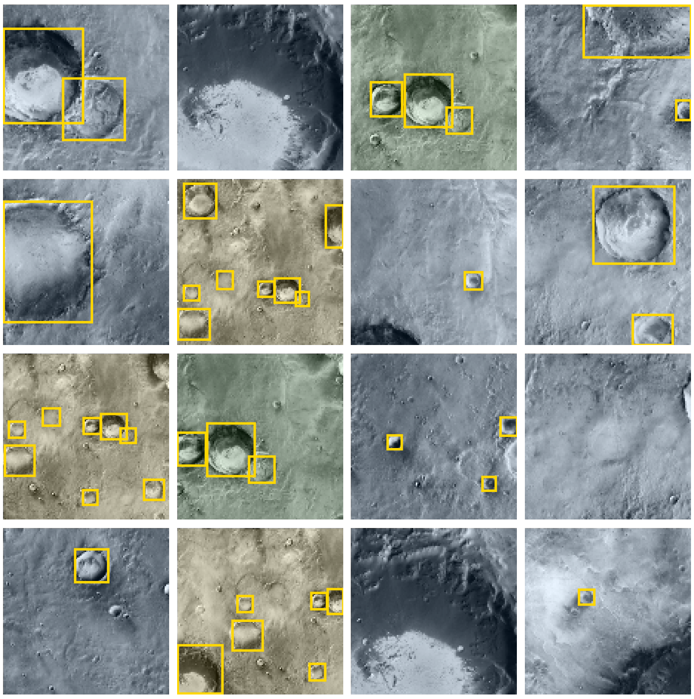

Figure 6.5: Inferences bounding boxes made in small patches of images. The color of each image represent their level of downsampling compared to the original image. Blue image patches correspond to the patches made at the resolution of the original image. Green patches at twice the resolution of the original image. Yellow patches at 4 times the resolution of the original image.

4. *Repeat*: This process is repeated until all detections have been examined.

By applying NMS, the algorithm effectively reduces multiple detections of the same object to a single, more accurate detection. This not only improves the accuracy of the detection results but also prevents overestimation of crater numbers in a given geological area.

Indeed, as we can see in figure 6.7, we now have only one bounding box of detection attributed to each crater.

6.2.4 - Improvement of our detection

While our detection tool successfully identifies craters, the bounding boxes it produces are not always perfectly aligned with actual crater rims in the image. Such misalignments, inherent to many object detection algorithms, can affect the precision of subsequent analyses, especially when crater geometry is important for classification or morphological studies. To address this, we implemented a refinement step that re-evaluates and updates the position and size of each detected crater directly from the image data. This enhancement builds upon the initial detection results, ensuring that the crater localisation is as accurate as possible before moving to the next stages of processing. In the chapter 2, we developed a tool developed to improve the precision of a crater database using a circle detection method called Hough transform. This optional step is proposed to improve the crater position. Hereafter the algorithm is shortly summarized.

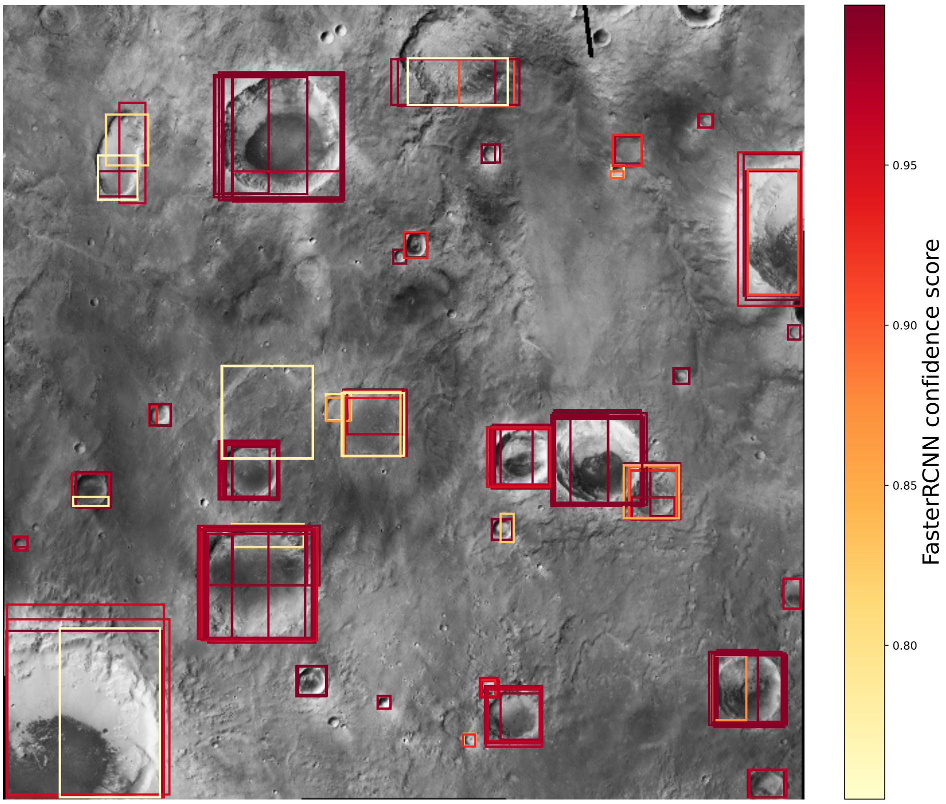

Figure 6.6: Inferences bounding boxes made in small patches of images and represented on the original image.

This tool takes as input the position and radius R of a given crater and it crops an image patch around it with a size of $4 \times R$. Then it applies to this image patch a canny edge detection filter (Van der Walt et al., 2014) which made crater edges appear as a complete or partial circle. In a next step it uses a method developed by Hough (1962) to detect lines in images and improved by Duda et al. (1972) to detect more complexes figures such as circles. Combining the position of the prediction made by our deep-learning model and the estimate from circle detection, we can improve the position of the prediction in a very impressive way. Indeed it works in 94% cases and it enables us to have a robust and precise database of craters such as seen in fig 6.8

6.2.5 - Restriction to a geological unit

In most cases, we may want to restrict our analysis to craters located within a specific geological unit, for example to study a particular terrain age or surface process. This restriction is applied using a shapefile delineating the unit boundaries. Usually the user defines it with the desired geometry (Fig. 6.9). If not, by default the full image is considered.

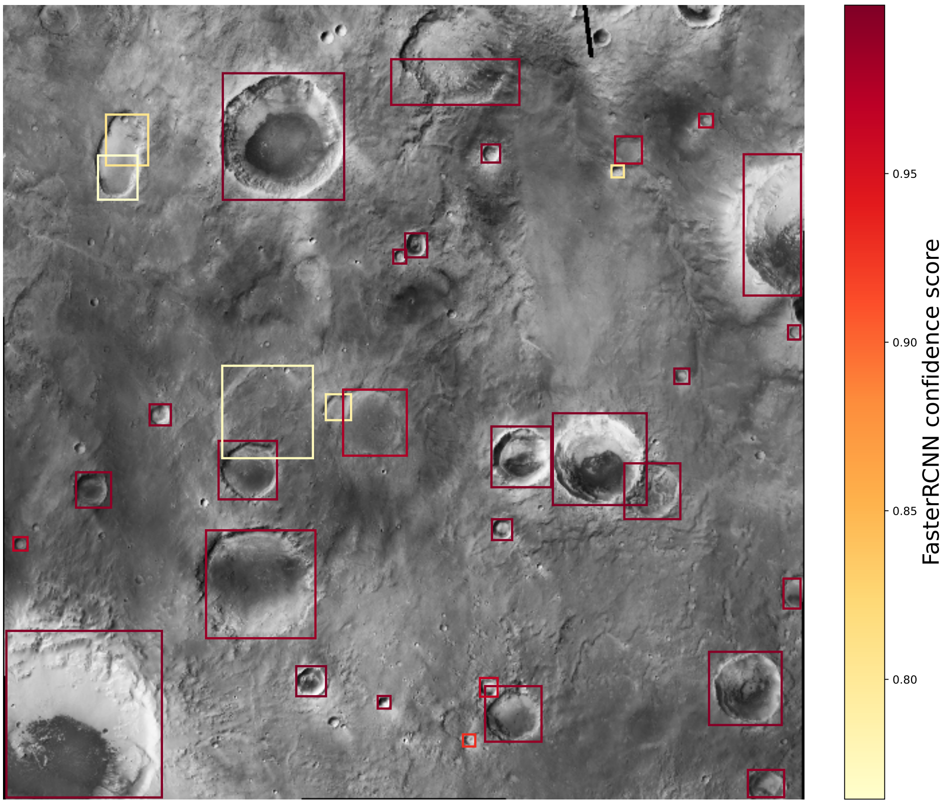

Figure 6.7: Inferences made on the images. the color of the bounding box correspond to the confidence score given by the algorithm

For each crater in our database, the geographical coordinates of its centre are compared to the polygon(s) in the shapefile. Only craters whose centres fall within the selected polygon are retained for further analysis. This centre-based criterion ensures a consistent and computationally efficient selection, avoiding partial inclusion ambiguities that would occur if a crater's rim intersected the unit boundary.

6.2.6 - Classification

Once the crater dataset has been restricted to the selected geological unit, the next step consists in assigning a morphological class to each crater. This classification is based on the geomorphological categories defined in section 4, which distinguish between various crater states such as fresh, degraded, eroded/buried, or secondary. The input data for this step are the crater images cropped with a size of 4 crater radius[2] according to the bounding boxes refined in the previous steps, ensuring that the crater is fully contained in the image while preserving its immediate surroundings. The classification itself is performed using our trained deep-learning model, which has been optimised to recognise morphological

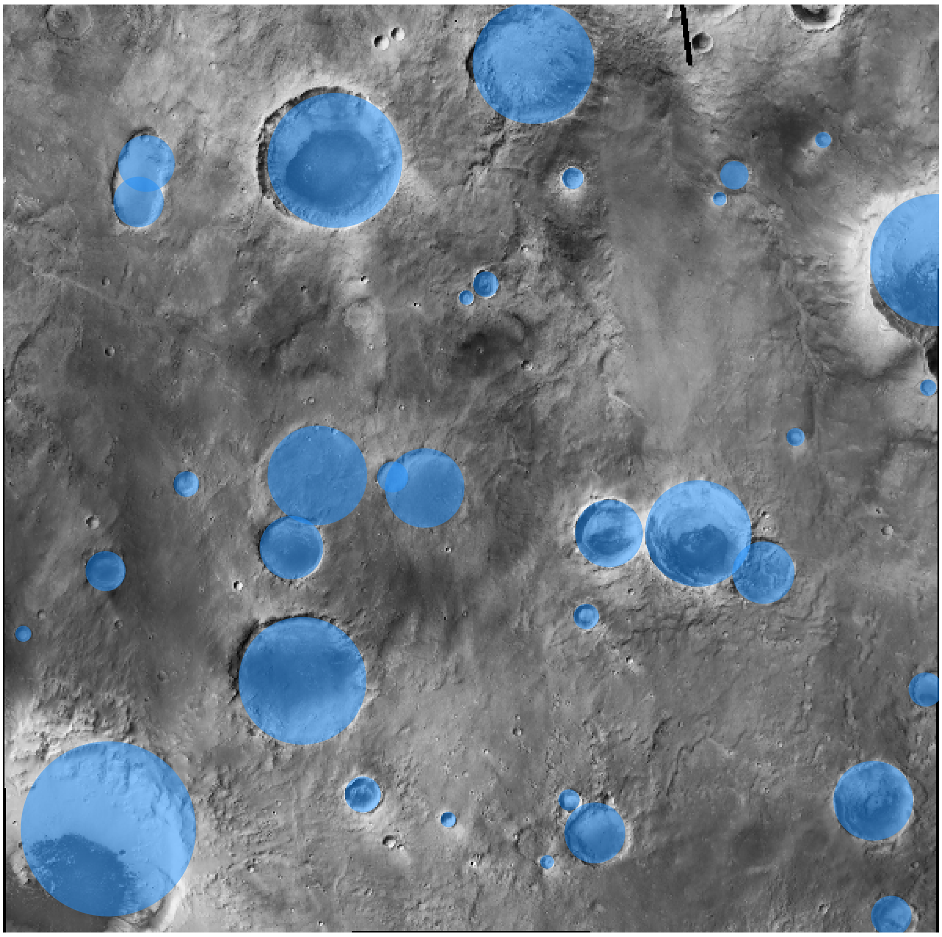

Figure 6.8: Craters corrected by the circle detection algorithm

features from high-resolution imagery. Each crater image is passed through the model, which outputs a probability score for each class. The class with the highest probability is assigned as the predicted morphology for that crater. To ensure robustness, predictions with probabilities below a certain confidence threshold are flagged for manual verification. This step is crucial for subsequent analyses, as it allows us to exclude secondary craters or highly degraded features that should not be included in crater-count dating. Moreover, the classification results can be cross-compared with independent datasets or used to evaluate spatial patterns in crater degradation, potentially revealing regional geological processes.

6.2.7 - Age determination

Now that we have the relevant craters, we use the standard technique to estimate an age (Hartmann, 2005). We include in our pipeline the python package *craterstats* (Michael et al., 2016b) to draw the crater-size frequency distribution curve and determine the age of the geological unit present in our image.

In the next section we will show examples of this datation process

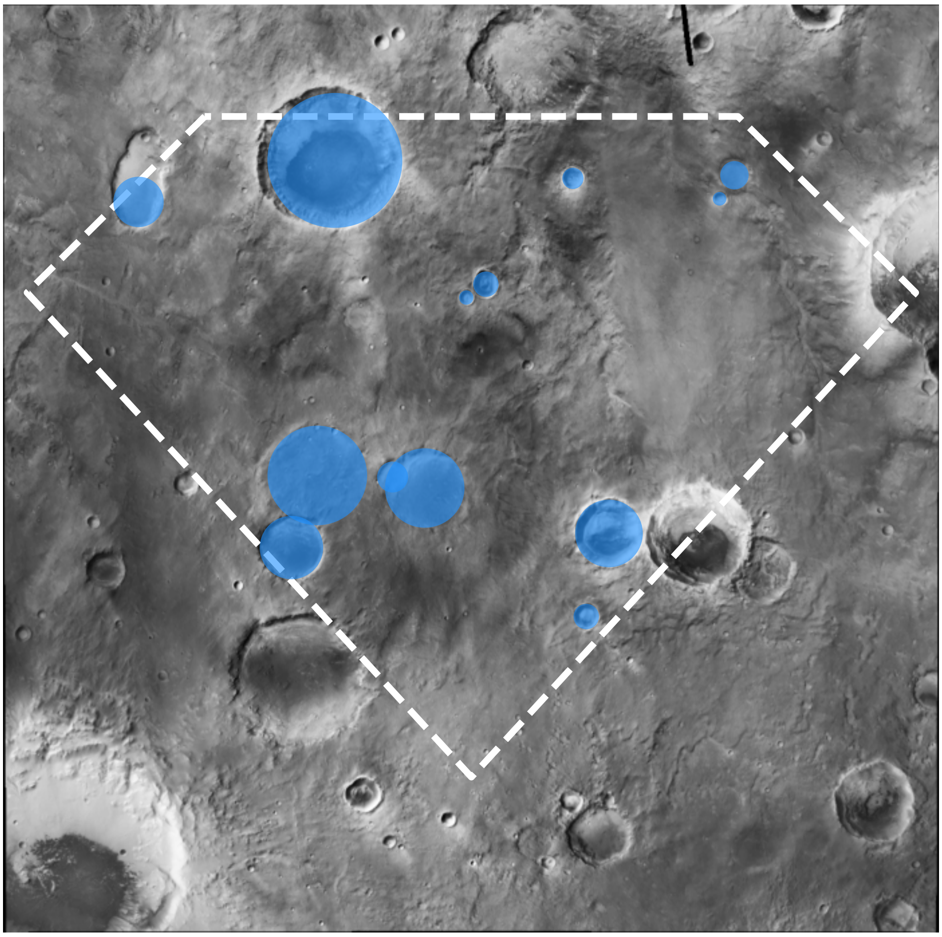

Figure 6.9: Craters used for datation selected in the area of interest (here taken as an arbitrary diamond shape).

6.3 - Results — datations

In order to show the full diversity of data that can be analyzed using the methodology presented in the previous section, we will present a few examples.

6.3.1 - Mars

MER-B landing site: Dating and analysis of a Noachian Terrain We applied the ACDC pipeline to the MER-B (Opportunity) landing site in Meridiani Planum, restricting the analysis to the mapped geological units and using CTX imagery as input (see Fig. 6.10). After detection, merging of the bounding boxes using non-maximum suppression, and refinement, the final crater set was used to derive crater size–frequency distributions (CSFDs) and model ages.

Overall, as can be seen in Fig.6.12, our ACDC-derived ages are consistent with published values calculated by Hynek et al. (2017) and shown in Fig. 6.11 for Meridiani Planum. In particular, for the cratered highland units (HMh), our fits yield Noachian ages near ∼3.9Gy, in line with the USGS map results reported by Hynek et al. (2017).

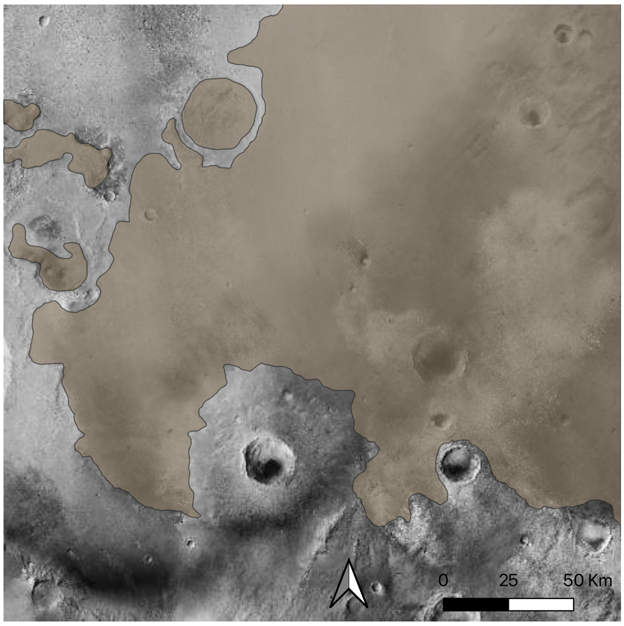

Figure 6.10: Meridiani Planum quadrangle where the MER-B has landed (-5.5266°E, 1.9462°S) superposed with a part of the geological unit defined by Hynek et al. (2017)

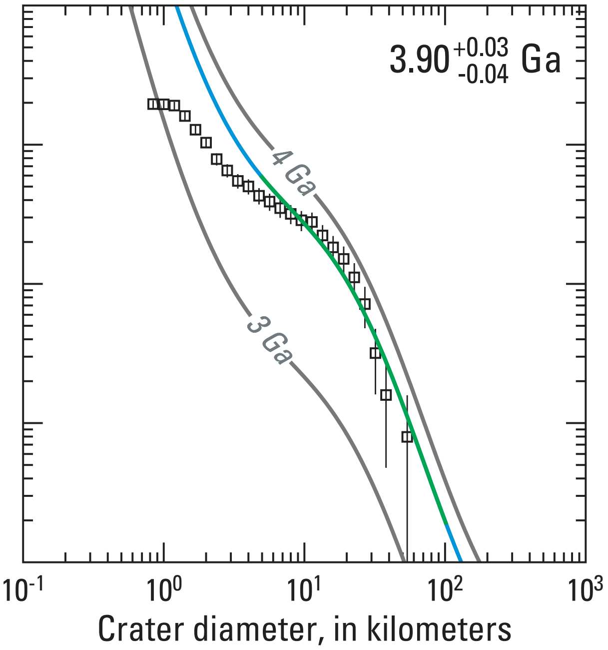

Figure 6.11: Age determination made by Hynek et al. (2017) of the corresponding geological unit presented in Fig. 6.10.

Zhurong landing site: Dating and analysis of an Early Amazonian Terrain The Zhurong rover, part of the Tianwen-1 mission, landed on 14^{th} May 2021 in southern Utopia Planitia (25.066° N, 109.925° E) within the Amazonian lowlands of Mars. This region is characterized by relatively smooth terrains, interpreted as resurfaced plains, with a sparse population of large craters but abundant small features such as secondary craters and pitted cones. Previous studies based on crater size–frequency distribution (CSFD) analysis have suggested resurfacing ages ranging from early to middle Amazonian, with significant variability depending on the chosen count area and interpretation of crater morphologies (Tanaka et al., 2014; Zhang et al., 2025).

In our analysis, we applied the same deep-learning–based detection and geomorphological classification pipeline as for other landing sites (chapter 3 and 4). We restricted the count area to the CTX quadrangle presented in Fig. 6.13, focusing on craters with diameters above 100m to ensure robust detection and minimize classification uncertainties. The resulting cumulative crater frequency curve shown in Fig. 6.14 was fitted using the Hartmann (2005) chronology model to estimate the model surface age. Our CSFD for Zhurong's surroundings yields an absolute model age of $\sim 3.04 \pm 0.2, Gy$ (Early Amazonian), in very good agreement with the model age from the Zhurong landing site found at 3.01 Gy(Wu et al., 2022). Notably, our results reinforce the interpretation that the plains in southern Utopia Planitia underwent significant resurfacing during the Amazonian, most likely through processes such as mud volcanism, ice-related sediment mobilization and volcanic flooding, which effectively reset

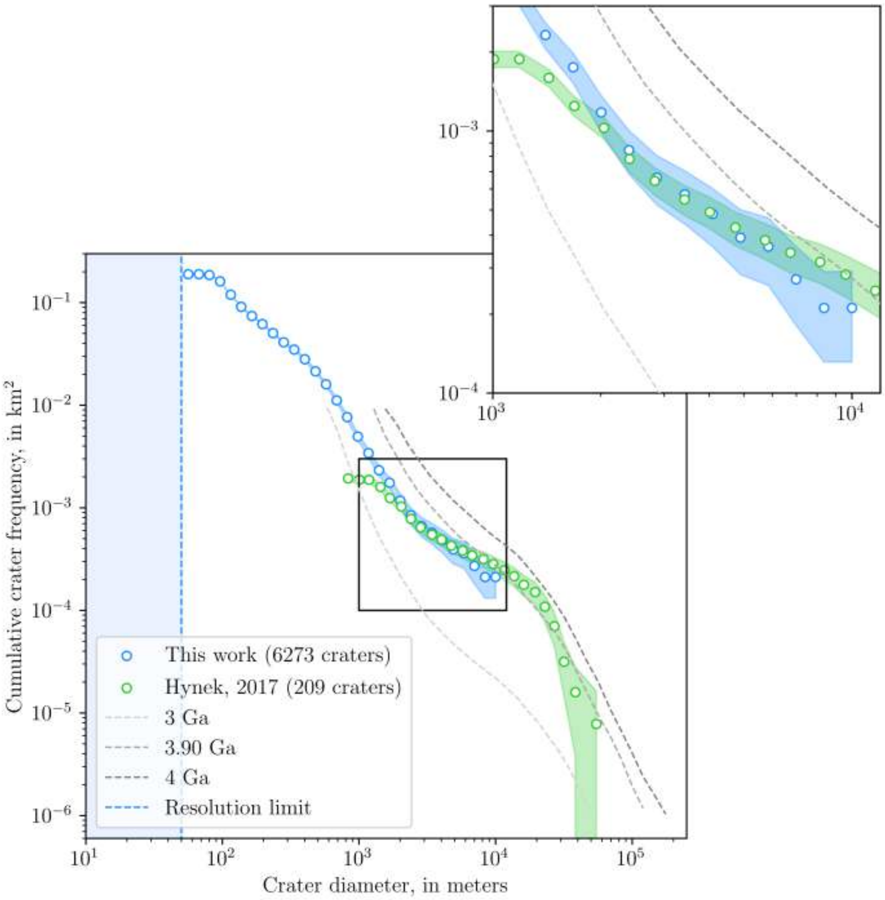

Figure 6.12: Cumulative crater frequency distribution (CCFD) for the Meridiani Planum geological unit defined in Fig 6.10. The green curve corresponds to the CCFD compiled by Hynek et al. (2017), while the blue curve represents the results obtained with our crater detection algorithm. In the overlapping crater size range, both curves show consistent results, which supports the reliability of our detections and demonstrates the robustness of the method when compared with established studies.

the small-crater population while preserving larger, older impact structures. Comparing our curve to that of Wu et al. (2022), we observe a similar slope in the 1–10 km diameter range, indicating a consistent crater production rate in this size interval. This agreement is particularly encouraging given that Utopia Planitia presents one of the most challenging contexts for crater dating due to its low crater density and the strong influence of resurfacing processes.

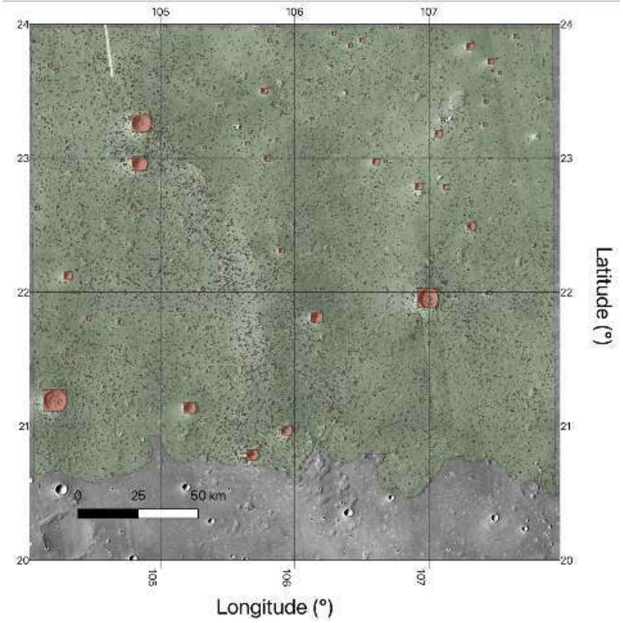

Figure 6.13: Utopia Planitia quadrangle near the Zhurong rover landind site (landing site : 25.066° N, 109.925° E) superposed with a part of the geological unit define by Zhang et al. (2025). The crater detections are made with our crater detection algorithm.

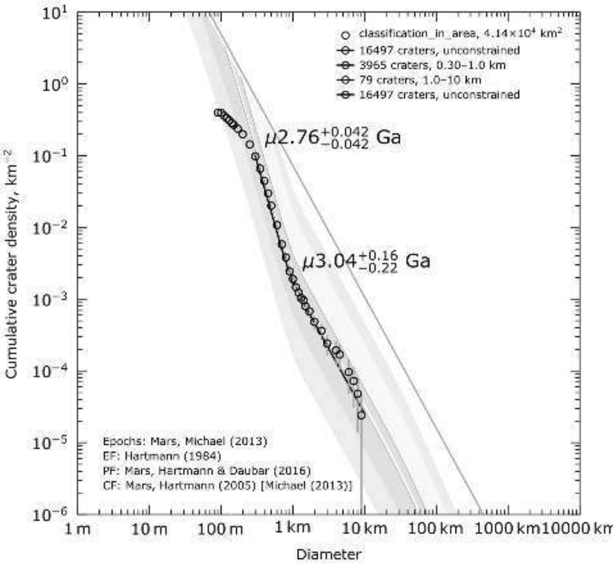

Figure 6.14: Age determination of the geological unit shown in Fig. 6.13, derived using our crater detection and characterization algorithm and compared with the results reported by Zhang et al. (2025). The inferences presented in this figure are sorted according to geomorphological features, ensuring that neither secondary nor ghost craters are included in this example.

6.3.2 - Moon (Kaguya-based analyses)

Mare Tranquillitatis For the Moon, we leveraged Kaguya datasets to run the ACDC pipeline: high-resolution imagery from the Terrain Camera (TC, ∼7.4m/pixel) for detection. After detection, fusion of the bounding boxes using non-maximum suppression, and refinement, the final crater and restriction to the spectrally consistent units defined by Bultel et al. (2023), we computed crater size–frequency distributions (CSFDs) and fit them to standard lunar chronology functions (Neukum et al., 2001) to obtain absolute model ages.

Our CSFD curves represented in Fig. 6.16 for multiple MI-defined basalt units yield late Imbrian model ages, consistent with the classic results that place most Imbrium mare flows between ∼3.8 and ∼3.0Ga, with a concentration in the 3.6–3.8Ga interval (Werner et al., 2023).

However, detection results should be interpreted with caution, as the crater identification is far from complete. While the detection network trained on Martian imagery is able to locate a fraction of lunar craters, many features remain undetected, particularly in regions where the regolith morphology strongly differs from Martian surfaces. Factors such as the higher albedo contrasts, the prevalence of bright ejecta rays, and the distinct degradation patterns of lunar craters contribute to a significant domain shift between the two datasets.

Moreover, the geomorphological classification stage, which was optimised for Martian crater types, does not generalize well to lunar imagery. The textural and morphological cues used by the classifier are often absent or expressed differently on the Moon, resulting to a high misclassification rate. Consequently, the morphological classes derived in this study for lunar craters must be considered unreliable, and the chronological analysis focuses solely on the detected crater positions and sizes. This highlights the importance of developing Moon-specific training datasets and models for both detection and classification to achieve results comparable in quality to those obtained for Mars.

Overall, the agreement with published CSFD solutions supports the robustness of our fully automated workflow while highlighting the expected sensitivity of model ages to unit definitions, secondary-crater handling, and completeness limits.

Thanks to the collaboration with B.Bultel, we were able to use their counting units to perform dating in the same area.

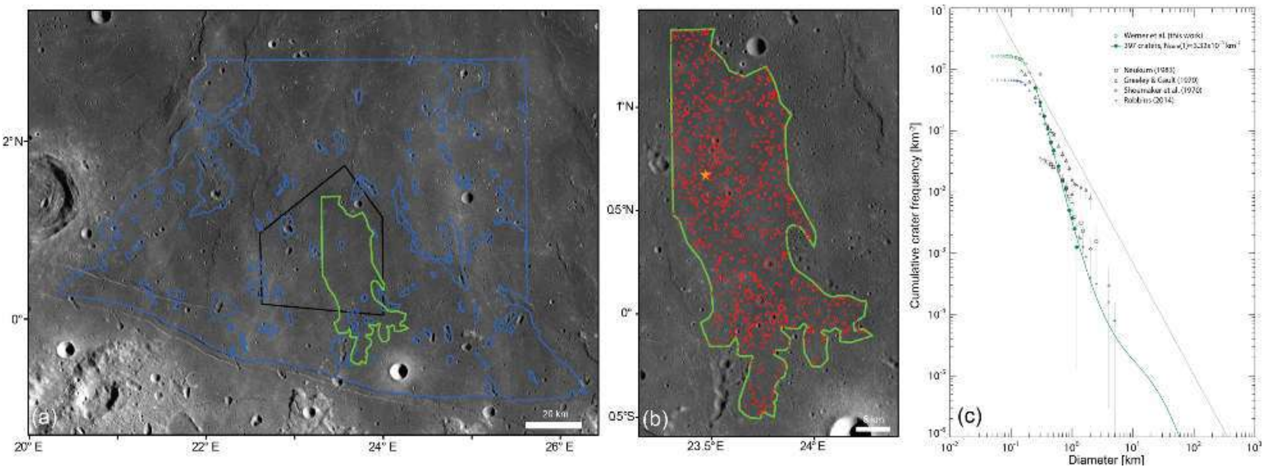

Figure 6.15: Figure from Werner et al., 2023 : Crater statistics at the Apollo 11 site unit. (a) Comparison of various counting units (green, Werner et al. and this work; black, Neukum et al., 1976a; blue, Robbins, 2014). (b) Counting unit with craters following. (c) The resulting crater size–frequency distributions. This figure is useful to be compare with Fig. 6.16.

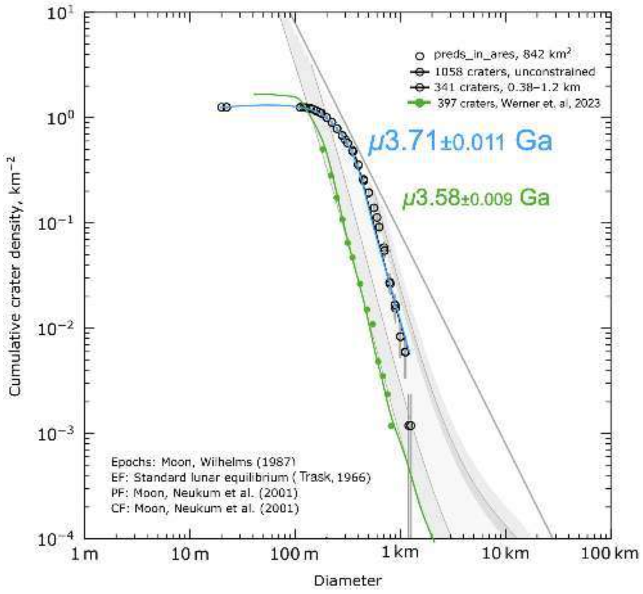

Figure 6.16: Crater statistics at the Apollo 11 site unit. Werner et al., 2023 counting units (green) shown in Fig. 6.15 and the detections made with our Mars-trained crater detection algorithm (blue).

6.4 - Discussion and conclusion

Our application of the deep-learning crater detection and classification workflow to CTX and Kaguya high-resolution imagery confirms the feasibility of generating robust crater size–frequency distributions (CSFDs) for both martian and lunar terrains across a range of geological contexts. The derived CSFDs closely follow the expected trends predicted by established lunar chronology models, particularly those of Neukum et al. (2001) and Hartmann (2005), within the uncertainties inherent to the measurement process.

For relatively young surfaces, such as the Moon's mare plains investigated here, the automated counts yield age estimates consistent with previous studies based on manual crater counts.

In martian highland regions, the CSFDs approach the saturation regime at small diameters, as expected from the dense impact history of the early Mars. Our method successfully captures this saturation roll-off, further supporting its validity.

Nevertheless, if the martian-trained model enables detection of craters on the moon, we observed that the precision of the detections is not optimal. Also, the classification tool definitely needs to be reinforced with lunar data to make the model able to detect the morphological specificities of lunar craters partly induced by space weathering.

Overall, these results demonstrate that our automated methodology can not only reproduce the outcomes of traditional lunar chronology techniques but also scale them to much larger areas and datasets in a much shorter time.

7 - Conclusion et perspectives

This thesis presents a comprehensive study dedicated to develop an automated framework for the detection, characterization, and chronological analysis of impact craters. In this conclusion chapter, we synthesize the main results obtained, discuss their significance in the broader context of planetary surface dating, and highlight the remaining open questions. We also outline future research directions that could further advance automated approaches to planetary chronology.

7.1 - General conclusion

The study of planetary surface chronology relies on the accurate identification, measurement, and interpretation of impact craters. Traditional approaches, based on manual crater counting, have provided decades of valuable data but remain intrinsically limited: the process is laborious, time-consuming, and subject to inter-operator variability (Benedix et al., 2020). As the volume of high-resolution planetary imagery has grown exponentially, such manual inventories like Robbins et al. (2012) are now impractical at global scale, making the development of robust automated detection methods an essential step forward.

Beyond detection alone, morphological classification of craters plays a critical role in planetary surface dating. The exclusion of secondary, highly degraded, or otherwise altered craters (Ghost craters) is essential to avoid significant biases in age estimates. While classification is routinely performed manually in traditional crater counting, it has rarely —if ever— been implemented in a fully automated, large-scale manner. This gap has limited the reliability and reproducibility of crater-based chronologies, especially when applied to extensive and morphologically diverse datasets such as those of Mars or the Moon.

Similarly, the determination of crater superposition orders which is an important tool for relative dating, remains an emerging field in automated planetary geomorphology. In this thesis, we developed and validated a preliminary framework for automatically determining these relationships. Although still in an exploratory stage, this approach already confirms interpretations drawn from cumulative crater frequency distributions curves (CCFDs) and opens the way for more quantitative applications.

By integrating these two methodological pillars —automatic crater detection and automated morphological classification— this work delivers a unified inference pipeline for planetary surface analysis. Such an end-to-end system, capable of processing large volumes of high-resolution imagery and outputting refined crater inventories ready for chronological interpretation, did not exist prior to this study. The resulting tool not only improves a process that was once manually done but it also improves the objectivity, reproducibility, and scalability of crater-based dating. In doing so, it provides the planetary science community with a robust framework for producing more accurate and consistent chronologies, ultimately enhancing our understanding of the geological evolution of planetary bodies.

7.2 - Advances in Automatic Crater Detection

In chapter 3, we presented the first major methodological axis of this thesis which was the development of a robust, fully automatic crater detection algorithm. Our detection model is able to operate at global scale, across all latitudes, and for a wide range of crater sizes. Traditional crater detection pipelines often rely on single-scale analysis, making them sensitive to variations in resolution, illumination, and local morphology. Such approaches tend to underperform in high-latitude regions, where illumination conditions are extreme and image distortions are more pronounced.

To overcome these limitations, we implemented a multi-scale detection strategy specifically tailored to Context Camera (CTX) global mosaics. Each image was processed at several spatial resolutions, ensuring that both large craters and smaller features were equally represented in the detection process. The resulting candidate lists from different scales were then merged through a non-maximum suppression step, which removed duplicate detections while preserving the highest-confidence candidates. We proved that this approach particularly is effective in reducing missed detections at the poles and in complex terrains such as heavily degraded highlands.

The detection model itself was based on a deep learning architecture optimized for object detection in planetary imagery. Leveraging transfer learning and a curated training set derived from the geometrically refined crater database, the network learned to recognize crater rims under diverse morphological and illumination conditions. Rigorous evaluation across different latitudes demonstrated that the model maintained high recall and precision even in areas traditionally challenging for automated detection.

By integrating multi-scale processing with deep learning-based detection, this pipeline represents a significant advance over previous methods. With a mAP_{50} score of ~ 0.8, it offers a scalable, consistent, and reproducible approach to global crater mapping, enabling the generation of comprehensive crater inventories suitable for chronological analyses and further geomorphological interpretation.

Finally, we would like to mention that in this work, we used the standard approach used in the deep learning scientific community, to ensure the robustness of the results. Since the approach is empirical, the artificial neural network is evaluated in a dataset, completely independant from the learning dataset and completely independant from the dataset used to optimise the parameters. At the end, this approach offers the best garanty for scientific applications. This aspect is taken into account through all the PhD.

7.3 - Automatic Crater Characterization

Beyond detecting the presence of craters, accurately describing their geometry and morphology is essential for reliable planetary surface dating. In particular, differentiating between primary craters and features such as secondaries, ghost craters, or craters with fluidized ejecta (Layered) is critical to avoid biases in size–frequency distribution analyses. Despite its importance, morphological classification has rarely been implemented in a fully automated way and at planetary scale, with most inventories relying on manual or semi-automatic classification prone to human subjectivity.

Building on the refined crater database obtained through the Hough transform pre-processing (see chapter 2), we trained a deep learning classification model capable of assigning each crater to one of four morphological classes defined by Lagain et al. (2021a): regular, secondary, ghost, or layered. The network architecture, based on the YOLOv11 framework, was optimized for small object classification in high-resolution planetary imagery as described in chapter 4.

To improve the model's robustness, the training set was balanced across classes and augmented with transformations simulating different illumination conditions, rotations, and noise levels. The final classifier achieved high overall accuracy of 0.80 on the validation set, with particularly strong performance for regular and secondary craters. However, as demonstrated in the lunar application case, morphological differences in regolith properties between Mars and the Moon can degrade classification accuracy, underscoring the importance of body-specific model training.

The resulting automatic classification step adds a critical layer of information to crater inventories, enabling the systematic exclusion of features that should not contribute to chronological models. Combined with the detection pipeline, this capability represents a significant step toward producing cleaner, more reliable datasets for planetary surface dating, and sets the stage for broader applications across different planetary bodies.

7.4 - Automatic Determination of Crater Superposition Order

Determining a correct and precise Cumulative Crater-Frequency Distribution curve is the most important operation to calculate the absolute age of planetary surfaces. Beyond size–frequency distribution analysis, one of the most direct indicators of relative age at the scale of individual craters is the order of superposition: if a crater overlaps or cuts another, it is necessarily younger.

In the chapter 5 of this thesis, we developed a preliminary framework to automatically identify superposition relationships between craters within a given inventory. The method analyses the spatial intersections between crater rims, comparing the geometry of overlaps to assess whether one crater partially or fully truncates another. By combining geometric reasoning with diameter and positional data, the algorithm assigns a relative age order to each pair of interacting craters. This process was applied to the geometrically refined and morphologically filtered inventories produced in earlier stages of the pipeline, ensuring that only relevant, well-defined craters were included.

Although this work represents a first step, it has already yielded scientifically valuable results. Our automated superposition detection order algorithm reach an impressive accuracy score of 0.975 on an independant evaluation dataset. It confirmed trends observed in cumulative crater frequency distributions (CCFDs) for specific regions, supporting the validity of the derived chronological interpretations. In the near future, integrating this method with the analytical framework proposed by Hirabayashi et al. (2024) will allow estimation of the number of buried or otherwise undetectable craters in each size bin. Such estimates will directly feed into refined age models, including those of Hartmann (1970) and Neukum (1983), by correcting for the incompleteness of observed populations.

By formalizing and automating the extraction of superposition information, this approach opens a new pathway for relative dating that complements and enhances traditional statistical methods. As the algorithm matures, it has the potential to become a standard tool in planetary chronology, enabling more precise reconstructions of surface evolution histories across diverse planetary bodies.

7.5 - ACDC: A New Tool for Planetary GIS Applications

A more technical outcome of this thesis is presented in chapter 6 as the integration of all developed components—crater poisition refinement, multi-scale crater detection and morphological crater classification—into a single, coherent framework: the Automatic Crater Detection and Characterization (ACDC) tool. Designed with reproducibility, scalability, and interoperability in mind, ACDC enables planetary scientists to process large volumes of high-resolution imagery and generate crater inventories directly usable with a python-compatible Geographic Information System (GIS) environments.

ACDC takes as input calibrated and georeferenced image mosaics, such as the global CTX mosaic of Mars, and gives as output crater catalogs enriched with geometric parameters, morphological labels, and relative age relationships. All results are stored in widely supported formats (e.g., shapefiles and CSV) that can be directly imported into standard GIS software. This design ensures compatibility with existing planetary mapping workflows, facilitating integration with ancillary datasets such as geological maps, topography, and mineralogical products.

By centralizing multiple analytical steps into a single automated pipeline, ACDC framework offers what has traditionally been made manually to make crater counting based age determination on given geologic units. Researchers can now move from raw imagery to a scientifically-certified crater database ready for chronological analysis, saving significant time while improving the consistency of results. The modular architecture of ACDC also makes it adaptable to new sensors, new planetary bodies, and analytical objectives.

Beyond its immediate applications in Mars science, ACDC's methodology is transferable to other planetary datasets, including lunar, hermean (on Mercury), and icy moon imagery. As such, it represents not only a contribution to the specific case studies addressed in this thesis, but also a versatile platform for advancing planetary surface dating and geomorphological mapping across the Solar System.

8 - Global Perspectives

Perspectives on Automatic Crater Detection and Characterization

From a methodological perspective, significant opportunities remain to advance automatic crater detection. When this project began, the state-of-the-art in convolutional neural network (CNN)-based object detection was represented by YOLOv3 and FasterRCNN. Since then, the field has rapidly evolved, with YOLOv11 now available and offering substantial improvements in speed and accuracy. While YOLOv11 has been employed in this thesis as a pure classifier (see Chapter 4), retraining a detection-specific model using this framework could yield higher precision and recall than earlier CNN architectures. Furthermore, emerging approaches based on attention mechanisms, such as transformer-based architectures (Vaswani et al., 2017), are already being explored for object detection (e.g., the upcoming YOLOv12). These could provide more flexible feature representation and better generalization across diverse imaging conditions.

Another promising perspective is the integration of domain knowledge through physics-informed neural networks (PINNs). Rather than training models solely to recognize the visual appearance of crater rims and ejecta, PINNs could incorporate physical laws governing impact crater formation directly into the learning process. This would enable the model to learn a more physically grounded concept of what constitutes a crater, potentially improving robustness under challenging imaging conditions and on morphologically diverse planetary surfaces specifically on the Moon where the space wheathering gives very specific properties to the regolith.

From a planetary science perspective, the rapid growth of global geomorphological databases provides opportunities to extend crater detection into broader geomorphological mapping. Datasets now exist for features such as Gullies, pitted cones, recent impact sites, and dark slope streaks for example (Noblet et al., 2024; Mills et al., 2024; Bickel et al., 2025a; Bickel et al., 2025b). Incorporating such inventories into training workflows could enable the development of multi-class geomorphological detectors, capable of identifying not only craters specific shape but a wide variety of landforms in a single inference pipeline. This would facilitate large-scale geological mapping and the detection of morphological correlations across different feature types.

Extending the detection dand classification framework to smaller crater populations, on the order of 100 m in diameter and below, represents another significant challenge and opportunity. At these scales, image resolution, illumination conditions, and surface texture play a critical role in detection performance. Features such as boulders, erosional pits, or patterned ground can exhibit morphologies that closely fits small craters, increasing the likelihood of false positives. Achieving reliable detection in this regime will require training on higher-resolution datasets, such as the full resolution dataset or even HiRISE images for Mars or LROC NAC images for the Moon, with careful curation of ground-truth annotations to capture the full diversity of small-crater morphologies. In addition, adapting the detection architecture to operate efficiently on very large images without downsampling—potentially through tiling strategies or multi-resolution inference—will be necessary to preserve fine-scale details. Successful extension to this size range would not only improve crater population statistics for young surfaces but also enable detailed studies of recent impact fluxes and surface modification processes.

Moreover, the transfer of the detection framework to other planetary bodies remains a key research direction. Preliminary experiments in this thesis have shown that the core detection pipeline performs reasonably well on lunar imagery, even with limitations described in section 6.4. Future work could improve cross-body generalization by reprocessing lunar or hermean imagery at global scale, retraining models with appropriate domain-specific data, and potentially incorporating reinforcement learning strategies to optimize performance in data-scarce or morphologically complex regions. Such efforts would pave the way for the creation of consistent, automated detection frameworks applicable across the Solar System.

Another important perspective when we talk about exporting the framework to other bodies lies in the fusion of data from multiple instruments to refine crater characterization and improve the detection robustness. In this thesis, the training step has done exclusively to images from the CTX mosaic, which provides uniform coverage of Mars at moderate resolution. While this approach was proved to be effective, the integration of complementary datasets could substantially increase positional accuracy and resilience to imaging artefacts. For example, combining CTX imagery with higher-resolution HiRISE data would allow for the refinement of crater rims in selected regions, while co-registering with HRSC stereo products or MOLA topography would provide additional constraints on rim elevation and circularity in three dimensions. Such multi-instrument approaches would mitigate issues related to illumination geometry, seasonal surface changes, or image artefacts present in a single dataset, ultimately producing more precise and reliable crater catalogs suitable for high-accuracy chronological analyses.

Perspectives on relative dating through crater superposition analysis

The preliminary framework for automated superposition analysis developed in this thesis (chapter 5) has demonstrated its potential to complement traditional crater size–frequency distribution (CSFD) methods by providing direct, geometry-based relative age relationships between craters. However, its current implementation is limited to identifying visible overlaps between crater rims and assigning relative ages accordingly. An important next step is to extend this framework to infer the number of craters that are no longer observable—either because they have been obliterated by subsequent impacts or buried by resurfacing events.

In this context, the analytical approach recently proposed by Hirabayashi et al. (2024) offers a promising path forward. Their work formulates a set of equations linking observed CSFDs to the total crater production function, accounting for the progressive loss of craters through superposition and erosion. By integrating these equations into the automated superposition pipeline, it would be possible to estimate, for each diameter bin, the number of craters that have been removed from the visible record. This, in turn, would allow for the reconstruction of a more complete impact chronology and the refinement of absolute age models such as those by Hartmann (1970) and Neukum (1983).

Realizing this integration will require several methodological advances. First, the automated detection of superposition events must be extended to distinguish between partial and full overlaps, as this distinction influences the inferred obliteration rate. Second, the algorithm should be capable of quantifying the clusters of superposition events, which may signal episodic resurfacing processes. Finally, a systematic validation campaign against manually interpreted superposition datasets will be essential to assess the accuracy and reliability of the derived obliteration estimates.

Such an integrated system — combining geometric superposition analysis with physically grounded loss-function models — would represent a step change in automated planetary chronology. It would not only refine surface age estimates but also provide insights into resurfacing histories and the dynamical processes governing crater population evolution over geological time.

Perspectives on the inference pipeline

The inference pipeline developed in this thesis (see chapter 6), represents a fully integrated framework for automatic crater detection, crater position refinement, morphological classification, and relative dating. As a modular and reproducible workflow, it offers a solid foundation for further development into tools that can be readily adopted by the planetary science community.

A natural next step is to package the pipeline as a QGIS plugin (QGIS Development Team, 2009). Such an implementation would enable users to run the full inference workflow directly within a familiar GIS environment, leveraging QGIS's capabilities for data visualization, spatial querying, and integration with other planetary datasets. This would lower the entry barrier for non-coder users, allowing planetary geologists to generate, visualize, and analyze crater catalogs without requiring extensive programming expertise.

Another promising direction is the integration of the pipeline into the ESA Planetary Science Archive[1] (Besse et al., 2018) or, but maybe later on, on the online planetary data visualization platforms, such as the MuTeD (Multi-Temporal Data) system maintained by the University of Münster[2](Heyer et al., 2018). Those plateform integrations would allow users to interactively explore the outputs of the pipeline—detection results, morphological classifications, and superposition relationships—overlaid on high-resolution planetary imagery. Such integration would not only enhance accessibility but also promote collaborative analysis, enabling researchers worldwide to inspect results, annotate features, and contribute feedback in real time.

Beyond these integration efforts, the inference pipeline could be extended to handle multi-body processing in a single deployment, allowing users to switch seamlessly between Mars, the Moon, and Mercury with body-specific detection and classification models. Coupled with standardized data export formats (Shapefiles, or database connections), this would facilitate interoperability with a wide range of planetary science tools, fostering reproducibility and cross-comparison of results between different missions and datasets.

---

[1] ESA PSA: `https://psa.esa.int/`

[2] University of Münster's MuTeD plateform: `https://muted.uni-muenster.de/`

References

Akiyama, Eiji et al. (Feb. 2016). “Planetary System Formation In The Protoplanetary Disk Around Hl Tauri”. In: *The Astrophysical Journal* 818.2, p. 158. ISSN: 1538-4357. DOI: 10.3847/0004-637x/818/2/158.

Alfvén, Hannes (Aug. 1977). “Electric currents in cosmic plasmas”. In: *Reviews of Geophysics* 15.3, pp. 271–284. ISSN: 1944-9208. DOI: 10.1029/rg015i003p00271.

Ali-Dib, Mohamad (Nov. 2022). “A machine-generated catalogue of Charon’s craters and implications for the Kuiper belt”. In: *Icarus* 386, p. 115142. ISSN: 0019-1035. DOI: 10.1016/j.icarus.2022.115142.

Ali-Dib, Mohamad et al. (July 2020). “Automated crater shape retrieval using weakly-supervised deep learning”. In: *Icarus* 345, p. 113749. ISSN: 0019-1035. DOI: 10.1016/j.icarus.2020.113749.

Appere, Thomas (July 2012). “Cycle actuel de l’eau sur Mars: étude des dépôts saisonniers de l’hémisphère nord par télédétection hyperspectrale (OMEGA/Mars Express)”. PhD thesis. Institut de Planétologie et d’Astrophysique de Grenoble. URL: https://theses.hal.science/tel-00745121v1.

Aquino, Marcelo Romero et al. (Oct. 2017). “The Effect and of Data and Augmentation on the Performance and of Convolutional and Neural”. In: *Brazilian Society of Computational Intelligence*. DOI: 10.21528/CBIC2017-51.

Baker, David M.H. et al. (Aug. 2011). “The transition from complex crater to peak-ring basin on the Moon: New observations from the Lunar Orbiter Laser Altimeter (LOLA) instrument”. In: *Icarus* 214.2, pp. 377–393. ISSN: 0019-1035. DOI: 10.1016/j.icarus.2011.05.030.

Baker, V. R. et al. (Aug. 1991). “Ancient oceans, ice sheets and the hydrological cycle on Mars”. In: *Nature* 352.6336, pp. 589–594. ISSN: 1476-4687. DOI: 10.1038/352589a0.

Baldwin, Ralph B. (Feb. 1971). “On the history of lunar impact cratering: The absolute time scale and the origin of planetesimals”. In: *Icarus* 14.1, pp. 36–52. ISSN: 0019-1035. DOI: 10.1016/0019-1035(71)90100-x.

Bandeira, L et al. (2008). “Crater mapping in the Gusev crater area using an automated method”. In: *Proceedings of the 3rd European Planetary Science Congress, p. A-00360-1. Abstract.*

Bandeira, LourenÇo et al. (Dec. 2007a). “Impact Crater Recognition on Mars Based on a Probability Volume Created by Template Matching”. In: *IEEE Transactions on Geoscience and Remote Sensing* 45.12, pp. 4008–4015. ISSN: 0196-2892. DOI: 10.1109/tgrs.2007.904948.

Bandeira, Lourenço et al. (Jan. 2012). “Detection of sub-kilometer craters in high resolution planetary images using shape and texture features”. In: *Advances in Space Research* 49.1, pp. 64–74. ISSN: 0273-1177. DOI: 10.1016/j.asr.2011.08.021.

Bandeira, Lourenço P. C. et al. (2007b). “Lecture Notes in Computer Science”. In: *Pattern Recognition and Image Analysis*. Springer Berlin Heidelberg. Chap. Development of a Methodology for Automated Crater Detection on Planetary Images, pp. 193–200. ISBN: 9783540728474. DOI: 10.1007/978-3-540-72847-4_26.

Barata, Teresa et al. (2004). "Automatic Recognition of Impact Craters on the Surface of Mars". In: *Image Analysis and Recognition*. Springer Berlin Heidelberg, pp. 489–496. ISBN: 9783540301264. DOI: 10.1007/978-3-540-30126-4_60.

Barboni, Melanie et al. (Jan. 2017). "Early formation of the Moon 4.51 billion years ago". In: *Science Advances* 3.1. ISSN: 2375-2548. DOI: 10.1126/sciadv.1602365.

Barlow, Nadine G. et al. (Nov. 2000). "Standardizing the nomenclature of Martian impact crater ejecta morphologies". In: *Journal of Geophysical Research* 102.E11, pp. 26 733–26 738. DOI: 10.1029/2000JE001258.

Becker, K. J. et al. (Dec. 2009). "Near Global Mosaic of Mercury". In: *American Geophysical Union, Fall Meeting 2009*, P21A–1189. URL: https://ui.adsabs.harvard.edu/abs/2009AGUFM.P21A1189B/abstract.

Bell III, JF et al. (2013). "Calibration and performance of the Mars reconnaissance orbiter context camera (CTX)". In: *International Journal of Mars Science and Exploration* 8, pp. 1–14. DOI: 10.1555/mars.2013.0001. URL: https://ui.adsabs.harvard.edu/abs/2013IJMSE...8....1B/abstract.

Benedix, G. K. et al. (Mar. 2020). "Deriving Surface Ages on Mars Using Automated Crater Counting". In: *Earth and Space Science* 7.3. DOI: 10.1029/2019EA001005.

Besse, S. et al. (Jan. 2018). "ESA's Planetary Science Archive: Preserve and present reliable scientific data sets". In: *Planetary and Space Science* 150, pp. 131–140. ISSN: 0032-0633. DOI: 10.1016/j.pss.2017.07.013.

Beuther, Henrik et al. (2014). *Protostars and planets VI*. University of Arizona Press.

Bibring, Jean-Pierre et al. (Apr. 2006). "Global Mineralogical and Aqueous Mars History Derived from OMEGA/Mars Express Data". In: *Science* 312.5772, pp. 400–404. ISSN: 1095-9203. DOI: 10.1126/science.1122659.

Bickel, V. T. et al. (2020). "Deep Learning-Driven and Detection and Mapping and of and Rockfalls on Mars". In: *IEEE Journal of Selected Topics in Applied Earth Observations and Remote Sensing* 13, pp. 2831–2841. DOI: 10.1109/JSTARS.2020.2991588.

Bickel, V. T. et al. (Feb. 2025a). "New Impacts on Mars: Systematic Identification and Association With InSight Seismic Events". In: *Geophysical Research Letters* 52.3. ISSN: 1944-8007. DOI: 10.1029/2024gl109133.

Bickel, Valentin Tertius et al. (May 2025b). "Streaks on martian slopes are dry". In: *Nature Communications* 16.1. ISSN: 2041-1723. DOI: 10.1038/s41467-025-59395-w.

Bishop, Christopher M (1995). *Neural networks for pattern recognition*. Oxford university press.

Boltwood, B. B. (Feb. 1907). "Ultimate disintegration products of the radioactive elements; Part II, Disintegration products of uranium". In: *American Journal of Science* s4-23.134, pp. 78–88. ISSN: 0002-9599. DOI: 10.2475/ajs.s4-23.134.78.

Bottke, W (May 2000). "Interpreting the Elliptical Crater Populations on Mars, Venus, and the Moon". In: *Icarus* 145.1, pp. 108–121. ISSN: 0019-1035. DOI: 10.1006/icar.1999.6323.

Bottke, William F. et al. (Aug. 2017). "The Late Heavy Bombardment". In: *Annual Review of Earth and Planetary Sciences* 45.1, pp. 619–647. ISSN: 1545-4495. DOI: `10.1146/annurev-earth-063016-020131`.

Bouley, Sylvain et al. (Mar. 2016). "Late Tharsis formation and implications for early Mars". In: *Nature* 531.7594, pp. 344–347. ISSN: 1476-4687. DOI: `10.1038/nature17171`.

Bouvier, Audrey et al. (Aug. 2010). "The age of the Solar System redefined by the oldest Pb–Pb age of a meteoritic inclusion". In: *Nature Geoscience* 3.9, pp. 637–641. ISSN: 1752-0908. DOI: `10.1038/ngeo941`.

Bowring, Samuel A. et al. (Jan. 1999). "Priscoan (4.00-4.03 Ga) orthogneisses from northwestern Canada". In: *Contributions to Mineralogy and Petrology* 134.1, pp. 3–16. ISSN: 1432-0967. DOI: `10.1007/s004100050465`.

Boyce, Joseph M. et al. (Jan. 2015). "Origin of the outer layer of martian low-aspect ratio layered ejecta craters". In: *Icarus* 245, pp. 263–272. ISSN: 0019-1035. DOI: `10.1016/j.icarus.2014.07.032`.

Breton, Sylvain et al. (May 2022). "Insight into martian crater degradation history based on crater depth and diameter statistics". In: *Icarus* 377, p. 114898. ISSN: 0019-1035. DOI: `10.1016/j.icarus.2022.114898`.

Brož, Petr et al. (Nov. 2014). "Shape of scoria cones on Mars: Insights from numerical modeling of ballistic pathways". In: *Earth and Planetary Science Letters* 406, pp. 14–23. ISSN: 0012-821X. DOI: `10.1016/j.epsl.2014.09.002`.

Buckland, Michael et al. (1994). "The relationship between Recall and Precision". In: *Journal of the American Society for Information Science* 45.1, pp. 12–19. DOI: `https://doi.org/10.1002/(SICI)1097-4571(199401)45:1<12::AID-ASI2>3.0.CO;2-L`.

Bultel, B. et al. (2023). "Sample-based Spectral and Mapping around Landing and Sites on the Moon—Lunar and Timescale Part 1". In: *The Planetary Science Journal* 04.08, p. 146. DOI: `10.3847/PSJ/acdc15`.

Bultel, Benjamin (2016). "Serpentinisation et carbonatation de la croute Martienne". PhD thesis. Université Claude Bernard Lyon 1. URL: `https://theses.hal.science/tel-01359052v1`.

Buslaev, Alexander et al. (Feb. 2020). "Albumentations: Fast and Flexible Image Augmentations". In: *MDPI Information* 11.2, p. 125. ISSN: 2078-2489. DOI: `10.3390/info11020125`.

Cameron, Alastair Graham Walter (1962a). "Formation of the solar nebula". In: *Icarus* 1.1-6, pp. 339–342. DOI: `10.1016/0019-1035(62)90033-7`.

— (1962b). "The formation of the sun and planets". In: *Icarus* 1.1-6, pp. 13–69. DOI: `10.1016/0019-1035(62)90005-2`.

— (1995). "The first ten million years in the solar nebula". In: *Meteoritics* 30.2, pp. 133–161. DOI: `10.1111/j.1945-5100.1995.tb01110.x`.

Canup, Robin M (Sept. 2008). "Accretion of the Earth". In: *Philosophical Transactions of the Royal Society A: Mathematical, Physical and Engineering Sciences* 366.1883, pp. 4061–4075. ISSN: 1471-2962. DOI: `10.1098/rsta.2008.0101`.

— (Nov. 2012). "Forming a Moon with an Earth-like Composition via a Giant Impact". In: *Science* 338.6110, pp. 1052–1055. ISSN: 1095-9203. DOI: `10.1126/science.1226073`.

Carr, Michael H (2007). *The surface of Mars*. Vol. 6. Cambridge University Press.

— (July 1973). “Volcanism on Mars”. In: *Journal of Geophysical Research* 78.20, pp. 4049–4062. ISSN: 21562202. DOI: https://doi.org/10.1029/JB078i020p04049.

— (May 2012). “The fluvial history of Mars”. In: *Philosophical Transactions of the Royal Society A: Mathematical, Physical and Engineering Sciences* 370.1966, pp. 2193–2215. ISSN: 1471-2962. DOI: 10.1098/rsta.2011.0500.

Carr, Michael H. et al. (June 2010). “Geologic history of Mars”. In: *Earth and Planetary Science Letters* 294.3–4, pp. 185–203. ISSN: 0012-821X. DOI: 10.1016/j.epsl.2009.06.042.

Chandnani, M. et al. (May 2019). “Geologic Analyses of the Causes of Morphological Variations in Lunar Craters Within the Simple-to-Complex Transition”. In: *Journal of Geophysical Research: Planets* 124.5, pp. 1238–1265. ISSN: 2169-9100. DOI: 10.1029/2018je005729.

Che, Xiaochao et al. (Nov. 2021). “Age and composition of young basalts on the Moon, measured from samples returned by Chang’e-5”. In: *Science* 374.6569, pp. 887–890. ISSN: 1095-9203. DOI: 10.1126/science.abl7957.

Chen, Min et al. (2018). “Lunar Crater Detection Based on Terrain Analysisand Mathematical Morphology MethodsUsing Digital Elevation Models”. In: *IEEE Transactions Geoscience and Remote Sensing*. DOI: 10.1109/TGRS.2018.2806371.

Cintala, Mark J et al. (July 1998). “Scaling impact melting and crater dimensions: Implications for the lunar cratering record”. In: *Meteoritics and Planetary Science* 33.4, pp. 889–912. DOI: 10.1111/j.1945-5100.1998.tb01695.x.

Cintala, Mark J. (1977). “Martian fresh crater morphology and morphometry-A pre-Viking review”. In: *Impact and Explosion Cratering: Planetary and Terrestrial Implications*, pp. 575–591. URL: https://adsabs.harvard.edu/pdf/1977iecp.symp..575C.

Claeys, Philippe et al. (2011). “Late Heavy Bombardment”. In: *Encyclopedia of Astrobiology*. Springer Berlin Heidelberg, pp. 909–912. ISBN: 9783642112744. DOI: 10.1007/978-3-642-11274-4_869.

Cohen, B. A. et al. (Dec. 2000). “Support for the Lunar Cataclysm Hypothesis from Lunar Meteorite Impact Melt Ages”. In: *Science* 290.5497, pp. 1754–1756. ISSN: 1095-9203. DOI: 10.1126/science.290.5497.1754.

Conway, Susan J. et al. (May 2025). “A global survey for dust devil vortices on mars using MRO context camera images enabled by neural networks”. In: *Planetary and Space Science* 259, p. 106072. ISSN: 0032-0633. DOI: 10.1016/j.pss.2025.106072.

Cornillon, Anne et al. (2025). “Possible Detection Of Hydrated Minerals Around Olympus Mons Volcano On mars”. In: *In Proceedings of the 56th Lunar and Planetary Science Conference, LPI Contribution No 1127*. URL: https://www.hou.usra.edu/meetings/lpsc2025/pdf/1127.pdf.

Costard, F. et al. (July 2019). “The Lomonosov Crater Impact Event: A Possible Mega-Tsunami Source on Mars”. In: *Journal of Geophysical Research: Planets* 124.7, pp. 1840–1851. ISSN: 2169-9100. DOI: 10.1029/2019je006008.

Costard, F. M. (June 1989). “The spatial distribution of volatiles in the Martian hydrolithosphere”. In: *Earth Moon and Planet* 45, pp. 265–290. DOI: 10.1007/BF00057747.

Costard, F. M. et al. (Nov. 2001). "Formation of Recent Martian Debris Flows by Melting of Near-Surface Ground Ice at High Obliquity". In: *Science* 295, pp. 110–113. DOI: DOI: 10.1126/science.1066698.

Costard, Francois et al. (Mar. 2017). "Modeling tsunami propagation and the emplacement of thumbprint terrain in an early Mars ocean". In: *Journal of Geophysical Research: Planets* 122.3, pp. 633–649. ISSN: 2169-9100. DOI: 10.1002/2016je005230.

Croft, Steven K. (Feb. 1985). "The scaling of complex craters". In: *Journal of Geophysical Research* 90.S02, pp. C828–C842. DOI: 10.1029/JB090iS02p0C828.

Cui, Zexian et al. (Dec. 2024). "A sample of the Moon's far side retrieved by Chang'e-6 contains 2.83-billion-year-old basalt". In: *Science* 386.6728, pp. 1395–1399. ISSN: 1095-9203. DOI: 10.1126/science.adt1093.

Ćuk, Matija et al. (Nov. 2012). "Making the Moon from a Fast-Spinning Earth: A Giant Impact Followed by Resonant Despinning". In: *Science* 338.6110, pp. 1047–1052. ISSN: 1095-9203. DOI: 10.1126/science.1225542.

Cuzzi, Jeffrey N. et al. (Jan. 2001). "Size-selective Concentration of Chondrules and Other Small Particles in Protoplanetary Nebula Turbulence". In: *The Astrophysical Journal* 546.1, pp. 496–508. ISSN: 1538-4357. DOI: 10.1086/318233.

Di, Kaichang et al. (Dec. 2014). "A machine learning approach to crater detection from topographic data". In: *Advances in Space Research* 54.11, pp. 2419–2429. ISSN: 0273-1177. DOI: 10.1016/j.asr.2014.08.018.

Dickson, J. L. et al. (June 2024). "The Global Context Camera (CTX) Mosaic of Mars: A Product of Information-Preserving Image Data Processing". In: *Earth and Space Science* 11.7. ISSN: 2333-5084. DOI: 10.1029/2024ea003555.

Downes, LenaM. et al. (2020). "Deep Learning Crater Detection for Lunar Terrain Relative Navigation". In: *American Institute of Aeronautics and Astronautics.* DOI: 10.2514/6.2020-1838.

Duda, Richard O. et al. (Jan. 1972). "Use of the Hough transformation to detect lines and curves in pictures". In: *Communications of the ACM* 15.1, pp. 11–15. ISSN: 1557-7317. DOI: 10.1145/361237.361242.

Edwards, CS et al. (Oct. 2011). "Mosaicking of global planetary image datasets: 1. Techniques and data processing for Thermal Emission Imaging System (THEMIS) multi-spectral data". In: *Journal of Geophysical Research: Planets* 116.E10. DOI: 10.1029/2010JE003755..

Emami, Ebrahim et al. (Aug. 2019). "Crater Detection Using Unsupervised Algorithms and Convolutional Neural Networks". In: *IEEE Transactions on Geoscience and Remote Sensing* 57.8, pp. 5373–5383. DOI: 10.1109/TGRS.2019.2899122.

Eugster, O. (2003). "Cosmic-ray Exposure Ages of Meteorites and Lunar Rocks and Their Significance". In: *Geochemistry* 63.1, pp. 3–30. ISSN: 0009-2819. DOI: 10.1078/0009-2819-00021.

Fawdon, Peter et al. (2024). "The high-resolution map of Oxia Planum, Mars; the landing site of the ExoMars Rosalind Franklin rove". In: *Journal of Maps* 20.1, p. 2302361. DOI: 10.1080/17445647.2024.2302361. eprint: https://doi.org/10.1080/17445647.2024.2302361. URL: https://doi.org/10.1080/17445647.2024.2302361.

Fernandes, V. A. et al. (Jan. 2013). "The bombardment history of the Moon as recorded by 40Ar-39Ar chronology". In: *Meteoritics and Planetary Science* 48.2, pp. 241–269. ISSN: 1945-5100. DOI: 10.1111/maps.12054.

Feuvre, Mathieu Le (2023). "Modeling the impact bombardment of the planets and moons, with applications to dating by crater counting". PhD thesis. Institut De Physique Du Globe De Paris. URL: https://hal.science/tel-04015436.

Fielder, Gilbert (1961). "Small-scale explosion craters, impact craters, and the physical structure of the Moon's surface". In: *Monthly Notices of the Royal Astronomical Society* 123.1, pp. 15–26. DOI: 10.1093/mnras/123.1.15.

Galloway, M.J. et al. (Oct. 2014). "Automated Crater Detection And Counting Using The Hough Transform". In: *IEEE International Conference on Image Processing (ICIP)*. DOI: 10.1109/ICIP.2014.7025316.

Giannakis, Iraklis et al. (Jan. 2024). "A flexible deep learning crater detection scheme using Segment Anything Model (SAM)". In: *Icarus* 408, p. 115797. ISSN: 0019-1035. DOI: 10.1016/j.icarus.2023.115797.

Gillies, Sean et al. (2007). *Shapely: manipulation and analysis of geometric objects*. toblerity.org. URL: https://github.com/Toblerity/Shapely.

Girshick, Ross et al. (2014). "Rich feature hierarchies for accurate object detection and semantic segmentation". In: *Proceedings of the IEEE conference on computer vision and pattern recognition*, pp. 580–587. URL: https://openaccess.thecvf.com/content_cvpr_2014/html/Girshick_Rich_Feature_Hierarchies_2014_CVPR_paper.html.

Gomes, R. et al. (May 2005). "Origin of the cataclysmic Late Heavy Bombardment period of the terrestrial planets". In: *Nature* 435.7041, pp. 466–469. ISSN: 1476-4687. DOI: 10.1038/nature03676.

Gorski, Krzysztof M et al. (2005). "HEALPix: A framework for high-resolution discretization and fast analysis of data distributed on the sphere". In: *The Astrophysical Journal* 622.2, p. 759.

Gotmare, Akhilesh et al. (2018). "A Closer Look at Deep Learning Heuristics: Learning Rate Restarts, Warmup And Distillation". In: URL: arXiv:1810.13243v1.

Goyal, Priya et al. (2018). "Accurate, Large Minibatch SGD: Training ImageNet in 1 Hour". In: URL: arXiv:1706.02677v2.

Guggisberg, S. et al. (1979). "Classification of the Apollo-11 mare basalts according to Ar39-Ar40 ages and petrological properties". In: *Lunar and Planetary Science Conference 10th*, pp. 1–39. URL: https://legacy.adsabs.harvard.edu/full/1979LPSC...10....1G.

Halim, Samuel H. et al. (July 2024). "Assessing the survival of carbonaceous chondrites impacting the lunar surface as a potential resource". In: *Planetary and Space Science* 246, p. 105905. ISSN: 0032-0633. DOI: 10.1016/j.pss.2024.105905.

Hartmann, W. K. et al. (1971). "Moon : Origin and Evolution of Multi-Ring Basins". In: *The Moon* 3, pp. 3–78. DOI: 10.1007/BF00620390.

Hartmann, W.K. et al. (1981). "Chronology of Planetary Volcanism by Comparative Studies of PlanetaryCraters". In: *Basaltic Volcanism on the Terrestrial Planets*. Pergamon Press:

Elmsford, NY, USA, pp. 1050–1127. URL: https://adsabs.harvard.edu/full/1981bvtp.book.....B.

Hartmann, William K. (May 1965a). “Secular changes in meteoritic flux through the history of the solar system”. In: *Icarus* 4.2, pp. 207–213. ISSN: 0019-1035. DOI: 10.1016/0019-1035(65)90062-x.

— (May 1965b). “Terrestrial and lunar flux of large meteorites in the last two billion years”. In: *Icarus* 4.2, pp. 157–165. ISSN: 0019-1035. DOI: 10.1016/0019-1035(65)90057-6.

— (Jan. 1966). “Early Lunar and Craterlng”. In: *Icarius* 5, pp. 406–418. DOI: 10.1016/0019-1035(66)90054-6.

— (Sept. 1970). “Lunar Cratering and Chronology”. In: *Icarius* 13, pp. 299–301. DOI: 10.1016/0019-1035(70)90059-X.

— (Jan. 1972). “Paleocratering of the Moon: Review of post-Apollo data”. In: *Astrophysics and Space Science* 17, pp. 48–64. DOI: 10.1007/BF00642541.

— (2003). *A Traveler’s Guide To Mars*. Vol. 1. Workman Publishing, New York. ISBN: 0-7611-2606-6.

— (Apr. 2005). “Martian cratering 8: Isochron refinement and the chronology of Mars”. In: *Icarus* 174.2, pp. 294–320. ISSN: 0019-1035. DOI: 10.1016/j.icarus.2004.11.023.

— (June 2019). “History of the Terminal Cataclysm Paradigm: Epistemology of a Planetary Bombardment That Never (?) Happened”. In: *Geosciences* 9.7, p. 285. ISSN: 2076-3263. DOI: 10.3390/geosciences9070285.

Hartmann, William K. et al. (Feb. 2001). “Cratering Chronology and the Evolution of Mars”. In: *Space Science Reviews* 96, pp. 165–194. DOI: 10.1007/978-94-017-1035-0_6.

Hartmann, William K. et al. (Jan. 2007). “Possible long-term decline in impact rates 2. Lunar impact-melt data regarding impact history”. In: *Icarus* 186.1, pp. 11–23. ISSN: 0019-1035. DOI: 10.1016/j.icarus.2006.09.009.

Haskin, Larry A. et al. (Sept. 1998). “The case for an Imbrium origin of the Apollo thorium-rich impact-melt breccias”. In: *Meteoritics and Planetary Science* 33.5, pp. 959–975. ISSN: 1945-5100. DOI: 10.1111/j.1945-5100.1998.tb01703.x.

Haslebacher, Caroline et al. (2023). “LineaMapper: A deep learning-powered tool for mapping linear surface features on Europa”. In: *Icarus*, p. 115722. ISSN: 0019-1035. DOI: https://doi.org/10.1016/j.icarus.2023.115722. URL: https://www.sciencedirect.com/science/article/pii/S0019103523002993.

He, Kaiming et al. (2017). “Mask R-CNN”. In: *Proceedings of the IEEE International Conference on Computer Vision (ICCV)*, pp. 2961–2969. URL: https://openaccess.thecvf.com/content_iccv_2017/html/He_Mask_R-CNN_ICCV_2017_paper.html.

He, Zijian et al. (2024). “Comprehensive Performance Evaluation of YOLOv11, YOLOv10, YOLOv9, YOLOv8 and YOLOv5 on Object Detection of Power Equipment”. In: URL: arXiv:2411.18871.

Head, J. W. et al. (Dec. 1999). “Possible Ancient Oceans onMars: Evidence from MarsOrbiter Laser Altimeter Data”. In: *Science* 286, pp. 2134–2137. DOI: 10.1126/science.286.5447.2134.

Head, J. W. et al. (2001). “Geological Processes and Evolution”. In: *Space Science Reviews*. DOI: 10.1023/A:1011953424736.

Head, James N. et al. (Nov. 2002). “Martian Meteorite Launch: High-Speed Ejecta from Small Craters”. In: *Science* 298.5599, pp. 1752–1756. ISSN: 1095-9203. DOI: 10.1126/science.1077483.

Head, James W. et al. (Sept. 2010). “Global Distribution of Large Lunar Craters: Implications for Resurfacing and Impactor Populations”. In: *Science* 329.5998, pp. 1504–1507. ISSN: 1095-9203. DOI: 10.1126/science.1195050.

Herrick, Robert R et al. (Jan. 1998). “Inversion of crater morphometric data to gain insight on the cratering process”. In: *Meteoritics and Planetary Science* 33.1, pp. 131–143. DOI: 10.1111/j.1945-5100.1998.tb01615.x.

Heyer, T. et al. (Sept. 2018). “The Multi-Temporal Database of Planetary Image Data (MUTED): A web-based tool for studying dynamic Mars”. In: *Planetary and Space Science* 159, pp. 56–65. ISSN: 0032-0633. DOI: 10.1016/j.pss.2018.04.015.

Hiesinger, H. et al. (Feb. 2012). “How old are young lunar craters?” In: *Journal of Geophysical Research: Planets* 117.E12. ISSN: 0148-0227. DOI: 10.1029/2011je003935.

Hildenbrand, A. et al. (Oct. 2023). “A giant volcanic island in an early Martian Ocean?” In: *Earth and Planetary Science Letters* 619, p. 118302. ISSN: 0012-821X. DOI: 10.1016/j.epsl.2023.118302.

Hirabayashi, Masatoshi et al. (Nov. 2024). “Crater Equilibrium State Characterization given Crater Production from a Single Power Law”. In: *The Planetary Science Journal* 5.11, p. 250. ISSN: 2632-3338. DOI: 10.3847/psj/ad8883.

Hooke, Robert (1665). *Micrographia*. London: J. Martyn and J. Allestry. URL: https://www.gutenberg.org/cache/epub/15491/pg15491.txt.

Horvath, David G. et al. (Sept. 2021). “Evidence for geologically recent explosive volcanism in Elysium Planitia, Mars”. In: *Icarus* 365, p. 114499. ISSN: 0019-1035. DOI: 10.1016/j.icarus.2021.114499.

Hosang, Jan et al. (July 2017). “Learning Non-Maximum Suppression”. In: *Proceedings of the IEEE Conference on Computer Vision and Pattern Recognition (CVPR)*, pp. 4507–4515. URL: https://openaccess.thecvf.com/content_cvpr_2017/html/Hosang_Learning_Non-Maximum_Suppression_CVPR_2017_paper.html.

Hough, Paul V. C. (Dec. 1962). *Method And Means for Recognizíng complex Patterns*. Tech. rep. 3096654. United States Patent Office.

Huang, Ya Huei et al. (July 2022). “Bombardment history of the Moon constrained by crustal porosity”. In: *Nature Geoscience* 15.7, pp. 531–535. ISSN: 1752-0908. DOI: 10.1038/s41561-022-00969-4.

Hynek, Brian M et al. (2017). “Geologic map of Meridiani Planum, Mars”. In: *US Geological Survey Scientific Investigations Map* 3356. DOI: https://doi.org/10.3133/SIM3356.

Ivanov, B. A. et al. (2007). “Exogenic Dynamics, Cratering and Surface Ages”. In: *Treatise on Geophysics*. Elsevier. Chap. 10-06, pp. 207–242. DOI: 10.1016/B978-044452748-6.00158-9.

Ivanov, Boris (2008). “Size-Frequency Distribution of Asteroids and Impact Craters: Estimates of Impact Rate”. In: *Catastrophic events caused by cosmic objects*. Ed. by Catastrophic events caused by cosmic objects. Springer. Chap. 2, pp. 91–116. DOI: 10.1007/978-1-4020-6452-4_2.

Ivanov, Boris A. (Feb. 2001). “Mars/Moon Cratering Rate Ratio Estimates”. In: *Chronology and Evolution of Mars* 87, pp. 87–104. DOI: 10.1023/A:1011941121102.

James, J. N. (1966). “The Voyage of Mariner IV”. In: *Scientific American* 214.3, pp. 42–53. ISSN: 00368733, 19467087. URL: http://www.jstor.org/stable/24931296 (visited on 07/14/2025).

Jegham, Nidhal et al. (2025). “YOLO Evolution: A Comprehensive Benchmark and Architectural Review of YOLOv12, YOLO11, and Their Previous Versions”. In: DOI: arXiv:2411.00201.

Jia, Mengna et al. (July 2020). “A catalogue of impact craters larger than 200 m and surface age analysis in the Chang’e-5 landing area”. In: *Earth and Planetary Science Letters* 541, p. 116272. ISSN: 0012-821X. DOI: 10.1016/j.epsl.2020.116272.

Jocher, Glenn et al. (2023). *Ultralytics YOLOv8*. Version 8.0.0. URL: https://github.com/ultralytics/ultralytics.

— (2025). *Ultralytics YOLOv8*. Version 11.0.0. URL: https://github.com/ultralytics/ultralytics.

Johansen, Anders et al. (Aug. 2007). “Rapid planetesimal formation in turbulent circumstellar disks”. In: *Nature* 448.7157, pp. 1022–1025. ISSN: 1476-4687. DOI: 10.1038/nature06086.

Kalra, Dayal Singh et al. (2024). “Why Warmup the Learning Rate? Underlying Mechanisms and Improvements”. In: *Advances in Neural Information Processing Systems* 37, pp. 111760–111801. URL: arXiv:2406.09405v2.

Kalynn, Jessica et al. (2013). “Topographic characterization of lunar complex craters”. In: *Geophysical Research Letters* 40.1, pp. 38–42. DOI: 10.1029/2012GL053608..

Kant, Immanuel (1755). *Allgemeine Naturgeschichte und Theorie des Himmels*. URL: https://web.viu.ca/johnstoi//kant/kant2e.htm.

Kato, Manabu et al. (2007). “The SELENE mission: present status and science goals”. In: *38th Annual Lunar and Planetary Science Conference*. 1338, p. 1211. URL: https://www.lpi.usra.edu/meetings/lpsc2007/pdf/1211.pdf.

Khanam, Rahima et al. (2024). “Yolov11: An Overview of th Key Architectural Enhancements”. In.

Kim, Jung Rack et al. (Oct. 2005). “Automated Crater Detection, A New Tool for Mars Cartography and Chronology”. In: *Photogrammetric Engineering and Remote Sensing* 71.10, pp. 1205–1217. DOI: 10.14358/PERS.71.10.1205.

Kinczyk, Mallory J. et al. (May 2020). “A morphological evaluation of crater degradation on Mercury: Revisiting crater classification with MESSENGER data”. In: *Icarus* 341, p. 113637. ISSN: 0019-1035. DOI: 10.1016/j.icarus.2020.113637.

Kingma, Diederik P et al. (2014). “Adam: A method for stochastic optimization”. In: *arXiv preprint arXiv:1412.6980*. URL: https://arxiv.org/abs/1412.6980.

Kirillov, Alexander et al. (2023). “Segment Anything”. In: *Proceedings of the IEEE/CVF international conference on computer vision*. IEEE, pp. 4015–4026. URL: https://openaccess.thecvf.com/content/ICCV2023/html/Kirillov_Segment_Anything_ICCV_2023_paper.html.

Kneissl, T. et al. (2016). “Treatment of non-sparse cratering in planetary surface dating”. In: *Icarius* 277, pp. 187–195. DOI: .org/10.1016/j.icarus.2016.05.015.

Kokubo, Eiichiro et al. (Jan. 1998). “Oligarchic Growth of Protoplanets”. In: *Icarus* 131.1, pp. 171–178. ISSN: 0019-1035. DOI: 10.1006/icar.1997.5840.

Kokubo, Eiichiro et al. (2000). “Evolution of a Circumterrestrial Disk and Formation of a Single Moon”. In: *Icarus* 148.2, pp. 419–436. ISSN: 0019-1035. DOI: 10.1006/icar.2000.6496. URL: https://www.sciencedirect.com/science/article/pii/S0019103500964960.

La Grassa, Ricardo et al. (2023). “YOLOLens: A Deep Learning Model Based on Super-Resolution to Enhance the Crater Detection of the Planetary Surfaces”. In: *MDPI Remote Sensing* 15.1171. DOI: 10.3390/rs15051171.

La Grassa, Riccardo et al. (Feb. 2025). “LU5M812TGT: An AI-Powered global database of impact craters ≥ 0.4 km on the Moon”. In: *ISPRS Journal of Photogrammetry and Remote Sensing* 220.Cadogan, pp. 75–84. ISSN: 0924-2716. DOI: 10.1016/j.isprsjprs.2024.11.010.

Lagain, A. et al. (Aug. 2021a). “Mars Crater and Database: A and participative project for the classification of and the morphological characteristics of large Martian and craters”. In: *The Geological Society of America Special Paper* 550, pp. 629–645. DOI: 10.1130/2021.2550(29).

Lagain, A. et al. (Feb. 2021b). “Model Age Derivation of Large Martian Impact Craters, Using Automatic Crater Counting Methods”. In: *Earth and Space Science* 8.2. ISSN: 2333-5084. DOI: 10.1029/2020ea001598.

Lagain, A. et al. (Nov. 2021c). “The Tharsis mantle source of depleted shergottites revealed by 90 million impact craters”. In: *Nature Communications* 12.1. ISSN: 2041-1723. DOI: 10.1038/s41467-021-26648-3.

Lagain, Anthony et al. (Mar. 2024). “Recalibration of the lunar chronology due to spatial cratering-rate variability”. In: *Icarus* 411, p. 115956. ISSN: 0019-1035. DOI: 10.1016/j.icarus.2024.115956.

Langevin, Y. et al. (July 2007). “Observations of the south seasonal cap of Mars during recession in 2004–2006 by the OMEGA visible/near-infrared imaging spectrometer on board Mars Express”. In: *Journal of Geophysical Research: Planets* 112.E8. ISSN: 0148-0227. DOI: 10.1029/2006je002841.

Laplace, Pierre-Simon (1796). *Exposition du système du monde.*

Latorre, F. et al. (2023). “Autonomous Crater Detection On Asteroids Using Afully-Convolutional Neural Network”. In: DOI: 10.1016/j.icarus.2023.115434.

Lecun, Y. et al. (Aug. 1998). “Gradient-based Learning Applied To Document Recognition”. In: *Proceedings of the IEEE* 86.11, pp. 2278–2324. ISSN: 1558-2256. DOI: 10.1109/5.726791.

Lee, C. (Aug. 2023). “Comparison of Automated Crater Catalogs for Mars From Benedix et al. (2020) and Lee and Hogan (2021)”. In: *Earth and Space Science* 10.9. ISSN: 2333-5084. DOI: 10.1029/2023ea003005.

Lee, Christopher (June 2019). “Automated crater detection on Mars using deep learning”. In: *Planetary and Space Science* 170, pp. 16–28. ISSN: 0032-0633. DOI: 10.1016/j.pss.2019.03.008.

Lee, Christopher et al. (Feb. 2021). “Automated crater detection with human level performance”. In: *Computers and Geosciences* 147, p. 104645. ISSN: 0098-3004. DOI: 10.1016/j.cageo.2020.104645.

Leighton, Robert B. et al. (Aug. 1965). “Mariner IV Photography of Mars: Initial Results”. In: *Science* 149.3684, pp. 627–630. URL: https://www.jstor.org/stable/1716664.

Lherm, Victor (2021). “Dynamique du fractionnement thermique et chimique lors de la différenciation des planètes telluriques”. PhD thesis. École Normale Supérieure de Lyon. URL: https://theses.hal.science/tel-03377150v1.

Liu, Jianjun et al. (July 2024). “A 76-m per pixel global color image dataset and map of Mars by Tianwen-1”. In: *Science Bulletin* 69.14, pp. 2183–2186. ISSN: 2095-9273. DOI: 10.1016/j.scib.2024.04.045.

Liu, Zhaoqin et al. (Apr. 12, 2018). “A global database and statistical analyses of (4) Vesta craters”. In: *Icarus* 311, pp. 242–257. ISSN: 0019-1035. DOI: 10.1016/j.icarus.2018.04.006.

Malarewicz, V. et al. (Feb. 2025). “Evidence for pre-Noachian granitic rocks on Mars from quartz in meteorite NWA 7533”. In: *Nature Geoscience* 18.3, pp. 207–212. ISSN: 1752-0908. DOI: 10.1038/s41561-025-01653-z.

Malin, Michael C. et al. (May 2007). “Context Camera Investigation on board the Mars Reconnaissance Orbiter”. In: *Journal of Geophysical Research* 112. DOI: 10.1029/2006JE002808..

Mangold, N. et al. (2003). “Debris flows over sand dunes on Mars: Evidence for liquid water”. In: *Journal of Geophysical Research* 108. DOI: 10.1029/2002JE001958,.

Mangold, N. et al. (Nov. 2021). “Perseverance rover reveals an ancient delta-lake system and flood deposits at Jezero crater, Mars”. In: *Science* 374.6568, pp. 711–717. ISSN: 1095-9203. DOI: 10.1126/science.abl4051.

Martinez, L. et al. (June 2025). “Robust automatic crater detection at all latitudes on Mars with Deep-learning”. In: *Planetary and Space Science* 260. DOI: 10.1016/j.pss.2025.106053.

Martins, Ricardo et al. (Jan. 2009). “Crater Detection by a Boosting Approach”. In: *IEEE Geoscience and Remote Sensing Letters* 6.1, pp. 127–131. DOI: 10.1109/LGRS.2008.2006004.

Masson, P. et al. (Feb. 2001). “Geomorphologic Evidence For Liquid Water”. In: *Space Science Reviews* 96, pp. 333–364. ISSN: 978-94-017-1035-0. DOI: 10.1007/978-94-017-1035-0_12.

Masson, Philippe (1984). “Géologie et morphologie de la Planète Mars (Geology and morphology of planet Mars)”. In: *Bulletin de l’Association de Géographes Français* 61.504, pp. 237–244. URL: https://www.persee.fr/doc/bagf_0004-5322_1984_num_61_504_5479.

Mastrobuono-Battisti, Alessandra et al. (Apr. 2015). “A primordial origin for the compositional similarity between the Earth and the Moon”. In: *Nature* 520.7546, pp. 212–215. ISSN: 1476-4687. DOI: 10.1038/nature14333.

Matchev, Konstantin T. et al. (Sept. 2022). “Unsupervised Machine Learning for Exploratory Data Analysis of Exoplanet Transmission Spectra”. In: *The Planetary Science Journal* 3.9, p. 205. ISSN: 2632-3338. DOI: 10.3847/psj/ac880b.

McCulloch, Warren S. et al. (Dec. 1943). “A logical calculus of the ideas immanent in nervous activity”. In: *The Bulletin of Mathematical Biophysics* 5.4, pp. 115–133. ISSN: 1522-9602. DOI: 10.1007/bf02478259.

McDougall, Ian et al. (1999). *Geochronology and Thermochronology by the 40Ar/39Ar Method*. Oxford University Press.

McEwen, Alfred S. et al. (2007). “Mars Reconnaissance Orbiter’s High Resolution Imaging Science Experiment (HiRISE)”. In: *Journal of Geophysical Research* 112. DOI: 10.1029/2005JE002605.

Mellon, Michael T. et al. (Jan. 2009). “Ground ice at the Phoenix Landing Site: Stability state and origin”. In: *Journal of Geophysical Research: Planets* 114.E1. ISSN: 0148-0227. DOI: 10.1029/2009je003417.

Melosh, H. J. (1997). “Impact cratering”. In: *Encyclopedia of Planetary Science*. Kluwer Academic Publishers, pp. 326–335. ISBN: 0412069512. DOI: 10.1007/1-4020-4520-4_183.

Michael, G.G. et al. (Feb. 2016a). “Systematic processing of Mars Express HRSC panchromatic and colour image mosaics: Image equalisation using an external brightness reference”. In: *Planetary and Space Science* 121, pp. 18–26. ISSN: 0032-0633. DOI: 10.1016/j.pss.2015.12.002.

Michael, G.G. et al. (Jan. 2025). “A global colour mosaic of Mars from Mars Express HRSC high altitude observations”. In: *Icarus* 425, p. 116350. ISSN: 0019-1035. DOI: 10.1016/j.icarus.2024.116350.

Michael, GG et al. (2016b). “Planetary surface dating from crater size-frequency distribution measurements: Poisson timing analysis”. In: *Icarus* 277, pp. 279–285.

Mills, M.M. et al. (May 2024). “A global dataset of pitted cones on Mars”. In: *Icarius* 418.116145. DOI: .org/10.1016/j.icarus.2024.116145.

Mitchell, Tom M (1997). “Does machine learning really work?” In: *AI magazine* 18.3, pp. 11–11. DOI: 10.1609/aimag.v18i3.1303.

Mojzsis, Stephen J. et al. (Jan. 2001). “Oxygen-isotope evidence from ancient zircons for liquid water at the Earth surface 4,300 Myr ago”. In: *Nature* 409.6817, pp. 178–181. ISSN: 1476-4687. DOI: 10.1038/35051557.

Montmerle, Thierry et al. (June 2006). “3. Solar System Formation and Early Evolution: the First 100 Million Years”. In: *Earth, Moon, and Planets* 98.1–4, pp. 39–95. ISSN: 1573-0794. DOI: 10.1007/s11038-006-9087-5.

Morbidelli, A. et al. (Mar. 2001). “A plausible cause of the late heavy bombardment”. In: *Meteoritics and Planetary Science* 36.3, pp. 371–380. ISSN: 1945-5100. DOI: 10.1111/j.1945-5100.2001.tb01880.x.

Morbidelli, A. et al. (May 2012). “Building Terrestrial Planets”. In: *Annual Review of Earth and Planetary Sciences* 40.1, pp. 251–275. ISSN: 1545-4495. DOI: 10.1146/annurev-earth-042711-105319.

Morbidelli, A. et al. (May 2018). “The timeline of the lunar bombardment: Revisited”. In: *Icarus* 305, pp. 262–276. ISSN: 0019-1035. DOI: 10.1016/j.icarus.2017.12.046.

Neukum, G et al. (Dec. 1976a). “Mars: A Standard Crater Curve and Possible New Time Scale”. In: *Science* 194.4272, pp. 1381–1387. DOI: 10.1126/science.194.4272.1381.

Neukum, G. (Mar. 1977). “Lunar Cratering”. In: *Philosophical Transactions of the Royal Society of London* 285.1327, pp. 267–272. URL: https://www.jstor.org/stable/74851.

— (Feb. 1983). “Meteorite Bombardment And Dating Of Planetary Surfaces”. PhD thesis. Ludwig-Maximilians University. URL: https://ntrs.nasa.gov/citations/19840027189.

Neukum, G. et al. (1976b). “Dating of Individual lunar craters”. In: *Lunar and Planetary Science Conference 7th*, pp. 2867–2881. URL: https://adsabs.harvard.edu/full/1976LPSC....7.2867N/0002867.000.html.

Neukum, G. et al. (1976c). “Effects of lava flows on lunar crater populations”. In: *The Moon* 15, pp. 205–222. DOI: 10.1007/BF00562238.

Neukum, G. et al. (1995). “Crater Size Distributions and Impact Probabilities from Lunar, Terrestrial-planet,and Asteroid Cratering Data”. In: *Hazards Due to Comets and Asteroids.* Gehrels, T., Ed.; University of Arizona Press: Tucson, AZ, USA, pp. 359–416.

Neukum, G. et al. (2001). “Cratering Records in the Inner Solar System in Relation to the Lunar Reference System”. In: *Chronology and Evolution of Mars.* DOI: 10.1007/978-94-017-1035-0_3.

Nizam, Nabila et al. (2022). “Development of Chaos Terrain as Subaqueous Slide Blocks in Galilaei Crater, Mars”. In: *MDPI Remote Sensing* 14.1998. DOI: .org/10.3390/rs14091998.

Noblet, A. et al. (Aug. 2024). “A global map of gullied hillslopes on Mars”. In: *Icarus* 418, p. 116147. ISSN: 0019-1035. DOI: 10.1016/j.icarus.2024.116147.

Norman, M. D. (Feb. 2009). “The Lunar Cataclysm: Reality or “Mythconception”?” In: *Elements* 5.1, pp. 23–28. ISSN: 1811-5217. DOI: 10.2113/gselements.5.1.23.

Norman, Marc D. et al. (Apr. 2003). “Chronology, geochemistry, and petrology of a ferroan noritic anorthosite clast from Descartes breccia 67215: Clues to the age, origin, structure, and impact history of the lunar crust”. In: *Meteoritics and Planetary Science* 38.4, pp. 645–661. ISSN: 1945-5100. DOI: 10.1111/j.1945-5100.2003.tb00031.x.

Parker, Mirjam van Kan et al. (June 2010). “3D structure of the Gusev Crater region”. In: *Earth and Planetary Science Letters* 294.3–4, pp. 411–423. ISSN: 0012-821X. DOI: 10.1016/j.epsl.2010.01.013.

Paszke, Adam et al. (2019). “PyTorch: An Imperative Style, High-Performance Deep Learning Library”. In: *Advances in Neural Information Processing Systems 32.* Curran Associates, Inc., pp. 8024–8035. URL: https://proceedings.neurips.cc/paper_files/paper/2019/file/bdbca288fee7f92f2bfa9f7012727740-Paper.pdf.

Pike, Richard J. (1976). “Crater dimensions from apollo data and supplemental sources”. In: *The Moon* 15.3–4, pp. 463–477. ISSN: 1573-0794. DOI: 10.1007/bf00562253.

Pike, Richard J. (July 1980). “Formation of complex impact craters: Evidence from Mars and other planets”. In: *Icarius* 43.1, pp. 1–19. DOI: 10.1016/0019-1035(80)90083-4.

Planetary Visualization, The Bruce Murray Laboratory for (2022). *CTX beta01 mosaic.* URL: https://murray-lab.caltech.edu/CTX/beta01.html.

— (2024). *CTX V01 mosaic.* URL: https://murray-lab.caltech.edu/CTX/index.html.

Poppe, Torsten et al. (Apr. 2000). “Analogous Experiments on the Stickiness of Micron-sized Preplanetary Dust”. In: *The Astrophysical Journal* 533.1, pp. 454–471. ISSN: 1538-4357. DOI: 10.1086/308626.

QGIS Development Team (2009). *QGIS Geographic Information System.* Open Source Geospatial Foundation. URL: http://qgis.org.

Qiua, Yuning et al. (Mar. 2024). “Lightweight tensorial convolutional neural network for lunar impact crater detection”. In: *Advances in Space Research* 74, pp. 518–527. DOI: 10.1016/j.asr.2024.03.028.

Quantin, C et al. (Jan. 2007). “Possible long-term decline in impact rates 1. Martian geological data”. In: *Icarus* 186.1, pp. 1–10. ISSN: 0019-1035. DOI: 10.1016/j.icarus.2006.07.008.

Quantin, C. et al. (Dec. 2004). “Ages of Valles Marineris (Mars) landslides and implications for canyon history”. In: *Icarus* 172.2, pp. 555–572. ISSN: 0019-1035. DOI: 10.1016/j.icarus.2004.06.013.

Quantin, Cathy et al. (June 2016). “Young Martian crater Gratteri and its secondary craters”. In: *Journal of Geophysical Research* 121, pp. 1118–1140. DOI: 10.1002/2015JE004864.

Quantin-Nataf, Cathy et al. (Mar. 2021). “Oxia Planum and The Landing Site for the ExoMars “Rosalind Franklin" Rover Mission: Geological Context and Prelanding Interpretation”. In: *Astrobiology* 21.3, pp. 345–366. ISSN: 1557-8070. DOI: 10.1089/ast.2019.2191.

Redmon, Joseph et al. (2016). “You Only Look Once: Unified, Real-Time Object Detection”. In: *Proceedings of the IEEE Conference on Computer Vision and Pattern Recognition (CVPR)*, pp. 779–788. URL: https://www.cv-foundation.org/openaccess/content_cvpr_2016/html/Redmon_You_Only_Look_CVPR_2016_paper.html.

Ren, Shaoqing et al. (June 2017). “Faster R-CNN and Towards Real-Time and Object and Detection with Region and Proposal Networks”. In: *IEEE Transactions on Pattern Analysis and Machine Intelligence* 39.06, pp. 1137–1149. DOI: 10.1109/TPAMI.2016.2577031.

Renson, Pierre et al. (2013). “Automatisation de la détection des cratères lunaires sur des images et MNT planétaires”. In: *Bulletin de la Societe Géographique de Liège* 61, pp. 81–96. URL: https://popups.uliege.be/0770-7576/index.php?id=416&file=1.

Robbins, S. J. (2013). “Revised Lunar Cratering Chronology for Planetary Geological Histories”. In: *In Proceedings of the 44th Lunar and Planetary Science Conference, LPI Contribution No 1719.* The Woodlands, TX, USA, p. 1619. URL: https://www.lpi.usra.edu/meetings/lpsc2013/eposter/1619.pdf.

Robbins, Stuart J. (Oct. 2014). “New crater calibrations for the lunar crater-age chronology”. In: *Earth and Planetary Science Letters* 403, pp. 188–198. ISSN: 0012-821X. DOI: 10.1016/j.epsl.2014.06.038.

— (Apr. 2019). “A New Global Database of Lunar Impact Craters >1–2 km: 1. Crater Locations and Sizes, Comparisons With Published Databases, and Global Analysis”. In: *Jour-*

nal of Geophysical Research: Planets 124.4, pp. 871–892. ISSN: 2169-9100. DOI: 10.1029/2018je005592.

Robbins, Stuart J. et al. (Mar. 2011a). “Distant secondary craters from Lyot crater, Mars, and implications for surface ages of planetary bodies”. In: *Geophysical Research Letters* 38.L05201. DOI: 10.1029/2010GL046450.

— (Oct. 2011b). “Secondary crater fields from 24 large primary craters on Mars: Insights into nearby secondary crater production”. In: *Journal Of Geophysical Research* 116.E10003. DOI: 10.1029/2011JE003820..

— (2012). “A new global database of Mars impact craters $\geq$ 1 km: 1. Database creation, properties, and parameters”. In: *Journal of Geophysical Research* 117.E05004. DOI: 10.1029/2011JE003966..

— (Aug. 2014). “The secondary crater population of Mars”. In: *Earth and Planetary Science Letters* 400, pp. 66–76. ISSN: 0012-821X. DOI: 10.1016/j.epsl.2014.05.005.

Robert A. Craddock Ted A. Maxwell, Alan D. Howard (1997). “Crater morphometry and modification in the Sinus Sabaeus and Margaritifer Sinus regions of Mars”. In: *Journal of Geophysical Research: Planets* 102.E6, pp. 13321–13340. DOI: 10.1029/97JE01084.

Robinson, M. S. et al. (Jan. 2010). “Lunar Reconnaissance Orbiter Camera (LROC) Instrument Overview”. In: *Space Science Reviews* 150.1–4, pp. 81–124. ISSN: 1572-9672. DOI: 10.1007/s11214-010-9634-2.

Ronneberger, Olaf et al. (2015). “U-Net: Convolutional Networks for Biomedical Image Segmentation”. In: *Medical image computing and computer-assisted intervention–MICCAI 2015: 18th international conference*. Ed. by Springer et al. Vol. III. 18. Springer, pp. 234–241.

Rosenblatt, Frank (1961). *Principles of neurodynamics. perceptrons and the theory of brain mechanisms*. Spartan books Washington, DC. URL: https://archive.org/details/principles-of-neurodynamics/page/n7/mode/2up.

Ruder, Sebastian (2016). “An overview of gradient descent optimization algorithms”. In: DOI: 10.48550/ARXIV.1609.04747.

Safronov, V et al. (Feb. 1994). “Formation and evolution of planets”. In: *Astrophysics and Space Sciences* 212, pp. 13–22. DOI: 10.1007/BF00984504.

Saito, Takaya et al. (Mar. 2015). “The Precision-Recall Plot Is More Informative than the ROC Plot When Evaluating Binary Classifiers on Imbalanced Datasets”. In: *PLOS ONE* 10.3. Ed. by Guy Brock, e0118432. ISSN: 1932-6203. DOI: 10.1371/journal.pone.0118432.

Salamuniccar, Goran et al. (2010). “Method for Crater and Detection From and Martian and Digital Topography and Data Using and Gradient and Value/Orientation and Morphometry and Vote and Analysis and Slip Tuning and Calibration”. In: *IEEE Transactions on Geoscience and Remote Sensing*. DOI: 10.1109/TGRS.2009.2037750.

Salamunićcar, Goran et al. (Jan. 2011). “MA130301GT catalogue of Martian impact craters and advanced evaluation of crater detection algorithms using diverse topography and image datasets”. In: *Planetary and Space Science* 59.1, pp. 111–131. ISSN: 0032-0633. DOI: 10.1016/j.pss.2010.11.003.

Salamunićcar, Goran et al. (Jan. 2012). “LU60645GT and MA132843GT catalogues of Lunar and Martian impact craters developed using a Crater Shape-based interpolation crater detection algorithm for topography data". In: *Planetary and Space Science* 60.1, pp. 236–247. ISSN: 0032-0633. DOI: 10.1016/j.pss.2011.09.003.

Schmidt, Frédéric et al. (Apr. 2009). "Albedo control of seasonal South Polar cap recession on Mars". In: *Icarus* 200.2, pp. 374–394. ISSN: 0019-1035. DOI: 10.1016/j.icarus.2008.12.014.

Schmidt, Frédéric et al. (2022). "Circumpolar ocean stability on Mars 3 Gy ago". In: *PNAS*. DOI: 10.1073/pnas.2112930118.

Schultz, Peter H. et al. (July 2016). "Origin and implications of non-radial Imbrium Sculpture on the Moon". In: *Nature* 535.7612, pp. 391–394. ISSN: 1476-4687. DOI: 10.1038/nature18278.

See, Judi E. et al. (Mar. 1995). "Meta-Analysis of the Sensitivity and Decrement in Vigilance". In: *Psychological Bulletin* 117.2, pp. 230–249. DOI: 10.1037/0033-2909.117.2.230.

Shi, Ke et al. (May 2022). "The gardening process of lunar regolith by small impact craters: A case study in Chang'E-4 landing area". In: *Icarus* 377, p. 114908. ISSN: 0019-1035. DOI: 10.1016/j.icarus.2022.114908.

Shoemaker, E. M. et al. (Jan. 1970). "Lunar Regolith at Tranquillity Base". In: *Science* 167.3918, pp. 452–455. ISSN: 1095-9203. DOI: 10.1126/science.167.3918.452.

Silburt, Ari et al. (Jan. 2019). "Lunar crater identification via deep learning". In: *Icarus* 317, pp. 27–38. ISSN: 0019-1035. DOI: 10.1016/j.icarus.2018.06.022.

Solomon, Sean C. et al. (Feb. 2005). "New Perspectives on Ancient Mars". In: *Science* 307.5713, pp. 1214–1220. ISSN: 1095-9203. DOI: 10.1126/science.1101812.

Speyerer, Emerson J. et al. (Oct. 2016). "Quantifying crater production and regolith overturn on the Moon with temporal imaging". In: *Nature* 538.7624, pp. 215–218. ISSN: 1476-4687. DOI: 10.1038/nature19829.

Stöffler, D. et al. (2001). "Stratigraphy And Isotope Ages Of Lunar Geologic Units:chronological Standard For The Inner Solar System". In: *Space Science Reviews* 96.1/4, pp. 9–54. ISSN: 0038-6308. DOI: 10.1023/a:1011937020193.

Strahler, Arthur N. (1957). "Quantitative analysis of watershed geomorphology". In: *Eos, Transactions American Geophysical Union* 38.6, pp. 913–920. ISSN: 0002-8606. DOI: 10.1029/tr038i006p00913.

Su, Shu et al. (2023). "Detection of Detached and Ice-fragments at Martian and Polar and Scarps Using and a Convolutional and Neural Network". In: *Ieee Journal of Selected Topics in Applied Earth Observations and Remote Sensing* we. DOI: 10.1109/JSTARS.2023.3238968.

Swedenborg, Emanuel (1734). *The Principia*.

Tanaka, K.L. et al. (May 2014). "The digital global geologic map of Mars: Chronostratigraphic ages, topographic and crater morphologic characteristics, and updated resurfacing history". In: *Planetary and Space Science* 95.mapping, pp. 11–24. ISSN: 0032-0633. DOI: 10.1016/j.pss.2013.03.006.

Tanaka, Kenneth L. (1986). "The Stratigraphy of Mars". In: *Journal of Geophysical Research*. DOI: 10.1029/JB091iB13p0E139.

Tao, Yu et al. (2021a). "Rapid Single Image-Based DTM Estimation from ExoMars TGO CaSSIS Images Using Generative Adversarial U-Nets". In: *MDPI Remote Sensing* 13.15, p. 2877. DOI: 10.3390/rs13152877.

Tao, Yu et al. (2021b). "Single Image Super-Resolution Restoration of TGO CaSSIS Colour Images: Demonstration with Perseverance Rover Landing Site and Mars Science Targets". In: *MDPI Remote Sensing* 13.9, p. 1777. DOI: 10.3390/rs13091777.

Tazaki, Ryo et al. (Feb. 3, 2025). "JWST Imaging of Edge-on Protoplanetary Disks. IV. Mid-infrared Dust Scattering in the HH 30 Disk". In: *The Astrophysical Journal* 980.1, p. 49. ISSN: 1538-4357. DOI: 10.3847/1538-4357/ad9c6f.

Tera, F. et al. (1973). "A Lunar Cataclysm at 3.9 AE and the Structure of LunarCrust." In: *In: Proceedings of the 4th Lunar and Planetary Science Conference.* Houston, TX, USA, p. 723.

Tera, Fouad et al. (Apr. 1974). "Isotopic evidence for a terminal lunar cataclysm". In: *Earth and Planetary Science Letters* 22.1, pp. 1–21. ISSN: 0012-821X. DOI: 10.1016/0012-821x(74)90059-4.

Toyokawa, Kosei et al. (May 2022). "Kilometer-scale crater size-frequency distributions on Ceres". In: *Icarus* 377, p. 114909. ISSN: 0019-1035. DOI: 10.1016/j.icarus.2022.114909.

Turner, G. et al. (1973a). "40Ar - 39Ar Chronology of Chondrites". In: *Meteoritics* 8, pp. 447–448. URL: https://articles.adsabs.harvard.edu/pdf/1973Metic...8..447T.

Turner, G. et al. (Mar. 1973b). "Argon Selenochronology". In: *In: Proceedings of the 4th Lunar Science Conference.* Houston, TX, USA, pp. 1889–1914. URL: https://articles.adsabs.harvard.edu/cgi-bin/nph-iarticle_query?1973LPSC....4.1889T&defaultprint=YES&filetype=.pdf.

Urbach, Erik R. et al. (June 2009). "Automatic detection of sub-km craters in high resolution planetary images". In: *Planetary and Space Science* 57.7, pp. 880–887. ISSN: 0032-0633. DOI: 10.1016/j.pss.2009.03.009.

Valantinas, A. et al. (June 2024). "Evidence for transient morning water frost deposits on the Tharsis volcanoes of Mars". In: *Nature Geoscience* 17.7, pp. 608–616. ISSN: 1752-0908. DOI: 10.1038/s41561-024-01457-7.

Van den Bossche, Joris et al. (2018). "Automated detection of planetary craters: open and reproducible benchmark platform for the Martian surface". In: *European Planetary Science Congress, Septembre 2018, Berlin*, EPSC2018–679. URL: https://meetingorganizer.copernicus.org/EPSC2018/EPSC2018-679-1.pdf.

Van der Walt, Stefan et al. (2014). "scikit-image: image processing in Python". In: *PeerJ* 2, e453.

Vaswani, Ashish et al. (2017). "Attention is All you Need". In: *Advances in neural information processing systems* 30. URL: https://proceedings.neurips.cc/paper/2017/file/3f5ee243547dee91fbd053c1c4a845aa-Paper.pdf.

VikingV1 (2001). *Mars Viking Global Color Mosaic 925m v1.* NASA AMES. URL: https://astrogeology.usgs.gov/search/map/mars_viking_global_color_mosaic_925m.

VikingV2 (2009). *Mars Viking Colorized Global Mosaic 232m v2.* NASA AMES. URL: https://astrogeology.usgs.gov/search/map/mars_viking_colorized_global_mosaic_232m.

Vinogradova, Tatiana et al. (2002). "Training of a crater detection algorithm for mars crater imagery". In: *IEEE Aerospace Conference.* DOI: 10.1109/AERO.2002.1035297.

Wagstaff, Kiri L. et al. (Nov. 2022). “Using machine learning to reduce observational biases when detecting new impacts on Mars”. In: *Icarus* 386, p. 115146. ISSN: 0019-1035. DOI: 10.1016/j.icarus.2022.115146.

Wang, Yiran et al. (Aug. 2019). “Active Machine Learning Approach for Crater Detection From Planetary Imagery and Digital Elevation Models”. In: *IEEE Transactions Geoscience and Remote Sensing* 49.8. DOI: 10.1109/TGRS.2019.2902198.

Wang, Yiran et al. (2025). “Automatic Classification of Primary and Secondary Craters Near Copernicus Crater With Updated Insights on Its Impact Trajectory and Age”. In: *Journal of Geophysical Research Planet*. DOI: 10.1029/2024JE008516.

Warner, Nicholas H. et al. (Oct. 2003). “Evolved lavas on Mars? Observations from southwest Arsia Mons and Sabancaya volcano, Peru”. In: *Journal of Geophysical Research* 108.E10, p. 5112. DOI: 10.1029/2002JE001969.

Werner, S. C. et al. (Mar. 2002). “The Near-Earth Asteroid Size–Frequency Distribution: A Snapshot of the Lunar Impactor Size–Frequency Distribution”. In: *Icarius* 156.1, pp. 287–290. DOI: 10.1006/icar.2001.6789.

Werner, S.C. et al. (Oct. 2011). “Redefinition of the crater-density and absolute-age boundaries for the chronostratigraphic system of Mars”. In: *Icarus* 215.2, pp. 603–607. ISSN: 0019-1035. DOI: 10.1016/j.icarus.2011.07.024.

Werner, Stephanie C. et al. (Mar. 2014). “The Source Crater of Martian Shergottite Meteorites”. In: *Science* 343.6177, pp. 1343–1346. DOI: DOI:10.1126/science.1247282.

Werner, Stephanie C. et al. (Aug. 2023). “Review and Revision of the Lunar Cratering Chronology—Lunar Timescale Part 2”. In: *The Planetary Science Journal* 4.8, p. 147. ISSN: 2632-3338. DOI: 10.3847/psj/acdc16.

Wetherill, GW (Mar. 1975). “Late heavy bombardment of the moon and terrestrial planets”. In: *In: Proceedings of the 6thLunar and Planetary Science Conference.* Vol. 2. A78-46668 21-91. Houston, TX, USA, pp. 1539–1561. URL: https://adsabs.harvard.edu/full/1975LPSC....6.1539.

Wetzler, P.G. et al. (Jan. 2005). “Learning to Detect Small Impact Craters”. In: *2005 Seventh IEEE Workshops on Applications of Computer Vision (WACV/MOTION’05) - Volume 1*. IEEE, pp. 178–184. DOI: 10.1109/acvmot.2005.68.

Wilde, Simon A. et al. (Jan. 2001). “Evidence from detrital zircons for the existence of continental crust and oceans on the Earth 4.4 Gyr ago”. In: *Nature* 409.6817, pp. 175–178. ISSN: 1476-4687. DOI: 10.1038/35051550.

Williams, David A et al. (Oct. 2007). “Hadriaca Patera: Insights into its volcanic history from Mars Express High Resolution Stereo Camera”. In: *Journal of Geophysical Research: Planets* 112.E10. DOI: 10.1029/2007JE002924..

Wu, Bo et al. (Mar. 2022). “Landing Site Selection and Characterization of Tianwen-1 (Zhurong Rover) on Mars”. In: *Journal of Geophysical Research: Planets* 127.4. ISSN: 2169-9100. DOI: 10.1029/2021je007137.

Xiao, Zhiyong et al. (Jan. 2024). “Impact Flux on the Moon”. In: *Space: Science andTechnology* 4. ISSN: 2692-7659. DOI: 10.34133/space.0148.

Xie, Minggang et al. (Jan. 2023). "A new chronology from debiased crater densities: Implications for the origin and evolution of lunar impactors". In: *Earth and Planetary Science Letters* 602, p. 117963. ISSN: 0012-821X. DOI: `10.1016/j.epsl.2022.117963`.

Xiuqin, Pan et al. (2019). "A Fundus Retinal Vessels Segmentation Scheme Based on the Improved Deep Learning U-Net Model". In: *IEEE Access*. DOI: `10.1109/ACCESS.2019.2935138`.

Yang, Shuojin et al. (2022). "High-resolution feature pyramid network for automatic Crater detection on Mars". In: *IEEE Transactions on Geoscience and Remote Sensing* 60, pp. 1–12. DOI: `10.1109/TGRS.2021.3104925`.

Young, J (1940). "A statistical investigation of diameter and distribution of lunar craters". In: *J. Brit. Astron. Assoc* 50.9, p. 309326.

Zaidi, Syed Sahil Abbas et al. (June 2022). "A survey of modern deep learning based object detection models". In: *Digital Signal Processing* 126, p. 103514. ISSN: 1051-2004. DOI: `10.1016/j.dsp.2022.103514`.

Zellner, Nicolle E. B. (May 2017). "Cataclysm No More: New Views on the Timing and Delivery of Lunar Impactors". In: *Origins of Life and Evolution of Biospheres* 47.3, pp. 261–280. ISSN: 1573-0875. DOI: `10.1007/s11084-017-9536-3`.

Zent, A (Aug. 2008). "A historical search for habitable ice at the Phoenix landing site". In: *Icarus* 196.2, pp. 385–408. ISSN: 0019-1035. DOI: `10.1016/j.icarus.2007.12.028`.

Zhang, Zongyu et al. (2025). "A Gigantic Flow on Mars Revealed by Zhurong Rover". In: *Nature Astronomy*. Under Review.

Zhou, Yi et al. (Oct. 2018). "Automatic detection of lunar craters based on DEM data with the terrain analysis method". In: *Planetary and Space Science* 160, pp. 1–11. ISSN: 0032-0633. DOI: `10.1016/j.pss.2018.03.003`.

Zuber, M. T. et al. (May 1992). "The Mars Observer laser altimeter investigation". In: *Journal of Geophysical Research: Planets* 97.E5, pp. 7781–7797. ISSN: 0148-0227. DOI: `10.1029/92je00341`.

Zuo, Wei et al. (Dec. 2016). "Contour-based automatic crater recognition using digital elevation models from Chang'E missions". In: *Computers and Geosciences* 97, pp. 79–88. ISSN: 0098-3004. DOI: `10.1016/j.cageo.2016.07.013`.